

THE APPLICATION OF ISOTHERMAL MICROCALORIMETRY TO THE STUDY
OF PARASITIC REACTIONS IN LITHIUM ION BATTERIES

by

Laura Elizabeth Downie

Submitted in partial fulfilment of the requirements
for the degree of Doctor of Philosophy

at

Dalhousie University
Halifax, Nova Scotia
July 2015

To my loving family

old and new,

TABLE OF CONTENTS

LIST OF TABLES	vi
LIST OF FIGURES	viii
ABSTRACT.....	xx
LIST OF ABBREVIATIONS AND SYMBOLS USED	xxi
ACKNOWLEDGEMENTS	xxv
CHAPTER 1 Introduction	1
1.1 Lithium Ion Cells	1
1.2 Components of Lithium Ion Cells.....	2
1.2.1 Overview	2
1.2.2 Positive Electrode	5
1.2.3 Negative Electrode.....	7
1.2.4 Electrolyte	9
1.2.5 Separator	11
1.2.6 Form Factor.....	12
1.3 Characterization of Cell Performance.....	13
1.4 Causes of Cell Failure	15
1.4.1 SEI Growth and Repair	15
1.4.2 Electrolyte Oxidation	17
1.4.3 Other Causes	19
1.5 Electrolyte Additives.....	20
1.6 Scope and Outline of Thesis	24

CHAPTER 2 Isothermal Microcalorimetry of Lithium Ion Cells	27
2.1 Introduction to Isothermal Microcalorimetry	27
2.2 Sources of Heat Flow in Lithium Ion Cells	27
2.2.1 Energy Balance Model.....	27
2.2.2 Polarization	31
2.2.3 Entropy.....	35
2.2.4 Parasitic Reactions	41
2.3 Previous Isothermal Microcalorimetry Studies of Lithium Ion Cells.....	42
2.4 Advantages and Limitations of Isothermal Calorimetry.....	45
CHAPTER 3 Experimental Techniques	47
3.1 Cell Construction	47
3.1.1 Electrolyte Preparation.....	47
3.1.2 Cell Preparation	47
3.1.3 Cell Formation	50
3.1.4 Summary of Cells and Preparation Methods Used in This Work.....	51
3.2 Cell Cycling	52
3.3 Gas Generation Measurements	54
3.4 Isothermal Microcalorimetry	56
3.4.1 Operation.....	56
3.4.2 Experimental Setup.....	59
3.4.3 Baseline and Calibration	61
3.4.4 Resolution, Stability, and Reproducibility.....	64
CHAPTER 4 The Impact of Electrolyte Additives Determined Using Comparitive Isothermal Microcalorimetry	67
4.1 Introduction and Motivation	67

4.2 Experimental Details.....	68
4.3 The Effect of Electrolyte Additives on NMC111/Graphite 4.2 V and 4.4 V Pouch Cells.....	70
4.3.1 The Effect of VC and Ternary Electrolyte Additive Blends on 4.4 V NMC111/Graphite Cells.....	70
4.3.2 The Effect of VC on the Open Circuit Heat Flow for 4.2 V NMC111/Graphite Pouch Cells.....	82
4.3.3 Comparison of Calorimetric Results to High Precision Cycling Results	85
4.4 Conclusions.....	91
CHAPTER 5 Determination of the Voltage Dependence of the Parasitic Heat Flow	92
5.1 Introduction and Motivation	92
5.2 Separation of the Total Heat Flow Into Components	93
5.2.1 The Time Independent Empirical Heat Flow Model	93
5.2.2 Fitting Method	95
5.3 Extraction of the Parasitic Heat Flow for a High Voltage LCO/Graphite Cell	96
5.3.1 Experimental Details.....	96
5.3.2 Results and Discussion	97
5.4 Effect of the Electrolyte on the Parasitic Heat Flow for NMC111/Graphite Pouch Cells.....	104
5.4.1 Experimental Details.....	104
5.4.2 Results and Discussion	105
5.5 Comparison of Parasitic Heat Flow Between LCO/Graphite and NMC111/Graphite Pouch Cells	114
5.6 Conclusions.....	117
CHAPTER 6 Determination of the Voltage and Time Dependence of the Parasitic Heat Flow	119
6.1 Introduction and Motivation	119

6.2 Inclusion of Time Dependence In The Parasitic Heat Flow	119
6.2.1 Identification of Time Dependence	119
6.2.2 The Time Dependent Empirical Heat Flow Model.....	122
6.2.3 Fitting Method	123
6.3 Extraction of the Voltage And Time Dependent Parasitic Heat Flow For HV- LCO/Graphite and NMC442/Graphite Cells	126
6.3.1 Experimental Details.....	126
6.3.2 Results and Discussion for HV-LCO/Graphite Pouch Cells	127
6.3.3 Results and Discussion for NMC442/Graphite Pouch Cells	137
6.4 Determination of the Impact of Electrolyte Additives and Solvents on NMC811/Graphite Pouch Cells	147
6.4.1 Introduction and Motivation	147
6.4.2 Experimental Details.....	148
6.4.3 Results and Discussion	149
6.5 Conclusions.....	166
CHAPTER 7 Examination of the Robustness of the Time Dependent Empirical Model.....	167
7.1 Introduction and Motivation	167
7.2 Inclusion of a Heat Flow Component Due To Hysteresis	168
7.2.1 Identification of the Need of a Hysteresis Term for NMC442/Graphite Cells.....	168
7.2.2 Hysteresis in Electrode Materials	175
7.2.3 The Time Dependent Empirical Model Including Hysteresis	180
7.3 Impact of Differences in Data Collection Methodologies	188
7.3.1 Increasing versus Decreasing Current	188
7.3.2 Impact of Current Choice.....	190
7.3.3 Impact of Variable Current Experiments over Wider Voltage Ranges	193

7.4 Conclusions.....	198
CHAPTER 8 Determination of the Impact of High Voltage Electrolyte Additives and Solvents.....	200
8.1 Introduction and Motivation	200
8.2 Experimental Details.....	200
8.3 Determination of the Impact of Electrolyte Composition on 4.7 V NMC442/Graphite Cells	202
8.3.1 Determination of the Impact of Electrolyte Composition up to 4.5 V.....	202
8.3.2 Using 1 mA Cycles to Determine the Impact of Electrolyte Composition up to 4.7 V	211
8.4 Comparison of Parasitic Heat Flow Results to Cell Performance	216
8.5 Conclusions.....	222
CHAPTER 9 The Use of Open Circuit Experiments To Examine The Origin and Implications of the Parasitic Heat Flow	224
9.1 Introduction and Motivation	224
9.2 Thought Experiments	224
9.3 Open Circuit Heat Flow Measurements.....	229
9.3.1 Experimental Details.....	229
9.3.2 Long Term Open Circuit Heat Flow Measurements.....	231
9.4 Conclusions.....	240
CHAPTER 10 Conclusions and Future Work	242
10.1 Conclusions.....	242
10.2 Future Work	246
REFERENCES.....	253
APPENDIX A License Agreements.....	268

LIST OF TABLES

Table 3.1: Suppliers and purities of all electrolyte components used.....	48
Table 3.2: Summary of formation protocols used throughout this work.	51
Table 3.3: Summary of cells used in this work.....	52
Table 3.4: Summary of cell preparation methods used in this work.....	52
Table 3.5: Resolution and accuracy of current and voltage, as well as the time between measurements (Δt) for charging systems used in this work.	53
Table 5.1: Summary of the parameters as determined from the fit to the time independent empirical model for an HV-LCO/graphite pouch cell containing 2% VC.	102
Table 5.2: Summary of root mean squared error of the total fit for all cells and all voltage ranges examined.	108
Table 6.1: Summary of the parameters describing the heat flow due to parasitic reactions as determined from the fit to the time dependent empirical model for HV-LCO/graphite pouch cells. Comparison is also made with respect to the time independent model.	132
Table 6.2: Summary of the parameters describing the heat flow due to parasitic reactions as determined from the fit to the empirical model for NMC442/graphite pouch cells.	139
Table 6.3: Summary of RMSE of fit for all NMC811/graphite cells for all voltage ranges investigated.	155
Table 6.4: Summary of measured ΔV for cycles 4 and 50 for cells containing 2% VC or P211M cycled to various upper cutoff voltages.	157

Table 7.1: Summary of extracted $R_{internal}$ and $V_{hysteresis}$ values and R^2 of linear fit for NMC442/graphite and NMC811/graphite pouch cells.	172
Table 7.2: Summary of extracted $R_{internal}$ and $V_{hysteresis}$ values and R^2 of linear fit for positive electrode half cells.	179
Table 7.3: Comparison of extracted parasitic heat flow parameters for NMC811/graphite cells containing P211M between 4.1 – 4.2 V for decreasing and increasing currents.	189
Table 7.4: Summary and comparison of extracted parameters of all heat flow components of NMC442/graphite pouch cells for three voltage ranges: 4.2 – 4.3 V, 4.3 – 4.4 V, 4.4 – 4.5 V for four- and six-current measurements..	192
Table 8.1: Summary of electrolyte compositions examined and amounts added to NMC442/graphite pouch cells.	201
Table 8.2: Summary of RMSE of fit for all NMC442/graphite cells for all voltage ranges examined.	203
Table 9.1: Comparison of measured heat flow, calculated $ I_pV $ values, the difference between them, and an extracted average reaction enthalpy at three time points of a low-V cell.	239

LIST OF FIGURES

Figure 1.1: Simplified schematic representation of a lithium ion cell.	3
Figure 1.2: Voltage as a function of capacity during galvanostatic cycling for graphite and layered metal oxide half cells, and for a corresponding layered metal oxide/graphite full cell.	5
Figure 1.3: Structure of a layered lithium metal oxide in the fully lithiated state..	6
Figure 1.4: SEM image of a NMC442 electrode..	7
Figure 1.5: Structure of graphite in the fully delithiated state..	8
Figure 1.6: SEM image of a graphite electrode..	8
Figure 1.7: Chemical structures of commonly used carbonate electrolyte solvents.....	10
Figure 1.8: Chemical structures of some reported beneficial non-carbonate electrolyte solvents and co-solvents.....	11
Figure 1.9: Three common lithium ion cell designs: a coin cell, a flat-wound pouch cell, and a cylindrically wound cell.	12
Figure 1.10: The deconstruction of a flat-wound pouch cell.	13
Figure 1.11: Three methods of evaluating cell performance: (a) discharge capacity fade, (b) charge endpoint capacity slippage, and (c) coulombic efficiency (CE).....	14
Figure 1.12: Simplified possible mechanisms of SEI growth where new SEI is formed (a) on the surface of the existing SEI or (b) closer to the negative electrode.....	17
Figure 1.13: Possible mechanisms of electrolyte oxidation during closed circuit conditions.....	18

Figure 1.14: Other possible degradation mechanisms, including (a) a shuttle and (b) transition metal dissolution..	19
Figure 1.15: Chemical structures of the electrolyte additives used in this thesis..	22
Figure 2.1: A graphical representation of the heat associated with polarization and inherent hysteresis.....	32
Figure 2.2: Discharge capacity as a function of current in terms of C rate for an NMC111/graphite pouch cell at -14 °C.	33
Figure 2.3: Voltage as a function of state of charge for an NMC442/graphite pouch cell charged at 10 mA (C/26) for 5 minutes then allowed to rest for 2 hours to illustrate the variation of the overpotential with state of charge.....	34
Figure 2.4: Lattice gas model of entropy and change in entropy with respect to the fraction of filled sites, x , in Li_xHost	36
Figure 2.5: Measured change in entropy as a function of state of charge using two methods, potentiometric and electrothermal impedance spectroscopy for three commercial cells made by KOKAM, Sony, and A123. Figure reproduced with permission from <i>Electrochim. Acta</i> 137 , 311 (2014) ¹⁹²	37
Figure 2.6: Voltage and corresponding heat flow as a function of specific capacity during a C/10 charge and discharge of an NMC111/Li coin cell.	38
Figure 2.7: Voltage and corresponding heat flow as a function of specific capacity during a C/10 charge and discharge of a graphite/Li coin cell.	39
Figure 2.8: Voltage and corresponding heat flow as a function of capacity during a C/10 charge and discharge of an NMC111/graphite coin cell.	40
Figure 2.9: Voltage and corresponding heat flow as a function of capacity during a C/22.5 charge and discharge of an LCO/graphite pouch cell.	41
Figure 3.1: Schematic of gas measurement experimental setup..	55

Figure 3.2: TAMIII isothermal microcalorimeter equipped with 12 calorimeters.	56
Figure 3.3: Schematic of the microcalorimeter measuring assembly used in the TAMIII.....	57
Figure 3.4: The lifter and sample ampoule assembly used in the TAMIII.	60
Figure 3.5: Heat flow response of a calibration cell during baseline process.....	62
Figure 3.6: Heat flow response during calibration process where 15 mA was applied to a 10 Ω resistor for three hours.....	62
Figure 3.7: Heat flow response of a pouch bag filled with 3:7 EC:EMC and 1M LiPF ₆ in 3:7 EC:EMC..	63
Figure 3.8: Variation in bath temperature of the TAMIII over a period of 2.5 months.....	65
Figure 3.9: Heat flow at open circuit conditions for 6 identical LCO/graphite pouch cells containing control electrolyte starting from 3.8 V.....	65
Figure 3.10: Cell-to-cell variation for NMC442/graphite pouch cells measured at 1 mA (C/260)	66
Figure 4.1: Complete experimental cycling protocol for all cells tested..	71
Figure 4.2: Example of observed heat flow as a function of voltage for cells containing control electrolyte and 4% VC measured at 10 mA.....	74
Figure 4.3: Heat flow as a function of voltage for cells containing control, 1% VC, 2% VC, 4% VC, 211MMDS, 211DTD, 211TMS measured at 10 mA (C/24) and 40°C.....	75
Figure 4.4: Zoom in of heat flow as a function of voltage up to 4.4 V for cells containing control, 1% VC, 2% VC, 4% VC, 211MMDS, 211DTD, 211TMS measured at 10 mA (C/24) and 40°C.	77

Figure 4.5: Difference in heat flow between additive-containing cells and control measured at 10 mA (C/24).....	78
Figure 4.6: Heat flow as a function of voltage for cells containing control, 1% VC, 2% VC, 4% VC, 211MMDS, 211DTD, 211TMS measured at 2 mA (C/120).....	80
Figure 4.7: Heat flow for control, 1% VC, 2% VC, and 4% VC cells measured during 25 hours of open circuit conditions starting from 4.2 V.....	84
Figure 4.8: Ultra high precision coulometry results for NMC111/graphite cells cycled between 2.8 – 4.2 V at C/20 and 40°C for a variety of electrolyte additives..	86
Figure 4.9: Electrochemical impedance spectra of NMC111/graphite cells collected after 16 ultra high precision charger cycles at 3.8 V and 10°C.....	88
Figure 4.10: Normalized discharge capacity as a function of cycle number for NMC111/graphite pouch cells cycled between 2.8 – 4.2 V at C/2.5 and 55°C	89
Figure 4.11: The fractional capacity remaining after 200 2.8 – 4.2 V cycles at C/2.5 and 55°C as a function of gas produced and coulombic inefficiency per hour.....	90
Figure 5.1: Heat flow as a function of voltage for an NMC111/graphite pouch cell showing that the heat flow varies smoothly and can be approximated using simple polynomial functions.....	94
Figure 5.2: Summary of narrow range variable rate experimental procedure for an HV-LCO/graphite pouch cell.....	98
Figure 5.3: Measured and calculated heat flows as a function of relative state of charge (rSOC) between 4.2 and 4.3 V for an HV-LCO/graphite pouch cell containing 2% VC at 10, 5, 2, and 1 mA.	99
Figure 5.4: Separation of the total measured heat flow into the extracted components: polarization, entropy, and parasitic heat flows	100

Figure 5.5: Measured and calculated heat flow as a function of rSOC between 4.2 – 4.3 V and 4.3 – 4.4 V for an HV-LCO/graphite pouch cell containing 2% VC at 10, 5, 2, and 1 mA.	102
Figure 5.6: Extracted parasitic heat flow as a function of rSOC between 4.2 and 4.4 V for an HV-LCO/graphite pouch cell containing 2% VC.....	103
Figure 5.7: Heat flow as a function of voltage measured during the fourth 10 mA cycle for NMC111/graphite pouch cells with various electrolytes.....	106
Figure 5.8: Measured and calculated heat flow as a function of rSOC between 4.0 and 4.1 V for NMC111/graphite pouch cells containing control and 2% VC at 10, 5, 2, and 1 mA.....	107
Figure 5.9: Extracted parasitic heat flow as a function voltage for NMC111/graphite pouch cells with various electrolytes.....	110
Figure 5.10: Extracted parasitic heat flow and average of 1 mA charge and discharge heat flows as a function of voltage between 4.1 – 4.2 V for NMC111/graphite cells containing a variety of electrolytes.	111
Figure 5.11: Extracted parasitic heat flow from 4.1 – 4.2 V and average of 1 mA charge and discharge heat flows from 4.2 – 4.3 V for NMC111/graphite cells containing a variety of electrolytes.....	114
Figure 5.12: Normalized parasitic heat flow as a function of voltage between 4.2 – 4.3V for HV-LCO/graphite and NMC111/graphite pouch cells containing control electrolyte plus 2% VC and 2% VC + 1% TTSPi + 1% MMDS.	115
Figure 5.13: SEM image of a graphite electrodes used in HV-LCO/graphite and NMC111/graphite pouch cells.....	117
Figure 6.1: Deviations between measured and calculated time independent heat flow of an HV-LCO/graphite pouch cell containing 2% VC.....	120

Figure 6.2: Evolution of measured heat flow over four consecutive 10 mA cycles of an HV-LCO/graphite pouch cell containing 2% VC between 2.8 – 4.4 V.....	121
Figure 6.3: Open circuit heat flow of an LCO/graphite pouch cell containing 1% VC showing a nearly linear time dependence over a $\Delta t = 50$ h segment after long experiment times.....	122
Figure 6.4: Screenshot of in-house developed software used to fit heat flow data with the time dependent empirical model.....	124
Figure 6.5: Comparison of calculated heat flow using a time independent and time dependent model for an HV-LCO/graphite pouch cell containing 2% VC.....	129
Figure 6.6: Measured and calculated heat flow as a function of voltage for HV-LCO/graphite pouch cells containing 2% VC and V211M..	130
Figure 6.7: Comparison of extracted parasitic heat flow as a function of voltage for an HV-LCO/graphite pouch cell containing 2% VC and V211M between a time independent and dependent model.....	131
Figure 6.8: Evolution of the extracted parasitic heat flow as a function of voltage and time for HV-LCO/graphite pouch cells containing 2% VC and V211M.....	133
Figure 6.9: Volume of gas produced during the wetting and formation procedure, and after the entire cycling procedure for HV-LCO/graphite cells containing 2% VC and V211M.	135
Figure 6.10: Voltage, heat flow, parasitic heat flow, and scaling factor as a function of time for HV-LCO/graphite pouch cells containing 2% VC and V211M.....	136
Figure 6.11: Measured and calculated heat flow as a function of voltage for NMC442/graphite pouch cells containing control and P211M at 10, 5, 2, and 1 mA.....	138

Figure 6.12: Evolution of the extracted parasitic heat flow as a function of voltage and time for an NMC442/graphite pouch cell containing control and P211M.....	140
Figure 6.13: Volume of gas produced during the first formation process, during the second formation process, and after all cycling was completed for NMC442/graphite cells containing control and P211M	142
Figure 6.14: Voltage, heat flow, parasitic heat flow, and scaling factor as a function of time for NMC442/graphite pouch cells containing control and P211M..	142
Figure 6.15: Measured heat flow as a function of voltage for NMC442/graphite pouch cells containing P211M during 1 mA cycles with one cycle where cells were charged to either 4.3, 4.5, or 4.6 V	143
Figure 6.16: Expanded view of heat flow as a function of voltage for NMC442/graphite pouch cells containing P211M during 1 mA cycles following one cycle to an upper cutoff voltage of either 4.3, 4.5, or 4.6 V.....	145
Figure 6.17: Measured heat flow as a function of time for NMC442/graphite pouch cells containing P211M for 1 mA cycles with one cycle where cells were charged to either 4.3, 4.5, or 4.6 V	146
Figure 6.18: Voltage versus capacity for NMC811/Li coin cells containing cycled at C/20 with an upper cutoff voltage of 4.1, 4.2, 4.3 and 4.4 V (vs. Li/Li ⁺).....	150
Figure 6.19: Discharge capacity as a function of cycle number for NMC811/graphite pouch cells containing 2%VC or P211M as a function of upper cutoff voltage.	150
Figure 6.20: Rietveld refinement results of <i>in situ</i> XRD data for an NMC811/Li half cell showing the extracted <i>a</i> and <i>c</i> lattice parameters as a function of cell voltage	152

Figure 6.21: Measured and calculated heat flow as a function of rSOC for an NMC811/graphite pouch cell containing 2% VC.....	154
Figure 6.22: The extracted polarization, entropic, and parasitic heat flow components as a function of the rSOC for NMC811/graphite cells containing 2% VC and P211M.	156
Figure 6.23: The extracted polarization, entropic, and parasitic heat flow components as a function of the rSOC for NMC811/graphite cells containing control, 2% VC, V211M, P211M, 2% TAP, and FEC:TFEC	159
Figure 6.24: Extracted parasitic heat flow as a function of rSOC between 4.1 - 4.4 V for NMC811/graphite pouch cells containing a variety of electrolytes	160
Figure 6.25: Extracted parasitic heat flow as a function of rSOC between 4.3 – 4.4 V for NMC811/graphite pouch cells containing a variety of electrolytes	162
Figure 6.26: Summary of the time dependent parasitic heat flow measured at the top of charge for NMC811/graphite cells between 4.1 and 4.4 V..	163
Figure 6.27: <i>In situ</i> gas generation as a function of cell voltage for NMC811/graphite pouch cells containing control, 2%VC, and 2%PES during the first C/20 charge up to 4.7 V.	164
Figure 7.1: The extracted polarization, entropic, and parasitic heat flow components as a function of rSOC for NMC442/graphite pouch cells containing control and V211M.	168
Figure 7.2: Voltage versus capacity for an NMC442/graphite pouch cell containing V211M as a function of current for three voltage ranges: 4.2 – 4.3 V, 4.3 – 4.4 V, and 4.4 – 4.5 V	170
Figure 7.3: Voltage as a function of rSOC for an NMC442/graphite cell containing V211M for 5, 2, and 1 mA cycles.....	171

Figure 7.4: Overpotential as a function of current for NMC442/graphite and NMC811/graphite pouch cells containing V211M.....	172
Figure 7.5: Heat flow as a function of rSOC and average heat flow at 0.5 rSOC for an NMC442/graphite pouch cell containing V211M as a function of current. ...	174
Figure 7.6: Average heat flow as a function of current for an NMC442/ graphite pouch cell containing V211M for three voltage ranges: 4.2 – 4.3 V, 4.3 – 4.4 V, and 4.4 – 4.5 V.. ..	175
Figure 7.7: Voltage as a function of rSOD for a graphite/Li half cell at three currents: C/2000, C/1000, and C/100	177
Figure 7.8: Overpotential as a function of current for a graphite/Li half cell at approximate rSOD values of 0.70, 0.74, 0.78, and 0.82.....	177
Figure 7.9: Voltage as a function of rSOC for NMC111/Li, NMC811/Li, NMC442/Li, and HV-LCO/Li half cells measured at five rates: C/20, C/30, C/40, C/50, and C/100.	178
Figure 7.10: Overpotential as a function of current for NMC442/Li, NMC111/Li, NMC811, and HV-LCO/Li half cells at 0.5 rSOC	179
Figure 7.11: Screenshot of modified in-house developed software used to fit heat flow data with the time dependent empirical model including hysteresis.	181
Figure 7.12: Extracted heat flows resulting from fitting method (i) during a 5 mA charge due to polarization, hysteresis, changes in entropy, and parasitic reactions	182
Figure 7.13: Extracted heat flows resulting from fitting method (ii) during a 5 mA charge due to hysteresis, changes in entropy, and parasitic reactions.	182

Figure 7.14: Extracted heat flows resulting from fitting method (iii) during a 5 mA charge due to polarization, hysteresis, changes in entropy, and parasitic reactions.	183
Figure 7.15: Extracted heat flows resulting from fitting method (iv) during a 5 mA charge due to polarization, hysteresis, changes in entropy, and parasitic reactions	183
Figure 7.16: Extracted heat flows resulting from fitting method (iv) during a 1 mA charge compared to the total measured heat flow.....	185
Figure 7.17: The extracted heat flow components as a function of rSOC for NMC442/graphite pouch cells containing control and V211M.....	186
Figure 7.18: Comparison of the extracted parasitic heat flow determined using the three-component time dependent empirical model and the four-component model that includes hysteresis for NMC442/graphite cells containing control and V211M	187
Figure 7.19: Measured and calculated heat flow for NMC811/graphite pouch cells containing P211M cycled between 4.1 – 4.2 V with decreasing currents and increasing currents.	189
Figure 7.20: Measured and calculated heat flow for NMC442/graphite pouch cells containing P211M cycled between 4.2 – 4.3 V using four currents and six currents.....	191
Figure 7.21: Voltage as a function of time showing the experimental protocol of cycling cells with variable currents over multiple narrow voltage ranges and one wide voltage range.	195
Figure 7.22: Calculated and measured heat flow between 4.2 – 4.3 V for NMC442/graphite pouch cells containing P211M cycled between either 4.2 – 4.3 V or 4.1 – 4.5 V.	196

Figure 7.23: Extracted components of total heat flow between 4.2 V and 4.4 V for NMC442/graphite pouch cells cycled either over narrow voltage ranges or a wide voltage range.	197
Figure 8.1: Measured and calculated heat flow as function of rSOC between 4.2 and 4.5 V for an NMC442/graphite pouch cell containing V211M	203
Figure 8.2: The extracted heat flow components as a function of rSOC for NMC442/graphite cells containing various electrolyte compositions	204
Figure 8.3: Extracted parasitic heat flow as a function of rSOC for NMC442/graphite pouch cells containing various electrolyte compositions.	205
Figure 8.4: Extracted parasitic heat flow as a function of rSOC for NMC442/graphite pouch cells containing control-based or fluorinated solvents	207
Figure 8.5: Summary of the time dependent parasitic heat flow measured at the top of charge for NMC442/graphite cells with various electrolyte compositions	210
Figure 8.6: Average of 1 mA charge and discharge heat flows as a function of voltage for NMC442/graphite cells containing various electrolytes cycled between 4.2 – 4.5 V and 4.2 – 4.7 V.....	212
Figure 8.7: Average of 1 mA charge and discharge heat flows as a function of voltage between 4.2 – 4.5 V during narrow voltage range cycling, a 1 mA 4.1 – 4.5 V cycle, and a 1 mA 4.1 – 4.7 V cycle for NMC442/graphite pouch cells containing control + P211M or FEC:TFEC.....	213
Figure 8.8: Measured heat flow as a function of voltage during narrow voltage range cycling, a 1 mA 4.1 – 4.5 V cycle, and a 1 mA 4.1 – 4.7 V cycle for NMC442/graphite pouch cells control + P211M or FEC:TFEC.	215

Figure 8.9: Normalized discharge capacity as a function of cycle number for NMC442/graphite pouch cells containing 2%VC and FEC:TFEC cycled between 2.8 – 4.5 V at 40 mA	217
Figure 8.10: Charge capacity as a function of cycle number for NMC442/graphite cells containing V211M and FEC:TFEC cycled at 2 mA between 4.2 – 4.3 V and 4.4 – 4.5 V (open symbols).	218
Figure 8.11: Images of separator from fully disassembled cells after being removed from calorimeter.....	220
Figure 8.12: Volume of gas produced during the first and second formation processes and after all cycling was completed in the calorimeter for NMC442/graphite cells containing various electrolyte compositions	221
Figure 9.1: Schematic of an idealized cell connected to a resistor either inside or outside the calorimeter.....	225
Figure 9.2: Schematics of shuttle mechanism and electrolyte oxidation occurring during open circuit conditions.....	226
Figure 9.3: Measured open circuit heat flow and calculated parasitic current as a function of time at open circuit starting at 4.1 V for a low-V cell.....	232
Figure 9.4: Measured open circuit heat flow, measured voltage, calculated I_p and heat flow from $ I_p V $ as a function of time at open circuit for low-V and high-V cells starting from 4.1 V, 4.2 V, and 4.3 V	234
Figure 9.5: Pair cell reproducibility of measured open circuit open heat flow as a function of time at open circuit starting at 4.1 V for low-V and high-V cells	237
Figure 9.6: Measured open circuit heat flow, measured voltage, calculated I_p and heat flow from $ I_p V $ as a function of time for a low-V cell during two open circuit segments starting at 4.2 V	238

ABSTRACT

In an ongoing effort to advance the understanding of how electrolyte composition impacts the performance and lifetime of lithium ion cells, this work introduces the use of isothermal microcalorimetry as a tool to measure the heat flow associated with the parasitic reactions that cause cell degradation. This technique is rapid, *in situ*, *in operando*, and the results are a direct function of voltage.

The majority of this work focuses on the development of the method to extract and understand the parasitic heat flow as a function of both voltage and time. This was achieved by measuring the heat flow for cells undergoing narrow voltage range cycling at various currents, then fitting the measured total heat flow to an empirical model to isolate each component of the heat flow as a function of state of charge. Particular emphasis was placed on the heat flow resulting from parasitic reactions and as such, this work presents the first direct measurements on the voltage-dependent impact of the electrolyte composition on the parasitic reactions occurring in lithium ion cells.

The parasitic heat flow was determined for LCO/graphite and several types of NMC/graphite pouch cells containing a variety of electrolyte compositions. Cells containing electrolyte additives that result in increased cell lifetimes were found to have decreased parasitic heat flows, and therefore decreased reaction rates, especially at high voltages. The determination of the time dependence of the parasitic heat flow highlighted profound changes in the reaction mechanisms as a function of voltage, including the observation of an increasing parasitic heat flow as a function of time for LCO/graphite cells containing 2%VC + 1%TTSPi + 1%MMDS above 4.3 V. Experiments on NMC442/graphite cells showed distinct differences in the voltage behaviour of the parasitic heat flow for cells containing either carbonate or fluorinated carbonate solvents, and showed that fluorinated solvents are only advantageous above 4.4 V.

The results presented in this work have provided valuable insight on the complex roles of the electrode and electrolyte compositions on the parasitic reactions in lithium ion cells, as well as how those roles depend on both voltage and time.

LIST OF ABBREVIATIONS AND SYMBOLS USED

a	a lattice parameter
c	c lattice parameter
CE	Coulombic efficiency
C_r	Heat capacity of the reference system
C_s	Heat capacity of the sample system
DEC	Diethyl carbonate (CAS#105-58-8)
DMC	Dimethyl carbonate (CAS# 616-38-6)
$\dot{d}q/dt$	Heat flow
dQ/dV	Differential capacity
$\dot{d}q_p/dt$	Parasitic heat flow
$\dot{d}q_r/dt$	Heat flow of reference system
DTD	1,3,2-dioxathiolane-2,2-dioxide (CAS# 1072-53-3)
e	Elementary electron charge
EA	Ethyl acetate (CAS# 141-78-6)
EC	Ethylene carbonate or 1,3-dioxolan-2-one (CAS# 96-49-1)
EDS	Energy dispersive spectroscopy
EIS	Electrochemical impedance spectroscopy
EMC	Ethyl methyl carbonate (CAS# 623-53-0)
F	Faraday constant
F_B	Buoyant force
FEC	Fluoroethylene carbonate or 4-Fluoro-1,3-dioxolan-2-one (CAS# 114435-02-8)
G	Gibbs free energy
GITT	Galvanostatic intermittent titration technique
HV-LCO	High voltage LiCoO ₂
I	Current
I_p	Parasitic current
k	Reaction rate

k_B	Boltzmann constant
k_s	Heat conductance of the sample system
L	Time factor (relative rate of change of the parasitic heat flow with time)
LCO	LiCoO ₂
LiBOB	Lithium bis(oxalato)borate (CAS# 244761-29-3)
LiFSI	Lithium bis(fluorosulfonyl)imide (CAS# 171611-11-3)
LiODFB	Lithium difluoro(oxalate)borate (CAS# 409071-16-5)
MMDS	Methylene methanedisulfonate or 1,5,2,4-dioxadithiane-2,2,4,4-tetraoxide (CAS# 99591-74-9)
MP	Methyl propanoate (CAS# 554-12-1)
$m_{balance}$	Mass measured by balance
m_{cell}	Mass of cell
n	Number of filled sites
N	Number of available sites
NMC111	Li[Ni _{1/3} Mn _{1/3} Co _{1/3}]O ₂
NMC442	Li[Ni _{0.42} Mn _{0.42} Co _{0.16}]O ₂
NMC811	Li[Ni _{0.8} Mn _{0.1} Co _{0.1}]O ₂
n_p	Number of points used in fit
OCV	Open circuit voltage
P	Pressure
P211M	2% PES + 1% TTSPi + 1% MMDS
PES	Prop-1-ene-1,3-sultone or 5H-oxathiole 2,2-dioxide (CAS# 21806-61-1)
PVDF	Poly(vinylidene fluoride) or poly(1,1-difluoroethylene) (CAS# 24937-79-9)
q	Heat
Q	Capacity
Q_c	Charge capacity
Q_d	Discharge capacity
q_p	Parasitic energy
R_{ct}	Charge transfer resistance
$R_{internal}$	Internal cell resistance
RMSE	Root mean squared error

rSOC	Relative state of charge
rSOD	Relative state of discharge
s	Entropy per site
S	Shuttle molecule
S	Total entropy
S_b	Seebeck coefficient
SEI	Solid electrolyte interphase
SEM	Scanning electron microscope
t	Time
T	Temperature
T_0	Temperature of environment
TAP	Triallyl phosphate (CAS# 1623-19-4)
TFEC	Bis(2,2,2-trifluoroethyl) carbonate (CAS# 1513-87-7)
TMS	1,3,2-dioxathiane 2,2-dioxide (CAS# 1073-05-8)
T_s	Temperature of the sample system
TTSP	Tris(trimethylsilyl) phosphate (CAS# 10497-05-9)
TTSPi	Tris(trimethylsilyl) phosphite (CAS# 1795-31-9)
U	Internal energy
UHPC	Ultra high precision charger
V211M	2% VC + 1% TTSPi + 1% MMDS
VC	Vinylene carbonate or 1,3-dioxol-2-one (CAS# 872-36-6)
V_{cell}	Cell volume
V_{cell}	Cell voltage
V_{eq}	Equilibrium cell voltage
V_{gas}	Volume of gas produced
$V_{hysteresis}$	Hysteresis voltage
V_r	Reference voltage difference
V_s	Sample voltage difference
W	Work
x	Fraction of filled sites
X	Electrolyte component molecule

XPS	X-ray photoelectron spectroscopy
XRD	X-ray diffraction
y_{calc}	Calculated data
y_{meas}	Measured data
z	Relative state of charge
$\Delta_{ox}H$	Oxidation enthalpy
Δ_rH	Reaction enthalpy
Δ_rH^{ave}	Weighted average of reaction enthalpies
$\Delta_{red}H$	Reduction enthalpy
Δ_rS	Reaction entropy
Δt	Experiment time range
ΔT_s	Difference in temperature between the sample system and environment
ΔV	Difference in average charge and discharge voltage
ε_s	Sample calibration constant
ε_r	Reference calibration constant
η	Overpotential
μ	Chemical potential
ρ_{fluid}	Fluid density
τ_r	Time constant of the reference system
τ_s	Time constant of the sample ampoule system
Φ	Rate of heat exchange
χ^2	Chi squared

ACKNOWLEDGEMENTS

First and foremost, I would like to sincerely thank my supervisor, Dr. Jeff Dahn, for all his encouragement, understanding, enthusiasm, and insistence on being mentally engaged. It has been an honour, and I am very grateful to have had the opportunity to learn from one of the best.

I would also like to acknowledge support from NSERC and the Dalhousie Research in Energy, Advanced Materials, and Sustainability (DREAMS) program. Thanks also go to the administration staff in the Physics Office, including, but not limited to, Barbara Gauvin and Tanya Timmins, as well as Janet MacDonald, the DREAMS coordinator.

Special thanks go to Larry Krause for welcoming me to the team during my internship at 3M in Minnesota, and introducing me to isothermal microcalorimetry. I would also like to acknowledge Vincent Chevrier and Lowell Jensen at 3M for their help, advice, and many laughs during my time there.

I would also like to acknowledge the many people in the Dahn Lab, past and present that have made these past years some of the best of my life. Thanks to David Stevens and Robbie Sanderson for always making sure the lab runs as smoothly as possible. Thank you to all the chicken coop members and honorary coop members for the always interesting and entertaining conversations and their friendship over the years.

A very heartfelt thanks go to my wonderful fiancé, Eric McCalla, for always supporting me, encouraging me, and reminding me that a little bit of chaos is a good thing even though our definitions of “little bit” are very different. I couldn’t have done this without you.

Last but not least, I would also like to thank my mom and dad, who always made sure I had a puzzle to work on and continually encouraged me as I tackled my most challenging puzzle yet.

CHAPTER 1

INTRODUCTION

1.1 LITHIUM ION CELLS

Lithium ion cells are currently used in a wide variety of applications, including portable electronics, power tools, medical devices, electric vehicles, grid-scale and the recently announced home-scale energy storage systems. These applications are demanding increased energy densities, decreased cell bulging due to gas production, fast charging capabilities, longer lifetimes, all while reducing cost. The relative importance of each technological demand depends significantly on the end use and presents its own unique challenges.

Recent advances in energy density have mainly originated from the development of higher capacity materials with increased operating voltage and often require tailoring of the electrode design. This is especially important for consumer electronics where space is limited. Lifetime, in terms of both calendar and cycle life, is particularly important for large scale systems such as electric vehicles and stationary energy storage systems, where battery replacement becomes prohibitively expensive. Electric vehicles such as the Tesla Model S typically have warranties of 8 years, but do not cover any loss of battery energy or power.^{1,2} One notable exception is the Nissan Leaf which now offers an additional 5 year or 100,000 km capacity loss warranty for “nine bars of capacity as shown on the vehicle’s battery capacity level gauge” out of twelve bars.³ Commercially available home energy storage systems, such as the Bosch BPT-S 5 Hybrid used for solar

energy storage, are anticipating battery lifetimes of more than 25 years⁴, while the battery manufacturer, Saft, offers a battery warranty extension of up to 15 years⁵.

The calendar and cycle lifetimes of lithium ion cells are well known to be primarily affected by parasitic reactions between the electrodes and electrolyte.^{6,7} To extend these lifetimes, the rate and extent of parasitic reactions must be reduced, which is typically done through electrode design and material choice, as well as electrolyte development.⁶⁻⁸ Increasing cell lifetimes presents a further challenge due to the difficulties associated with accurately extrapolating the effect of a particular component measured on short time scales of weeks or months to the performance over the lifetime of the cell on the order of tens of years. Therefore it is of utmost importance to be able to measure and quantify the impact of changes in cell components in a precise manner that correlates to long term performance.

1.2 COMPONENTS OF LITHIUM ION CELLS

1.2.1 Overview

Lithium ion cells are known as “rocking-chair” systems, where the lithium ions reversibly intercalate and deintercalate into and out of the electrode materials, or “rock”, during charge and discharge. Figure 1.1 shows a schematic of a lithium ion cell. The positive and negative active electrode materials are commonly a layered metal oxide and graphite, respectively. They are combined with small amounts of binder, typically polyvinylidene fluoride (PVDF), and conductive diluent, typically carbon black, to ensure good adhesion to the current collector and to increase electronic conductivity within the

electrode, respectively. These components are then mixed with N-methyl-2-pyrrolidone (NMP) as a solvent and coated on current collectors, aluminum for the positive electrode and copper for the negative electrode. These current collectors are then connected to the external circuit. The electrodes are separated by electronically insulating, microporous polyolefin separators that allow for the passage of ions while ensuring the electrons pass through the external circuit. The cell is filled with an electrolyte which is composed of a lithium salt dissolved in a mixture of aprotic organic solvents, usually carbonates.

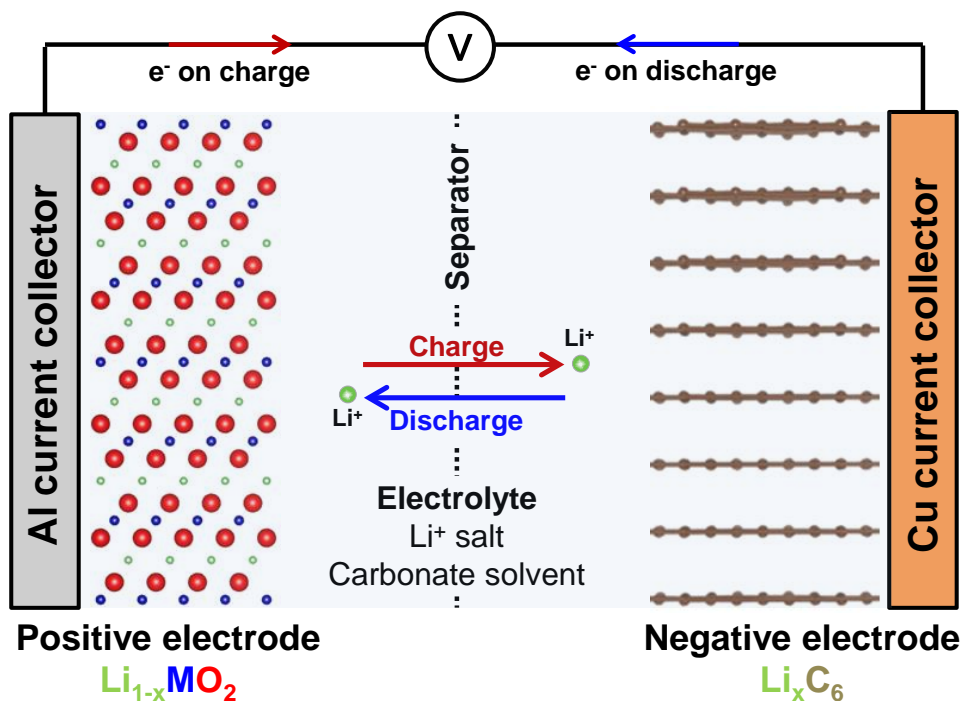
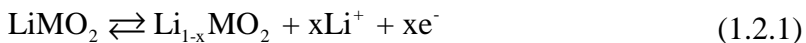


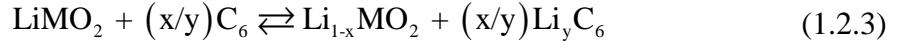
Figure 1.1: Simplified schematic representation of a lithium ion cell.

During the charging process of a cell, lithium ions are deintercalated from the positive electrode material and intercalated into the negative electrode material. The opposite occurs on discharge. For a metal oxide positive electrode and graphite negative electrode, the positive and negative half cell (vs Li/Li^+) reactions are, respectively⁹:





The overall full cell reaction is therefore given by:



For all reactions given, the top arrow represents the charge direction and the bottom arrow represents discharge.

The process of charging and discharging (referred to as cycling) results in a change in voltage as a function of time according to the changes in chemical potential.

The measured equilibrium cell voltage, V_{eq} , is given by:

$$V_{eq} = \frac{-1}{e} (\mu_{positive} - \mu_{negative}) \quad (1.2.4)$$

where e is the elementary charge, and $\mu_{positive}$ and $\mu_{negative}$ are the chemical potentials of the active positive and negative electrode materials, respectively, defined as the change in Gibbs free energy with respect to the lithium content. During galvanostatic (constant current) cycling, the cell voltage is measured as a function of time. However, it is often plotted as a function of capacity, Q , measured in Ah or mAh, and given by:

$$Q = \int I(t) \cdot dt = I \cdot t \quad (1.2.5)$$

where I is the galvanostatic current and t is the time per charge or discharge.

Figure 1.2 shows the voltage as a function of capacity during galvanostatic cycling for graphite and metal oxide half cells (vs Li/Li⁺), as well as the corresponding full cell. The capacities of positive and negative electrode reference half cells have been scaled and translated to match the observed voltage vs capacity behaviour of the full cell.¹⁰ As the cell is charged and lithium is moved from the positive electrode to the negative electrode active material, the overall full cell voltage increases. Figure 1.2 also

shows a feature of most lithium ion cells; full cell capacity is usually limited by the positive electrode. The capacities per unit area of the two electrodes are balanced such that when the positive electrode material is fully charged, the negative electrode material is not fully lithiated. This is a safety feature to minimize, and ideally prevent, the deposition of highly reactive metallic lithium on the negative electrode.

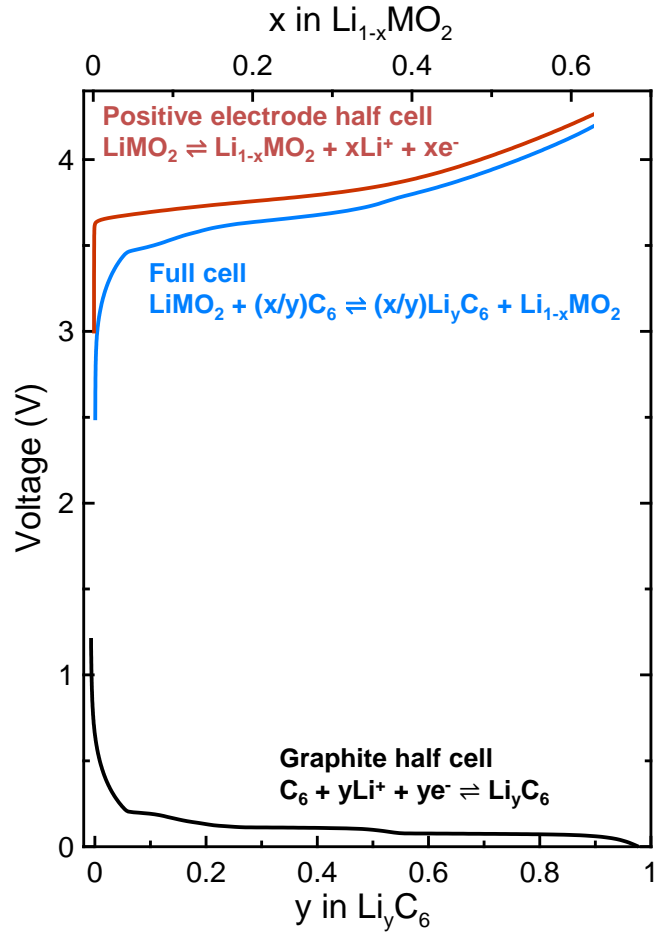


Figure 1.2: Voltage as a function of capacity during galvanostatic cycling for graphite (black) and layered metal oxide (red) half cells, and for a corresponding layered metal oxide/graphite full cell (blue).

1.2.2 Positive Electrode

The most widely used active positive electrode active materials in commercially available lithium ion cells are the layered lithium transition metal oxides, which have the

general form $\text{Li}[\text{M}]\text{O}_2$, where M can be made up of various combinations of Ni, Mn, Co, Al, etc. Figure 1.3 shows the structure of such materials, highlighting the alternating pattern of MO_2 slabs and lithium layers. During cycling, the lithium atoms intercalate and deintercalate along the layers. Commonly used layered metal oxides include LiCoO_2 (LCO)¹¹, $\text{Li}[\text{Ni}_x\text{Mn}_y\text{Co}_{1-x-y}]\text{O}_2$ ¹²⁻¹⁶ (NMC111 for $x = y = 0.33$, NMC442 for $x = y = 0.42$, NMC811 for $x = 0.8$ and $y = 0.1$, etc), and $\text{Li}[\text{Ni}_{0.8}\text{Co}_{0.15}\text{Al}_{0.05}]\text{O}_2$ (NCA)¹⁷.

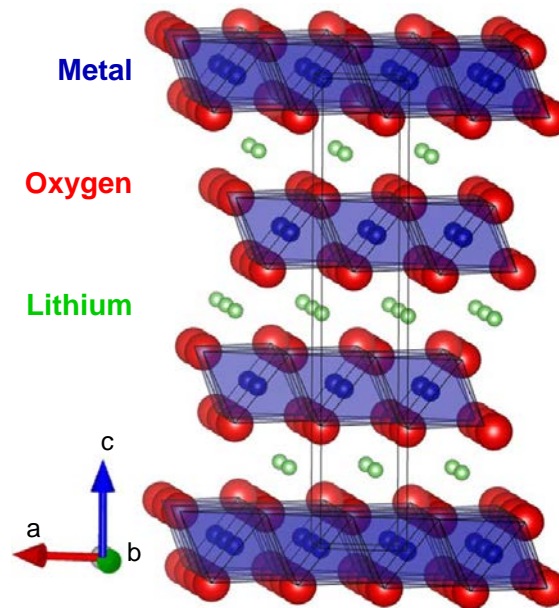


Figure 1.3: Structure of a layered lithium metal oxide in the fully lithiated state. Metal, oxygen, and lithium atoms are shown in blue, red, and green, respectively.

Figure 1.4 shows a scanning electron microscope (SEM) image of a machine-made positive electrode composed of 96% NMC442, 2% PVDF, and 2% carbon black (LiFUN Technology). The active material particle size is on the order of $10\ \mu\text{m}$, and the mixture of binder and carbon black is seen as a moss-like covering between active particles. Electrodes are also typically calendered to give the highly packed, low porosity electrode shown in Figure 1.4.

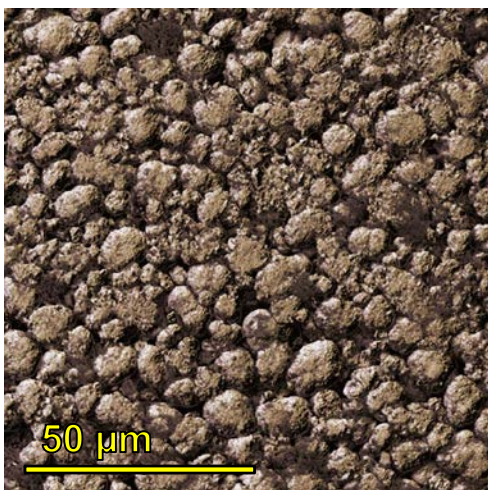


Figure 1.4: SEM image of an NMC442 electrode. False colour was added for depth perspective.

1.2.3 Negative Electrode

By far the most common negative electrode active material found in commercially available lithium ion cells is graphite. Graphite is widely used due to its low reduction potential vs Li/Li^+ (average potential of 0.1 V vs Li/Li^+), low volume expansion during lithiation (approximately 10%), increased safety compared to lithium metal, and high gravimetric capacity (372 mAh/g theoretical).^{9,18,19} Figure 1.5 shows the structure of graphite in the fully delithiated state, where graphene sheets with carbon atoms in a honeycomb arrangement are stacked in an ABAB manner. During lithiation, the lithium intercalates between the graphene layers and the structure adopts an AAAA stacking arrangement.²⁰

Figure 1.6 shows an SEM image of a machine-made negative electrode composed of 95.4% synthetic flake graphite, 1.1% carboxymethyl cellulose and 2.2% butadiene rubber as binders, and 1.3% conductive carbon black (LiFUN Technology). There is a

much larger variation in particle size and a reduced surface area compared with the positive electrode.

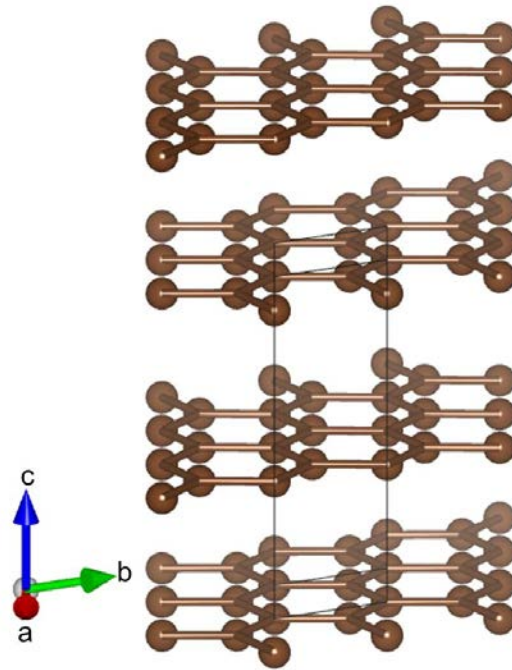


Figure 1.5: Structure of graphite in the fully delithiated state. Carbon atoms are shown in brown.

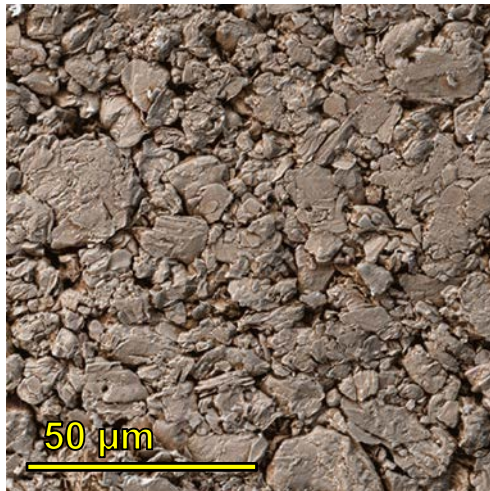


Figure 1.6: SEM image of a graphite electrode. False colour added for depth perspective.

1.2.4 Electrolyte

Many lithium ion cells use a liquid electrolyte that consists of a lithium salt, dissolved in a mixture of aprotic organic solvents. The most commonly used salt is lithium hexafluorophosphate, LiPF_6 , due to its salt solutions having high ionic conductivity (10^{-2} S/cm), high lithium cation transference number (≈ 0.35)⁹, good safety performance, and minimal corrosion of aluminum cell components at high voltages.²¹ Many other lithium salts have been explored, including lithium perchlorate (LiClO_4),²²⁻²⁵ lithium tetrafluoroborate (LiBF_4),^{26,27} lithium bis(trifluoromethanesulfonyl)imide (LiTFSI or HQ-115),²⁸⁻³⁴ lithium bis(fluorosulfonyl)imide (LiFSI),³⁵⁻³⁷ lithium bis(oxalato)borate (LiBOB),³⁸⁻⁴⁴ and lithium difluoro(oxalato)borate (LiODFB)^{42,44}. These salts all have advantages and disadvantages which have been extensively studied; however, LiPF_6 remains the salt of choice, with the above listed salts occasionally added in small concentrations as electrolyte additives.⁴⁵

Most solvents currently used in lithium ion cells are linear or cyclic carbonates such as ethylene carbonate (EC), dimethyl carbonate (DMC), ethylmethyl carbonate (EMC), and diethyl carbonate (DEC), the structures of which are shown in Figure 1.7. These carbonates are aprotic, polar, allow for the solvation of lithium salts at high concentrations (>1 M), and have wide electrochemical stability windows.⁹ In order to exploit the various benefits of each of the above carbonates a solvent blend is typically required in order to meet the demands of a particular application with respect to the operating temperature range, conductivity, capacity retention, etc. For example, EC has a very large dielectric constant⁴⁶ and is known to reduce capacity fade for graphite electrodes,¹⁹ but is a solid at room temperature. Therefore, it is incorporated with linear

carbonates such as EMC that lower the melting point and viscosity while maintaining the beneficial properties of EC.⁹

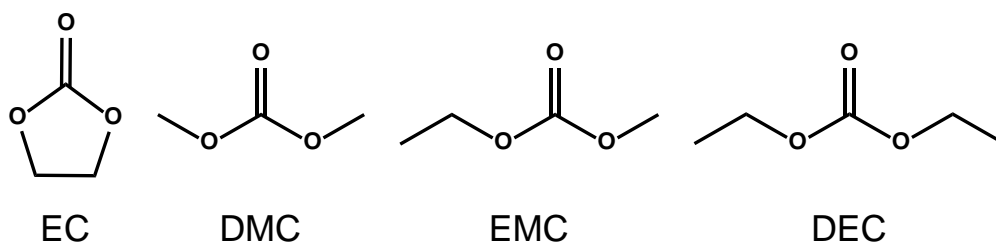


Figure 1.7: Chemical structures of commonly used carbonate electrolyte solvents.

In an effort to increase energy density, there has been a push to move to higher voltage systems such as those containing so-called “5 V” positive electrode materials like $\text{LiNi}_{0.5}\text{Mn}_{1.5}\text{O}_4$.^{47,48} However, the typical carbonate solvents are oxidized at such high voltages, where the decomposition has been reported to begin as low as 4.0 V^{23,49} and up to 4.5 V vs Li/Li^+ .^{46,50–52} One class of solvents used to extend the stability window are fluorinated carbonates,^{46,53,54} the most common of which is fluoroethylene carbonate^{55,56} (FEC). Several other fluorinated cyclic and linear carbonates have been investigated as both full solvent systems and co-solvents,^{6,46,54,57–59} and continue to garner interest in the battery community. One such fluorinated linear carbonate investigated in this thesis is bis(2,2,2-trifluoroethyl carbonate) (TFEC) which has shown to improve the protective passivation film that forms on the negative electrode.^{57,60,61} Figure 1.8 shows the chemical structures of FEC and TFEC.

Another class of non-carbonate solvents is linear carboxylic esters. These have mainly been developed as co-solvents used for low temperature ($-60\text{ }^\circ\text{C}$) applications due to their low viscosity, but result in poor passivation films on the negative electrode.^{6,62} Recently, Petibon *et al.*^{63,64} have successfully shown good cycling performance from EC-

free solvents containing ethyl acetate (EA) and methyl propanoate (MP), the structures of which are shown in Figure 1.8. The issue of a poor passivation film associated with such esters was addressed by adding a high concentration of LiFSI and/or vinylene carbonate to EA or MP.

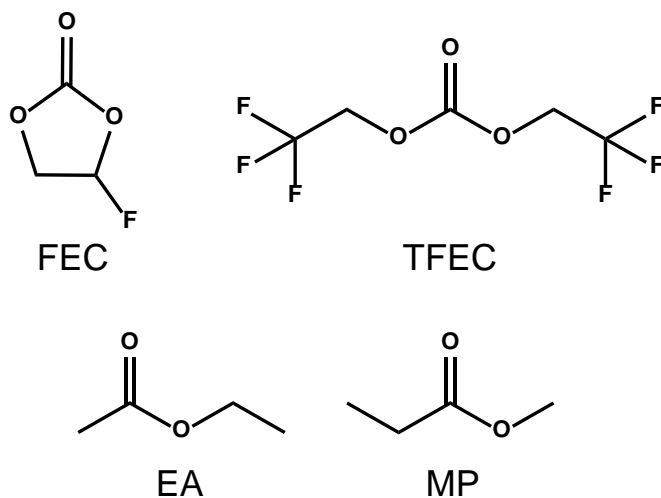


Figure 1.8: Chemical structures of some reported beneficial non-carbonate electrolyte solvents and co-solvents.

1.2.5 Separator

To prevent direct contact between the positive and negative electrodes, an electronically insulating separator is required. Such a separator must also be ionically permeable.⁶⁵ In most commercial lithium ion cells, a thin microporous polyolefin separator is used that is predominately made from polyethylene, polypropylene, or some layering of the two.⁹ More recently, ceramic coatings have been applied to the side of the separator in contact with the positive electrode intended for high voltage use. This serves to mitigate decomposition of the polyolefin at high voltages and to prevent direct contact of the positive and negative electrodes in case of high temperature melting of the polyolefin.⁶⁵⁻⁶⁸

1.2.6 Form Factor

Figure 1.9 shows three common types of form factors of lithium ion cells, a coin cell, a flat-wound pouch cell, and a cylindrically wound cell. A fourth common form factor not pictured is a prismatic cell, which resembles a pouch cell but instead has a hard exterior casing. Coin cells are particularly well suited for materials testing, as only a $\sim 1 \text{ cm}^2$ electrode is needed, but hand-coated electrodes can lead to large cell-to-cell variations. They are also used for half cell testing, where metallic lithium is the counter electrode. Cylindrically wound cells (typically 18 mm diameter and 65 mm length) have machine coated and wound electrodes, as well as excellent reproducibility, but even if available, require too much electrolyte and material to be feasible for most academic lab-scale experiments. Small dry pouch cells with machine-made electrodes purchased from a reputable supplier are a good middle-ground for electrolyte studies, and are increasingly commercially relevant as portable electronic devices are becoming progressively thinner. Such pouch cells were used throughout this thesis.



Figure 1.9: Three common lithium ion cell designs. From left to right: a coin cell, a flat-wound pouch cell, and a cylindrically wound cell.

Figure 1.10 shows the arrangement of the cell components within a small flat-wound pouch cell. The exterior aluminized polyethylene pouch has been moulded to hold the “jelly roll”, the wound electrode and separator stack. Tabs connected to the positive and negative current collectors serve as cell terminals. They have been cut off of the jelly roll in Figure 1.10 in order to remove the roll from the pouch cell. The electrodes are machine coated on both sides of each current collector, and wound with a layer of separator between each electrode.

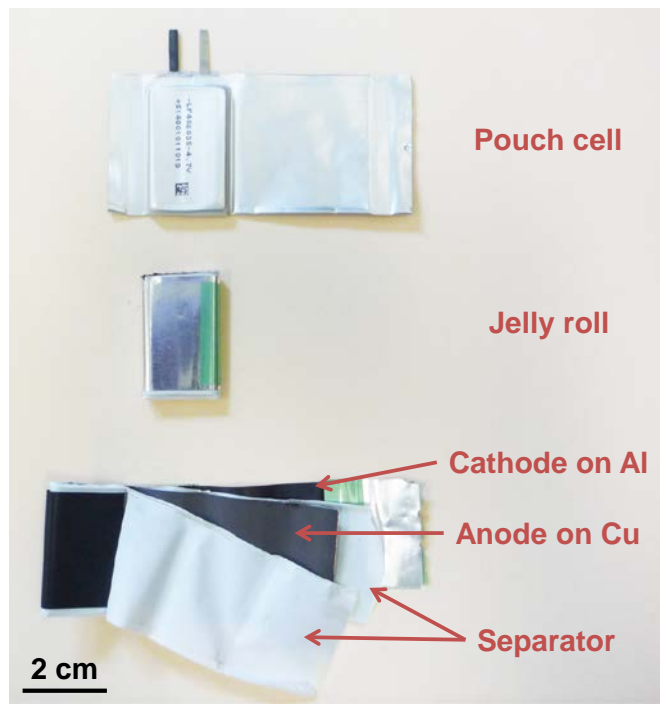


Figure 1.10: The deconstruction of a flat-wound pouch cell.

1.3 CHARACTERIZATION OF CELL PERFORMANCE

Figure 1.11 shows three methods of evaluating the performance of a lithium ion cell using galvanostatic cycling. Figure 1.11a shows the most common method used, where the cell capacity during either charge or discharge is monitored as a function of

cycle count. As the cell ages, some of the initial supply of lithium is lost in passivation films or electrical disconnection of particles, resulting in a decrease in capacity, known as capacity fade. The lifetime of a lithium ion cell is frequently taken as the time it takes to reach a certain fraction of the initial capacity. While easiest to measure, extrapolating the capacity fade to estimate lifetime can sometimes lead to spurious results.^{69,70,7}

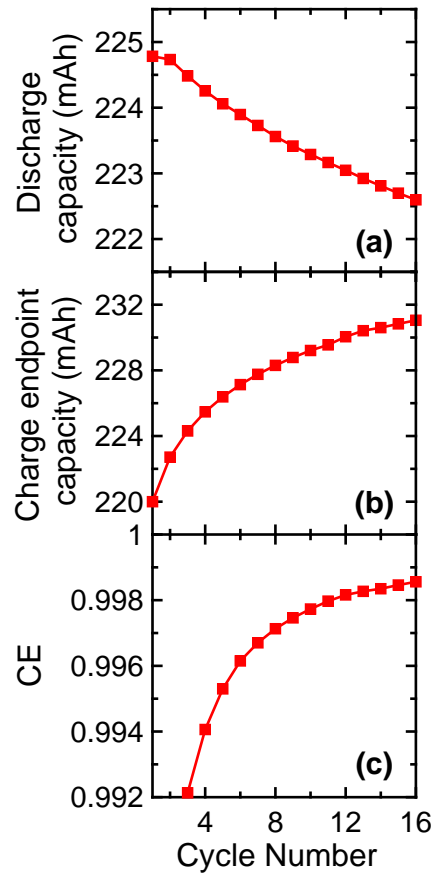


Figure 1.11: Three methods of evaluating cell performance: (a) discharge capacity fade, (b) charge endpoint capacity slippage, and (c) coulombic efficiency (CE).

Figure 1.11b and Figure 1.11c show two evaluation methods based on high precision coulometry.⁶⁹⁻⁷¹ Figure 1.11b shows the evolution of the absolute measured capacity at the top of charge, known as the charge endpoint capacity, as a function of cycle number. As parasitic reactions occur within a cell, Smith *et al.*⁷⁰ demonstrated that

the rate at which the charge endpoint capacity increases is related to the rate of parasitic reactions occurring at the positive electrode.

Figure 1.11c shows the coulombic efficiency (CE) as a function of cycle count, where the CE is defined as:

$$\text{CE} = \frac{Q_d}{Q_c} \quad (1.2.6)$$

where Q_d is the discharge capacity and Q_c is the capacity of the immediately preceding charge. The CE is a measure how much charge is delivered compared to how much is put in to the system, where a $\text{CE} \equiv 1$ for every cycle would indicate no charge is lost and the cell should last forever.⁶⁹⁻⁷¹

1.4 CAUSES OF CELL FAILURE

1.4.1 SEI Growth and Repair

While commonly used electrolytes are stable over a wide voltage range, there are no practical solvents which are thermodynamically stable throughout the entire voltage range experienced in a cell.^{9,72,73} This is especially true at the negative electrode, as the reduction potentials of most solvents and salts vs Li/Li^+ are significantly above the potential of the negative electrode during cycling. Indeed, the reduction of chemical components during the first charge is observed around 0.8 – 1.3 V vs Li/Li^+ .⁷⁴⁻⁷⁶ Fortunately, the reduction products usually precipitate and form an ionically conductive, electrically insulating passivation film that inhibits further reaction in a manner similar to oxide formation on aluminum. This film is known as the solid electrolyte interphase (SEI)⁷⁷ since it has similar properties to a solid electrolyte.

The SEI builds up on both electrode surfaces, is highly dependent on the electrode materials, salts, and solvents used within the cell^{23,73,78–82}, and is critical to good cell performance.^{9,45,6,72,73,77,80,83,84}

In carbonate solvents, the formation of the SEI on graphite electrodes is thought to originate mainly from the reduction of the solvent and reactions with active lithium from the graphite electrode.^{25,73,80,85} The role of the salt has also been investigated, both in terms of its effect on solvent reduction, and of its own decomposition.^{73,80,86} Several surface sensitive experimental techniques been used to examine the composition of the SEI, and have identified compounds such as lithium oxide (Li₂O), lithium carbonate (Li₂CO₃), lithium fluoride (LiF), lithium ethylene dicarbonate (LEDC, (CH₂COCO₂Li)₂), other lithium alkyl carbonates, lithium alkoxides, polymeric species, organophosphates, etc.^{9,73,83,85–87} Similar species have also been identified on the positive electrode.^{8,88–93}

The formation of the SEI irreversibly consumes lithium, and therefore results in a large irreversible capacity loss during the first cycle and continued capacity fade as the SEI is formed and repaired during cycling.^{9,83} Figure 1.12 shows a simplified possible mechanism of SEI growth. Figure 1.12a shows a case where new SEI is formed on the surface of the existing SEI.⁷⁰ Figure 1.12b shows a case where electrolyte diffuses through the existing SEI to form new SEI closer to the graphite surface.^{70,94} In both of these cases, active cyclable lithium from the electrode is irreversibly lost.

The formation of the SEI is diffusion limited, and has been shown to obey a $t^{1/2}$ dependence^{69,94} for good passivation, resulting in a decreased rate of charge loss with time. However, thermodynamically or mechanically unstable films can lead to continual reaction and lithium consumption.^{70,73}

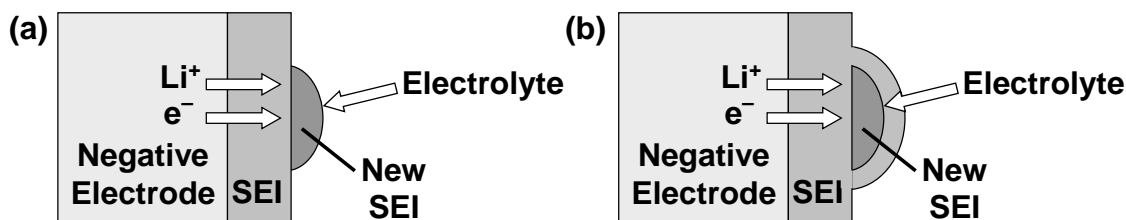


Figure 1.12: Simplified possible mechanisms of SEI growth where new SEI is formed (a) on the surface of the existing SEI or (b) closer to the negative electrode. Figures provided by Chris Burns and are adapted from *J. Electrochem. Soc.*, **158**, A1136 (2011)⁷⁰.

1.4.2 Electrolyte Oxidation

Another cause of cell degradation is the parasitic oxidation of the electrolyte which is not associated with cyclable lithium loss.⁷⁰ Since there is no appreciable capacity loss in the short term, the impact of electrolyte oxidation is not always apparent in early cycles, but eventually results in a rapid loss in capacity due to solvent depletion.⁷⁰ The oxidation of the electrolyte becomes increasingly important with increased voltage. Above 4.5 V, it has been observed that the parasitic reactions that occur at the positive electrode are the dominant cause of the cell failure.^{6,95} In addition to voltage, the rate of parasitic oxidation has also been shown to be dependent on the positive electrode active material, electrolyte composition, passivation films, and temperature.^{6,46,70,95-97}

Figure 1.13 shows two possible mechanisms of electrolyte oxidation during closed circuit operation. Figure 1.13a shows a component of the electrolyte being oxidized at the positive electrode to form soluble products which then migrate to the low potential negative electrode and are reduced to form insoluble products on the negative electrode surface. It is not necessary, nor expected, that all of these products would precipitate. Figure 1.13b shows the reverse, where the electrolyte is first reduced at the negative electrode and the reduced species is subsequently oxidized at the positive electrode.

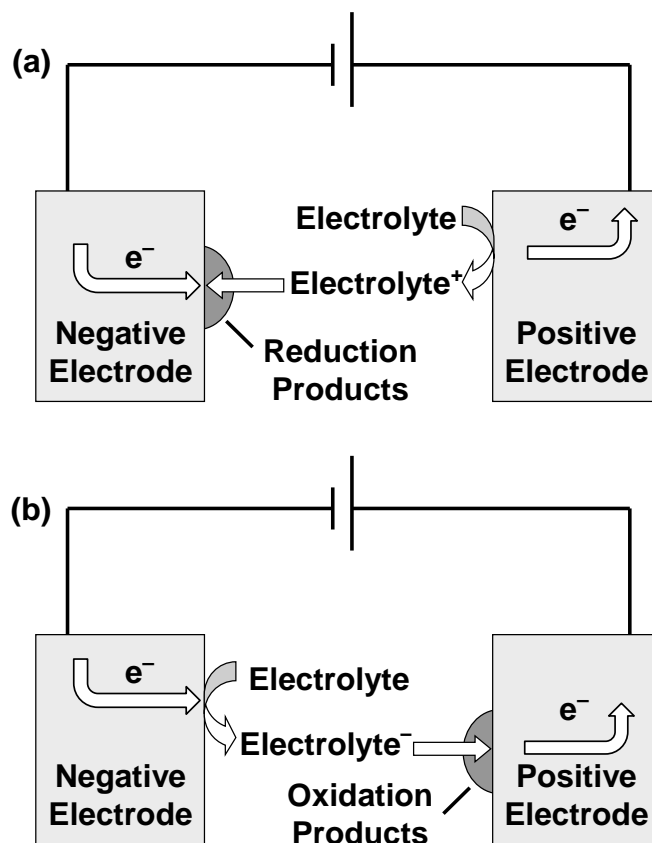


Figure 1.13: Possible mechanisms of electrolyte oxidation during closed circuit conditions. Figures provided by Chris Burns and are adapted from *J. Electrochem. Soc.*, **158**, A1136 (2011)⁷⁰.

Though not pictured, similar processes would occur at open circuit where, to maintain charge neutrality in the electrode, a lithium ion would be deintercalated from the negative electrode and another would be intercalated into the positive electrode. This would result in a decrease in cell voltage, since at high voltages where such oxidation occurs the graphite electrode voltage curve is nearly flat. Open circuit storage experiments performed by Sinha *et al.*⁹⁷ showed the voltage drop during storage is a good measure of the rate of electrolyte oxidation. Experiments by Fathi *et al.*⁹⁶ also clearly demonstrated that this rate increases with increasing cell voltage and that electrolyte oxidation is non-negligible even at moderate voltages.

1.4.3 Other Causes

Figure 1.14 shows two other possible degradation mechanisms in lithium ion cells. Figure 1.14a shows the case of an electrochemical shuttle. This is very similar to electrode oxidation discussed in 1.4.2, except that the neutral species is regenerated upon reduction. This process results in charge transfer (or Li^+ transfer for open circuit conditions), does not consume lithium, and can be highly reversible for certain species such as 2,5 ditertbutyl-1,4-dimethoxybenzene.^{70,98}

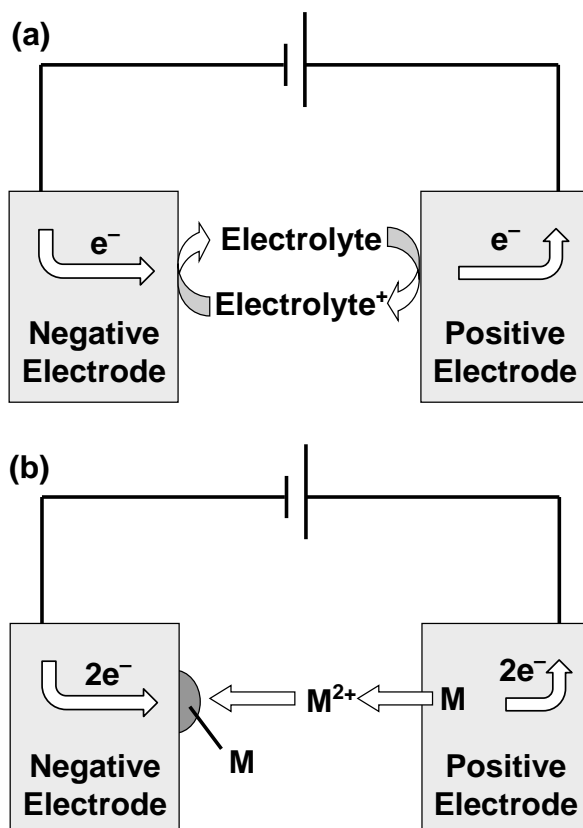


Figure 1.14: Other possible degradation mechanisms, including (a) a shuttle and (b) transition metal dissolution. Figures provided by Chris Burns and are adapted from *J. Electrochem. Soc.*, **158**, A1136 (2011)⁷⁰.

Figure 1.14b shows the case of transition metal dissolution from the positive electrode, which is then reduced and precipitates on the negative electrode. Surface

techniques such as energy dispersive spectroscopy (EDS) and x-ray photoelectron spectroscopy (XPS) have observed this behaviour through the identification of the presence of transition metals on negative electrodes after cycling.^{8,99-103} Pieczonka *et al.*¹⁰³ have also identified transition metal dissolved in the electrolyte. The extent of metal dissolution has been found to depend on the composition and potential of the positive electrode material, as well as the electrolyte composition.^{8,100,103} Similar to the shuttle mechanism, transition metal dissolution does not consume lithium and results in charge transfer (or Li^+ transfer during open circuit), but would result in capacity fade due to a loss of active material.

1.5 ELECTROLYTE ADDITIVES

The most common and arguably the most effective way of addressing the degradation mechanisms discussed in Section 1.4 is to use electrolyte additives. These are chemicals present at amounts typically below 5% by weight that significantly improve the performance of lithium ion cells. There are hundreds of known additives which have proved beneficial by making improvements in several different ways.

Many additives are thought to help form a more stable SEI that contains less lithium, which can also reduce the amount of gas released by changing the reaction pathways during SEI formation.⁴⁵ Examples of additives commonly believed to act in this manner include: vinylene carbonate (VC)¹⁰⁴⁻¹⁰⁹, vinyl ethylene carbonate (VEC)¹¹⁰⁻¹¹⁴, vinyl acetate (VA)¹¹⁵, fluoroethylene carbonate (FEC)^{55,116}, boron-based compounds such as trimethoxyboroxine (TMOBX)⁵⁶, lithium bis(oxalato)borate (LiBOB)³⁸⁻⁴⁴, lithium oxalyldifluoroborate (LiODFB)^{42,44}, etc. It is claimed that the SEI can also be

protected using a LiPF_6 salt stabilizer such as tris(2,2,2-trifluoroethyl)phosphite since PF_5 has been shown to deteriorate the SEI.^{117,118}

Other additives have been proposed for protection of the positive electrode material by scavenging water or HF which can cause transition metal dissolution such as butylamine¹¹⁹ and N,N-diethylamino trimethylsilane.^{120,121} The positive electrode can also be protected by adding an additive such as LiBOB¹²² that is thought to react with any dissolved transition metal ions to form a protective film on the positive electrode surface.

Though not mentioned in the previous section, the corrosion of cell components such as the aluminum and copper current collectors can also contribute to cell failure. To prevent this corrosion, additives such as LiBOB and LiODFB can be used to protect the aluminum^{123,124}, while succinonitrile can be used to protect the copper^{125,126}.

Lithium ion cells are also plagued by safety concerns, thus additives that prevent overcharge by either a shuttle mechanism or current shut down, or act as fire-retardants can be used.^{45,46}

Despite extensive investigations into the benefits of these electrolyte additives, their role is not particularly well understood. One such example is with the popular additive, vinylene carbonate. Several studies^{104–109} report that the increase in full cell lifetime is caused by VC being reduced on the surface of graphite, forming a more stable SEI. However, more recent studies^{97,127–132} have challenged this thought, reporting that the benefit of VC arises primarily from limiting electrolyte oxidation and possible transition metal dissolution reactions at the positive electrode.

Figure 1.15 shows the chemical structures of the electrolyte additives examined throughout this thesis. From top to bottom and left to right the additives are: vinylene carbonate (VC), prop-1-ene-1,3-sultone (PES), 1,3,2-dioxathiolane-2,2-dioxide (DTD),

1,3,2-dioxathiane 2,2-dioxide (TMS), methylene methanedisulfonate (MMDS), tris(trimethylsilyl)phosphate (TTSP), tris(trimethylsilyl)phosphite (TTSPi), triallyl phosphate (TAP), and lithium bis(fluorosulfonyl)imide (LiFSI).

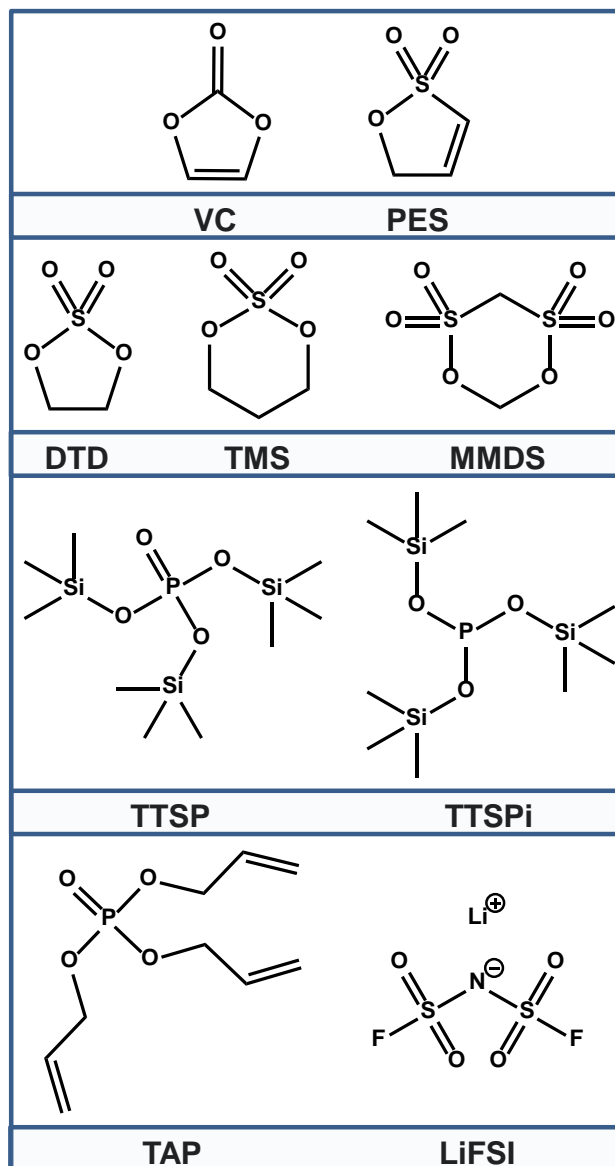


Figure 1.15: Chemical structures of the electrolyte additives used in this thesis. Abbreviations are described in the text and in the list of symbols on page xxii.

The proposed role of VC was described above. The use of PES has been suggested as an alternative to VC for its stability at high temperatures and reduced gas

evolution.¹³³⁻¹³⁶ It has been reported that PES is preferentially reduced, resulting in a stable SEI on both the negative and positive electrodes.¹³⁷⁻¹³⁹ Ultra high precision experiments by Xia *et al.*¹³⁴ and Nelson *et al.*¹³³ have confirmed that NMC111/graphite pouch cells containing varying concentrations of PES result in improved coulombic efficiencies, decreased charge endpoint capacity slippage, and decreased gas generation, but at the expense of an increased charge transfer impedance.

The beneficial impact of DTD has been proposed as resulting from the reductive formation of a film rich in organic compounds and organosulfites, which limits the parasitic degradation of the solvent and salt.^{76,140,141} Despite the similarities in chemical structure to DTD, TMS was found to have little impact on electrochemical performance or surface film composition when used alone compared to non-TMS containing electrolytes.^{76,140} MMDS has been repeatedly shown to form a protective film on the positive electrode for a variety of positive electrode materials, which results in a decrease in electrolyte oxidation at the positive electrode^{75,142-145}. Therefore, MMDS is especially useful at high voltages.

Published patents promote the benefit of TTSP and TTSPi based on improved cell performance at high voltage and high temperatures.^{146,147} It has since been shown that these compounds are preferentially oxidized at the positive electrode and form a protective film on the positive electrode.¹⁴⁸⁻¹⁵¹ Sinha *et al.*¹⁵² have also shown with high precision coulometry that these compounds reduce the parasitic reaction rate while simultaneously reducing the charge transfer resistance.

Relatively little is known about TAP, but it has been found to be a component of commercial electrolyte which is promoted for high voltage application. Published patents show that TAP results in a low first cycle irreversible capacity and improved capacity

retention during cycling¹⁵³, suggesting that TAP participates in SEI formation on the negative electrode.

Lastly, LiFSI has been shown to improve the stability of the graphite SEI through preferential reduction of high concentrations of the FSI anion¹⁵⁴, as well as the stability of the electrolyte by trapping PF₅ which can lead to electrolyte decomposition¹⁵⁵. However, LiFSI has also been shown to corrode the aluminum current collector, which can be addressed by the addition of LiPF₆ to the electrolyte.³⁷

It is clear that the role of electrolyte additives is extremely complex, and is the subject of extensive theoretical and experimental research and development. The complete understanding of even a single additive is a daunting task. Furthermore, several studies have reported that combinations of electrolyte additives can have synergistic effects on cell performance^{37,7,76,156–161,152}. In particular reference to the additives studied in this thesis, Xia *et al.*⁷⁶ examined combinations of VC with each of three sulfur-containing additives, DTD, TMS, and MMDS, while Sinha *et al.*¹⁵² examined combinations of VC with TTSP and/or TTSPi. Both studies showed distinct benefits of these additive combinations on overall cell performance and lifetime. Therefore, the work presented in this thesis also investigates the potential benefit of additive blends, in comparison to single additive studies.

1.6 SCOPE AND OUTLINE OF THESIS

In an ongoing effort to better the understanding of how electrolyte additives impact the performance of lithium ion cells, this work introduces the use of isothermal microcalorimetry as a tool to measure the heat flow associated with the parasitic reactions

causing cell degradation. This was done *in situ* and as a function of voltage, while more standard electrochemical techniques can only determine the cycle-averaged impact of an additive. While isothermal microcalorimetry has been previously used on lithium ion cells, there have been no published efforts to characterize the heat flow resulting from parasitic reactions in full, commercially relevant cells.

The majority of this work focuses on the development of the method to extract and understand the parasitic heat flow. As the method was developed, examples of the determination of the impact of a variety of electrolyte additives and additive blends on several different cell chemistries were explored.

Chapter 2 introduces the technique of isothermal microcalorimetry and its application to the study of lithium ion cells. The sources of heat flow as current was applied to a cell are discussed, and a literature review of previous isothermal calorimetry experiments is presented.

Chapter 3 provides a summary of the experimental techniques used throughout this thesis.

Chapter 4 introduces the first method of determining the impact of electrolyte additives using isothermal microcalorimetry. By varying only the electrolyte composition, the only difference in measurable heat flow for low current cycles is a direct result of differences in parasitic heat flow. This comparative method was applied to NMC111/graphite pouch cells for a variety of additives and additive blends. The results from calorimetric measurements were then compared to typical electrochemical tests to verify the methodology.

Chapter 5 describes a method of separating the total measured heat flow into three components: polarization, entropic, and parasitic by exploiting the current dependences

of each term. This allowed for the isolation of the heat flow resulting from parasitic reactions as a function of state of charge. The method was demonstrated using LCO/graphite cells and extended to NMC111/graphite cells with several electrolyte additives. Comparisons to commercial electrolyte were also made.

Chapter 6 builds upon the method developed in Chapter 5 by incorporating time dependence to the parasitic heat flow. As the parasitic reactions progress, the presence of passivation films result in a decreased reaction rate with time. This effect was added to the model, allowing for the extraction of both the time and voltage dependence of the parasitic heat flow for individual cells. The method was demonstrated using the same LCO/graphite cells as in Chapter 5, and was then extended to NMC811/graphite cells to explore the observed failure mechanism in such cells.

Chapter 7 further improved the model developed in Chapters 5 and 6 through an examination of the robustness of the time dependent model. It is shown that the inclusion of a heat flow component arising from hysteresis was required due to the very small currents used.

Chapter 8 applies the model developed in Chapter 7 to the examination of the effect of electrolyte additives and solvents on the time and voltage parasitic heat flow up to 4.7 V in NMC442/graphite pouch cells.

Chapter 9 presents an effort to understand the origin and implications of the parasitic heat flow through a series of thought experiments and long term open circuit heat flow measurements.

Chapter 10 summarizes the results presented in this thesis and lays the ground work for possible future experiments which can use the methods developed herein to thoroughly explore the meaning and implications of the parasitic heat flow.

CHAPTER 2

ISOTHERMAL MICROCALORIMETRY OF LITHIUM ION CELLS

2.1 INTRODUCTION TO ISOTHERMAL MICROCALORIMETRY

Isothermal calorimetry is a technique which measures the rate of heat flow to or from a sample *in situ* at near-constant temperature. The first such calorimeter was invented by Lavoisier and Laplace in the 1780s¹⁶², but it was not until the introduction of small thermoelectric devices that the modern isothermal calorimeter designed by Wadsö became popular.^{163–165} Such modern calorimeters are exceptionally sensitive and are capable of measuring heat flows down to the 100 nW-scale. Isothermal microcalorimetry can be used for an immense variety of applications ranging from food science, to pharmacology, to cement hydration, and is now used as a NATO standard (STANAG 4582) for testing the stabilities of nitrocellulose-based propellants.¹⁶⁶

This chapter will explore the use of isothermal microcalorimetry in the study of lithium ion cells.

2.2 SOURCES OF HEAT FLOW IN LITHIUM ION CELLS

2.2.1 Energy Balance Model

Starting from the first law of thermodynamics, the total change in internal energy of a system is equal to the heat supplied to the system plus the work done on the system. That is:

$$dU = \bar{d}q + \bar{d}W \quad (2.2.1)$$

where U is the internal energy, q is the heat, W is the work, and the system is defined here as the lithium ion cell. The change in heat to the cell with respect to time, t , is called the heat flow and is given by:

$$\left. \frac{\bar{d}q}{dt} \right|_{to\ cell} = \frac{dU}{dt} - \frac{\bar{d}W}{dt} \quad (2.2.2)$$

The isothermal calorimeter measures the heat flow from the cell, which equal to the negative of the heat flow to the cell, and is therefore:

$$\left. \frac{\bar{d}q}{dt} \right|_{measured} = - \left. \frac{\bar{d}q}{dt} \right|_{to\ cell} = - \frac{dU}{dt} + \frac{\bar{d}W}{dt} \quad (2.2.3)$$

As a result of Equation 2.2.3, an exothermic process occurring in the cell will be measured as a positive heat flow by the calorimeter. Throughout the rest of this Section and thesis, equations describing the heat flow are given in terms of the measured heat flow as defined above.

When a current is applied to an ideal cell, the work done on the system is equal to the electrical work done by the electrons as they move through the external circuit as well as by changes in cell volume against ambient pressure as a result of gas generation or consumption. And therefore one can write Equation 2.2.3 as:

$$\frac{\bar{d}q}{dt} = - \frac{dU}{dt} + \left(IV_{cell} - P \frac{dV}{dt} \right) \quad (2.2.4)$$

where I is the current, V_{cell} is the cell voltage, P is the ambient pressure, and V is the cell volume. An upper-bound of heat flow resulting from work done due to changes in volume can be estimated using parameters appropriate to the cells and experiments used throughout this work. A 1 mL change in cell volume against an ambient pressure of 1

atm (1.013×10^5 Pa) over 50 h would result in a heat flow of $-0.6 \mu\text{W}$. This is smaller than the heat flow measurement uncertainty and is therefore has a negligible effect on the measured heat flow throughout the rest of this thesis.

The sum of the internal energy and P - V work in Equation 2.2.4 is given by the enthalpy, H , which for constant temperature and pressure can also be expressed using the definition of Gibbs free energy under such conditions:

$$dH = TdS + dG \quad (2.2.5)$$

where G is Gibbs free energy, T is the temperature, and S is the entropy. Substituting Equation 2.2.5 into Equation 2.2.4, it follows that:

$$\frac{dq}{dt} = -T \frac{dS}{dt} - \frac{dG}{dt} + IV_{cell} \quad (2.2.6)$$

In the intercalation compounds used as active materials, the lithium atoms occupy a certain fraction of the total available sites according to the state of charge of the electrode. If the material has N available lithium sites and n of those are filled, then the fraction of filled sites x is given as $x = n/N$. For example, in the fully discharged state of graphite, $x = 0$ corresponds to Li_0C_6 , and in the fully charged state $x = 1$ corresponds to Li_1C_6 . Therefore it is useful to express Equation 2.2.6 in terms of x . Applying the chain rule to Equation 2.2.6 yields:

$$\frac{dq}{dt} = -T \left(\frac{dS}{dx} \right) \left(\frac{dx}{dt} \right) - \left(\frac{dG}{dn} \right) \left(\frac{dn}{dx} \right) \left(\frac{dx}{dt} \right) + IV_{cell} \quad (2.2.7)$$

Both positive and negative electrodes need to be considered, where the rate of change of the fraction of filled sites for the positive and negative electrode materials, dx_+/dt and dx_-/dt , respectively, are related to the current by:

$$\frac{dx_{\pm}}{dt} = \mp \frac{I}{Ne} \quad (2.2.8)$$

where e is the electron charge.

Furthermore, it is often useful to work in terms of entropy per site, s , rather than the total entropy, S . Applying the above considerations, Equation 2.2.7 can be written as¹⁶⁷⁻¹⁶⁹:

$$\frac{\dot{d}q}{dt} = -NT \left[\left(\frac{ds_+}{dx_+} \right) \left(\frac{-I}{Ne} \right) + \left(\frac{ds_-}{dx_-} \right) \left(\frac{I}{Ne} \right) \right] - \left[\mu_+ N \left(\frac{-I}{Ne} \right) + \mu_- N \left(\frac{I}{Ne} \right) \right] + IV_{cell} \quad (2.2.9)$$

where the + and – subscripts represent the positive and negative electrodes, respectively.

Equation 2.2.9 simplifies to:

$$\frac{\dot{d}q}{dt} = \frac{T}{e} \left[\left(\frac{ds_+}{dx_+} \right) - \left(\frac{ds_-}{dx_-} \right) \right] I - \left[\frac{-1}{e} (\mu_+ - \mu_-) \right] I + IV_{cell} \quad (2.2.10)$$

Using the definition of the equilibrium cell voltage, V_{eq} , given by Equation 1.2.4,

Equation 2.2.10 further simplifies to:

$$\frac{\dot{d}q}{dt} = \frac{T}{e} \left[\left(\frac{ds_+}{dx_+} \right) - \left(\frac{ds_-}{dx_-} \right) \right] I + I\eta \quad (2.2.11)$$

where $\eta = V_{cell} - V_{eq}$ and is the overpotential or difference of the cell voltage from its thermodynamic equilibrium voltage at any given state of charge.

Equation 2.2.11 describes the heat flow as a result of intercalation of an ideal full cell when a current is applied. However, parasitic reactions, such as those discussed in Section 1.4, occur and will therefore produce a heat flow.^{167,170,171} The heat flow from the cell associated with parasitic reactions, $\dot{d}q_p/dt$, is added to Equation 2.2.11 to give:

$$\frac{\dot{d}q}{dt} = \frac{T}{e} \left[\left(\frac{ds_+}{dx} \right) - \left(\frac{ds_-}{dx} \right) \right] I + I\eta + \frac{\dot{d}q_p}{dt} \quad (2.2.12)$$

where an exothermic parasitic heat flow would be measured by the calorimeter as a positive heat flow.

Beginning from Equation 2.2.11, Thomas and Newman¹⁷² developed an energy balance equation that explicitly included the effect of heats of mixing resulting from concentration gradients within particles, across the electrode, across the electrolyte, and within pores. Using full cell simulations, the relative magnitudes of each of the four sources of heats of mixing were estimated at a $C/3$ discharge rate (where C/x is a shorthand notation that represents a current that would result in a complete charge or discharge in x hours). It was found that in a realistic cell, the largest of the four sources examined was two orders of magnitude smaller than the heats associated with polarization and changes in entropy in the electrode materials. Therefore, throughout this thesis, the heat flow associated with enthalpies of mixing is treated as negligible and not explicitly included in the energy balance equation.

The energy balance model used throughout this thesis is given by Equation 2.2.12. The three terms in Equation 2.2.12 describe the three sources that contribute to the total heat flow of a full cell: changes in entropy of the two electrode active materials, cell polarization, and parasitic heat flow, respectively. Each of these three terms will be discussed separately in the following sections.

2.2.2 Polarization

The second term in Equation 2.2.12, $I\eta$, is the thermal power from cell polarization, where η is the overpotential or potential difference of the cell from its thermodynamic equilibrium voltage at any given state of charge. As the difference between the true open circuit voltage and the voltage under passage of current increases, an increase in thermal power is observed.

The overpotential in a lithium ion cell results in a difference in voltage between charge and discharge. Figure 2.1 shows the voltage of an NMC111/graphite coin cell for one full cycle. The area between the voltage curves provides a direct measure of the total heat associated with polarization and inherent hysteresis of the electrode materials.^{173–175} The observed overpotential in a cell is a result of several contributions including internal cell resistance from passivation films on both electrodes, diffusion effects within the electrodes and active material particles and concentration gradients in the electrolyte, among others.^{176,177} These effects are all highly dependent on the current applied to the cell, the temperature, and the state of charge of the cell.

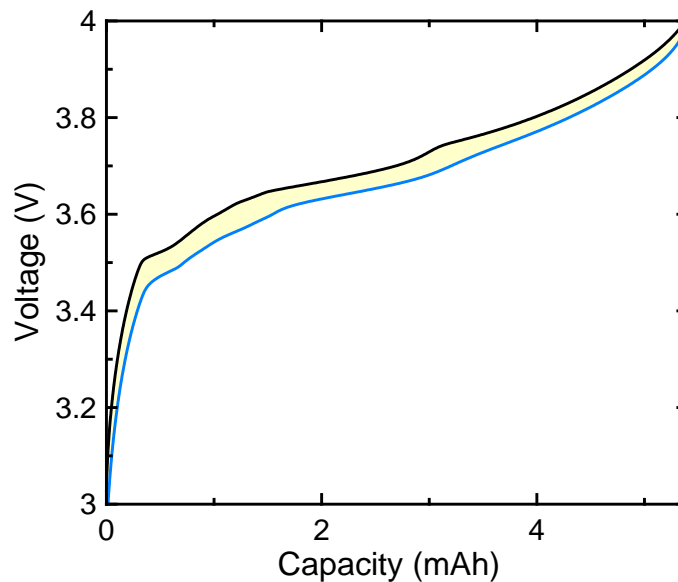


Figure 2.1: Voltage as a function of capacity for an NMC111/graphite coin cell during a C/10 charge (black) and discharge (blue). The shaded region (yellow) is a graphical representation of the heat associated with polarization and inherent hysteresis.

Figure 2.2 shows the discharge capacity as a function of C rate for an NMC111/graphite pouch cell at -14°C . At higher currents, the polarization increases such that the attainable capacity decreases. This effect is especially pronounced at low temperatures.

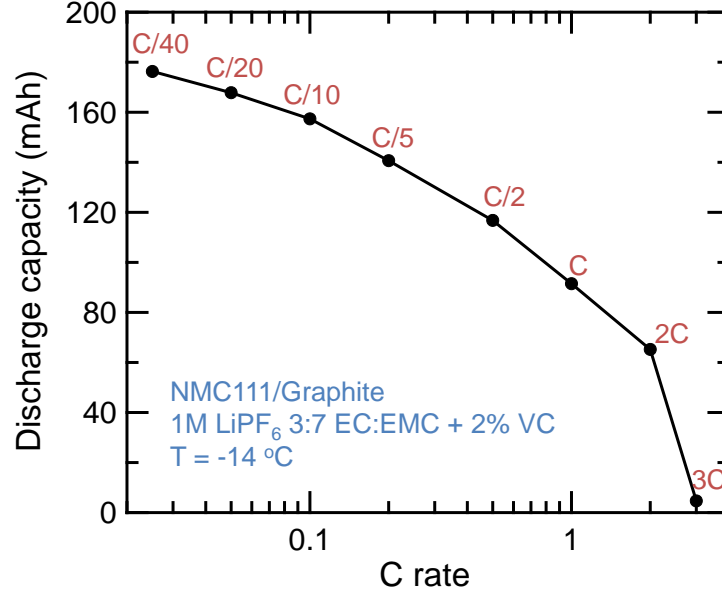


Figure 2.2: Discharge capacity as a function of current in terms of C rate for an NMC111/graphite pouch cell at -14 °C. Data were provided by Rémi Petibon.

Figure 2.3 shows the results of a galvanostatic intermittent titration technique (GITT) experiment for an NMC442/graphite pouch cell at 40°C. C/26 (10 mA) charge pulses were applied for 5 minutes followed by a 2 hour relaxation period, over a voltage range of 3.2 – 4.7 V. The observed difference between the voltage after the charge pulse and the voltage after the relaxation period gives a good measure of the overpotential at the given state of charge.^{178,179} The bottom panels of Figure 2.3 show two zoomed in segments of the voltage curve. The scaling for both panels is identical to facilitate comparison. These panels clearly show that the overpotential changes as a function of state of charge, and increases dramatically at the top of charge.

At the small currents used throughout this thesis, no diffusion limitations are expected. The total overpotential is therefore treated as resulting from the sum of an internal cell resistance, $R_{internal}$, and inherent hysteresis in the electrode materials, that is:

$$\eta = IR_{internal} + V_{hysteresis} \quad (2.2.13)$$

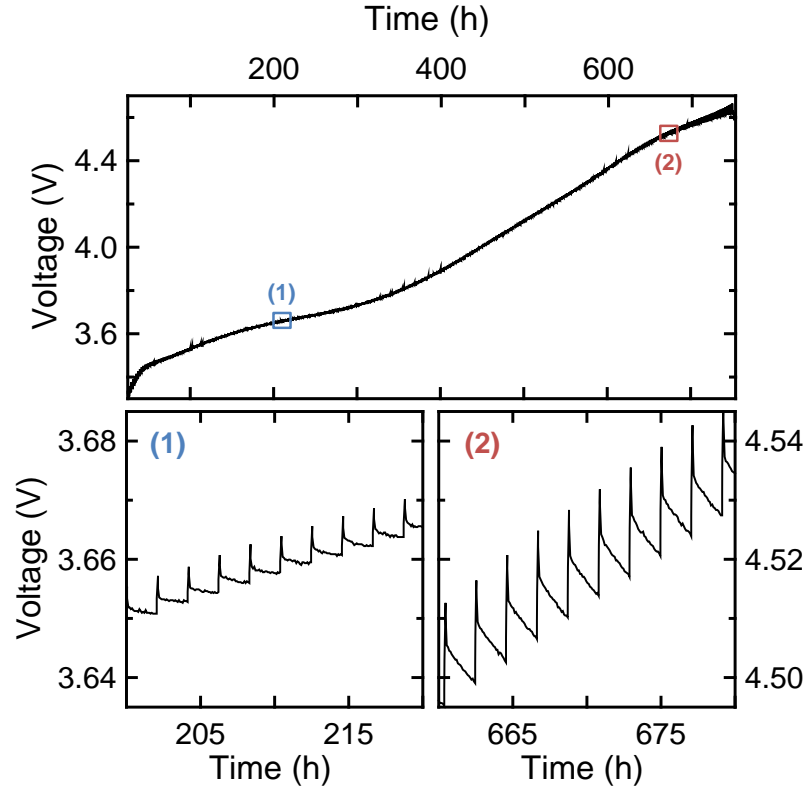


Figure 2.3: Voltage as a function of state of charge for an NMC442/graphite pouch cell at 40 °C. The cell was charged at 10 mA (C/26) for 5 minutes then allowed to rest for 2 hours to illustrate the variation of the overpotential with state of charge.

The hysteresis voltage, $V_{hysteresis}$, is the difference between the measured cell voltage and the thermodynamic open circuit voltage in the limit of zero current. The observed hysteresis is on the order of a few millivolts for commonly used electrodes¹⁷⁴ and throughout most of thesis is considered negligible. The impact of the hysteresis term is explored in detail in Chapter 7.

The measured heat flow associated with cell polarization, excluding hysteresis, is therefore proportional to the current squared and is given by:

$$\frac{dq}{dt}_{polarization} = I^2 R_{internal} \quad (2.2.14)$$

As a result, the heat flow due to polarization is always exothermic.

2.2.3 Entropy

The first term in Equation 2.2.12 is the heat flow associated with changes in the entropy of the active materials. It is proportional to the current, and is therefore a reversible heat flow, *i.e.*, if an exothermic event occurs during charge, then the corresponding event during discharge produces an endothermic signal.

In the simple case of a material that is well characterized using a mean field lattice gas approximation where the lithium atoms are randomly distributed on the active material lattice, the entropy is simply the Boltzmann constant, k_B , times the natural logarithm of the number of ways to organize n atoms on N sites. Using Stirling's approximation, this gives:

$$S = -Nk_B [x \ln x + (1-x) \ln (1-x)] \quad (2.2.15)$$

The change in entropy with respect to x is therefore:

$$\frac{dS}{dx} = Nk_B [\ln(1-x) - \ln(x)] \quad (2.2.16)$$

Figure 2.4 shows the entropy and the derivative of entropy as a function of x in Li_xHost for the lattice gas model. At the extremes of intercalation where the host is either nearly empty or nearly full, the entropy changes rapidly with x , resulting in a large heat flow. The lattice gas model gives a good approximation for some systems, such as $\text{Li}_x\text{Mo}_6\text{Se}_8$, where the coulomb repulsion between Li atoms is very weak due to large Li-Li separation and good ion screening.^{167,180} However, most commonly used electrode materials such as graphite, NMC, and LCO have much more complex entropy profiles.

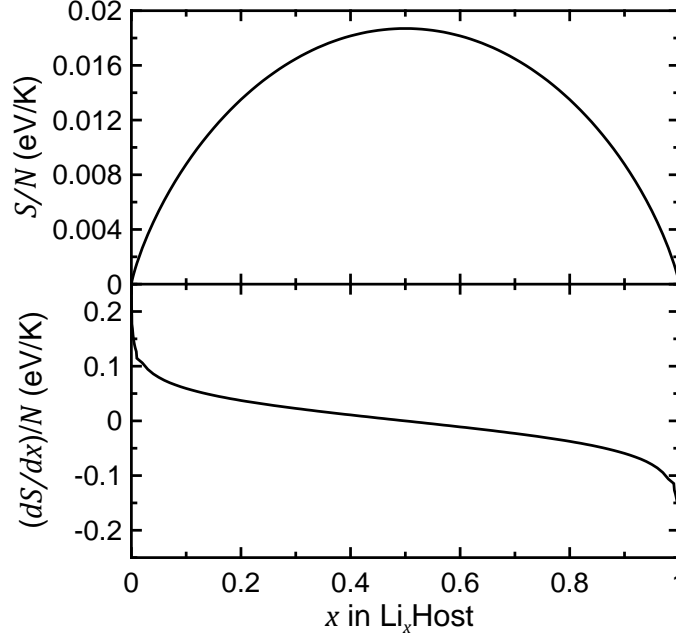


Figure 2.4: Lattice gas model of (top) entropy and (bottom) change in entropy with respect to the fraction of filled sites, x , in Li_xHost .

In general, the change in entropy per site at constant pressure is given by^{180,181}:

$$\frac{ds}{dx} = e \frac{dV_{eq}}{dT} \quad (2.2.17)$$

Based on Equation 2.2.17, the most common method of determining the change in entropy for a cell is using a potentiometric method where the open circuit voltage is determined for a series of temperatures. This type of measurement has been done for a variety of half cells including graphite/Li^{182–185}, $\text{LiMn}_2\text{O}_4/\text{Li}$ ^{172,186}, LCO/Li ¹⁸⁵, $\text{NMC111}/\text{Li}$ ¹⁸⁷, NCA/Li ¹⁸⁴, $\text{LiAl}_{0.2}\text{Mn}_{1.8}\text{O}_{4-\delta}\text{F}_{0.2}/\text{Li}$ ¹⁷², $\text{LiAl}_{0.17}\text{Mn}_{1.83}\text{O}_{3.97}\text{S}_{0.03}/\text{Li}$ ¹⁸⁶, as well as for several full cells including $\text{LCO}/\text{graphite}$ ^{185,188–191}, $\text{NCA}/\text{graphite}$ ^{184,192}, and $\text{LiFePO}_4/\text{graphite}$ ¹⁹². This method is a tedious process as it takes 20 – 35 hours^{190,192,193} for every state of charge.

Recently, Schmidt *et al.*¹⁹² introduced a new rapid technique of determining the change in entropy using electrothermal impedance spectroscopy (ETIS). The ETIS

method measures the thermal impedance and the cell surface temperature in order to calculate the reversible heat flow when a sinusoidal current is applied to the cell. The reversible heat flow is then used to calculate the change in entropy. Figure 2.5 shows a figure from Schmidt *et al.*¹⁹² comparing the entropy as a function of state of charge determined using the potentiometric method (Equation 2.2.17) and the ETIS method for three commercial cells. Examining the entropy profiles for such cells, it is clear that both the positive and negative electrodes contribute to the total change in entropy and that a lattice gas model is not adequate to describe the commonly used electrode materials.

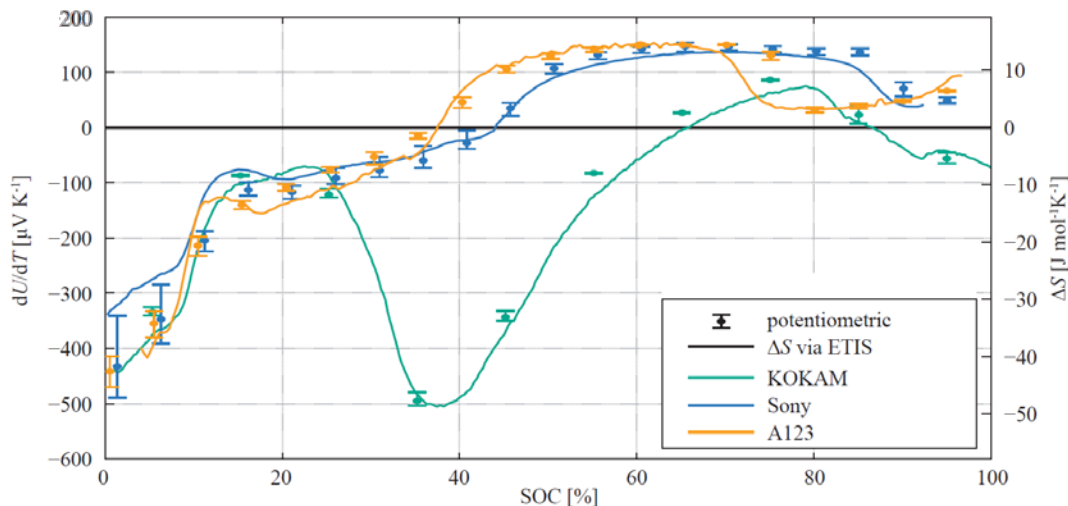


Figure 2.5: Measured change in entropy (right axis) as a function of state of charge using two methods, potentiometric (symbols) and electrothermal impedance spectroscopy (ETIS, lines) for three commercial cells made by KOKAM (NCA-LCO blend/graphite, green), Sony (LiFePO₄/graphite, blue), and A123 (LiFePO₄/graphite, gold). Figure reproduced with permission from *Electrochim. Acta* **137**, 311 (2014)¹⁹².

The change in entropy can also be easily determined using isothermal calorimetric methods.¹⁸⁰ As discussed in Section 2.2.1, the heat flow contribution from changes in entropy is the only term which is reversible. Therefore, changes in entropy can be estimated by examining the deviation from the midpoint heat flow between charge and discharge.

Figure 2.6 shows the voltage and corresponding measured heat flow as a function of specific capacity during a full cycle at C/10 and 40°C for an NMC111/Li half cell coin cell. The voltage curve of NMC111 is smooth and no large changes in entropy are expected. Correspondingly, the separation between the charge and discharge heat flow is smooth over the entire capacity range.

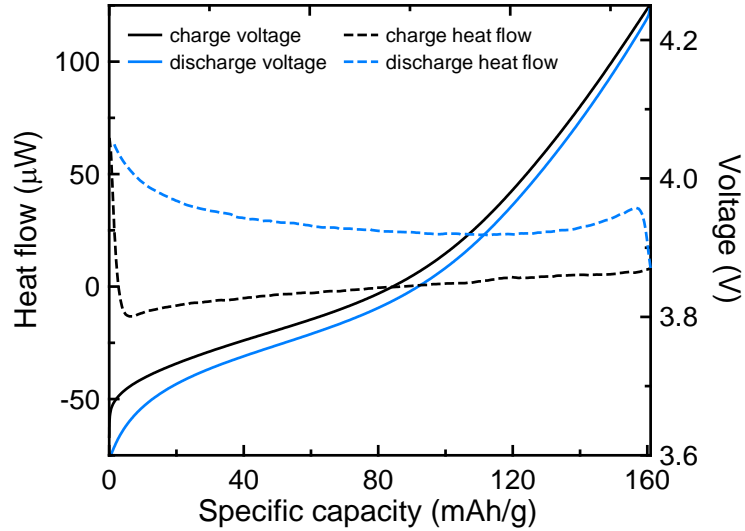


Figure 2.6: Voltage (solid lines) and corresponding heat flow (dashed lines) as a function of specific capacity during a C/10 charge (black) and discharge (blue) of an NMC111/Li coin cell.

Figure 2.7 shows the voltage and corresponding measured heat flow as a function of specific capacity during a full cycle at C/10 and 40°C for a graphite/Li half cell coin cell. In contrast to the positive half cell, the graphite half cell voltage curves are not smooth and measured heat flow has several entropy-related features. As lithium is intercalated and deintercalated into and out of the graphite structure, it is well known that the graphite passes through several staging transitions.¹⁹⁴ The voltage plateaus represent two-phase coexistence regions while the discontinuities are a result of first order transitions between different staging phases. The discontinuities observed in the heat flow are a direct result of these phase transitions, as demonstrated by McKinnon *et al.*¹⁸⁰

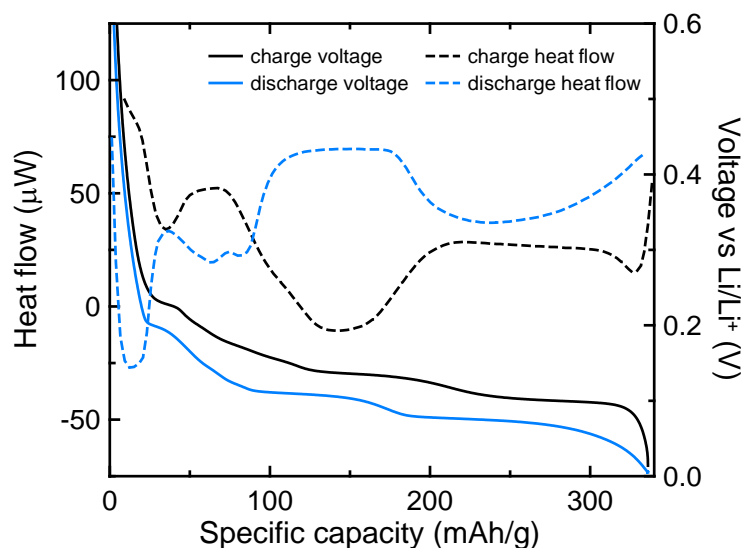


Figure 2.7: Voltage (solid lines) and corresponding heat flow (dashed lines) as a function of specific capacity during a C/10 charge (black) and discharge (blue) of a graphite/Li coin cell.

Figure 2.8 shows the voltage and corresponding measured heat flow as a function of capacity during a full cycle at C/10 and 40°C for an NMC111/graphite full cell where the corresponding half cell data for each electrode is given in Figure 2.6 and Figure 2.7. As expected, the measured heat flow during charge of the NMC111/graphite cell is a qualitative sum of the heat flow during charge of the NMC111/Li half cell and the discharge of the graphite/Li half cell (or the reverse for the full cell discharge). In taking this sum, the heat flow associated with the change in entropy of the lithium metal electrodes in the half cells should cancel since lithium is being plated during charge of the NMC111/Li half cell and stripped during discharge of the graphite/Li half cell (or the reverse for the full cell discharge). However, this sum is not exact due to slight differences in the electrodes between the half cells and full cell, as well as possible parasitic heat flow resulting from reactions at the Li electrode.

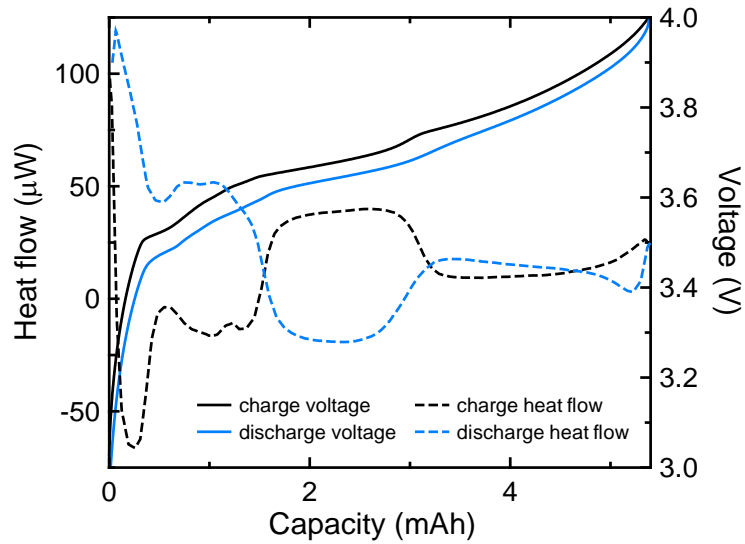


Figure 2.8: Voltage (solid lines) and corresponding heat flow (dashed lines) as a function of capacity during a C/10 charge (black) and discharge (blue) of an NMC111/graphite coin cell.

The contribution of changes in entropy to the heat flow as a function of state of charge of the full cell shown in Figure 2.8 is in good qualitative agreement with the change in entropy observed for the $\text{LiFePO}_4/\text{graphite}$ cells shown in Figure 2.5. This is not surprising as the staging transitions in graphite result in most of the features in the entropy profile of many full cells. One notable exception is LCO/graphite cells, as LCO proceeds through an order-disorder transition slightly above and below $x = 0.5$ in Li_xCoO_2 .¹⁹⁵ Figure 2.9 shows the voltage and corresponding heat flow as a function of capacity for a full cycle at C/22.5 and 40°C for an LCO/graphite pouch cell. The heat flow profile shows the contribution from the changes in entropy from graphite as well as the order-disorder transition in LCO which appears in this cell at approximately 4.05 V.

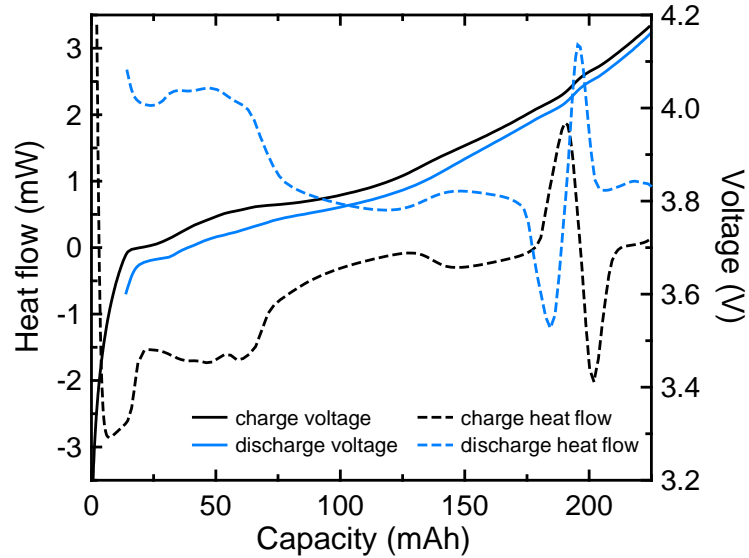


Figure 2.9: Voltage (solid lines) and corresponding heat flow (dashed lines) as a function of capacity during a C/22.5 charge (black) and discharge (blue) of an LCO/graphite pouch cell.

2.2.4 Parasitic Reactions

The last term in Equation 2.2.12, $\dot{d}q_p/dt$, is the heat flow associated with reactions other than intercalation, which is herein called the parasitic heat flow. This term is thought to be independent of current.^{170,171} Since there is not one single reaction occurring in a cell, the total measured parasitic heat flow is a result of the sum of all parasitic processes occurring in the cell and will be a function of the rate and enthalpy of reaction of each reaction. As was discussed in Section 1.4, the reaction rates are dependent on cell voltage, time, temperature, electrode morphologies, etc, but not current. The origin and functional form of the parasitic heat flow will be explored in detail in Chapter 9.

The reduction of the rate of parasitic reactions occurring within cells is essential to extending cell lifetimes. Therefore, it is of utmost importance to be able to measure and quantify these reactions in a precise manner.

2.3 PREVIOUS ISOTHERMAL MICROCALORIMETRY STUDIES OF LITHIUM ION CELLS

The technique of isothermal microcalorimetry has often been combined with electrochemical measurements to study the heat flow generated from lithium ion cells. Many positive electrode materials have been studied using half cells, including: LiCoO_2 ¹⁹⁶, $\text{Li}_{1+x}[\text{Ni}_{1/3}\text{Mn}_{1/3}\text{Co}_{1/3}]_{1-x}\text{O}_2$ ¹⁸⁷, $\text{Li}_x\text{Mo}_6\text{Se}_8$ ¹⁸⁰, $\text{Li}_x\text{Mn}_2\text{O}_4$ ^{186,197}, $\text{Li}_{1+x}\text{Mn}_{2-y}\text{Al}_z\text{O}_4$ ¹⁹⁸, $\text{Li}_x\text{Al}_{0.17}\text{Mn}_{1.83}\text{O}_{3.97}\text{S}_{0.03}$ ¹⁸⁶, $\text{LiAl}_{0.2}\text{Mn}_{1.8}\text{O}_{4-\delta}\text{F}_{0.2}$ ¹⁹⁹, $\text{LiNi}_{0.8}\text{Co}_{0.15}\text{Al}_{0.05}\text{O}_2$ ¹⁸⁴, and carbon-coated LiFePO_4 ²⁰⁰. Heat flows from some commonly used negative electrode materials have also been studied using half cells, including: graphite¹⁹⁶, mesocarbon microbead carbon¹⁸³, and $\text{Li}_{4/3}\text{Ti}_{5/3}\text{O}_4$ ²⁰¹. Isothermal calorimetric studies of some full cells have also been reported, including: $\text{LiCoO}_2/\text{graphite}$ ^{185,189,196}, $\text{LiCoO}_2/\text{hard carbon}$ ²⁰², $\text{LiNi}_{0.8}\text{Co}_{0.15}\text{Al}_{0.05}\text{O}_2/\text{hard carbon}$ ²⁰³, and $\text{LiMn}_2\text{O}_4/\text{Li}_{4/3}\text{Ti}_{5/3}\text{O}_4$ ²⁰⁴.

The goal of many of the above referenced experiments was the identification and separation of heat flow due to polarization and entropy, with particular emphasis on applying the results to thermal modeling and heat management systems. As was discussed in Section 2.2.3, the contribution of changes in entropy to the total heat flow can be much larger than the contribution from polarization for moderate currents. Therefore, many of the prior microcalorimetry studies above explored the effect of positive and negative electrode material choice on the total heat flow. For example, Lu *et al.*¹⁹⁸ and Bang *et al.*¹⁸⁶ investigated the doping LiMn_2O_4 with Li, Al, and S to suppress the order-disorder transitions in LiMn_2O_4 as a way to reduce the rate of heat evolution.

The identification of the heat flow associated with changes in entropy also led to some interesting studies on the effect of long term cycling¹⁸⁵ and storage²⁰³ on the

degradation of the active materials. Kobayashi *et al.*¹⁸⁵ compared the heat flow from new commercial LCO/graphite cells to identical cells that were cycled for 700 cycles. Through careful examination of the changes in the heat flow associated with the graphite and LCO materials, they found that the observed capacity fade from long term cycling was governed predominately by the degradation of graphite. Saito *et al.*²⁰³ explored the effect of very long term storage (> 700 d) at a high state of charge for three different temperatures on the heat flow when cycled at C/10 and C/1. The cells which exhibited the largest capacity fade had the largest heat generation at high rate, while little difference was observed at C/10. This was attributed to an increase in the cell resistance, although there was no discussion of changes in heat flow profile resulting from possible material degradation.

The heat flow model used in most of these previous studies was largely based on the general energy balance derived by Newman *et al.*^{168,169} (Equation 2.2.11), which assumed that the heat flow arising from side reactions was negligible. The measured heat flow was typically separated into reversible and irreversible components, by either approximating the overpotential to determine the polarization, and/or by estimating the entropy changes by measuring the change in open circuit voltage as a function of temperature. These methods only present a very rough approximation of the relative contribution of each heat flow source. All of these studies, including the two studies aiming to explore the effect of cell degradation^{185,203}, failed to include the heat resulting from parasitic reactions.

With the recent introduction of extremely sensitive microcalorimeters, Krause *et al.*¹⁷³ demonstrated how to isolate the parasitic energy, q_p , per cycle from the measured heat flow and electrochemical data. This was achieved by integrating the heat flow signal

with respect to time over an entire cycle (charge and discharge) to arrive at a thermal energy per cycle. Since the heat flow due to changes in entropy is reversible, the integration over the full cycle cancels out this contribution. The thermal energy per cycle due to cell polarization can be calculated by taking the area of the voltage curve hysteresis as shown in Figure 2.1. The remaining source of thermal energy is the heat from parasitic reactions, which can be calculated by subtracting the energy from cell polarization from the total thermal energy. This can be expressed as:

$$q_p = \left[\int_0^{t_d} \frac{dq_d}{dt} dt + \int_0^{t_c} \frac{dq_c}{dt} dt \right] - \left[\int_0^{t_c} I_c V_c dt - \int_0^{t_d} I_d V_d dt \right] \quad (2.2.18)$$

where the subscripts *c* and *d* refer to charge and discharge, respectively. Equation 2.2.18 requires that no capacity is lost between charge and discharge; however, in practice, small changes in capacity can be tolerated without significant decreases in accuracy. Krause *et al.*¹⁷³ compared the calculated parasitic energy per cycle between constant current and constant capacity cycling and found excellent agreement, confirming that small capacity losses can be well tolerated in Equation 2.2.18.

The parasitic energy per cycle, q_p , defined in Equation 2.2.18, can also be used to extract the enthalpy of reaction between the electrode and electrolyte in the case of symmetric cells.^{173,205} A symmetric cell is a type of cell where the two electrodes are identical but at full state of charge one electrode is fully lithiated while the other is fully delithiated.²⁰⁶ It has been shown for graphite/graphite symmetric cells that the coulombic efficiency is correlated to the irreversible loss of lithium.⁴¹ Therefore, the number of moles of lithium lost in one cycle can be calculated from the loss in capacity over that cycle. If the parasitic energy is a result of reactions between the lithiated electrode and the electrolyte, then plotting the parasitic energy as a function of moles of

Li^+ lost yields a linear relationship, the slope of which is the reaction enthalpy.^{173,205} The intercept of such a plot gives the amount of parasitic energy that is due to reactions that do not consume Li^+ . However, this method provides no information about the voltage dependence of these parasitic reactions.

2.4 ADVANTAGES AND LIMITATIONS OF ISOTHERMAL CALORIMETRY

The heat flow of a lithium ion cell is a simultaneous probe of the evolution of the cell impedance measured as polarization, changes in active materials that result in changes in entropy, and parasitic reactions occurring within the cell. While all of these properties can be individually characterized, the typical techniques used are usually either performed at a limited number of points along the voltage curve, require data which are averaged over a full cycle, or require the disassembly of the cell. The advantage of isothermal microcalorimetry is that it is an *in operando*, non-destructive, and non-invasive method. Furthermore, the heat flow is collected as electrochemical tests are performed, so most electrochemical analysis that would otherwise be carried out can be completed in parallel to the calorimetric data.

There are also several limitations of isothermal microcalorimetry measurements. Due to the requirement of extremely stable temperatures, it can take up to 24 hours for a cell to reach thermal equilibrium. Therefore, any process that occurs rapidly after cell construction cannot be investigated. It is also not particularly well-suited to studies of the formation process in cells for safety reasons, as this step is where manufacturing defects, which can lead to internal short circuits, are discovered. Although rare, a short circuit produces a very significant amount of heat which can damage the sensors inside the

calorimeter. When using larger format cells with high sensitivity isothermal microcalorimeters, such as the one used throughout this thesis, cycling must be done at relatively low currents to avoid any loss of data due to the time constant of the calorimeter. Furthermore, each source of heat flow results from the sum of all processes occurring within the cell. For example, in a full cell there is no direct separation between heat flows resulting from the individual electrodes. This will also prevent the identification of individual parasitic reactions, as the resulting heat flow is averaged over all reactions. However, being able to extract the heat flow due to all parasitic reactions as a function of time and voltage, as will be shown in this thesis, is an important step towards the understanding of the reactions that ultimately lead to cell failure.

CHAPTER 3

EXPERIMENTAL TECHNIQUES

3.1 CELL CONSTRUCTION

3.1.1 Electrolyte Preparation

Electrolyte solutions were prepared in an argon-filled glovebox. Most electrolytes used throughout this work are based on a control electrolyte composed of a 1 M solution of LiPF_6 in a 3:7 ratio of ethylene carbonate (EC):ethyl methyl carbonate (EMC). Early experiments used a commercially premixed 3:7 ratio by weight, while later experiments were premixed 3:7 by volume, leading to slightly different molar ratios of EC:EMC. Electrolyte additives were added to the control electrolyte in terms of weight percent. All solutions were made in small plastic Nalgene polyethylene bottles and were prepared no more than 24 h before filling of cells to minimize degradation, and no less than about 3 h to ensure complete dissolution of solids. Table 3.1 details the suppliers and purities for all salts, solvents, and electrolyte additives used throughout this thesis. All chemical acronyms are given in Section 1.5.

3.1.2 Cell Preparation

The pouch cells used throughout this thesis were machine-made and provided dry (no electrolyte added) and vacuum sealed from the manufacturer. LCO/graphite pouch cells were provided by Umicore N.V.(Cheonan, Korea), while all others were supplied by

Table 3.1: Suppliers and purities of all electrolyte components used.

Category	Chemical	Supplier	Purity
Salt	LiPF ₆	BASF	99.94%
	LiFSI	HSC Co.	99.95%
Solvent	3:7 EC:EMC*	BASF	< 20 ppm H ₂ O
	FEC	BASF	99.94%
	TFEC	3M Co.	unknown
	EA	BASF	99.99%
	MP	BASF	99.99%
	VC	BASF	99.8%
Additive	PES	Lianchuang Medicinal Chemistry Co.	98.2%
	DTD	Sigma Aldrich	98%
	TMS	Sigma Aldrich	98%
	MMDS	Guangzhou Tinci Co. Ltd.	98.70%
	TTSP	TCI America	> 98%
	TTSPi	TCI America	> 95%
	TAP	TCI America	> 94%

* For both by weight and by volume solutions

LiFUN Technology (Xinma Industry Zone, Golden Dragon Road, Tianyuan District, Zhuzhou City, Hunan Province, PRC, 412000).

The pouch cells from LiFUN were 40 mm long by 20 mm wide and 3.5 mm thick. The positive electrode formulations were similar between all cells examined. As an example, NMC111/graphite pouch cells balanced to 4.4 V operation had a positive electrode formulation of 96.2:1.8:2.0 active material:carbon black:PVDF binder, while the negative electrode formation was 95.4:1.3:1.1:2.2 active material:carbon black:carboxymethyl cellulose (binder):styrene-butadiene rubber (binder). The positive electrode coating was 47.5 μm thick on both sides of an Al current collector to give a total electrode thickness of 105 μm with total dimensions of 200 mm long by 26 mm

wide. The negative electrode coating was 50 μm thick on each side of a Cu current collector to give a total electrode thickness of 110 μm with total dimensions of 204 mm long by 28 mm wide. Both electrodes also had small regions that were only coated on one side at the end of the current collectors such that the active area was approximately 100 cm^2 . The positive and negative electrodes were calendared to densities of 3.55 g/cm^3 and 1.55 g/cm^3 , respectively, resulting in area densities of 16 mg/cm^3 and 9.5 mg/cm^3 , respectively. The separators used in these pouch cells had a total thickness of 20 μm and were made from microporous polypropylene with a 4 μm thick Al_2O_3 ceramic coating (particle size about 1 – 2 μm in diameter) on the side in contact with the positive electrode. The electrodes and separators were flat-wound into a jelly roll, as shown in Figure 1.10.

In order to remove any residual water from the electrode surfaces, the pouch cells were cut open below the manufacturer seal and vacuum dried at 80°C overnight (~ 14 h). They were then directly transferred to an argon-filled glovebox without exposure to ambient air. The cells were then filled using a syringe with 0.7 – 1.2 g of electrolyte, depending on the cell type and solvent density. The specific amounts of electrolyte used in each cell are given in each Chapter.

Once filled, the cells were squeezed several times to allow the liquid to soak into the jelly roll and when there was no visible pool of liquid on top of the jelly roll, the cells were sealed for 4 – 6 s at 150 – 165°C using a compact vacuum sealer (MSK-115V, MTI Corp.) at 85 – 94% of full vacuum. The sealing procedure evolved over time as it was being optimized, and therefore the specific sealing parameters for each batch of cells are summarized in Section 3.1.4, as well as given in the relevant Chapters.

3.1.3 Cell Formation

After being filled with electrolyte, the cells were removed from the glovebox and underwent wetting and formation procedures. The initial wetting step ensures that electrolyte fills all pores within the electrodes and separator such that current densities are more uniform within each electrode. This is especially important for high energy density cells that contain highly calendared electrodes.²⁰⁷ The wetting procedure used for all cells throughout this work was a C/20 charge to 1.5 V followed by a 24 h hold at 1.5 V, all done in a 40°C temperature-controlled box.

The formation procedure results in the initial SEI formation on the electrode surfaces. The SEI composition and stability, and consequently the cell performance, is highly dependent on this formation step.^{84,207} The formation procedure used for commercial cells is typically proprietary and therefore little information is known. However, some protocols involving two-step current charging²⁰⁸, pulse charging²⁰⁹, and elevated temperature aging⁹⁹ have been reported. It is clear that the formation of lithium ion cells is not a clearly defined process, and as such, the protocol evolved over the course of experiments performed here. Five different formation protocols were used for cells tested in the calorimeter, and are summarized in Table 3.2. Common to every protocol is a degassing step, where the cells were weighed to determine the amount of gas produced as discussed in Section 3.3, then brought back into an argon-filled glovebox. They were cut below the previous seal to release any gas that was produced, and then resealed according to the initial sealing procedure. The specific formation protocols for each batch of cells are summarized in Section 3.1.4, as well as given in the relevant Chapters.

Table 3.2: Summary of formation protocols used throughout this work.

Name	Procedure
A	<ol style="list-style-type: none"> 1. Charge at C/100 for 10 hours 2. Charge at C/15 to 4.2 V 3. Discharge at C/15 to 3.775 V 4. Degas
B	<ol style="list-style-type: none"> 1. Charge at C/100 for 10 hours 2. Charge at C/15 to 4.4 V 3. Discharge at C/15 to 2.8 V 4. Charge at C/15 to 3.8 V 5. Degas
C	<ol style="list-style-type: none"> 1. Charge at C/20 to 3.8 V 2. Degas
D	<ol style="list-style-type: none"> 1. Charge at C/20 to 3.8 V 2. Degas 3. Charge at C/20 to 4.1 V
E	<ol style="list-style-type: none"> 1. Charge at C/20 to 3.8 V 2. Degas 3. Charge at C/20 to 4.5 V 4. Degas

3.1.4 Summary of Cells and Preparation Methods Used in This Work

Table 3.3 gives a summary of the types of pouch cells used throughout this work, including the positive and negative electrode active materials, the designed upper cutoff voltage, the cell capacity, as well as the manufacturer. Table 3.4 gives a summary of the sealing procedure (percentage of full vacuum, sealing time and temperature), wetting procedure, and selected formation procedure as defined in Table 3.2. The amount of electrolyte added to each cell is given in the relevant Chapters as this was also dependent on the solvent system examined.

Table 3.3: Summary of cells used in this work.

Shorthand Name	Positive Electrode	Negative Electrode	Upper cutoff voltage	Capacity	Source
HV-LCO	LiCoO ₂	Graphite	4.45 V	200 mAh	Umicore
NMC111 4.2 V	Li[Ni _{1/3} Mn _{1/3} Co _{1/3}]O ₂	Graphite	4.2 V	220 mAh	LiFUN
NMC111 4.4 V	Li[Ni _{1/3} Mn _{1/3} Co _{1/3}]O ₂	Graphite	4.4 V	240 mAh	LiFUN
NMC811	Li[Ni _{0.8} Mn _{0.1} Co _{0.1}]O ₂	Graphite	4.5 V	220 mAh	LiFUN
NMC442†	Li[Ni _{0.42} Mn _{0.42} Co _{0.16}]O ₂	Graphite	4.7 V	260 mAh	LiFUN

† Cells from two manufacturing batches were used

Table 3.4: Summary of cell sealing, wetting, and formation procedures used in this work.

Shorthand Name	% of full vacuum during seal	Sealing time (s)	Sealing temp. (°C)	Wetting procedure	Formation procedure*
HV-LCO	94%	6	150	24 h at 1.5 V	C
NMC111 4.2 V	85%	4	160	24 h at 1.5 V	A
NMC111 4.4 V†	85%	4	160	24 h at 1.5 V	B
	85%	5	150	24 h at 1.5 V	C
NMC811	87.5%	6	160	24 h at 1.5 V	D
NMC442‡	85%	6	165	24 h at 1.5 V	E
	87.5%	5	160	24 h at 1.5 V	E

* Procedures defined in Table 3.2

† Different experiments run on the same manufacturing batch of cells

‡ Experiments conducted on cells from two different manufacturing batches

3.2 CELL CYCLING

While inside the calorimeter, the cells were connected to charging systems which delivered a current and measured the voltage. For most calorimetry experiments

presented here, a commercial Maccor Series 4000 charger was used. One calorimetry experiment, discussed in Chapter 9, used an in-house built ultra high precision charger (UHPC)²¹⁰ for cycling. Complementary cycling data performed outside of the calorimeter using a Maccor 4000, the UHPC, and a commercial charger from Neware are also presented. Table 3.5 gives a summary of the resolution and accuracy for the supplied and measured current and measured voltage, as well as the time between measurements for the Maccor 4000, Neware BTS-5V1mA, and the UHPC.⁷¹

Table 3.5: Resolution and accuracy of current and voltage and time between measurements (Δt) for charging systems used in this work.⁷¹

Charger	Current setpoint resolution	Voltage sense resolution	Current sense accuracy	Voltage sense accuracy	Δt
Maccor 4000	0.0015% of full scale	$\sim 150 \mu\text{V}$	0.02 - 0.05% of full scale	2 mV (10 V max)	0.01 s
Neware BTS-5V1mA	0.0015% of full scale	$\sim 75 \mu\text{V}$	0.05% of full scale	2.5 mV (5 V max)	5 s
UHPC Dalhousie	0.002% of full scale	$1 \mu\text{V}$	<0.003% of full scale	< 0.2 mV (5V max)	<1 s by interpolation

The foremost advantage of the UHPC is the precision and accuracy of the measured capacity, and correspondingly CE. This is achieved by the addition of a high precision resistor that is monitored in line with a second digital multimeter (Keithley 2000). This allows for real time current measurements to determine capacity instead of relying on the assumption of a constant current. The noise of CE measurements is further reduced by software processing that uses linear interpolation to determine the exact moments when the preset voltage limits are reached. This minimizes the error associated

with voltage overshoot, which varies from cycle to cycle, and calculates the capacities and CE in the desired voltage range. The precision of CE measurements using the UHPC and the Maccor 4000 are approximately 5 ppm and 100 ppm, respectively, while the accuracy of such measurements are 30 ppm and 1200 ppm, respectively.²¹⁰

3.3 GAS GENERATION MEASUREMENTS

The volume of gas generated in a pouch cell can be determined using Archimedes' principle. This can be done either *in situ* or *ex situ*²¹¹, although all measurements done in this thesis were performed *ex situ* unless otherwise stated. By completely submerging a cell in a fluid, the buoyant force, F_B , acting on the cell is equal to the weight of the fluid displaced and the displaced fluid volume is equal to the cell volume, V_{cell} , that is:

$$F_B = \rho_{fluid} V_{cell} g \quad (3.3.1)$$

where ρ_{fluid} is the density of the fluid. The buoyant force, and therefore the cell volume, can be indirectly monitored by suspending the submerged cell from a balance. Figure 3.1 shows a schematic of the gas measurement experimental setup used. The tension in the thin wire hook used to suspend the cell is equal to the weight measured by the balance, and the sum of all forces acting on the cell must equal zero for static equilibrium. Therefore the mass measured by the balance, $m_{balance}$, for a submerged cell of mass m_{cell} , is given by:

$$m_{balance} = (m_{cell}) - (\rho_{fluid} V_{cell}) \quad (3.3.2)$$

A measurement of the change in measured mass by the balance can then be used to calculate the change of cell volume, that is:

$$\Delta m_{balance} = (\Delta m_{cell}) - (\Delta(\rho_{fluid} V_{cell})) = -\rho_{fluid} \Delta V_{cell} \quad (3.3.3)$$

The change in cell volume is assumed to be approximately equal to the volume of gas produced during a particular experiment. Equation 3.3.3 can be rearranged to give a simple expression for the volume change of the cell, ΔV_{cell} , and therefore an approximation of the volume of gas produced, V_{gas} :

$$V_{gas} = \Delta V_{cell} = -\frac{\Delta m_{balance}}{\rho_{fluid}} \quad (3.3.4)$$

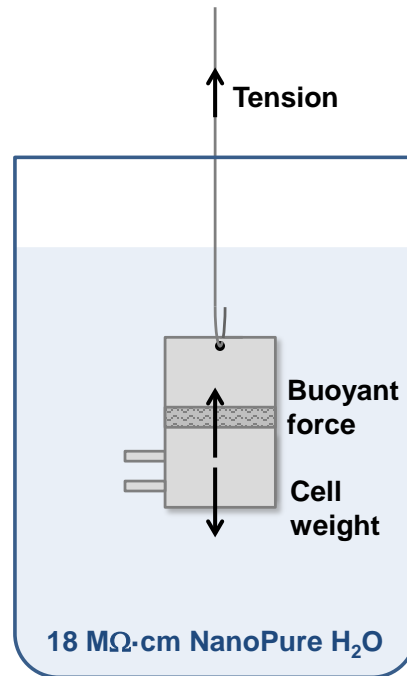


Figure 3.1: Schematic of gas measurement experimental setup. The wire suspending the cell is attached to the bottom of a balance.

As indicated in Figure 3.1, NanoPure water (Barnstead NanoPure, Thermo Scientific) was used for the gas volume measurements performed here. The resistivity of this water is 18.2 MΩ-cm, which prevents discharge of the cell by limiting any flow of current between the two leads which are separated by approximately 0.5 cm. The fluid

density at room temperature (20°C) is 0.9982 g/cm³, which simplifies Equation 3.3.4 without significant loss in accuracy to:

$$V_{gas} = \Delta V_{cell} = -\Delta m_{balance} \quad (3.3.5)$$

3.4 ISOTHERMAL MICROCALORIMETRY

3.4.1 Operation

All isothermal microcalorimetry experiments were performed using a TAM (Thermal Activity Monitor) III heat flow calorimeter from TA Instruments that is equipped with twelve 20 mL microcalorimeters, as pictured in Figure 3.2.

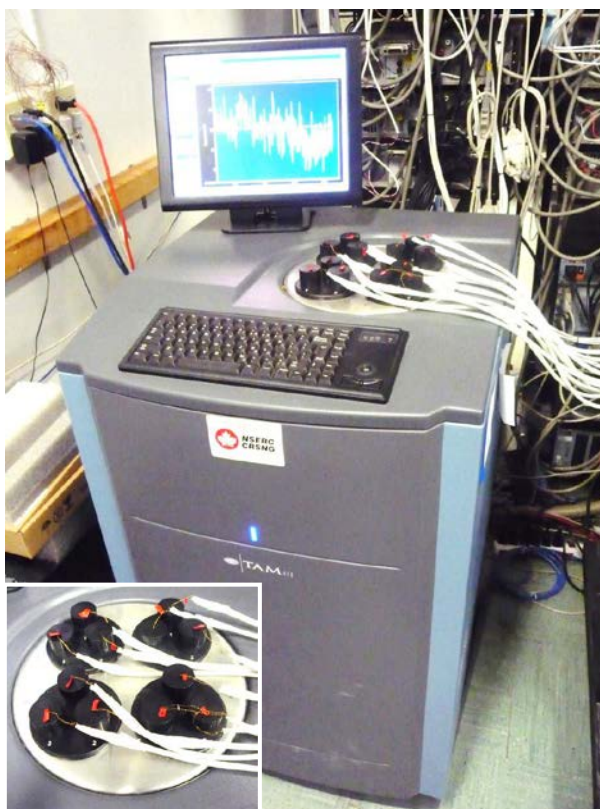


Figure 3.2: TAMIII isothermal microcalorimeter equipped with 12 calorimeters.

Figure 3.3 shows a schematic diagram of the measuring assembly for one of the microcalorimeters installed in the TAM III. The rate of heat produced by the sample, \dot{dq}/dt , is given by:

$$\frac{\dot{dq}}{dt} = \Phi + C_s \left(\frac{dT_s}{dt} \right) \quad (3.4.1)$$

where Φ is the rate of heat exchange and is $C_s(dT_s/dt)$ the rate of heat accumulation, where C_s is the heat capacity of the sample, and T_s is the sample temperature. The rate of heat exchange is governed by Newton's law of cooling and is given by:

$$\Phi = k_s (T_s - T_0) = k_s (\Delta T_s) \quad (3.4.2)$$

where k_s is the sample heat conductance, T_0 is the environment temperature, and ΔT_s is difference in temperature between the sample and environment.

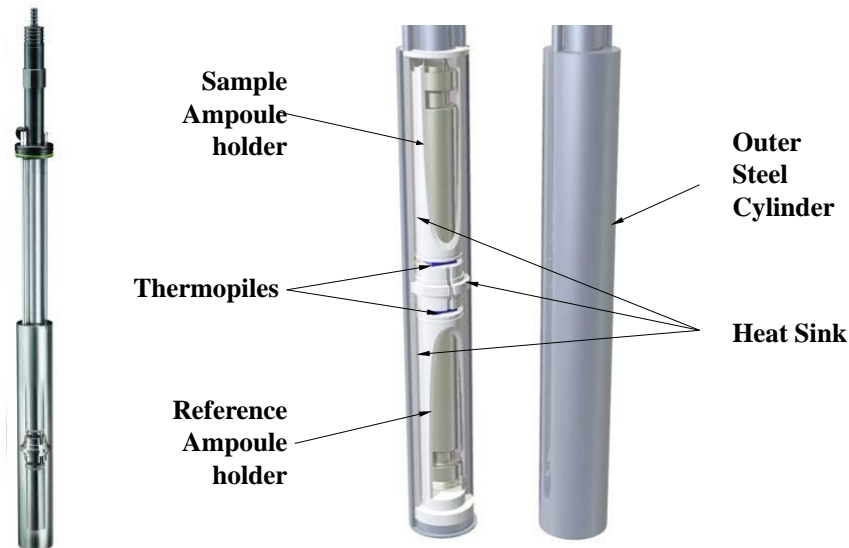


Figure 3.3: Schematic of the microcalorimeter measuring assembly used in the TAMIII. Figure provided by Dr. Caleb MacDonald, TA Instruments staff scientist.

Using the lumped thermal capacitance method, k_s can be expressed as²¹²:

$$k_s = \frac{C_s}{\tau_s} \quad (3.4.3)$$

where τ_s is the time constant of the sample ampoule system, which is shown in Figure 3.3. The rate of heat exchange of the sample is measured by the calorimeter using thermopiles, where the temperature gradient between the sample and environment produces a measurable voltage difference, V_s . Therefore it is convenient to use the Seebeck coefficient of the thermopile, S_b , which is defined here by:

$$S_b = \frac{V_s}{\Delta T_s} \quad (3.4.4)$$

Combining Equations 3.4.1 through 3.4.4, the heat flow can be expressed as²¹²:

$$\frac{dq}{dt} = \varepsilon_s \left(V_s + \tau_s \frac{dV_s}{dt} \right) \quad (3.4.5)$$

Equation 3.4.5 is known as the Tian-Calvet equation where ε_s is the calibration constant and is given by:

$$\varepsilon_s = \frac{C_s}{S_b \cdot \tau} \quad (3.4.6)$$

The time constant is determined by the calorimeter by applying a known heat on the sample side with a heating ring (not pictured in Figure 3.3) and measuring the time taken to reach 1-(1/e) (63.2%) of the final value. The average time constant of the calorimeters in the TAMIII is 297(3) s. The calibration constant is determined such that the rate of heat production is equal to the measured rate of heat exchange.

As shown in Figure 3.3, the TAMIII microcalorimeter is a twin system, meaning every calorimeter channel has a sample and reference cell, which is used to decrease the signal noise.¹⁶⁶ Following a similar derivation as above, the heat flow of the reference system, \dot{q}_r/dt , can be expressed as:

$$\frac{dq_r}{dt} = \varepsilon_r \left(V_r + \tau_r \frac{dV_r}{dt} \right) \quad (3.4.7)$$

where ε_r , V_r , and τ_r are the calibration constant, voltage difference, and time constant for the reference ampoule system, respectively. The reference system is at equilibrium and therefore $\dot{d}q_r/dt = 0$, allowing for the subtraction of Equation 3.4.5 and 3.4.7 to give the twin system measured sample heat flow:

$$\frac{\dot{d}q}{dt} = \varepsilon_s \left(V_s + \tau_s \frac{dV_s}{dt} \right) - \varepsilon_r \left(V_r + \tau_r \frac{dV_r}{dt} \right) \quad (3.4.8)$$

Under the assumptions that the heat conductance and heat capacities of the sample and reference systems are equal, that is:

$$k_s = k_r = k \quad (3.4.9)$$

$$C_s = C_r = C \quad (3.4.10)$$

then the measured heat flow of the sample is given by:

$$\frac{\dot{d}q}{dt} = \varepsilon \left[(V_s - V_r) + \tau \frac{d(V_s - V_r)}{dt} \right] \quad (3.4.11)$$

The second term in Equation 3.4.11 is known as the Tian correction and is used to account for the response time of the calorimeter. In the TAMIII mode of operation used throughout this work, the Tian correction is not applied, and therefore, the heat flow reported by the calorimeter is the steady-state version of Equation 3.4.11, given by:

$$\frac{\dot{d}q}{dt} = \varepsilon (V_s - V_r) \quad (3.4.12)$$

3.4.2 Experimental Setup

The 20 mL stainless steel sample ampoule shown in Figure 3.3 is lowered into the measurement position using a lifter. Figure 3.4 shows a schematic of the lifter assembly and a photo of the cell attachment within the sample ampoule.

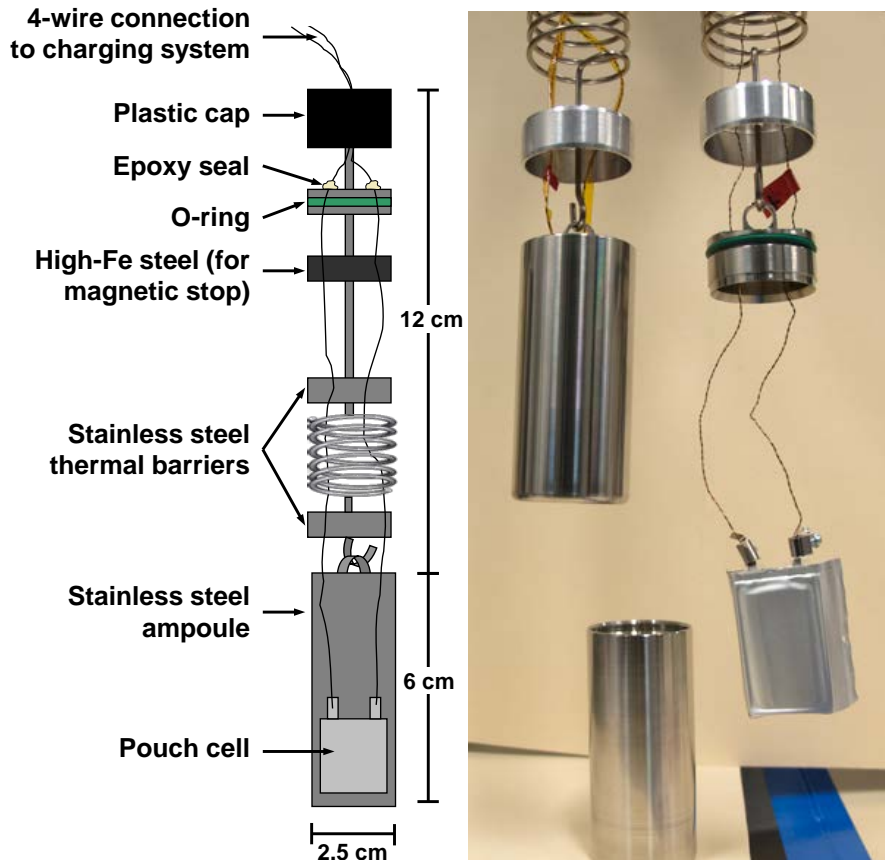


Figure 3.4: The lifter and sample ampoule assembly used in the TAMIII.

The lifter is made up of a series of thermal barriers to prevent heat transfer away from the thermopile detector, with the top-most having an o-ring to provide a good seal. The very bottom of the lifter has a hook that is used to suspend the sample ampoule. To allow for the passage of wires to connect a lithium ion cell, small holes were drilled into the cap of the ampoule, through all the thermal barriers and up through the top plastic lifter cap. Once the wires were fed through, the top-most drilled hole was sealed with a small amount of Torr Seal (Varian Inc.) epoxy resin. A four-wire configuration (current and voltage for both positive and negative electrodes) was used. In order to reduce heat transfer through the wires, 32 gauge dual-twist cryogenic polyimide coated phosphor bronze wires (LakeShore Cyrotronics Inc.) that have a low thermal conductivity (48

W/m·K at 300 K) were used.²¹³ The polyimide coating prevents short circuiting of the cell. In order to connect the cell to a current source for charging and discharging, the wires were connected to the cell tabs, and the whole cell was placed at the bottom of the sample ampoule, as shown in the photograph in Figure 3.4. The other ends of the wires, which come out through the top of the lifter, were spliced to a cat5e Ethernet cable, which can be seen in Figure 3.2. The cables were then connected to an Ethernet feed-through block, where the other ends were then connected to the desired cell charger system. This feed-through system allows for easy switching between charging systems.

3.4.3 Baseline and Calibration

The calorimeter is internally calibrated, but to better replicate the cell conditions, each calorimeter was manually calibrated before each experiment using a $10.00 \pm 0.01 \Omega$ precision resistor inserted into a dry pouch cell. The resistor leads were soldered to the wires and the calibration cell was placed into the ampoule that was then lowered into measuring position. The system was allowed to equilibrate for a minimum of 24 hours, and then an offset was applied to set the baseline to $0.0 \mu\text{W}$ using the heat flow response during the previous 4 – 6 hours of measurement. Figure 3.5 shows an example of the measured heat flow of a calibration cell during the baseline process. This process zeroed any contribution from the materials, tape, solder, etc.

Once the baseline was set, a current of 15 mA was applied to the calibration cell for 3 hours. The measured heat flow was then compared to the expected heat flow of 2.25 mW, allowing the gain of the calorimeter to be set. Figure 3.6 shows the heat flow response during the calibration process. When using the same calibration cells, the

baseline heat flow for each calorimeter typically remained constant within ± 500 nW and the measured heat flow from the passage of current through the resistor was within 1% of the previously calibrated value.

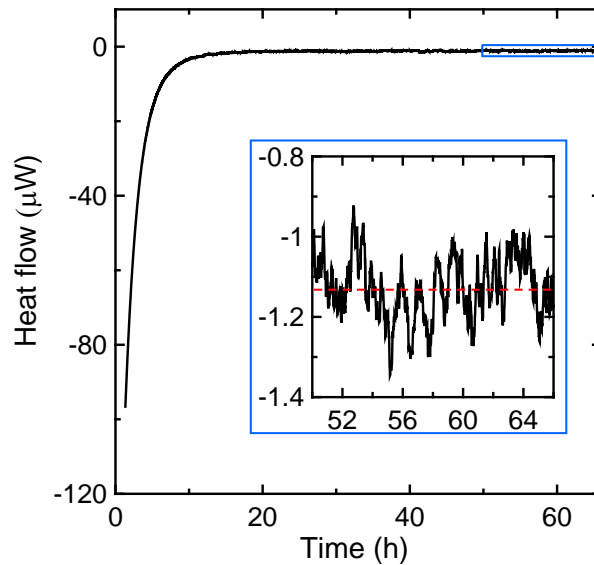


Figure 3.5: Heat flow response of a calibration cell. After thermal equilibration, the measured heat flow over a period of several hours (dashed red line, inset) was set to 0.0 μ W using an applied offset.

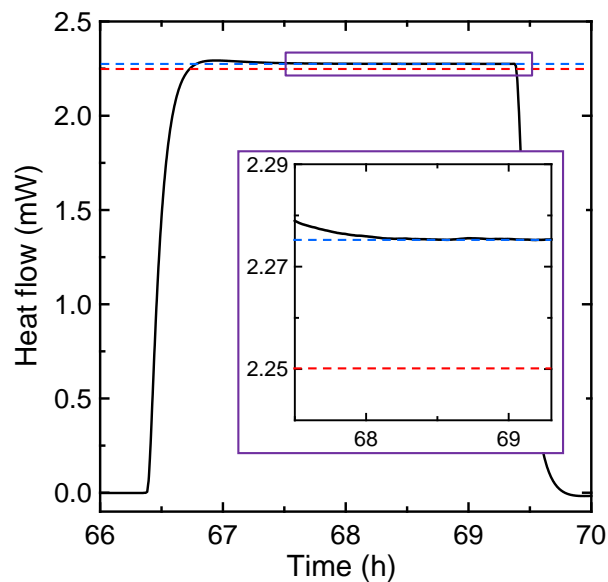


Figure 3.6: Heat flow response during calibration process where 15 mA was applied to a 10 Ω resistor for three hours. The gain was set such that the measured heat flow (blue dashed line) was equal to the expected heat flow (red dashed line).

The calorimeters were baselined and calibrated between every set of experiments, ensuring that the measured heat flow of pouch cells was as accurate as possible and only a result of the sources described in Section 2.2.

Since the calibration cell was dry, it must be confirmed that the electrolyte provides no additional source of heat flow through potential interactions with the pouch bag material or temperature-induced reactions in absence of the electrode materials. To accomplish this, an empty pouch (no jelly roll) of the same material and dimensions as used for pouch cells was filled with 0.9 g of control solvent (3:7 EC:EMC) and another was filled with 0.9 g of control electrolyte (1M LiPF₆ in 3:7 EC:EMC). Both cells were sealed and inserted into the calorimeter after the baseline was set using a calibration cell as described above. Figure 3.7 shows the heat flow response from the pouches containing only solvent or electrolyte. After thermal equilibration was reached, no discernable heat flow was detected (inset of Figure 3.7) for either case.

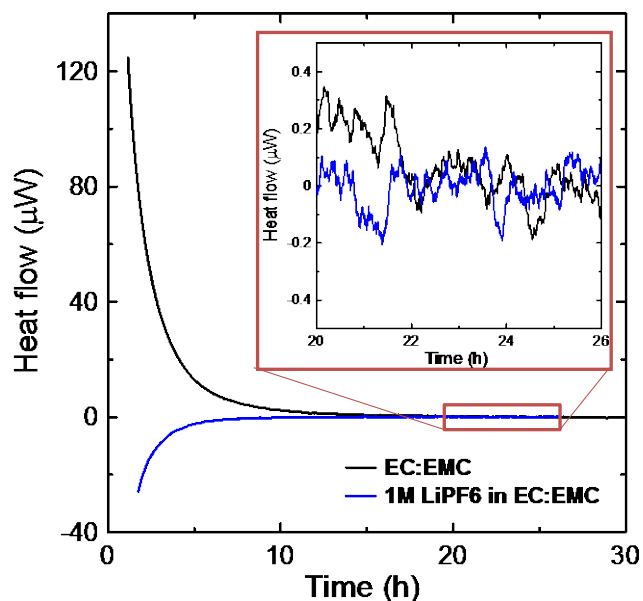


Figure 3.7: Heat flow response of a pouch bag filled with 3:7 EC:EMC (black) and 1M LiPF₆ in 3:7 EC:EMC (blue). Inset: response after equilibration.

The noticeably different heat flow profiles after insertion into the calorimeter ($t < 10$ h) is a result of differences in the amount of time between loading the empty pouch bag into the sample ampoule and insertion into the calorimeter. One hour passed before the lifter and sample ampoule containing the pouch bag with 1M LiPF₆ was lowered into the calorimeter, giving the ampoule plenty of time to cool, while the lifter and ampoule containing the pouch with only solvent was inserted into the calorimeter after only approximately 5 minutes.

3.4.4 Resolution, Stability, and Reproducibility

The TAMIII can measure the heat flow of a sample over 6 orders of magnitude, $10^{-2} - 10^{-8}$ W, has a sensitivity of approximately 100 nW and a conservative estimate of accuracy of less than ± 1 μ W. The isothermal bath temperature can be set between 15 and 150°C with a < 0.01 mK/24h temperature stability and ± 0.1 mK precision.¹⁶⁶ The calorimeter temperature is monitored at various locations within the machine with a series of 32 platinum resistance thermometer temperature sensors, and the bath temperature is controlled with a proprietary system of Pelletier coolers and fine heating elements.¹⁶⁶ Figure 3.8 shows the variation in bath temperature from the set point over a period of 2.5 months, demonstrating the remarkable stability of the TAMIII.

Figure 3.9 shows the measured heat flows of six nominally identical LCO/graphite pouch cells containing control electrolyte starting at 3.8 V. The cells were formed to 3.8 V prior to loading into the calorimeter. After thermal equilibration (inset of Figure 3.9), the measured heat flows of all cells were within 4 μ W of each other. This variance is greater than the accuracy of the TAMIII, and therefore cell-to-cell variation due to slight

differences in cell manufacturing, amount of electrolyte added, etc is the limiting factor in heat flow data accuracy. The variation of the measured capacity of the six cells shown in Figure 3.9 was 1.2%, the variation in voltage at $t = 100$ h was 0.1%, and the variation of the amount of electrolyte added was $< 1\%$.

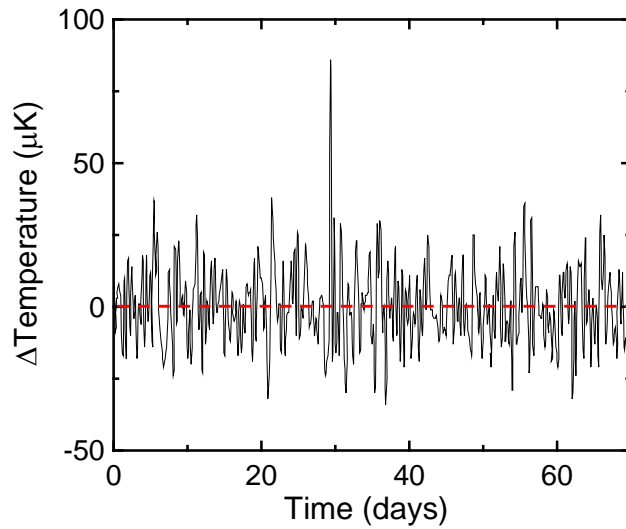


Figure 3.8: Variation in bath temperature of the TAMIII over a period of 2.5 months.

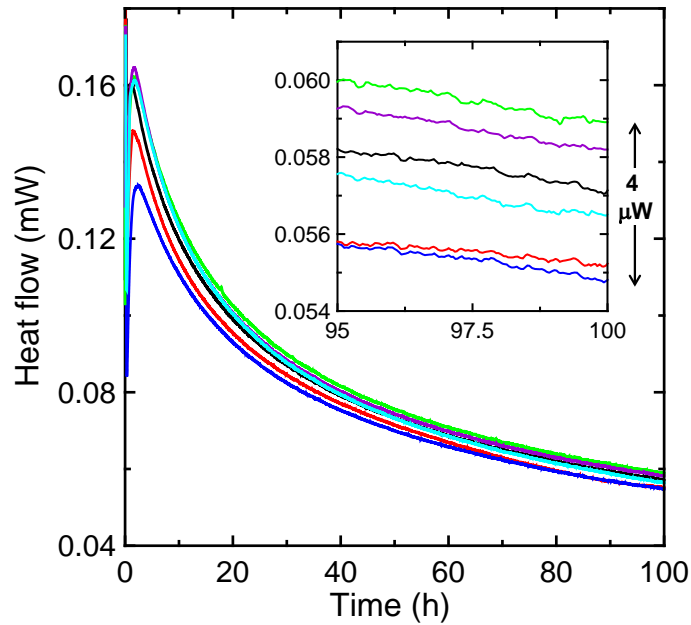


Figure 3.9: Measured heat flow at open circuit conditions after formation and insertion into the calorimeter for 6 identical LCO/graphite pouch cells containing control electrolyte starting from 3.8 V.

The variation in heat flow for nominally identical cells during cycling was also investigated. Figure 3.10a shows the measured heat flow during a 1 mA (C/260) cycle at the top of charge (4.1 – 4.3 V) for four nominally identical NMC442/graphite pouch cells containing control electrolyte to which 2% PES + 1% TTSPi + 1% MMDS was added. Figure 3.10b shows the deviation of the measured heat flow from the average heat flow of the four cells. Throughout the voltage range examined, the measured heat flow of each of the cells was within approximately $\pm 4 \mu\text{W}$ of the average. The average standard deviation of the measured heat flow between the four cells taken at 2 mV intervals over the voltage range examined was $1.9 \mu\text{W}$, in good agreement with the variation in the open circuit heat flow (Figure 3.9). Therefore the uncertainty associated with the heat flow measurements presented throughout this thesis is limited by the cell-to-cell reproducibility and is conservatively estimated to be $\pm 4 \mu\text{W}$.

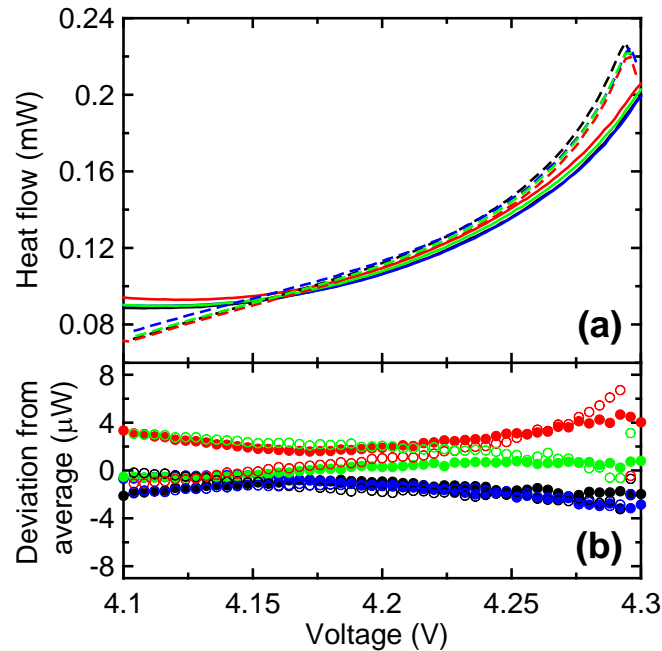


Figure 3.10: (a) Measured heat flow as a function of voltage for four identical NMC442/graphite pouch cells charged (solid lines) and discharged (dashed lines) at 1 mA (C/260) and (b) deviation of the measured heat flow from the average heat flow during charge (solid symbols) and discharge (open symbols).

CHAPTER 4

THE IMPACT OF ELECTROLYTE ADDITIVES DETERMINED USING COMPARITIVE ISOTHERMAL MICROCALORIMETRY

4.1 INTRODUCTION AND MOTIVATION

As was discussed in Chapter 1, the use of electrolyte additives is a common method that has been shown to extend calendar and cycle life and reduce parasitic reactions.^{6,7,45,46,70} However, it is not well understood how these additives are functioning and exactly where in the charge-discharge cycle they prove advantageous, even with single additive systems. Therefore, it is of distinct interest to be able to determine the voltage-dependent advantage of a particular additive or additive blend, which can aid in the understanding of how that additive or additive blend impacts cell performance.

To determine the impact of electrolyte additives, isothermal microcalorimetry was used to qualitatively compare the heat flow between cells that only vary in concentration of additive. In this case, with all other sources being identical, the measured difference in heat flow arises from differences in parasitic heat flow. The benefit of this method is that it is done as a function of state of charge, thereby providing a simple and quick method of determining exactly where and to what extent the additive or additive blend is reducing parasitic reactions. Investigating the voltage dependence of the impact of an additive on cell performance using typical cycling experiments would be extremely tedious if any appreciable voltage resolution was desired. This is a distinct advantage of isothermal microcalorimetry experiments. As a demonstrative example of this technique, the effect

of varying concentrations of VC alone and of ternary additive blends on NMC111/graphite pouch cells was examined. The results of isothermal microcalorimetry experiments were then compared to ultra high precision coulometry and long term cycling results.

4.2 EXPERIMENTAL DETAILS

Two types of machine-made $\text{LiNi}_{1/3}\text{Mn}_{1/3}\text{Co}_{1/3}\text{O}_2$ (NMC111)/graphite pouch cells 0.35 cm thick x 2 cm wide x 3 cm high were provided dry and vacuum sealed from Whenergy (now LiFUN Technology). One batch of cells was balanced for operation to 4.2 V with a capacity of 220 mAh, while the second batch was balanced for operation to 4.4 V with a capacity of 240 mAh. The pouches were cut open and dried overnight (approximately 14 h) at 80°C under vacuum to remove any residual water in the cells. The cells were then directly transferred to an argon-filled glovebox without exposure to ambient air, where they were filled with 0.85 g of electrolyte for isothermal microcalorimetry experiments and 0.90 g for ultra high precision charger (UHPC) and extended cycling experiments.

The control electrolyte was 1M LiPF_6 in 3:7 by weight EC:EMC. The electrolyte additives used in this work were VC, TTSP, TTSPi, DTD, and TMS, the suppliers and purities of which are given in Chapter 3. The combinations of the above additives studied using isothermal microcalorimetry were: 1% VC, 2% VC, 4% VC, 2% VC + 1% TTSPi + 1% MMDS, 2% VC + 1% TTSPi + 1% DTD, and 2% VC + 1% TTSPi + 1% TMS, where all percentages are given in weight percent added to control electrolyte. As shorthand notation, the cells are identified by the electrolyte additive(s), and the three

ternary additive blends are referred to as 211MMDS, 211DTD, and 211TMS, respectively. Duplicate cells were made for 4.4 V cells containing 1% VC, 2% VC, 4% VC, and 211MMDS to verify reproducibility between supposedly identical cells. Similar combinations were used for UHPC and extended cycling measurements, with the addition of quaternary electrolyte additive blends, where instead of 1% TTSPi in the ternary blends, 0.5% TTSP + 0.5% TTSPi was used.

Once the cells were filled with electrolyte, they were sealed with a compact vacuum sealer (MSK-115V, MTI Corp.) at 85% of full vacuum (-86.1 kPa gauge pressure or 15.2 kPa absolute pressure). Once sealed, the cells were removed from the glovebox and were formed. For the isothermal microcalorimetry experiments, the 4.2 V balanced cells were held at 1.5 V for 24 hours at 40°C to complete wetting, then charged at 2 mA for 10 hours, then charged at 15 mA to 4.2 V, and then discharged at 15 mA to 3.775 V. The 4.4 V balanced cells were also held at 1.5 V for 24 hours, charged at 2 mA for 10 hours, but were then charged at 15 mA to 4.4 V, then discharged at 15 mA to 2.8 V, and then charged at 15 mA to 3.8 V. For UHPC and long term cycling experiments, the cells were held at 1.5 V for 24 hours, then charged at 11 mA to 3.5 V, with the exception of the cells containing 2% VC + 1%MMDS + 0.5%TTSP + 0.5%TTSPi, which were held at 1.5 V for 24 hours, charged at 11 mA to 4.2 V, then discharged at 11 mA to 3.8 V. This led to extra time for the SEI films to mature compared to the other cells.

Once the cells were finished formation, they were transferred back to an argon-filled glovebox and were cut open under the previous seal to release any gas produced and resealed as previously described. All cycling of cells during formation and while inside the microcalorimeter were performed using a Maccor series 4000 automated test system (Maccor Inc.). UHPC measurements were performed using a charging system built in-

house²¹⁰, and long term cycling measurements were performed using a Neware charger system (Neware Battery Testing Instruments, Shenzhen, PRC).

Ex situ gas volume measurements were performed using the Archimedes method described in Chapter 2. Electrochemical impedance spectroscopy (EIS) measurements were conducted on the NMC111/graphite pouch cells after cycling on the UHPC. Cells were charged or discharged to 3.80 V before they were moved to a 10°C temperature controlled box. AC impedance spectra were collected with ten points per decade from 100 kHz to 10 mHz with a signal amplitude of 10 mV at $10.0 \pm 0.1^\circ\text{C}$.¹³¹

4.3 THE EFFECT OF ELECTROLYTE ADDITIVES ON NMC111/GRAPHITE 4.2 V AND 4.4 V POUCH CELLS

Methodologies used in this Section are adapted and reprinted with permission from *ECS Electrochem. Lett.*, **2**, A106 (2013)¹³². Copyright 2013, The Electrochemical Society.

4.3.1 The Effect of VC and Ternary Electrolyte Additive Blends on 4.4 V NMC111/Graphite Cells

Figure 4.1 shows the complete cycling protocol after formation and degassing used for cells tested inside the microcalorimeter at 40°C. Figure 4.1a shows the measured heat flow and Figure 4.1b shows the corresponding voltage profile. For simplicity, only the data for a control cell (no additives) and a cell containing 4% VC are shown. The cycling protocol can be broken up into the following steps:

- i. 24 hours at open circuit, stating at 3.8 V
- ii. 10 mA (C/24) discharge to 2.8 V and charge to 4.2 V
- iii. 10 mA (C/24) discharge to 2.8 V and charge to 4.3 V
- iv. 10 mA (C/24) discharge to 2.8 V and charge to 4.4 V
- v. 10 mA (C/24) discharge to 3.6 V
- vi. 2 mA (C/120) discharge to 2.8 V and charge to 3.6 V
- vii. 10 mA (C/24) charge to 4.0 V
- viii. 2 mA (C/120) (charge to 4.2 V and discharge to 3.9 V) x2
- ix. 2 mA (C/120) (charge to 4.3 V and discharge to 3.9 V) x2
- x. 2 mA (C/120) charge to 4.4 V and discharge to 3.9 V

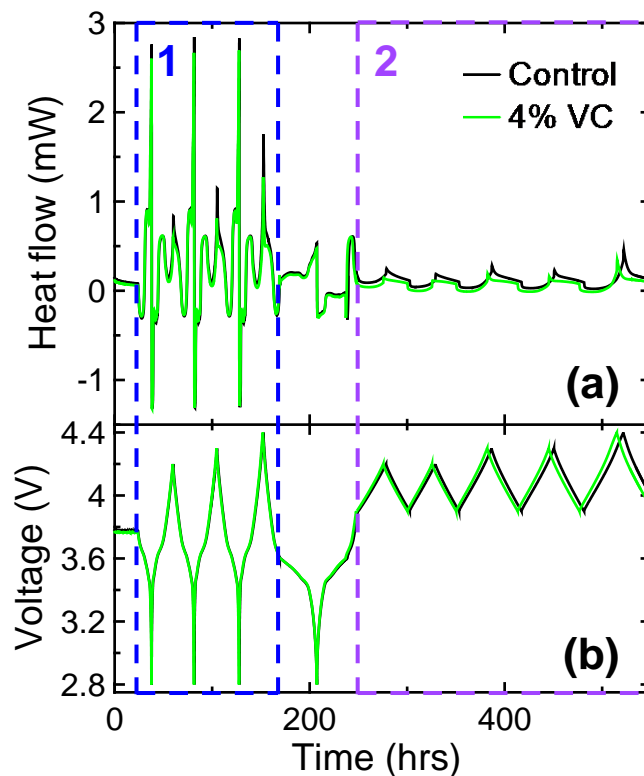


Figure 4.1: Complete experimental cycling protocol for all cells tested. Only data for control (black) and control + 4% VC (green) are shown for simplicity. Panel (a) shows the measured heat flow and panel (b) shows the corresponding voltage profile. Two distinct segments are highlighted, 10 mA full range cycling to progressively higher upper cutoff voltages (segment 1, blue) and 2 mA top of charge cycling (segment 2, purple).

Figure 4.1 highlights two distinct areas of interest out of the entire protocol. Segment 1 (blue) includes steps ii – iv, which are full range 10 mA (C/24) cycles to progressively higher upper cutoff voltages. Segment 2 (purple) includes steps viii – x, which are narrow range 2 mA (C/120) cycles at the top of charge also to progressively higher upper cutoff voltages. Cells containing 211DTD and 211TMS were stopped and removed from the calorimeter after segment 1.

The measured heat flow of the cell during cycling has contributions from three sources: entropy, polarization, and parasitic heat flow from both the positive and negative electrodes.¹⁶⁷ Both the entropy and polarization contributions are current dependent terms. Figure 4.1a shows this effect by examining the heat flow in segment 1 (10 mA) compared to that in the same voltage range in segment 2 (2 mA), the magnitude of the heat flow is larger with increased current while the structure of the features remains the same. Graphite has large changes in entropy during charge and discharge due to the staging transitions¹⁹⁴, while the change in entropy during cycling for NMC111 is largely constant, as discussed in Chapter 2. Therefore the majority of the reversible structure in the heat flow profile in Figure 4.1a is attributed to graphite. Polarization results in a mostly constant exothermic heat flow throughout both charge and discharge. The remainder of the signal is the result of parasitic heat flow.

Figure 4.1b shows the different voltage ranges and currents used to explore the voltage dependent effect of electrolyte additives in a targeted and concise experiment. Initial cycles were done at a higher rate over a large voltage range, where each cycle increased the upper cutoff voltage by 0.1 V. This served to get an overview of the heat flow over a wide voltage range. Multiple cycles were then done at the top of charge at lower rates, where again the upper cutoff voltage was increased in increments of 0.1 V.

This served to examine the effect of electrolyte additives under conditions where the relative contributions of changes in entropy and polarization to the total heat flow are minimized.

The machine-made pouch cells used in this experiment were nominally identical as they varied only by electrolyte composition. The variation in capacity, and therefore active mass loading, between cells was less than 2% in this case. With sufficiently small currents, the contributions from changes in entropy and polarization would be identical for all cells, such that the only difference in heat flow will be the result of differences in heat flow due to parasitic reactions. Figure 4.1a shows that the heat flow of the cell containing 4% VC was noticeably smaller than that from the control cell. Though not shown here in the interest of brevity, all cells containing an electrolyte additive or additive blend had heat flows below that of the control cell. Figure 4.1a also shows that the observed difference between the heat flow of the control cell and the 4% VC cell changed as a function of state of charge. This is particularly evident by examining the difference in heat flow at successively larger upper cutoff voltages in both segments 1 and 2. Even at low rates, the heat flow evolved from the pouch cells was 2 – 3 orders of magnitude greater than the noise level of the instrument, allowing for extremely precise differentiation between cells.

Since the total heat flow and cell voltage were measured simultaneously, the heat flow can directly be plotted as a function of voltage. Figure 4.2 shows the results of plotting the observed heat flow as a function of voltage for a 10 mA charge to 4.4 V and 10 mA discharge (step iv), where again for simplicity only data for control and 4% VC containing cells are shown. The apparent peaks in heat flow at the start of discharge that occur at approximately 4.35 V are an artefact due to the response time of the calorimeter.

Figure 4.2 shows that the addition of 4% VC had little or no effect below 3.8 V. There was very little capacity below 3.5 V and the heat flow is very large due to changes in entropy in graphite and so the heat flow is only plotted from 3.6 V to highlight the impact of 4% VC at high voltage. Above 3.8 V, 4% VC dramatically reduced the measured heat flow. Since the contributions of polarization and changes in entropy were negligibly different between the two cells, this reduction in measured heat flow was therefore attributed to a reduction in parasitic heat flow. This shows the ability of isothermal microcalorimetry to easily and directly determine the voltage-dependence of the parasitic reactions and over what voltage ranges VC or other additives provide their benefit.

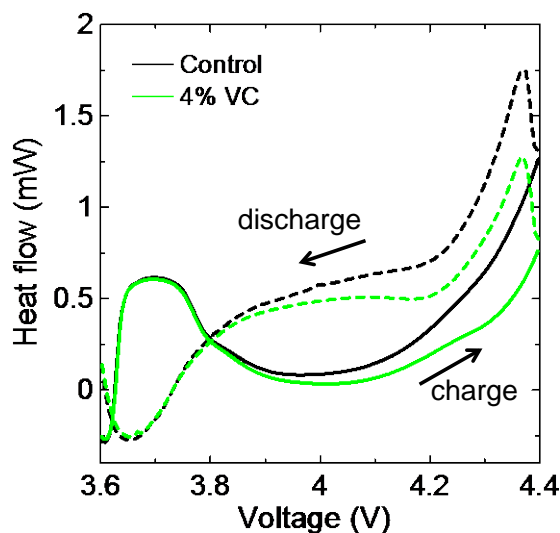


Figure 4.2: Example of observed heat flow as a function of voltage for cells containing control electrolyte (black) and 4% VC (green) for a 10 mA charge (solid lines) and 10 mA discharge (dashed lines).

In order to appreciate the impact of parasitic heat flow on cell lifetime, a simple order of magnitude calculation can be done. The pouch cells used in this experiment, and throughout this thesis, store an electrical energy of about 1 Wh. If all the electrolyte in the cell reacted with lithium to form lithium alkyl carbonates or lithium carbonate, the energy released would be on the same order of magnitude, 1 Wh. Therefore, a sustained

parasitic heat flow of $100 \mu\text{W}$ in these pouch cells would consume all of the electrolyte in 10000 hours, or 1 year. Therefore, parasitic heat flows on the order of $100 \mu\text{W}$ are a significant cause for concern in these cells.

Figure 4.3 shows the heat flow as a function of voltage during segment 1 described in Figure 4.1 (10 mA cycling to progressively higher upper cutoff voltages). Figure 4.3a shows the heat flow for a cycle up to 4.2 V for cells with a varying electrolyte additive composition. For clarity, pair cell data are not shown. All cells containing electrolyte additives had a reduced heat flow above 3.8 V compared to control.

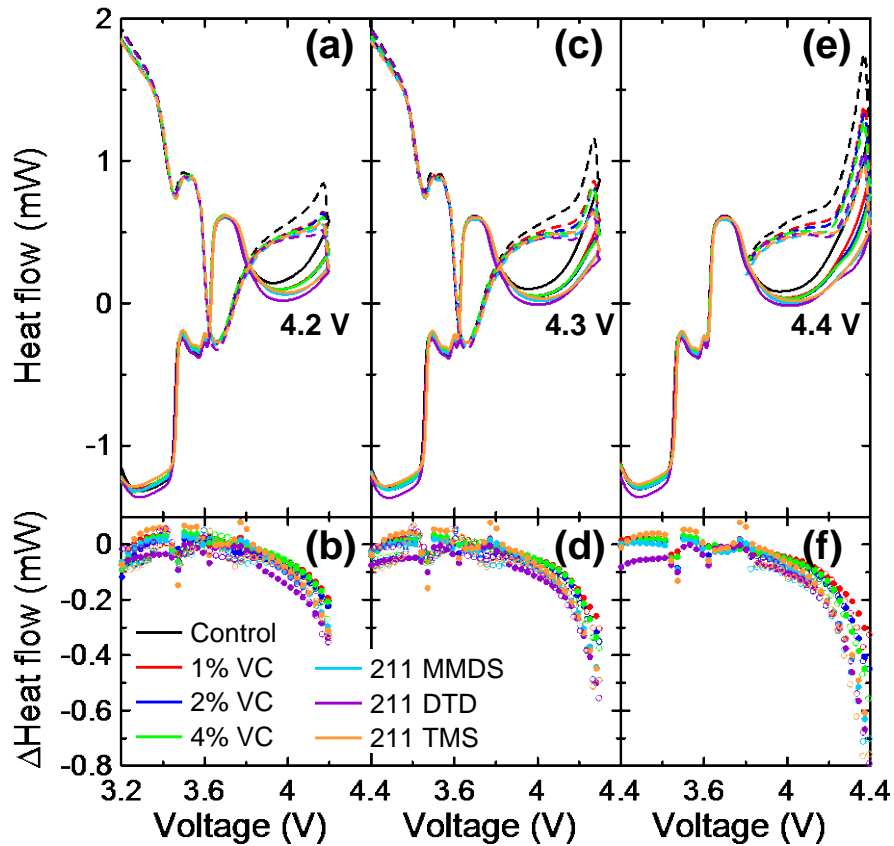


Figure 4.3: Panels (a), (c), and (e) show the heat flow as a function of voltage during a 10 mA (C/24) charge (solid lines) to an upper cutoff voltage of (a) 4.2 V, (c) 4.3 V, and (e) 4.4 V and 10 mA (C/24) discharge (dashed lines). Data shown for control (black), 1% VC (red), 2% VC (blue), 4% VC (green), 211MMDS (pale blue), 211DTD (purple), and 211TMS (orange). Panels (b), (d), and (f) show the corresponding difference in heat flow as a function of voltage between additive-containing cells and control during charge (filled symbols) and discharge (open symbols) up to (b) 4.2 V, (d) 4.3 V, and (f) 4.4 V.

Figure 4.3c and Figure 4.3e show the effect of an increased upper cutoff voltage on the total observed heat flow and the impact of the electrolyte composition. The total heat flow during both charge (solid lines) and discharge (dashed lines) increased dramatically above 4.2 V, indicating there was an increase in likely both heat flows due to polarization and parasitic reactions. However, even at 10 mA (C/24), the current was sufficiently small such that to a good approximation, the contributions of polarization and changes in entropy to the total heat flow were small and were nearly identical between cells, such that any differences in measured heat flow were attributable to differences in parasitic heat flow.

The bottom panels of Figure 4.3 show the difference obtained by subtracting the heat flow of the control cell (no additives) from the heat flow of the additive-containing cells as a function of voltage. A negative value indicates a lower heat flow compared to control. This comparative method is a good measure of the reduction in parasitic heat flow due to the additive, assuming that the reaction enthalpies with and without the additive are negligibly different. Throughout the entire voltage range, the heat flow for additive-containing cells was reduced. The reduction of heat flow was increasingly pronounced with increased voltage. Since the potential, and therefore reactivity, of the graphite electrode remains essentially constant in this voltage range, the presence of electrolyte additives results in a reduction in parasitic reactions that occur at the positive electrode. The high voltage performance of these cells is of particular importance, and therefore the measured heat flow and difference from control up to 4.4 V were examined in greater detail.

Figure 4.4 shows the heat flow as a function of voltage during the 10 mA cycle up to 4.4 V for cells containing a variety of electrolyte additives. Where available, pair cell

data are shown, and for the most part, show good reproducibility between cells. The heat flow at high voltage is highlighted and very clearly shows that especially above 4.2 V there was a significant impact due to the electrolyte additives, and that impact was increasingly pronounced at higher voltages. At small current, the contributions of entropy and polarization to the total heat flow were nearly identical between cells that vary only by electrolyte additive content. Therefore, differences in measured heat flow between cells are, to first-order, attributable to differences in parasitic heat flow. The impact of electrolyte additives is therefore best understood by comparing the heat flow from a cell containing the additive(s) of interest to a cell containing no additive.

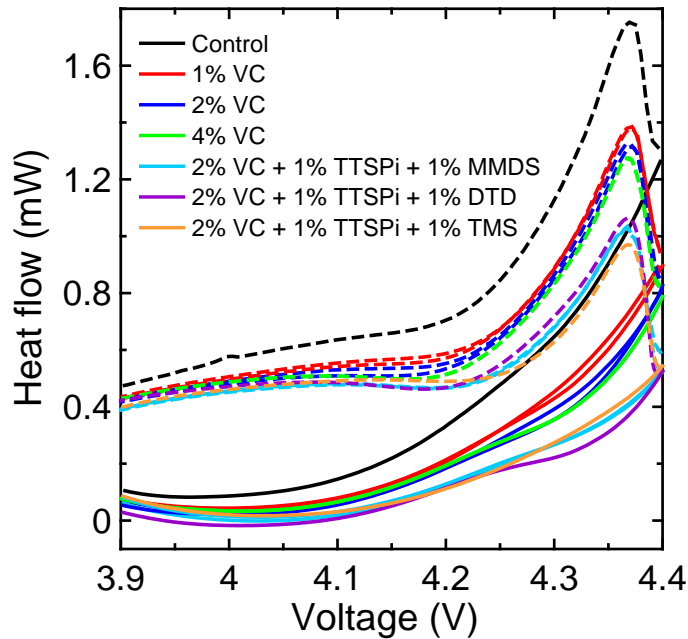


Figure 4.4: Measured heat flow during a 10 mA (C/24) charge (solid lines) and discharge (dashed lines) for cells containing no additives (control, black), 1% VC (red), 2% VC (blue), 4% VC (green), 211MMDS (pale blue), 211DTD (purple), and 211TMS (orange).

Figure 4.5 shows the difference in heat flow between additive-containing cells and the control cell for the 10 mA cycle up to 4.4 V. For clarity, where pair cell data were available, the average difference in heat flow was plotted. Every electrolyte additive

combination examined reduced the heat flow compared to control, and that reduction was increasingly pronounced with increased voltage. Below approximately 4.0 V, the reduction in heat flow as a result of all additive combinations tested was similar. Since all additive combinations tested contained VC, this suggests that the presence of a sufficient amount of VC is the dominant factor in the reduction of parasitic heat flow at intermediate voltages.

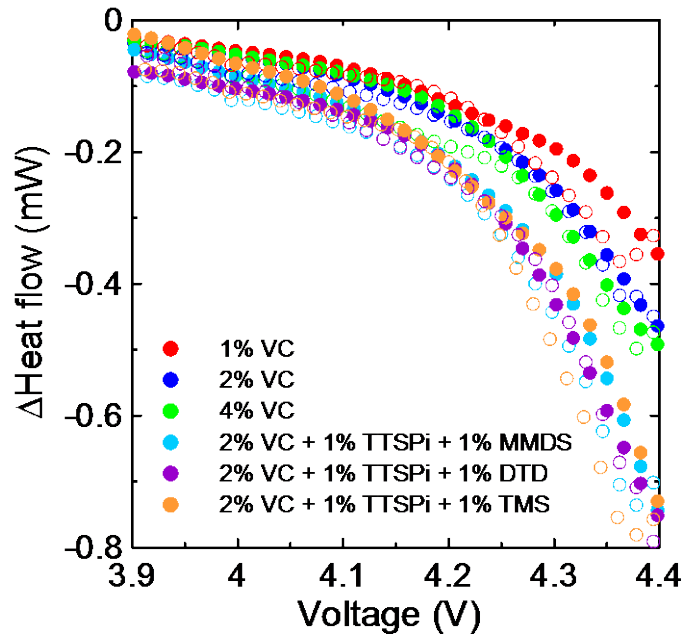


Figure 4.5: Difference in heat flow between additive-containing cells and control (no additive) for 10 mA charge (filled symbols) and discharge (open symbols) for 1% VC (red), 2% VC (blue), 4% VC (green), 211MMDS (pale blue), 211DTD (purple), and 211TMS (orange).

Above 4.0 V, the reductions in heat flow for three ternary electrolyte additive blends (211MMDS, 211DTD, and 211TMS) began to separate from those cells containing only VC, and showed a greater reduction in parasitic heat flow. The ternary blends had lower parasitic heat flows than for the same total weight percentage of a single additive (4% VC), demonstrating that this reduction in parasitic heat flow is a result of the

additive composition, and not simply the total concentration. The beneficial impact of TTSPi and the sulphur-containing additives MMDS, DTD, and TMS is especially apparent above 4.2 V. At 4.2 V, the cells containing solely VC reduced the parasitic heat flow by 120 – 150 μW , while the 211 blends reduced the parasitic heat flow by 205 – 220 μW . At 4.4 V, the cells containing the 211 ternary additive blends reduced the parasitic heat flow by about 750 μW compared to control, while the cells containing 1%, 2%, and 4% VC reduced the parasitic heat flow by 370 μW , 460 μW , and 510 μW , respectively. The reduction in heat flow for pair cells had an average absolute difference ranging from 6 μW for 211MMDS cells to 17 μW for 4% VC. This is in good agreement with previous studies on such additives, where it was found that the benefits of the sulphur-containing additives and TTSPi occur at high voltages due to the formation of a protective passivation film on the positive electrode that prevents further electrolyte oxidation.^{76,140–143,148,149,151} As previously discussed, a parasitic heat flow of 100 μW would consume all the electrolyte in these cells within about one year. Therefore, a reduction in parasitic heat flow of 750 μW is immensely significant in prolonging the lifetime of such cells. Therefore it is expected that the 211 electrolyte blends will yield cells with higher coulombic efficiency and lower charge endpoint capacity slippage than cells containing control electrolyte or cells with 2% VC, even when charged only to 4.2 V. This will be explored in Section 4.3.3.

Figure 4.6 shows the heat flow as a function of voltage during segment 2 described in Figure 4.1 (2 mA cycling to progressively higher upper cutoff voltages) for cells containing control electrolyte, 1% VC, 2%VC, 4%VC, and 211MMDS. At 2 mA, the contributions of polarization and changes in entropy to the measured heat flow are negligible. The contribution of polarization and changes in entropy scale with current

squared and current, respectively. Therefore the heat flows from these two sources are reduced by a factor of 25 and 5, respectively, between 10 mA (Figure 4.3 - Figure 4.5) and 2 mA cycling (Figure 4.6). This can be verified by examining the difference in heat flow between charge and discharge at a given voltage, as the entropic contribution is the only reversible component to the total heat flow. At 4.0 V, the separation is approximately 0.4 mW at 10 mA, and indeed Figure 4.6 shows a separation of approximately 0.08 mW at 2 mA.

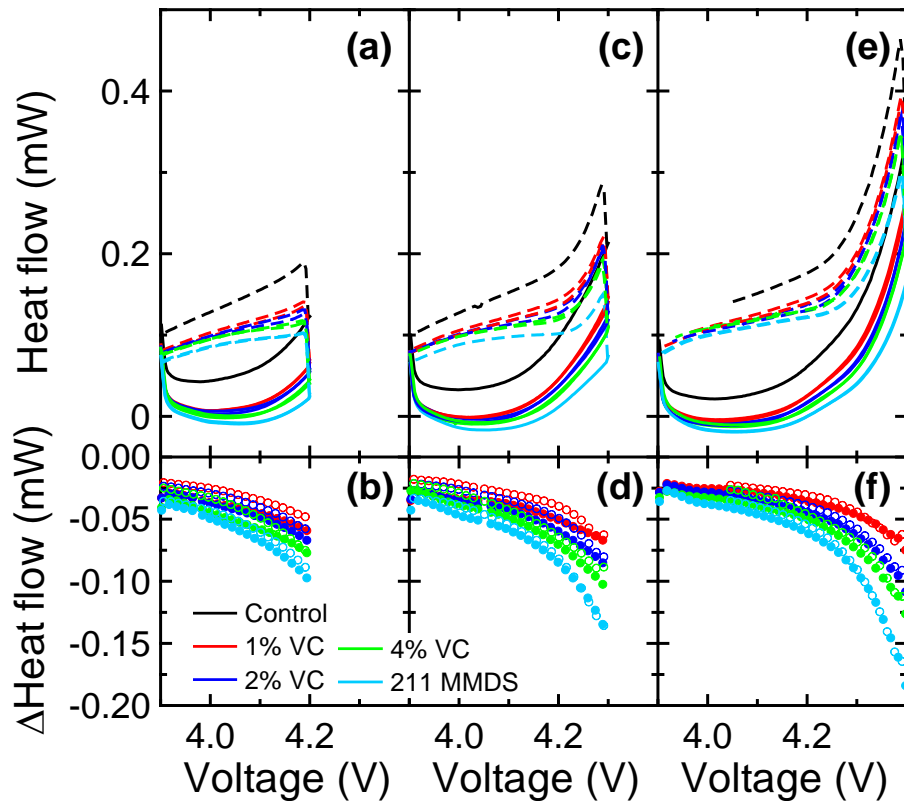


Figure 4.6: Panels (a), (c), and (e) show the heat flow as a function of voltage during a 2 mA (C/120) charge (solid lines) to an upper cutoff voltage of (a) 4.2 V, (c) 4.3 V, and (e) 4.4 V and 2 mA (C/120) discharge (dashed lines). Data shown for control (black), 1% VC (red), 2% VC (blue), 4% VC (green), and 211MMDS (pale blue). Panels (b), (d), and (f) show the corresponding difference in heat flow as a function of voltage between additive-containing cells and control during charge (filled symbols) and discharge (open symbols) up to (b) 4.2 V, (d) 4.3 V, and (f) 4.4 V.

The top panels of Figure 4.6 show the measured heat flow during low rate (C/120) charge (solid lines) and discharge (dashed lines) for the first cycle in the given voltage range. For all cells except control, pair cell data were plotted, and the heat flow for such pairs were virtually indistinguishable. This indicates that the differences between pair cell heat flow observed during 10 mA cycling is likely a result of differences in cell impedance. This further highlights the need for very low rate experiments in order to be certain that differences in total heat flow are attributable solely to differences in parasitic heat flow.

The bottom panels of Figure 4.6 show the difference obtained by subtracting the heat flow of the control cell from that of the additive-containing cells as a function of voltage. Pair cell data were averaged for clarity. The differences in heat flow from control observed at 2 mA were noticeably smaller than those observed at 10 mA (Figure 4.3). As the parasitic reactions progress with time, the reactive electrode surfaces become passivated, resulting in a reduced reaction rate and increased coulombic efficiency.^{69,214} Therefore, it is expected that the measured parasitic heat flow decreases with time, especially over the duration of the experiments performed here. A smaller difference in heat flow compared to control can also be partially explained if the additive-containing cells had a smaller impedance, and therefore smaller polarization heat flow, than the control cell. The relative impact of the electrolyte additives is unchanged, the ternary additive blend 211MMDS gives the largest reduction in parasitic heat flow especially above 4.2 V. At 4.4 V, after more than 500 hours of cycling, the average reduction in heat flow compared to control for cells containing 1% VC, 2% VC, 4% VC, and 211MMDS were 81 μW , 110 μW , 128 μW , and 182 μW , respectively, with average

absolute differences between pair cell data of 4 μW , 3 μW , 1.5 μW , and 1.0 μW , respectively.

4.3.2 The Effect of VC on the Open Circuit Heat Flow for 4.2 V NMC111/Graphite Pouch Cells

One method to isolate the parasitic heat flow is to measure the heat flow in the limit of current going to zero, i.e., open circuit. Since no current is applied to the cells, the open circuit heat flow measurements provide a near direct measure of the heat flow due to parasitic reactions. This assumes that as the parasitic reactions proceed, the self-discharge current associated with Li^+ intercalation into the positive electrode material and deintercalation out of the negative electrode materials are sufficiently small to result in negligible heat flow associated with entropy changes and polarization. There is a further assumption that the heat flow associated with the enthalpy of mixing as the concentration gradients relax under open circuit conditions is negligible. Thomas *et al.*¹⁷² estimated the magnitudes of heats of mixing with particles, across the electrode, across the electrolyte, and within pores and found that in a realistic cell even the largest of the four sources examined was two orders of magnitude lower than the heat associated with polarization and changes in entropy. Furthermore, even if it were measurable, it would be similar between cells varying only by a few percentage of an electrolyte additive. Therefore, the comparison of open circuit heat flow is an excellent way to isolate the change in parasitic heat flow as a function of electrolyte additive. However, such open circuit measurements are done at single voltages, and do not have the same benefit of determining the voltage

dependent impact of electrolyte additives. Therefore open circuit measurements are considered complementary to cycling experiments.

Open circuit heat flow measurements were not conducted on the same 240 mAh NMC111/graphite pouch cells investigated in Section 4.3, but rather on similar 220 mAh NMC111/graphite pouch cells from the same manufacturer, but balanced to 4.2 V. Additionally, as described in Section 4.3.1, the formation procedure for the cells used in this experiment varied slightly from the procedure used for the 4.4 V cells. Prior to open circuit experiments, the cells proceeded through a full range cycle from 2.8 V to 4.2 V at 10 mA (C/22), then several narrow range cycles at the top of charge between 3.9 V and 4.2 V at 2 mA (C/110).

Figure 4.7a shows the evolution of the heat flow for 220 mAh NMC111/graphite pouch cells designed for 4.2 V operation during open circuit conditions following a 2 mA (C/110) charge to 4.2 V. The open circuit segment began approximately 240 h after cells were loaded into the calorimeter. Results are shown for cells containing no electrolyte (control), 1% VC, 2% VC, and 4% VC. A pronounced reduction in parasitic heat flow was seen with increasing amounts of VC, where a significant reduction in parasitic heat flow compared to control was observed for 1% VC, while an increased amount of VC provided only modest improvements over 1% VC. The total measured heat flow and the difference in heat flow between cells decreased with time at open circuit, consistent with the passivation of electrode surfaces. After 25 h at open circuit conditions, the measured heat flow was 336 μ W, 74 μ W, 54 μ W, and 48 μ W for control, 1% VC, 2% VC, 4% VC cells, respectively. The open circuit heat flow results are consistent with the reduction in parasitic heat flow with increased experiment time seen for similar cells in Section 4.3, even despite the differences in cell construction and cycling history.

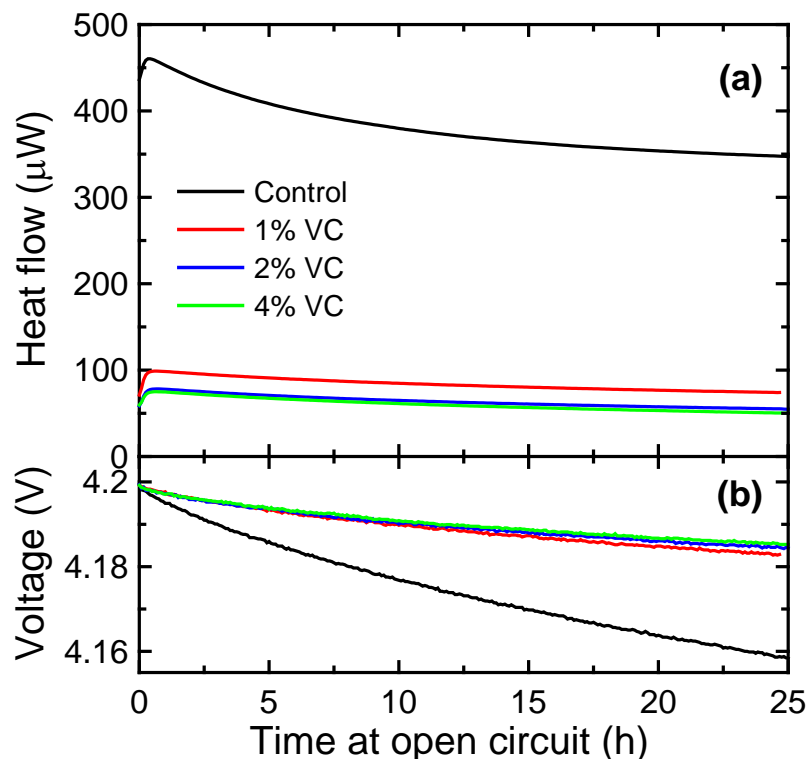


Figure 4.7: (a) Measured heat flow for control (black), 1% VC (red), 2% VC (blue), and 4% VC (green) cells during 25 hours of open circuit conditions, starting from 4.2 V. (b) Corresponding measured cell voltage during the storage period.

Figure 4.7b shows the corresponding measured voltage drop during the open circuit measurements. The voltage decay is consistent with the heat flow results, which is to be expected. Sinha *et al.*^{97,130} showed that the magnitude of the voltage drop during open circuit storage experiments can be correlated to parasitic reactions between the electrolyte and electrode surfaces. The relationship between the observed voltage drop and the measured open circuit heat flow will be discussed further in Chapter 9. In the context of the comparative impact of electrolyte additives, it is sufficient to say Figure 4.7b shows that a reduced voltage drop is qualitatively correlated to a reduction in parasitic heat flow. Therefore the addition of VC reduces parasitic reactions occurring at positive electrode, such as electrolyte oxidation, in good agreement with previously

reported results^{97,127–132}. It would be expected that the ternary additive blends would result in a further reduction in open circuit heat flow compared to VC-containing cells.

4.3.3 Comparison of Calorimetric Results to High Precision Cycling Results

The impact and benefits of electrolyte additives are typically evaluated using long term, high rate, repeated cycling experiments and examining the resulting capacity fade. More recently, high precision⁷¹ and ultra high precision²¹⁰ coulometry techniques have been used to evaluate a variety of electrolyte additives by examining coulombic efficiency and charge endpoint capacity slippage, as well as capacity fade. Increases in coulombic efficiency and decreases in charge endpoint capacity slippage have been shown to be good measures of reductions in parasitic reactions between the electrolyte and electrode surfaces. Together with electrochemical impedance spectroscopy measurements, these ultra high precision measurements have been shown to be good predictors of cell lifetimes.⁷ It is therefore important to verify that the results obtained with isothermal microcalorimetry are consistent with those obtained with ultra high precision coulometry.

All UHPC and long term cycling experiments presented in this section were performed and analyzed by a number of people within the Dahn lab, including Lin Ma, David Wang, Jian Xia, Kathlyne Nelson, and Nupur Sinha. Results herein have reproduced with permission from *J. Electrochem. Soc.*, **161**, A1261 (2014)²¹⁵. Copyright 2014, The Electrochemical Society.

Figure 4.8 shows UHPC results for 220 mAh NMC111/graphite cells balanced for operation to 4.2 V, cycled between 2.8 – 4.2 V at C/20 and 40°C. A variety of electrolyte

additive combinations were examined, including 2% and 3% VC, 2% VC + 1% TTSPi + 1% MMDS, 2% VC + 0.5% TTSP + 0.5% TTSPi + 1% MMDS, 2% VC + 0.5% TTSP + 0.5% TTSPi + 1% DTD, and 2% VC + 0.5% TTSP + 0.5% TTSPi + 1% TMS. The ternary and quaternary additive blends follow a similar “211”-type recipe that includes 2% VC, 1% total of TTSP and TTSPi, and 1% of a sulfur-containing additive.

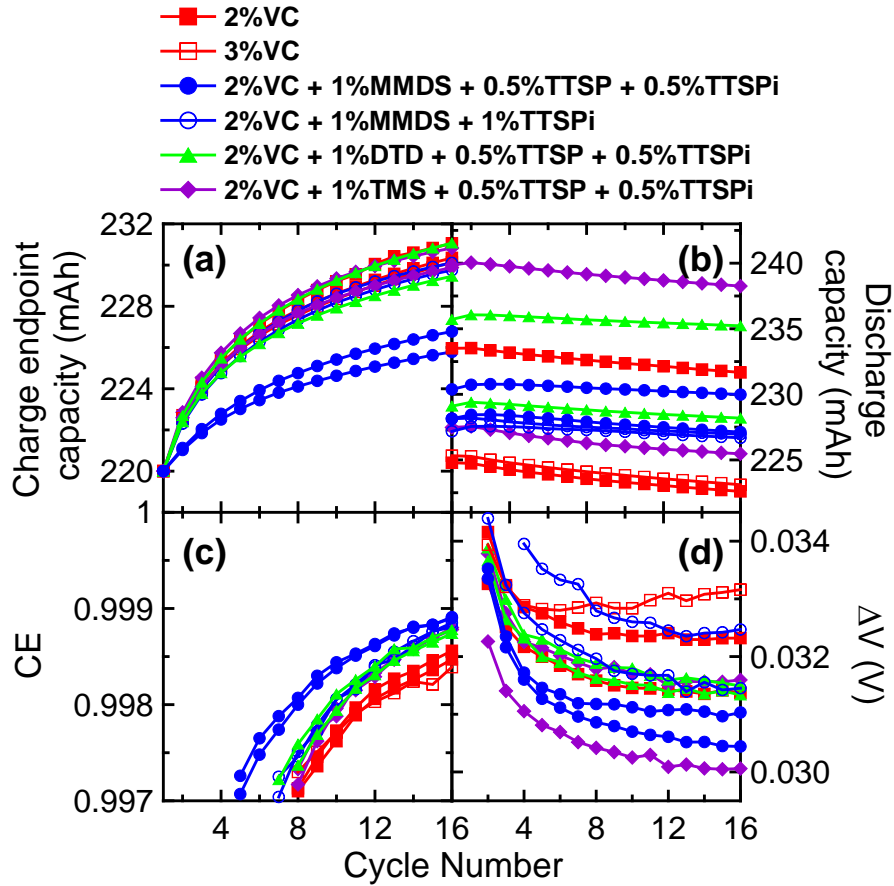


Figure 4.8: Ultra high precision coulometry results for NMC111/graphite cells cycled between 2.8 – 4.2 V at C/20 and 40°C. Results are shown for a variety of electrolyte additives, as indicated in the legend. Panel (a) shows the charge endpoint capacity normalized such that all cells start at the same capacity for comparative purposes, panel (b) shows the discharge capacity, panel (c) shows the coulombic efficiency, and panel (d) shows ΔV , the difference in average charge and discharge voltage, all plotted as a function of cycle number.

Figure 4.8a shows the charge endpoint capacity normalized such that all cells start at the same capacity for comparative purposes, Figure 4.8b shows the discharge capacity,

Figure 4.8c shows the coulombic efficiency, and Figure 4.8d shows ΔV , the difference in average charge and discharge voltage, all plotted as a function of cycle number.

Figure 4.8a shows that cells containing the quaternary electrolyte blend with MMDS have noticeably smaller rate of endpoint capacity slippage than all other cells tested. This is likely mainly an artefact of the difference in formation procedure of these cells compared to the others. With exception of that one additive combination, the rate of charge endpoint capacity slippage is very similar between all additives tested, with only a modest improvement from the ternary and quaternary blends. Figure 4.8b shows that rate of change of the discharge capacity for the cells containing ternary and quaternary additive blends is smaller than for cells containing only VC, i.e., the additive blends reduce capacity fade compared to VC alone. Figure 4.8c shows that all of the ternary and quaternary additive blends resulted in a similar coulombic efficiency which is higher than for the cells containing only VC. This is in excellent agreement with the calorimetric results presented in Section 4.3. Figure 4.8d shows that up to 16 cycles, none of cells containing ternary and quaternary additive blends show an increase in ΔV , while the cell containing 3% VC begins to show an increase in ΔV starting at approximately cycle 6. All the results presented in Figure 4.8 highlight the benefit of the ternary and quaternary electrolyte additive blends, which is in good agreement with isothermal microcalorimetry measurements.

Figure 4.9 shows the electrochemical impedance spectra of cells collected at 3.8 V and 10°C after the 16 UHPC cycles discussed in Figure 4.8. To compare the effect of additives, their impact on the change of the charge transfer resistance, R_{ct} , which is measured by the diameter of the semicircle, is examined. Here, what is being called R_{ct} includes the contact resistance between the active particles and current collectors, Li^+

transfer resistance from the electrolyte to the electrode through the SEI, and electron transfer resistance to the active material for both the positive and negative electrodes.²¹⁶ In agreement with previously reported results,²¹⁷ R_{ct} increases with an increasing amount of VC. Compared to 2% VC, the cells containing ternary and quaternary electrolyte additive blends have a lower R_{ct} , which has been shown to be a contributing factor to promoting cells with long lifetimes⁷.

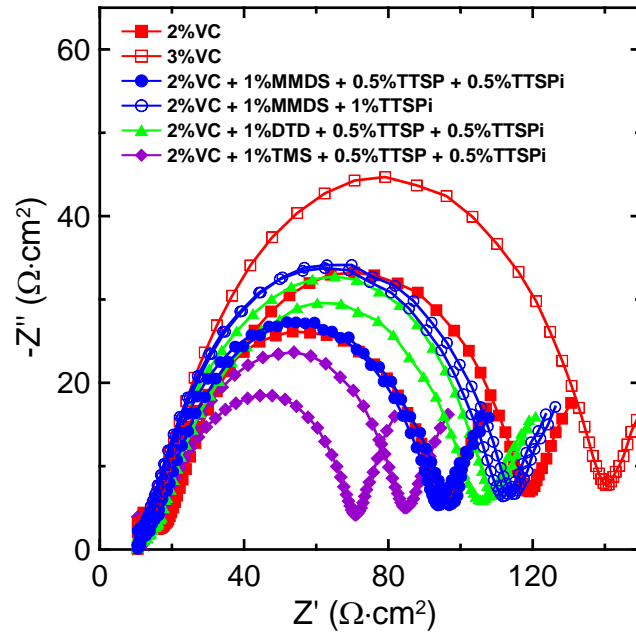


Figure 4.9: Electrochemical impedance spectra of NMC111/graphite cells collected after 16 ultra high precision charger cycles at 3.8 V and 10°C. Results are shown for additive combinations listed in the legend.

Figure 4.10 shows the normalized discharge capacity as a function of cycle number for 240 mAh NMC111/graphite cells cycled between 2.8 – 4.2 V at C/2.5 and 55°C. Extended high temperature cycling was performed for cells containing 2% and 3% VC, and the ternary additive blends 211MMDS, 211DTD, and 211TMS, while such experiments were not performed for the cells containing quaternary additive blends. Figure 4.10 shows that 211MMDS and 211DTD have much better capacity retention than

cells containing only VC or 211TMS. The capacity retention results can be discussed and understood by examining both the gas produced during cycling that can lead to a loss in stack pressure and the coulombic inefficiency per hour ($CIE/h = (1-CE)/(\text{time of one cycle in hours})$), which is a good measure of the parasitic reaction rate.

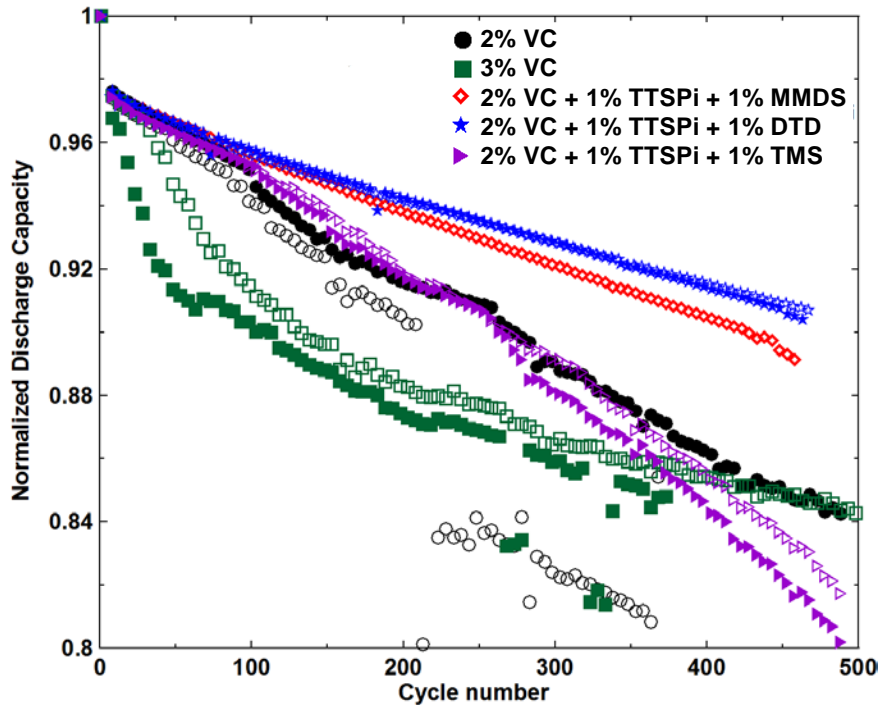


Figure 4.10: Normalized discharge capacity as a function of cycle number for NMC111/graphite pouch cells cycled between 2.8 – 4.2 V at C/2.5 and 55°C. Results are shown for additive combinations listed in the legend, and duplicate cell data are given by corresponding open symbols.

Figure 4.11a shows the fractional capacity remaining after 200 cycles between 2.8 and 4.2 V at C/2.5 and 55°C as a function of the amount gas produced during those cycles. The amount of gas generation and the capacity fade are well correlated for the cells measured, suggesting that the onset of “noisy” data and rapid capacity loss is a result of a significant loss in cell stack pressure. Figure 4.11b shows that the fractional capacity remaining is also well correlated to the CIE/h measured after 14 cycles of UHPC cycling

at 40°C, where the cells with the smallest capacity fade had the smallest parasitic reaction rate. Since the capacity fade is well correlated to both volume of gas produced and parasitic reaction rate, it follows that some of the products of the parasitic reactions are gaseous.

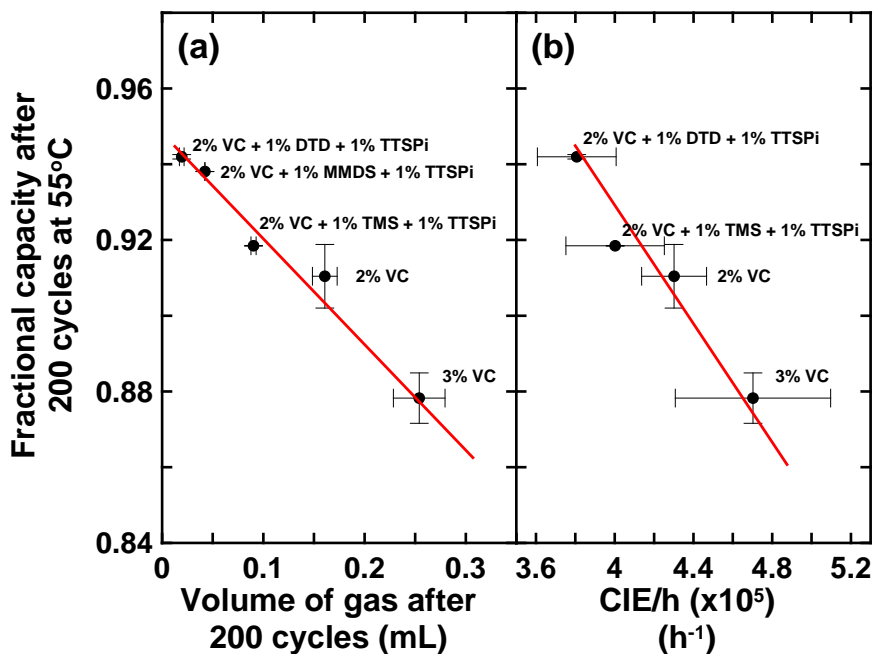


Figure 4.11: The fractional capacity remaining after 200 cycles between 2.8 – 4.2 V at C/2.5 and 55°C as a function of (a) gas produced after 200 cycles at C/2.5 and 55°C and (b) coulombic inefficiency per hour measured during UHPC cycling at C/20 and 40°C.

In all of the UHPC and long term cycling experiments performed, the ternary and quaternary electrolyte additive blends have shown to be beneficial for NMC111/graphite pouch cells. Compared to VC alone, the ternary and quaternary electrolyte additives result in reduced parasitic reaction rates, lower charge transfer resistance after cycling, and better capacity retentions for long term high temperature cycling. These results are in good agreement with the isothermal microcalorimetry measurements presented in Sections 4.3.1 and 4.3.2. Therefore the effect of an additive on the measured heat flow is a good measure of the impact of that additive on cell performance.

4.4 CONCLUSIONS

Isothermal microcalorimetry is a powerful technique able to measure the voltage range over which any additive or additive combination is most effective with quick and simple experiments. This in turn will help efforts to understand electrolyte additives and how to best choose an appropriate additive combination for a particular cell chemistry and operating condition. As a demonstration of the technique, the effect of VC and ternary additive blends on NMC111/graphite pouch cells was examined.

All additives dramatically reduced parasitic reactions at high voltages compared to control, implying that it reduced parasitic reactions that occur at the positive electrode. Compared to VC alone, the ternary additive blends containing 2% VC, 1% TTPSi, and 1% of either MMDS, DTD, or TMS reduced the parasitic heat flow even further. This reduction in parasitic heat flow was shown to correlate to UHPC and long term cycling experiments where compared to VC alone, the ternary electrolyte additives had higher coulombic efficiencies, lower charge endpoint capacity slippage rates, lower charge transfer impedance, reduced gas generation, and decreased capacity fade in long term, high temperature cycling experiments.

CHAPTER 5

DETERMINATION OF THE VOLTAGE DEPENDENCE OF THE PARASITIC HEAT FLOW

5.1 INTRODUCTION AND MOTIVATION

Results presented in this Chapter are reprinted with permission from *J. Electrochem. Soc.*, **161**, A1782 (2014)²¹⁸. Copyright 2014, The Electrochemical Society.

In the previous Chapter, differences in heat flow were examined between NMC111/graphite pouch cells that varied only in electrolyte composition. Since both polarization and entropic heat flow contributions were nearly identical between cells, this difference method determined the relative reduction in parasitic heat as a function of voltage due to the electrolyte composition. However, the absolute magnitude of the voltage-dependent parasitic heat flow for individual cells cannot be determined with this method.

In this Chapter, a three-component model of the heat flow was used (polarization, changes in entropy, and parasitic heat). By varying the current over narrow voltage ranges, the contributions of each of the heat flow sources as a function of state of charge was isolated. The measured heat flow was fit using a model where each contribution is a polynomial function of the state of charge. The coefficients of the polynomials were determined by least-square fitting. Of particular importance, the fitting parameters associated with the parasitic heat flow allowed for the extraction of the voltage-dependence of the parasitic heat flow for an individual cell. This analysis was

particularly useful for drawing conclusions about the behaviours of electrolyte additives across different cell chemistries where the method of relative differences in heat flow cannot be used. As a first demonstrative example, the parasitic heat as a function of voltage was determined here for a high voltage LiCoO₂ (HV-LCO)/graphite cell containing 2% VC. The method was then extended to examine the effect of electrolyte composition on the parasitic heat flow in NMC111/graphite cells. A comparison between the parasitic heat flows observed for HV-LCO/graphite and NMC111/graphite pouch cells containing the same electrolyte was also made.

5.2 SEPARATION OF THE TOTAL HEAT FLOW INTO COMPONENTS

5.2.1 The time independent empirical heat flow model

As developed in Section 2.2.1, the total measured heat flow from the passage of current in a cell is given by¹⁶⁷:

$$\frac{\bar{d}q}{dt} = I\eta + \frac{T}{e} \left[\left(\frac{ds_+}{dx} \right) - \left(\frac{ds_-}{dx} \right) \right] I + \frac{\bar{d}q_p}{dt} \quad (5.2.1)$$

Equation 5.2.1 details the three sources that contribute to the heat flow ($\bar{d}q/dt$) of a full cell: cell polarization, changes in entropy, and parasitic heat flow. The first term in Equation 5.2.1, $I\eta$, is the heat flow resulting from the overpotential. In this Chapter, the effect of hysteresis was treated as being negligible; therefore, as developed in Section 2.2.2, this heat flow is a result of polarization and is proportional to I^2 . The second term in Equation 5.2.1 is the heat flow associated with the change in entropy and is proportional to the current, implying that it is therefore a reversible heat flow. The last term in Equation 5.2.1, $\bar{d}q_p/dt$ is parasitic heat flow and is independent of current. Here,

these reactions are considered to be time independent; the impact of time on the parasitic heat flow will be examined in detail in Chapter 6.

Over small voltage ranges each of these contributions to the heat flow can be approximated by simple functions of the state of charge. Figure 5.1 shows an example of measured heat flow as a function of voltage for an NMC111/graphite pouch cell containing control electrolyte (same data as shown in Figure 4.2). Fitting the heat flow profile as a function of state of charge over a wide voltage range with an empirical model would require an excessive number of parameters. Therefore 0.1 V-wide voltage ranges over which the heat flow varies smoothly can be fit with low-order polynomial functions of the state of charge to avoid over-parameterization of the data.

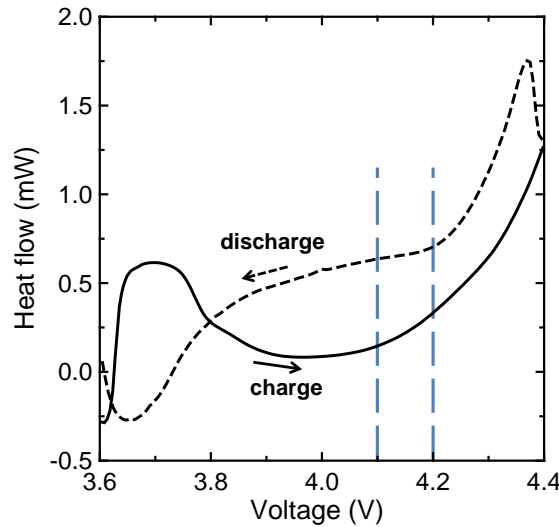


Figure 5.1: Measured heat flow (black) as a function of voltage during a C/24 (10 mA) charge (solid lines) and discharge (dashed line) of an NMC111/graphite pouch cell containing control electrolyte. Over narrow voltage ranges (between the blue dashed lines) the heat flow varies smoothly and can be approximated using simple polynomial functions.

By varying the current over the same narrow voltage range, the series of measured heat flow curves can be fit using least squares minimization to extract simple functions describing the heat flow of each separate component. The heat flow can be expressed as:

$$\frac{dq}{dt} = f_{polarization}(z) \cdot I^2 + f_{entropy}(z) \cdot I + f_{parasitic}(z) \quad (5.2.2)$$

where z is the relative state of charge (rSOC) and I is the current. The values of rSOC range from 0 to 1 for each voltage range examined. Simple polynomial functions are used to model the heat flow, typically linear or quadratic in rSOC. For example, $f_{polarization} = A_0 + A_1 \cdot z$, $f_{entropy} = B_0 + B_1 \cdot z$ and $f_{parasitic} = C_0 + C_1 \cdot z$ could be selected. Non-linear least squares minimization then finds the values of the six parameters in the above example, that give the best agreement between model and data collected at all currents. The extracted functions then give the relative contributions of each term, allowing for the extraction of the voltage-dependence of the parasitic heat flow for an individual cell.

5.2.2 Fitting method

To determine the optimal set of parameters of the empirical model that describe the experimental data collected over each voltage range for all currents examined, a chi squared, χ^2 , minimization was performed. The χ^2 of the total fit is given by:

$$\chi^2 = \sum_i \frac{(y_{meas_i} - y_{calc_i})^2}{y_{meas_i}} \quad (5.2.3)$$

where y_{meas_i} and y_{calc_i} are the measured and calculated heat flows of the i^{th} data point, respectively. The parameters used in the fit were optimized using a generalized reduced gradient (GRG2) nonlinear algorithm implemented in Microsoft Excel Solver to minimize χ^2 .

For each current segment, an appropriate data range was selected based on the time constant of the calorimeter. When the current polarity is reversed, there should be a

large instantaneous discontinuity in the measured heat flow proportional to twice the entropic contribution. However, due to the response time of the calorimeter, there is a lag in the heat flow measurements. The time constant of the calorimeter is approximately 300 s, therefore the measured heat flow takes 15 minutes to reach 95% ($= 1 - e^{-3}$) of the true signal. As a result, the first 15 – 20 minutes of the collected heat flow following a change in current were manually excluded from the fit. This can impact a significant portion of the larger current segments, depending on the capacity in that voltage range. For example, for a voltage range with 10 mAh of capacity, 15 minutes is 25% of the charge or discharge time at 10 mA, while only 5% at 2 mA.

The total quality of fit of the model to the experimental data is given by the root mean squared error, RMSE, which is given by:

$$RMSE = \sqrt{\frac{\sum_i (y_{meas_i} - y_{calc_i})^2}{n_p}} \quad (5.2.4)$$

where n_p is the number of points used in the fit.

5.3 EXTRACTION OF THE PARASITIC HEAT FLOW FOR A HIGH VOLTAGE LCO/GRAPHITE CELL

5.3.1 Experimental Details

High voltage LiCoO₂ (HV-LCO)/graphite pouch cells (200 mAh) designed to operate to 4.45 V were obtained dry and sealed (no electrolyte) from Umicore (Cheonan, Korea). The pouch cells were prepared according to the method described in Section 3.1.2 and were filled with 0.700 ± 0.005 g of control (1M LiPF₆ in 3:7 by weight

EC:EMC) electrolyte to which 2% VC was added. Once filled, the cells were sealed to 94% vacuum with a 6 second sealing time at 150°C.

Wetting and formation were done in a $40. \pm 0.1^\circ\text{C}$ temperature-controlled box. The cells were held at 1.5 V for 24 hours to ensure wetting was complete, then charged at C/20 to 3.8 V to complete the formation step. The cells were then degassed as described in Chapter 3.

The cells were then transferred to the calorimeter, and were cycled using a Maccor series 4000 automated test system. The HV-LCO/graphite cells were left at open circuit conditions for 24 hours to allow for thermal equilibration. The cells were then charged and discharged between 2.8 – 4.4 V four times at 10 mA (C/20) to allow for stabilization of the SEI layers. The cells were charged to 4.1 V at 10 mA, then proceeded through a charge-discharge segment between 4.1 – 4.2 V at 10 mA, 5 mA, 2 mA, and finally 1 mA. This variable rate step was repeated for the voltage ranges 4.2 – 4.3 V and 4.3 – 4.4 V.

5.3.2 Results and Discussion

Figure 5.2 shows the current, voltage, and corresponding measured heat flow of an HV-LCO/graphite cell during the variable rate experiment described above. By the same method outlined in Chapter 4, the heat flow and voltage data were then time-synchronized to give the heat flow as a function of voltage. This was then converted to heat flow as a function of rSOC for each voltage segment to allow for fitting to the time independent empirical model described in Section 5.2.

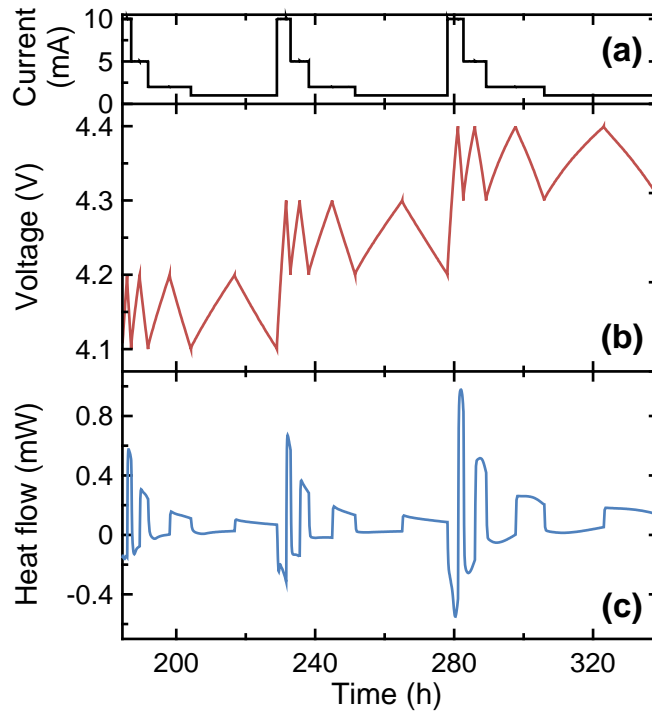


Figure 5.2: Summary of narrow range variable rate experimental procedure showing the (a) current, (b) voltage, and (c) resulting heat flow of an HV-LCO/graphite pouch cell.

Figure 5.3 shows the measured heat flow (symbols) over a narrow voltage range, 4.2 – 4.3 V, for decreasing currents for an HV-LCO/graphite pouch containing 2% VC. The series of curves were modeled using linear functions for each of the three sources of heat flow as described in Section 5.2. The resulting calculated heat flow is given by the solid lines. With larger currents, the state of charge changes rapidly at the charge-discharge and discharge-charge switch points. The calorimeter has a time constant of approximately 300 s, therefore the curvatures seen at both high and low states of charge (and the resulting deviations from the calculated heat flow) are due to the response time of the calorimeter. These regions, denoted by open symbols in Figure 5.3, were manually excluded in the fitting of the experimental data as described in Section 5.2.2. This was done throughout the thesis for all segments fit, but the explicit graphical distinction between included and excluded data points is only shown in Figure 5.3. This relatively

simple model is in good agreement with the measured heat flow, and therefore allows for the accurate separation of different sources of heat flow. Figure 5.3 also shows the ability of this model to extract the parasitic heat flow ($f_{parasitic}(z)$ in Equation 5.2.2, dashed line) as a function of voltage, which will be explored in greater detail.

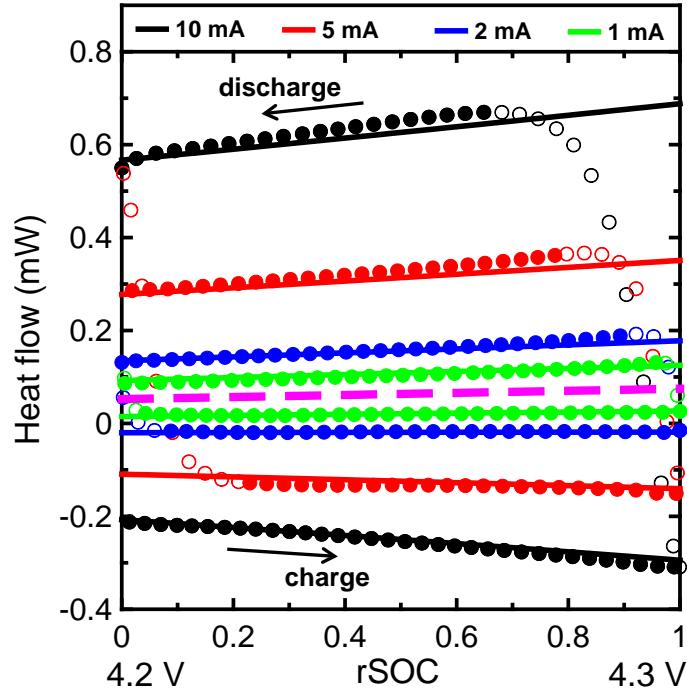


Figure 5.3: Measured heat flow (symbols) as a function of relative state of charge (rSOC) between 4.2 and 4.3 V for an HV-LCO/graphite pouch cell containing 2% VC at various currents: 10 mA (black), 5 mA (red), 2 mA (blue), and 1 mA (green). Data not used in the fit are denoted by open symbols. The extracted total heat flow for each current (solid lines) as a result of fitting the experimental data to the time independent empirical model and the extracted parasitic heat flow (dashed magenta line) are also shown.

Figure 5.4 shows the extracted relative contributions of each of the three components of the total heat flow for a: (a) 10 mA and (b) 1 mA charge in the 4.2 – 4.3 V range. Figure 5.4a shows that at 10 mA ($C/20$) the largest contribution to the total heat flow was due to changes in entropy. The heat from polarization was exothermic and nearly constant, and the heat due to parasitic reactions was exothermic and increased with voltage. Figure 5.4b shows that at 1 mA ($C/200$), the contribution from polarization

decreased by a factor of 100 and was nearly zero. The total heat flow then only had contributions from changes in entropy and parasitic heat flow. Since the entropy contribution to the heat flow is reversible, it changes sign between charge and discharge. Therefore, at very small currents the parasitic heat flow is very closely approximated by the average between the charge and discharge heat flows. For example, the extracted parasitic heat flow in Figure 5.3 was virtually centered between the charge and discharge data collected at 1 mA, as expected, based on this analysis. Figure 5.4 also shows that at higher currents, like those commonly used in automotive and other high power applications, the heat flow will be mainly due to changes in entropy and polarization. The parameters determined using this simple model could therefore be used in the design of thermal management systems, where predicting the amount of heat produced during cycling at various currents is essential.

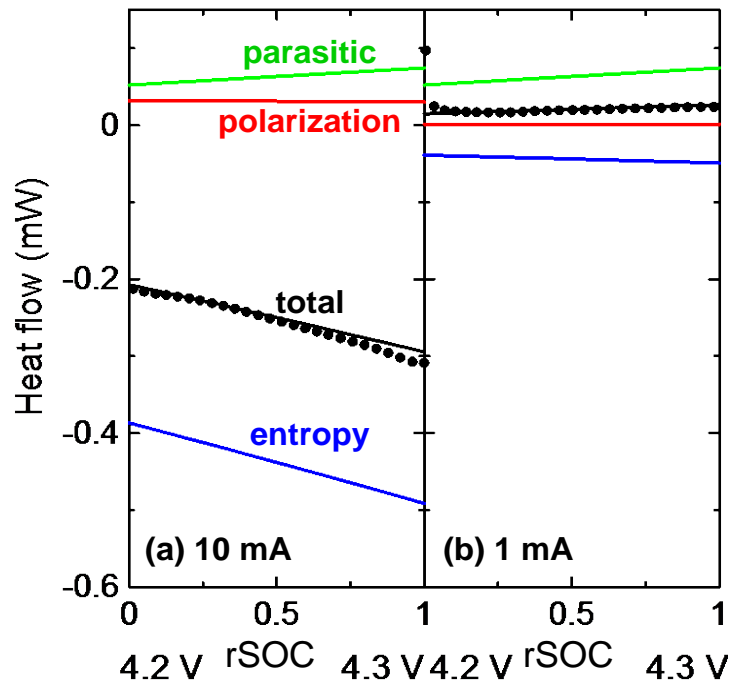


Figure 5.4: Separation of the total measured heat flow during charge (symbols) into the extracted components (lines): polarization (red), entropy (blue), and parasitic (green), and the sum of these components (black) at (a) 10 mA and (b) 1 mA.

Figure 5.5 shows the measured heat flow (symbols) and calculated heat flow (solid lines) over two narrow voltage ranges, (a) 4.2 – 4.3 V (also shown in Figure 5.3) and (b) 4.3 – 4.4 V, for decreasing currents for an HV-LCO/graphite pouch cell which contains 2% VC. Figure 5.5b shows that even with more complex heat flow responses, relatively simple models can be used to fit the data. To model the total heat flow from 4.3 – 4.4 V linear functions of rSOC were used for the polarization and parasitic heat flow contributions, while a quadratic function was used for the entropic contribution. The resulting calculated heat flow is in excellent agreement with the measured data. The extracted parasitic heat (dashed line) continues to increase with voltage and matches up very well with the extracted parasitic heat from the previous voltage range. In addition, the parasitic heat flow is again located virtually at the midpoint between the 1 mA charge and discharge total heat flow data.

Table 5.1 gives the extracted parameters and the total root mean squared error of the fit using the time independent empirical model for the two voltage segments shown in Figure 5.5. The A_i , B_i , and C_i parameters correspond to contributions from polarization, changes in entropy, and parasitic heat flow, respectively, where the index i gives the order of rSOC for that parameter (i.e., z^i). For example, a quadratic entropic contribution function is given by $f_{entropy} = B_0 + B_1 \cdot z + B_2 \cdot z^2$. The RMSE of the fits are very good and near the limit of the measurement uncertainties.

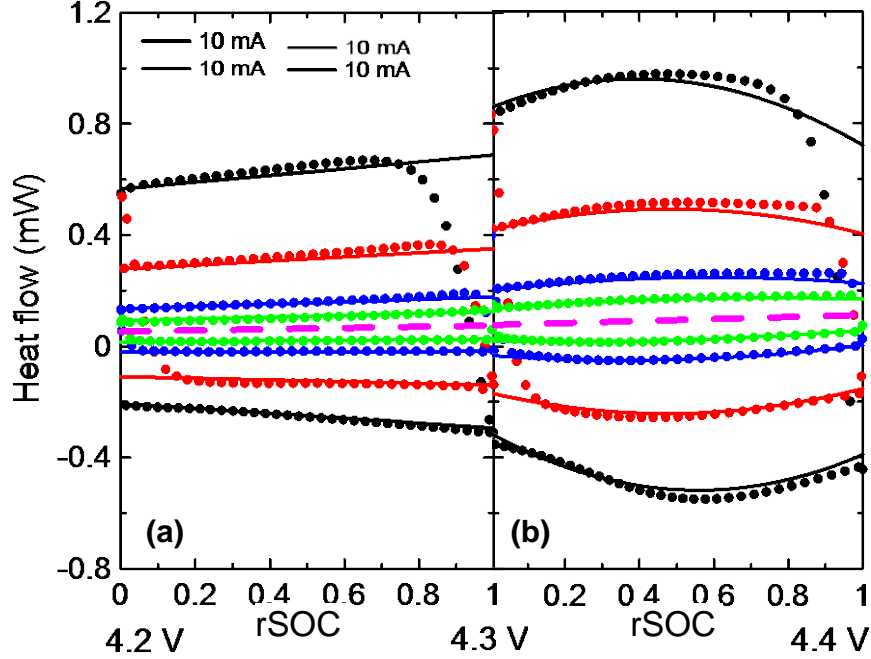


Figure 5.5: Measured heat flow (symbols) as a function of rSOC between (a) 4.2 – 4.3 V and (b) 4.3 – 4.4 V for an HV-LCO/graphite pouch cell containing 2% VC at various currents: 10 mA (black), 5 mA (red), 2 mA (blue), and 1 mA (green). The extracted total heat flow for each current (solid lines) as a result of fitting the experimental data and the extracted parasitic heat flow (dashed magenta line) are also shown.

Table 5.1: Summary of the parameters as determined from the fit to the time independent empirical model for an HV-LCO/graphite pouch cell containing 2% VC. The total root mean squared error of the fit is also given.

Contribution	Parameter	Voltage range	
		4.2 - 4.3 V	4.2 - 4.3 V
Polarization	A_0 ($\mu\text{W}/\text{mA}^2$)	1.27	1.96
	A_1 ($\mu\text{W}/\text{mA}^2$)	-0.052	-1.42
Changes in entropy	B_0 ($\mu\text{W}/\text{mA}$)	-38.7	-58.5
	B_1 ($\mu\text{W}/\text{mA}$)	-11.8	-62.6
	B_2 ($\mu\text{W}/\text{mA}$)	—	65.5
Parasitic heat flow	C_0 (μW)	52.3	74.9
	C_1 (μW)	22.4	37.0
	RMSE (μW)	3.1	4.0

Figure 5.6 shows the extracted parasitic heat flow for the same HV-LCO/graphite pouch cell which contains 2% VC over the two voltage ranges investigated. The parasitic heat increases with voltage as expected, and increases more sharply at higher voltages, indicating an increasing rate of reaction. The level of 100 μW is denoted in Figure 5.6 by a dashed red line. As discussed in Chapter 4, using order of magnitude calculations, a sustained parasitic heat flow of 100 μW would consume all of the electrolyte in these pouch cells in approximately one year. Therefore, determining the absolute magnitude of the parasitic heat as a function of voltage is crucial. This is of particular importance in the automotive industry for example, where the cells spend a significant amount of time at high states of charge. This method could assist in the determination of an appropriate operating voltage range.

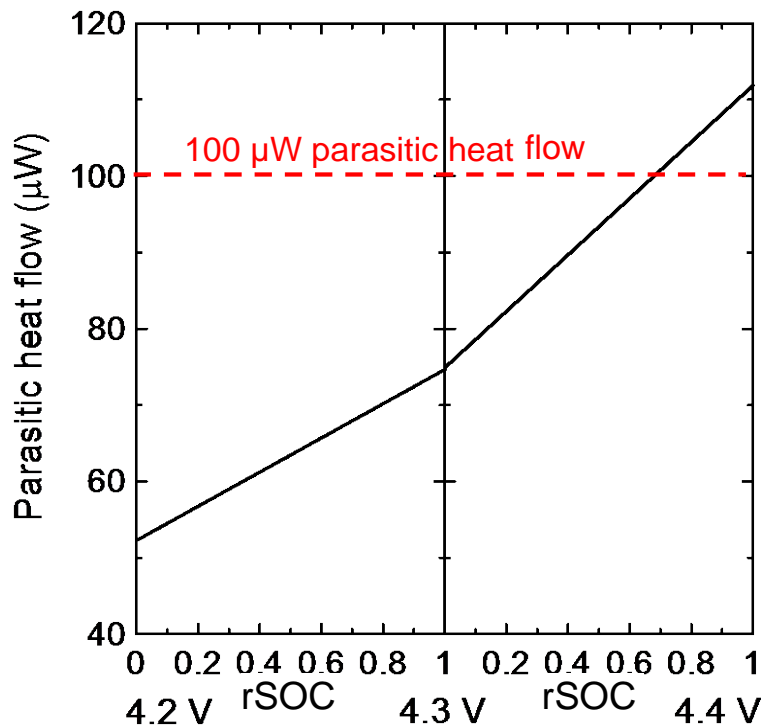


Figure 5.6: Extracted parasitic heat flow as a function of rSOC between 4.2 and 4.4 V for an HV-LCO/graphite pouch cell containing 2% VC.

The variable rate method combined with a relatively simple time independent empirical model of the total heat flow is capable of separating the total measured heat flow into its components using an HV-LCO/graphite pouch cell as a demonstrative example. Of particular importance, this method results in the determination of the parasitic heat flow as a function of voltage for individual cells. This method can be used for a variety of cell chemistries and electrolyte additives. The application of this empirical model to NMC111/graphite cells containing a variety of electrolytes is examined in the following section.

5.4 EFFECT OF THE ELECTROLYTE ON THE PARASITIC HEAT FLOW FOR NMC111/GRAPHITE POUCH CELLS

5.4.1 Experimental Details

$\text{Li}[\text{Ni}_{1/3}\text{Mn}_{1/3}\text{Co}_{1/3}]\text{O}_2$ (NMC)/graphite pouch cells (220 mAh) designed to operate up to 4.4 V were obtained dry and sealed from LiFUN. The pouch cells were prepared according to the method described in Section 3.1.2 and were filled with 0.900 ± 0.005 g of electrolyte.

Three commercially available electrolytes marketed for high voltage applications from two reputable suppliers were tested. Cells containing these electrolytes are denoted by company “A” and company “B” – 1 and company “B” – 2. These were compared to lab-prepared electrolytes where the control electrolyte was 1M LiPF_6 in 3:7 by volume of EC:EMC. Several electrolyte additives were also added to the control electrolyte including VC, PES, TTSP, TTSPi, and MMDS, the acronyms, suppliers, and purities of

which are given in Chapter 3. The combinations of the above additives studied were: 2% VC, 2% VC + 1% TTSP + 1% MMDS, 2% VC + 1% TTSPi + 1% MMDS, and 2% PES + 1% TTSPi + 1% MMDS, where all percentages are given in weight percent added to control electrolyte. Duplicate cells were prepared to verify reproducibility for all electrolytes except for control and 2% VC. Once filled, the cells were sealed with a compact vacuum sealer (MSK-115V, MTI Corp.) at 85% vacuum with a 5 second sealing time at 150°C.

Wetting and formation were done in the same manner as described for the HV-LCO/graphite cells in the previous Section. Once loaded into the calorimeter, the NMC111/graphite cells equilibrated for 24 h, then were then charged and discharged between 2.8 – 4.2 V at 10 mA (C/22). The cells then proceeded into variable rate tests for the voltage ranges of 3.9 – 4.0 V, 4.0 – 4.1 V, and 4.1 – 4.2 V, at each of 10 mA, 5 mA, 2 mA, and 1 mA, as described in Section 5.3.1. Following the variable rate test, the pouch cells proceeded to complete one 1 mA cycle between 3.9 – 4.3 V.

5.4.2 Results and Discussion

Figure 5.7 shows the heat flow as a function of voltage at the top of charge for NMC111/graphite pouch cells containing several commercial and lab-prepared electrolytes. The cells were first cycled at 10 mA (C/22) between 2.8 and 4.2 V. The top of charge of the fourth such cycle is shown. Using the method discussed in Chapter 4, the differences in the observed heat flow between cells that vary only in electrolyte composition are a result of differences in the parasitic heat flow. Consistent with the results presented in Chapter 4, all commercial electrolytes and lab-prepared electrolytes

containing electrolyte additives significantly reduced the heat flow compared to control electrolyte. This reduction in heat flow was increasingly pronounced at higher voltages, also in good agreement with results in Chapter 4. Despite being marketed as high voltage electrolytes, the cells containing commercial electrolyte had larger heat flows than all the additive-containing lab-prepared electrolytes tested. As previously noted, the difference method gives no information about the magnitude of the voltage-dependent parasitic heat flow for individual cells, and therefore the parasitic heat flow was isolated using the methods described in Sections 5.2 and 5.3.

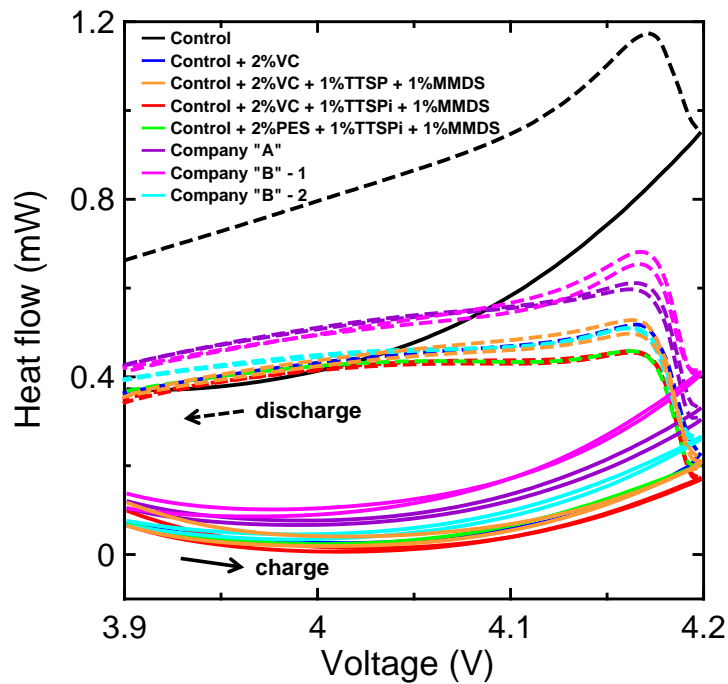


Figure 5.7: Measured heat flow as a function of voltage during the fourth charge (solid lines) and discharge (dashed lines) NMC111/graphite pouch cells at 10 mA (C/22) with various electrolytes as indicated in the legend.

Figure 5.8a shows the measured heat flow (symbols) over a narrow voltage range, 4.0 – 4.1 V, for decreasing currents for NMC111/graphite pouch cell with control electrolyte. The series of curves were fit using quadratic functions for each of the three

sources of heat flow in Equation 5.2.2. The resulting calculated heat flow is given by the solid lines and the extracted parasitic heat is given by the dashed magenta line. Figure 5.8b shows the measured heat flow (symbols) over the same voltage range, 4.0 – 4.1 V, for an NMC111/graphite pouch cell containing control electrolyte to which 2% VC was added (herein referred to as 2% VC). The resulting calculated heat flow is given by the solid lines and the extracted parasitic heat is given by the dashed magenta line. The agreement between the experimental data and the model for both cells is excellent. As was observed for HV-LCO/graphite cells in Section 5.3, the extracted parasitic heat flow lies virtually at the midpoint of the 1 mA charge and discharge heat flow data.

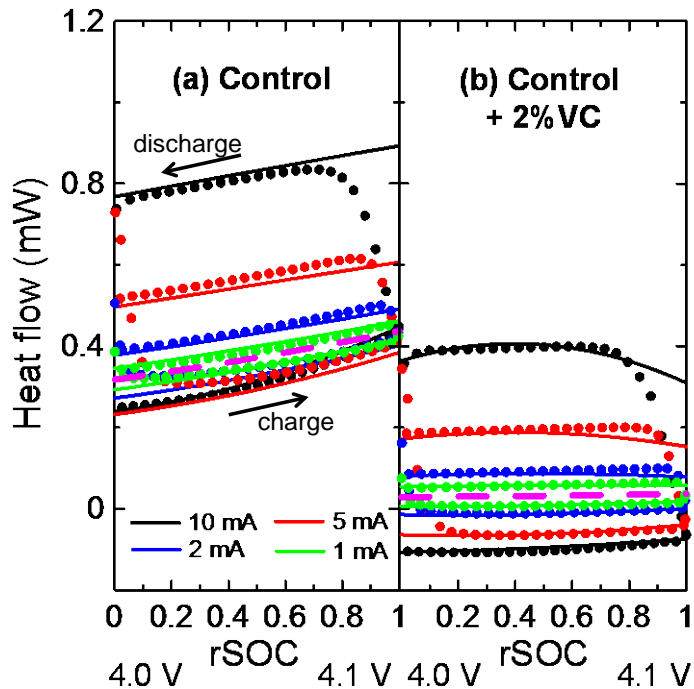


Figure 5.8: Measured heat flow (symbols) as a function of relative state of charge (rSOC) between 4.0 and 4.1 V for an NMC111/graphite pouch cell containing (a) control and (b) 2% VC at various currents: 10 mA (black), 5 mA (red), 2 mA (blue), and 1 mA (green). The extracted total heat flow for each current (solid lines) as a result of fitting the experimental data and the extracted parasitic heat flow (dashed magenta line) are also shown.

The difference in overall heat flow and parasitic heat flow between the control cell (Figure 5.8a) and the 2% VC cell (Figure 5.8b) is remarkable. This agrees with the earlier cycling data shown in Figure 5.7. The parasitic heat flow of the control cell is much larger and increases more rapidly at high voltage.

The variable rate narrow range heat flow was modeled and fit for all electrolytes for the three voltage ranges examined, 3.9 – 4.0 V, 4.0 – 4.1 V, 4.1 – 4.2 V. The fits for all cells for all voltage ranges are not shown in the interest of brevity, with Figure 5.8 giving two representative fitting examples. The resulting RMSE of all such fits are given in Table 5.2, showing that Figure 5.8 is indeed representative of the quality of all fits.

Table 5.2: Summary of root mean squared error of the total fit for all cells and all voltage ranges examined.

Electrolyte	RMSE of total fit (μW)		
	3.9 - 4.0 V	4.0 - 4.1 V	4.1 - 4.2 V
Control [†]	11.2	11.3	16.8
Control + 2% VC [‡]	6.1	2.8	3.8
Control + 2% VC + 1% TTSP + 1% MMDS	6.4 6.2	3.7 3.4	3.9 3.9
Control + 2% VC + 1% TTSPi + 1% MMDS	5.9 5.6	3.2 2.8	3.6 3.2
Control + 2% PES + 1% TTSP + 1% MMDS	5.8 5.4	4.5 2.9	3.1 3.5
Company "A"	6.9 6.7	3.3 3.3	3.9 3.7
Company "B" - 1	7.1 7.0	5.5 3.8	4.5 3.6
Company "B" - 2	5.5 5.8	3.4 3.2	4.2 3.8

[†] Figure 5.8a [‡] Figure 5.8b

Figure 5.9 shows the extracted parasitic heat flow as a function of voltage for all electrolytes examined. It is immediately obvious that the heat flow due to parasitic reactions for control electrolyte is significantly larger than for all other electrolytes and increases dramatically at high voltage, in good agreement with the results presented in Figure 5.7. All three commercial electrolytes provide a substantial reduction in the parasitic heat flow. However, two of the commercial electrolytes, Company “A” and Company “B” – 1, are less effective under the experimental conditions here. It is shown that all additive-containing lab-prepared electrolytes reduce the parasitic heat flow significantly over the entire voltage range examined and the increase in rate of reaction as a function of voltage is reduced compared to cells containing control and Company “A” and “B” – 1 electrolytes. The 100 μW level is also shown for the NMC111/graphite pouch cell as a guide. From these results, the control cell would be expected to have a very poor performance (low coulombic efficiency, large capacity fade, etc.) as has been observed in tests using ultra high precision coulometry.^{7,129}

Figure 5.9 also serves to validate the assumption that for identical cell chemistries, the difference in heat flows between cells that vary only in electrolyte composition is a good measure of the change in the parasitic heat due to that electrolyte. As an example, at 4.2 V the difference between the extracted parasitic heats between control and 2% VC is 475 μW . This is significantly lower than the measured difference of 725 μW from Figure 5.7; however, approximately 250 hours had elapsed between reaching 4.2 V during cycle 4 (Figure 5.7) and reaching 4.2 V during the variable rate testing (Figure 5.9).

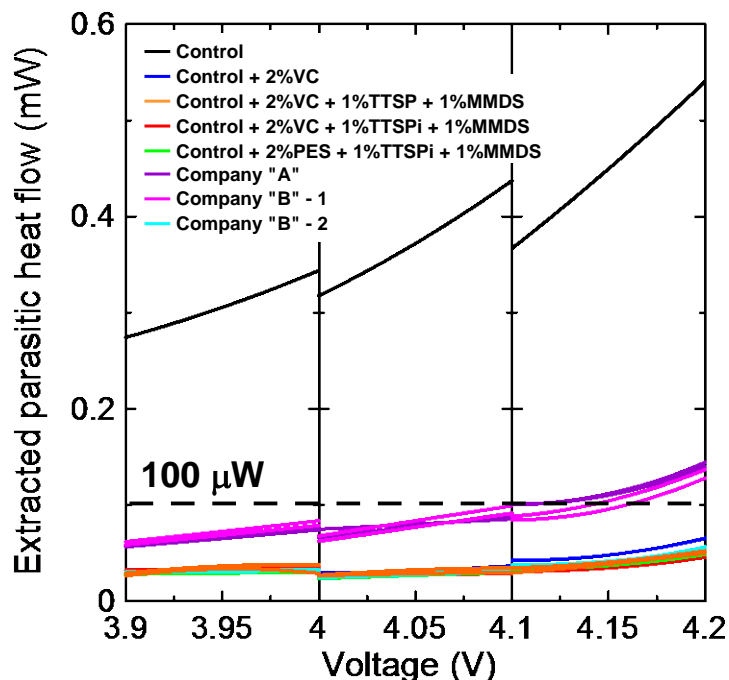


Figure 5.9: Extracted parasitic heat flow as a function voltage for NMC111/graphite pouch cells with various electrolytes as indicated in the legend.

The reduction in parasitic heat over time is qualitatively consistent with previously determined effects of time on charge consumption by SEI layers on the negative and positive electrodes^{69,214}, as well as the previously observed decrease in open circuit heat flow with time as discussed in Chapter 4 (Section 4.3.2). The reduction of parasitic heat over time is also seen by examining the discontinuities in the extracted parasitic heat for the different voltage segments; it is especially noticeable for the control cell. Each variable rate segment (charge and discharge for 0.1 V segment at 10 mA, 5 mA, 2 mA, and 1 mA) takes approximately 60 – 80 hours depending on the capacity in that voltage range, and therefore it is not unreasonable to expect the extracted parasitic heat to decrease between variable rate segments. The parasitic heat flows presented here are, therefore, not absolute values that are valid over the entire cell lifetime, but are a measure of the parasitic heat flow of the cell at that point in time. The impact of

including a time dependency in the parasitic heat flow is examined in detail in the following Chapter.

It is difficult to visually ascertain differences between many of the electrolytes in Figure 5.9 due to the large parasitic heat flow of the cell containing control electrolyte. Furthermore, since the high voltage operation of lithium ion cells is of interest here, Figure 5.10 shows the extracted parasitic heat flow for all cells except control from 4.1 – 4.2 V. As was discussed in the previous section, at 1 mA the polarization contribution to the heat flow is negligible and therefore the average of the total measured heat flows for a 1 mA charge and discharge is a good approximation of the parasitic heat flow. Figure 5.10 shows that there is an excellent agreement between the extracted parasitic heat flow from the empirical model (solid lines) and the 1 mA average heat flow (dashed lines), further confirming the validity of the simple empirical model.

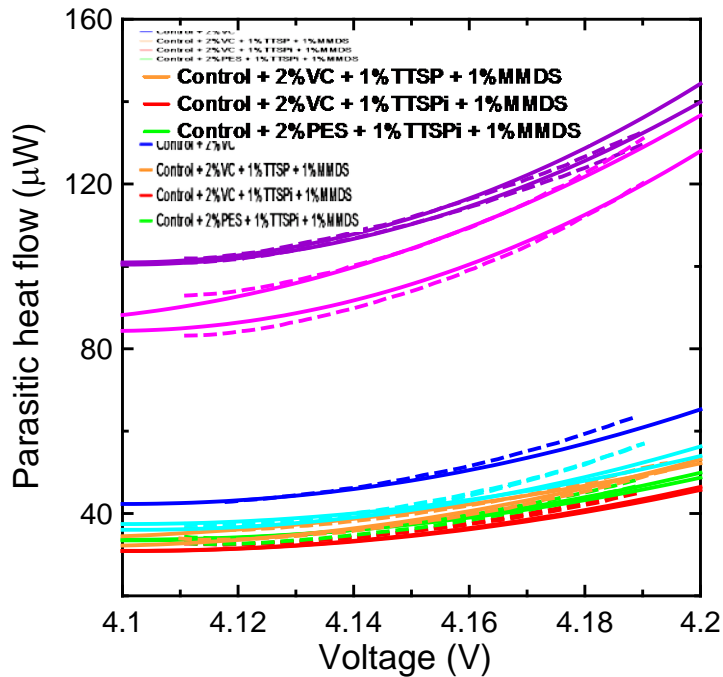


Figure 5.10: Extracted parasitic heat flow (solid lines) and average of 1 mA charge and discharge heat flows (dashed lines) as a function of voltage between 4.1 – 4.2 V for NMC111/graphite cells containing a variety of electrolytes as indicated in the legend.

Figure 5.10 also highlights the difference in high voltage performance of the various electrolytes in terms of the parasitic reaction rates. Out of the commercial “high voltage” electrolyte blends, the only one that competes with 2% VC is Company “B” – 2, under the experimental conditions described here. The three ternary electrolyte additive blends that have previously shown good cycling performance, high coulombic efficiencies, and low charge endpoint capacity slippages (Chapter 4, Section 4.4) give the lowest absolute parasitic heat flows, consistent with the results of Chapter 4. The cell with the lowest parasitic heat flow up to 4.2 V was control + 2% VC + 1% TTSPi + 1% MMDS. The additive blends with TTSP instead of TTSPi, or PES instead of VC both had very slightly higher parasitic heat flows.

Examination of the pair cell data in Figure 5.10 shows excellent reproducibility for cells which had the smallest parasitic heat flows. However, pair cells containing commercial electrolytes from Company “A” and Company “B” – 1 showed significant deviations. This was also observed in the long term cycling experiments shown in Chapter 4, Figure 4.10, where the cells with the largest capacity fade had the worst cell-to-cell reproducibility. One possible explanation is that cells with an increased parasitic reaction rate produce more degradation products which can then deposit on the electrodes, react with other cell or electrolyte components, create gaseous by-products, etc. These processes can dramatically alter the protective passivation layers on both electrodes which have been shown to result in significant differences in cell performance.^{6,46,73,84,219,220} Poor reproducibility between machine-made cells, especially those with commercial electrolytes, and large parasitic heat flows may also indicate that the films formed on the electrodes are poorly passivating or otherwise unstable. Therefore, it is suggested that relatively small and highly reproducible parasitic heat

flows between pair cells is an indication of the formation of good, stable SEI layers. Previous literature on MMDS^{75,142-145}, TTSP and TTSPi^{148,149,151,221} all suggest the benefit of these additives arise from their preferential oxidation at the positive electrode and subsequent formation of a protective SEI on both electrodes. Such passivation films would result in the suppression of electrolyte oxidation occurring at high voltages, in good agreement with both the observed lowered parasitic heat flow and good pair cell reproducibility.

To examine the impact of the electrolytes at increased cell voltages, after the variable rate tests, one 1 mA charge-discharge cycle was performed between 3.9 – 4.3 V. Figure 5.11 shows the extracted parasitic heat flow from the empirical model between 4.1 – 4.2 V (same data as in Figure 5.10) as well as the approximate parasitic heat flow using the midpoint of the 1 mA total heat flows between 4.2 – 4.3 V. Again, the effect of time on the parasitic heat flow is shown through the discontinuities in heat flow between voltage segments. The extracted parasitic heat flow was determined from data collected 345 – 400 h after formation, while the approximate parasitic heat flow was determined from data collected 530 – 650 h after formation.

Figure 5.11 shows that at high voltages the parasitic heat flow, and therefore the parasitic reaction rate, increases considerably, as indicated by a roughly two-fold increase over only 0.1 V. The rate of increase in parasitic heat flow for the three cells containing ternary electrolyte additive blends is noticeably smaller than for the cell containing only 2% VC and the three commercial “high voltage” electrolytes. This is in good agreement with the results presented in Chapter 4, where the effectiveness of the ternary electrolyte additive blends was increasingly pronounced at higher voltages. This suggests the benefit of these electrolyte additives arises from decreased reactivity at the positive electrode, as

the potential and therefore reactivity of the graphite electrode is nearly constant in this voltage range. Again, this is in good agreement with existing literature on the benefits of these additives as discussed in Chapter 1.

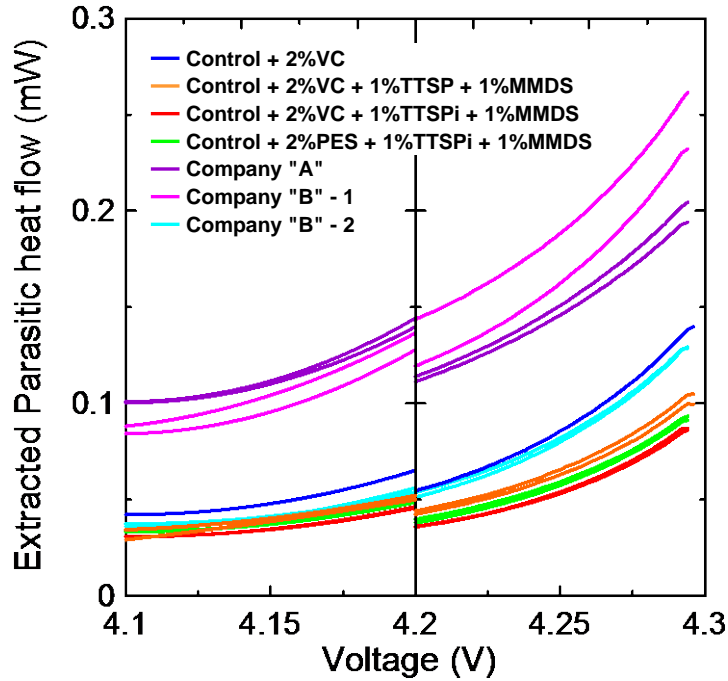


Figure 5.11: Extracted parasitic heat flow from 4.1 – 4.2 V and average of 1 mA charge and discharge heat flows from 4.2 – 4.3 V for NMC111/graphite cells containing a variety of electrolytes as indicated in the legend.

5.5 COMPARISON OF PARASITIC HEAT FLOW BETWEEN LCO/GRAPHITE AND NMC111/GRAPHITE POUCH CELLS

The previously used difference method (Chapter 4 and Figure 5.7) can only be used for cells with the same electrode materials, as the heat flow due to changes in entropy are entirely dependent on the electrode materials. However, by extracting the absolute magnitude of the parasitic heat as done in this Chapter, comparisons across different cell chemistries can be made. In order to account for differences in capacity between cell

types, the parasitic heat flow is normalized to the cell capacity¹⁷³, 200 mAh for the HV-LCO/graphite cells examined in Section 5.3 and 220 mAh for the NMC111/graphite cells examined in Section 5.4. Figure 5.12 shows the normalized extracted parasitic heat flow HV-LCO/graphite and NMC111/graphite pouch cells containing control electrolyte plus either 2% VC or 2% VC + 1% TTSPi + 1% MMDS (the latter data were not shown for HV-LCO/graphite cells in Section 5.3). Unfortunately, there is no overlapping voltage range between the two cell types for the extracted parasitic heat flows from the empirical model fitting, but the 1 mA average heat flow for the NMC111/graphite cells up to 4.3 V can be used as an approximate parasitic heat flow, as shown in Figure 5.10.

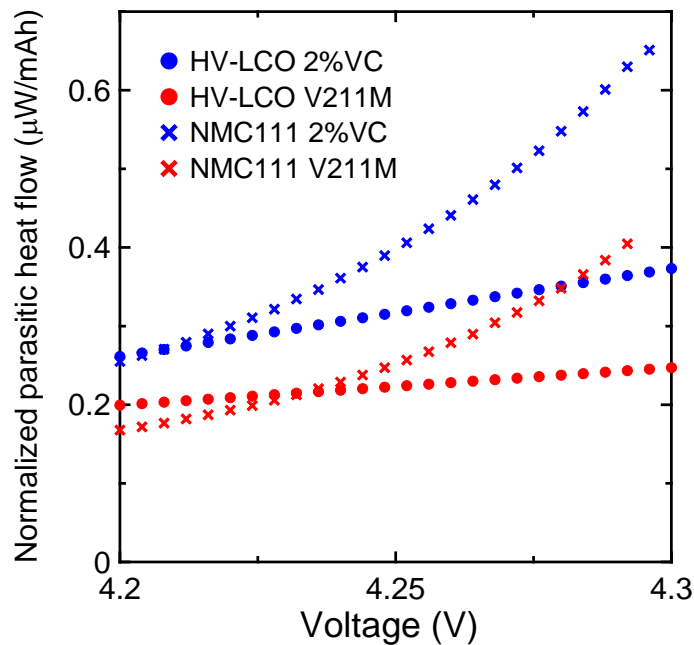


Figure 5.12: Normalized parasitic heat flow as a function of voltage between 4.2 – 4.3V for HV-LCO/graphite (circles) and NMC111/graphite (crosses) pouch cells containing control electrolyte plus 2% VC (blue) and 2% VC + 1% TTSPi + 1% MMDS (V211M, red). Extracted parasitic heat flows for the HV-LCO/graphite cells were determined from data collected 230 – 280 h after formation, while the 1 mA approximate parasitic heat flows for NMC111/graphite cells were determined 530 – 650 h after formation.

Figure 5.12 shows that the addition of TTSPi and MMDS results in a reduction in parasitic heat flow for both cell chemistries examined. This reduction is more pronounced at increased voltage and is very similar for both HV-LCO/graphite and NMC111/graphite pouch cells.

In comparing results between the two examined cell chemistries, it is important to note that the extracted parasitic heat flows for the HV-LCO/graphite cells were determined from data collected 230 – 280 h after formation, while the 1 mA approximate parasitic heat flows for NMC111/graphite cells were determined 530 – 650 h after formation. Therefore the SEI layers on the electrodes of the NMC111/graphite cells had nearly 300 h longer to mature, and the measured parasitic heat flows would decrease correspondingly in that time. It is thus difficult to compare parasitic heat flows extracted after varying elapsed time. However, the data presented in Figure 5.12 clearly show that the parasitic heat flow of the NMC111/graphite cells are larger than that of the HV-LCO/graphite cell above 4.23 V, despite the difference in elapsed time. This suggests that if the parasitic heats were determined at the same time after formation, the NMC111/graphite cell would likely have a higher parasitic heat flow than the HV-LCO/graphite cell over a much wider voltage range.

While tempting, it is not possible to attribute this difference solely to the choice in positive electrode material. In addition to the different positive electrode materials, the graphite electrodes for these two cell types are notably different. Figure 5.13 shows that the active graphite particles in the HV-LCO/graphite cells are much larger than those in NMC111/graphite cells. As a result, the electrodes in the HV-LCO/graphite cells have a lower surface area, which is well known to result in reduced reaction rates with the electrolyte.^{173,214,220,222} Therefore, it is possible that the lower parasitic heat flows

observed for HV-LCO/graphite cells compared to NMC111/graphite cells can be attributed to differences in **both** the positive and negative electrode active materials.

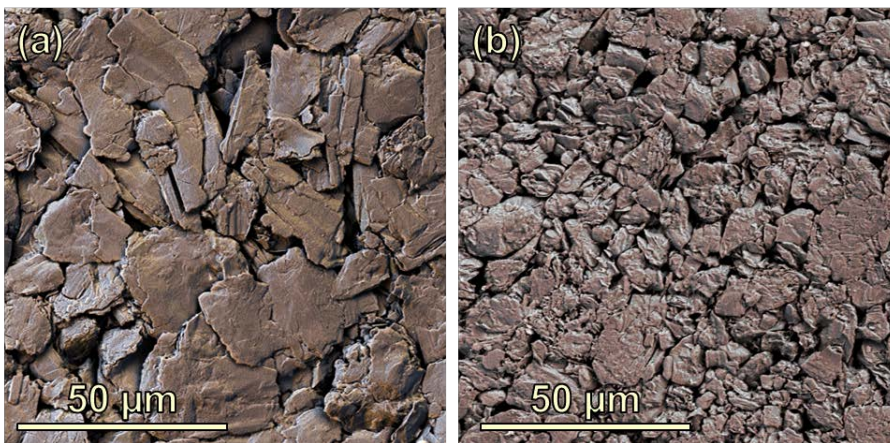


Figure 5.13: SEM image of a graphite electrode used in (a) HV-LCO/graphite and (b) NMC111/graphite pouch cells. False colour added for depth perspective.

5.6 CONCLUSIONS

Empirical modeling of isothermal microcalorimetry measurements is a powerful technique which allows for the determination of the voltage dependence of the parasitic heat flow with relatively quick and simple experiments. Using a three-component empirical model to separate the total measured heat flow into its components has been shown to be effective in the isolation of the parasitic heat flow as a function of voltage for individual cells. This allows for cross-chemistry comparisons, as well as the determination of the impact of electrolyte composition. This will aid in efforts to understand how electrolyte additives provide benefits to the cell, as well as giving some insight into choosing an appropriate cell chemistry and electrolyte additive combination for the desired operating conditions.

As a demonstrative example, the parasitic heat flow as a function of voltage was first determined for an HV-LCO/graphite cell. The technique was then applied to NMC111/graphite pouch cells containing a variety of commercial and lab-prepared electrolytes. Compared to control electrolyte, all commercial electrolytes and additive-containing electrolytes dramatically reduced the parasitic heat flow, especially at high voltages. From the electrolyte compositions examined, the cells containing lab-prepared ternary electrolyte additive blends had the lowest parasitic heat flow, in agreement with results from Chapter 4.

The results presented here used a time independent model to fit the experimental data. However, the effect of time on the observed parasitic heat flow was highlighted in a qualitative manner. The inclusion of time dependence in the parasitic heat flow is explored in detail in the following Chapter.

CHAPTER 6

DETERMINATION OF THE VOLTAGE AND TIME DEPENDENCE OF THE PARASITIC HEAT FLOW

6.1 INTRODUCTION AND MOTIVATION

Data presented in this Chapter are reprinted with permission from *J. Phys. Chem. C*, **118**, 29533 (2014)²²³. Copyright 2015, The American Chemical Society. A portion of the data presented in Section 6.4 is reprinted with permission from *J. Electrochem. Soc.*, **162**, A1401 (2015)²²⁴. Copyright 2015, The Electrochemical Society.

Building upon the model described in the previous Chapter, the introduction of time dependence into the parasitic heat flow is proposed, and implemented. The resulting time dependent empirical heat flow model is shown to be a more accurate description of the experimental data. This model is then used to investigate the voltage and time dependent impact of several electrolyte additives and solvents on the parasitic heat flow, with particular emphasis on high voltage operation, across three different cell chemistries: HV-LCO/graphite, NMC442/graphite, and NMC811/graphite.

6.2 INCLUSION OF TIME DEPENDENCE IN THE PARASITIC HEAT FLOW

6.2.1 Identification of Time Dependence

The time independent model described in Chapter 5 provided good fits to the experimental data; however, it was observed that the extracted parasitic heat flow evolved

with time as would be expected for electrode passivation processes. The narrow range voltage segments take approximately 40 – 80 h depending on the capacity in that voltage window, and the experiments are performed on relatively young cells (starting approximately 150 – 200 h after formation). It is therefore expected that the parasitic heat flow would not remain constant during the time of the narrow voltage range experiments. Figure 6.1 shows the results of the time independent fitting of an HV-LCO/graphite cell that was described in Chapter 5. The largest deviations between the experimental and calculated heat flows are seen at the largest currents, which occur first chronologically.

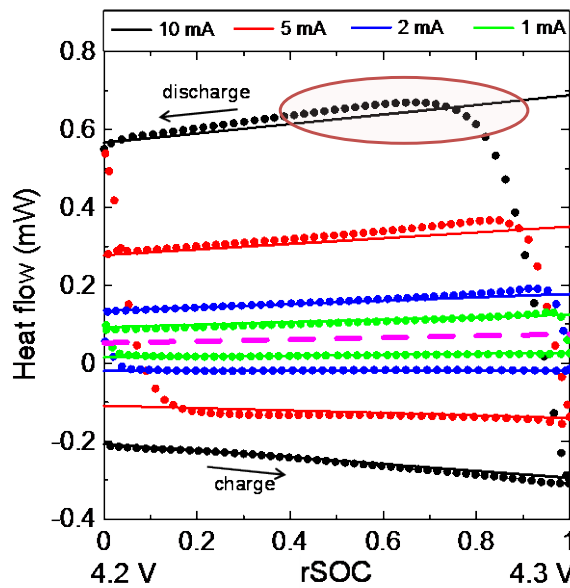


Figure 6.1: Comparison of measured (symbols) and calculated (solid lines) heat flow of an HV-LCO/graphite pouch cell containing 2% VC between 4.2 – 4.3 V. The calculated heat flow was determined by time independent empirical model. Some deviations observed are highlighted by the red oval.

Furthermore, Figure 6.2 shows the evolution of the total measured heat flow for four successive full voltage range charges at a rate of C/20 (10 mA) for an HV-LCO/graphite cell containing 2% VC. Data are shown for 3.7 – 3.9 V (Figure 6.2a) and 4.2 – 4.4 V (Figure 6.2b). For both voltage ranges a decrease in heat flow with cycle

count, and therefore time, was observed. The contributions from polarization and changes in entropy remain nearly constant between cycles, while the rate of parasitic reactions decreases with time as a result of the passivation films on the electrodes.^{69,214} Therefore, the observed decrease in total heat flow here is attributed primarily to a decrease in parasitic heat flow. This is consistent with the evolution of the heat flow seen in Figure 6.2, where the impact of the cycle count (and therefore time) increases as a function of cell voltage.

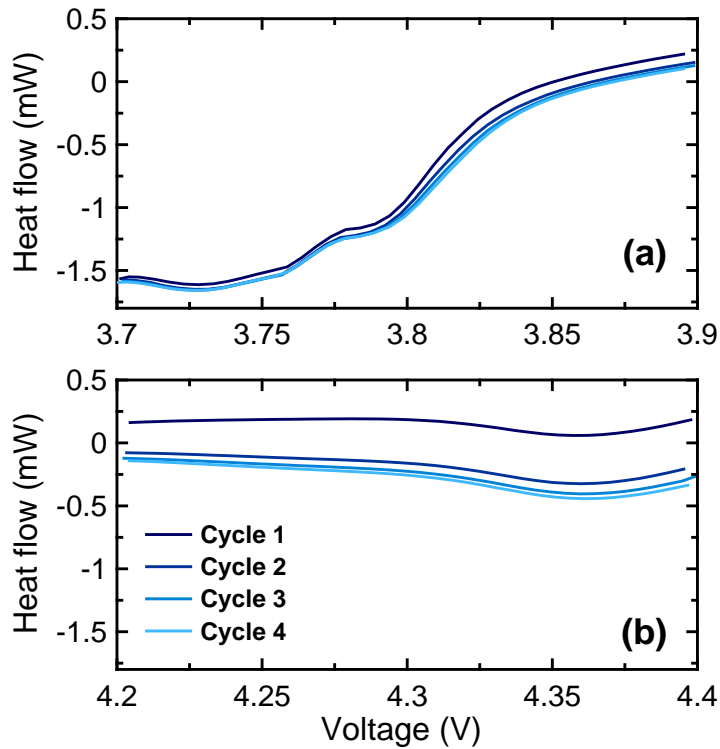


Figure 6.2: Evolution of measured heat flow over four consecutive 10 mA (C/20) cycles of an HV-LCO/graphite pouch cell containing 2% VC between 2.8 – 4.4 V. Data shown during charges between (a) 3.7 – 3.9 V and (b) 4.2 – 4.4 V.

Figure 6.3 shows the evolution of the measured heat flow for an LCO/graphite pouch cell containing 1% VC during open circuit conditions after being formed to 3.8 V, left at open circuit for 100 h at 40°C, then loaded into the calorimeter. Since no current was applied to the cell, the only source of heat flow is a result of parasitic reactions. This

includes small contributions from polarization and entropy as a result of self-discharge, the relative magnitudes of which will be discussed in Chapter 9. Figure 6.3 clearly shows an overall non-linear time dependent decay of the heat flow as a result of passivation-type processes. However, after a sufficient passage of time (150 – 200 h), the parasitic heat flow decreases roughly linearly with time over narrow time ranges ($\Delta t = \sim 50$ h).

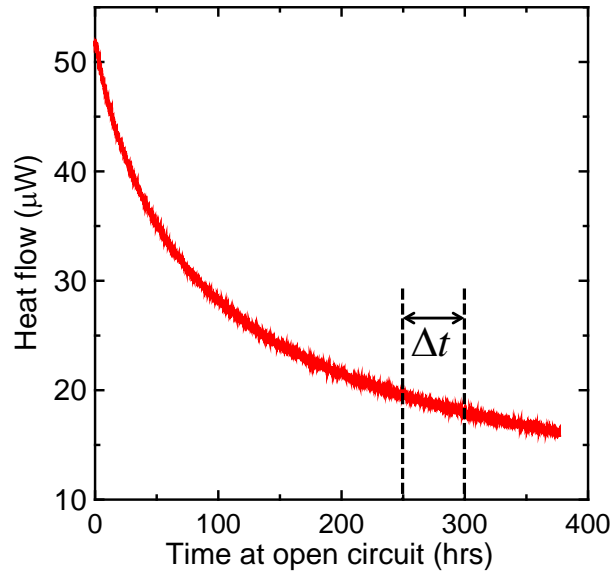


Figure 6.3: Heat flow of an LCO/graphite pouch cell containing 1% VC over 380 hours of open circuit conditions, starting at 3.8 V. A section of 50 h is highlighted showing a nearly linear time dependence over a $\Delta t = 50$ h segment after long experiment times.

6.2.2 The Time Dependent Empirical Heat Flow Model

The time dependent empirical model builds upon the time independent model developed in Section 5.2.1. The same data acquisition method of narrow range cycling with various currents is used. Such experiments begin approximately 150 – 200 h after formation and data collection for each voltage range takes approximately 40 – 80 h depending on the capacity in that range. Therefore using a linear function to describe the

time dependence of the parasitic heat flow is a reasonable assumption, as highlighted in Figure 6.3. The time dependent parasitic heat flow can therefore be expressed as:

$$\frac{dq_p}{dt}(z, t) = \frac{dq_p}{dt}(z) \cdot (1 - L\Delta t) \quad (6.2.1)$$

where z is the relative state of charge (rSOC), L is the relative rate of change of the parasitic heat flow with time, and Δt is the elapsed time from the start of the segment being modeled.

The proposed time dependent empirical heat flow model is therefore given by:

$$\frac{dq}{dt}(z, t, I) = f_{polarization}(z) \cdot I^2 + f_{entropy}(z) \cdot I + f_{parasitic}(z) \cdot (1 - L\Delta t) \quad (6.2.2)$$

where $f_{polarization}$, $f_{entropy}$, and $f_{parasitic}$ are polynomial functions of the rSOC as described in Section 5.2.1. The parameters of each of these functions and the time factor, L , that best describe the experimental data are determined through least-squares minimization.

6.2.3 Fitting method

To aid in data processing and fitting, in-house software was written by Asher Wright. Figure 6.4 shows a screenshot of the software as it is being used to fit the heat flow of an HV-LCO/graphite pouch cell containing 2% VC to the time dependent empirical model where all components are modeled as quadratic functions of rSOC in Equation 6.2.2. The software takes the data files generated by the charging system and the calorimeter as inputs and synchronizes the two files to allow the heat flow to be plotted as a function of voltage. The rSOC is also calculated for the narrow range voltage segments from the cycling data. The data to be used in the fit for each current segment in a narrow range experiment are selected manually by the user. Tick marks indicating the

rSOC when one, three, and four calorimeter time constants have passed are displayed (not shown in Figure 6.4) to help ensure data lying within the calorimeter response time are not included in the fit.

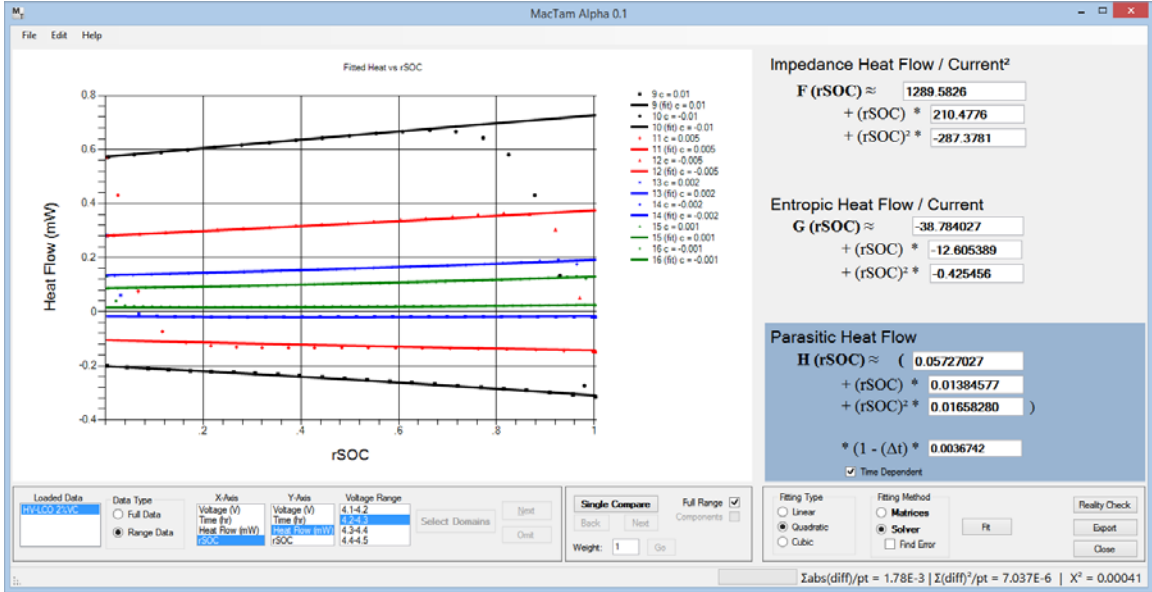


Figure 6.4: Screenshot of in-house developed software used to fit heat flow data with the time dependent empirical model.

Once the data have been selected, the fitting proceeds in two stages. The preliminary data fitting is done using a least squares approximation from linear algebra, called the “matrices fitting method” in the software. This method cannot fit any time dependence, and so the heat flow is modeled according to Equation 5.2.2 during this step. Assuming quadratic functions of rSOC for each of the heat flow components, this equation can be rewritten as:

$$\frac{dq}{dt} = (A_0 I^2 + B_0 I + C_0) + (A_1 I^2 + B_1 I + C_1) \cdot (z) + (A_2 I^2 + B_2 I + C_2) \cdot (z^2) \quad (6.2.3)$$

The data are first separated into subsets where each set corresponds to a particular current. Then for the each value of I , indexed by i , the heat flow can be fit to a quadratic equation of the form:

$$\left(\frac{dq}{dt}\right)_i = \alpha_i + \beta_i z + \gamma_i z^2 \quad (6.2.4)$$

such that:

$$\alpha_i = A_0 I_i^2 + B_0 I_i + C_0 \quad (6.2.5)$$

$$\beta_i = A_1 I_i^2 + B_1 I_i + C_1 \quad (6.2.6)$$

$$\gamma_i = A_2 I_i^2 + B_2 I_i + C_2 \quad (6.2.7)$$

Therefore for each value of I , each of Equations 6.2.5, 6.2.6, and 6.2.7 define a linear equation in terms of the fitting parameters, A_0, B_0, C_0 ; A_1, B_1, C_1 ; and A_2, B_2, C_2 , respectively. The generated set of linear equations is then solved using linear algebra techniques to perform a least squares approximation for an over-defined system of equations²²⁵ (for the example above, the 9 fitting parameters are defined by 24 equations for the case of 4 charge and 4 discharge currents). The resulting parameters then serve as a good initial guess for the non-linear least squares χ^2 minimization performed through Microsoft Excel Solver, as previously described in Section 5.2.2. In this step, the time dependence is included in the fit. Figure 6.4 shows the extracted parameters in the right panel, with polarization, entropic, parasitic, and time factor terms measured in units of mW/mA^2 , $\mu\text{W}/\text{mA}$, mW , and h^{-1} , respectively.

The mean squared error of the total fit is calculated and displayed, from which the root mean squared error is easily obtained. The in-house software also estimates the error on each extracted parameter using the jackknife method.²²⁶ Therefore a good quality fit was considered achieved once the total fit RMSE and parameter uncertainties were minimized. Graphs were also always plotted during the fitting process to ensure good visual agreement between the experimental and calculated heat flows.

6.3 EXTRACTION OF THE VOLTAGE AND TIME DEPENDENT PARASITIC HEAT FLOW FOR HV-LCO/GRAPHITE AND NMC442/GRAPHITE CELLS

6.3.1 Experimental Details

Two types of small machine-made pouch cells were used in these experiments. High voltage LiCoO₂ (HV-LCO)/graphite pouch cells (200 mAh) balanced for 4.4 V operation and Li[Ni_{0.42}Mn_{0.42}Co_{0.16}]O₂ (NMC442)/graphite pouch cells (260 mAh) balanced for 4.7 V operation were obtained dry and sealed from Umicore and LiFUN Technology, respectively. The cells were prepared as described in Chapter 3, and were filled with either 0.70 g or 0.90 g of electrolyte for the HV-LCO/graphite or NMC442/graphite cells, respectively.

The control electrolyte was 1M LiPF₆ in 3:7 by volume EC:EMC. Electrolyte additives used in this work were VC, PES, TTSPi, and MMDS. The combinations of the above additives studied were 2% VC, 2% VC + 1% TTSPi + 1% MMDS, and 2% PES + 1% TTSPi + 1% MMDS, where all additive amounts are given as weight percents. Once cells were filled with electrolyte, they were sealed at 94% of full vacuum with a 6 second sealing time at 150°C for the HV-LCO/graphite cells and at 85% of full vacuum with a 6 second sealing time at 165°C for the NMC442/graphite cells.

Wetting and formation were done in 40. ± 0.1°C temperature-controlled boxes. All cells were held at 1.5 V for 24 hours to ensure complete wetting, then charged at C/20 to 3.8 V. All electrochemical cycling was done using a Maccor series 4000 automated test system. The cells were then degassed as described in Chapter 3. The NMC442/graphite cells went through one additional formation step where after the first degas they were charged at C/20 to 4.5 V, then degassed a second time.

Once transferred to the calorimeter, the HV-LCO/graphite cells were cycled according to the protocol described in Section 5.3.1. One batch of NMC442/graphite pouch cells was subjected to similar experimental conditions as the HV-LCO/graphite pouch cells, only with different voltage segments. The 24 hour open circuit segment was followed by four cycles between 2.8 – 4.5 V at 10 mA (C/26). The cells then proceeded into variable rate tests for the voltage ranges of 4.1 – 4.2 V, 4.2 – 4.3 V, 4.3 – 4.4 V, and 4.4 – 4.5 V, each at 10 mA, 5 mA, 2 mA, and 1 mA. The remaining NMC442/graphite pouch cells were cycled three times between 2.8 – 4.3 V at 10 mA (C/26) outside of the calorimeter in a $40. \pm 0.1^\circ\text{C}$ temperature-controlled box, then loaded into the calorimeter. Once in the calorimeter, the cells proceeded through the 24 hour open circuit segment and then one more 10 mA (C/26) 2.8 – 4.3 V segment. The cells were then charged to 4.1 V at 10 mA, then proceeded through two charge-discharge cycles between 4.1 – 4.3 V at 1 mA, one cycle between 4.1 and various upper cutoff voltages (one cell to each of 4.3, 4.5, and 4.6 V) at 1 mA, and finally three cycles between 4.1 – 4.3 V at 1 mA. The second batch of NMC442/graphite cells was prepared and loaded into the calorimeter by Sarah Hyatt.

6.3.2 Results and Discussion for HV-LCO/Graphite Pouch Cells

Figure 6.5 shows the experimental heat flow (symbols) over a narrow voltage range, 4.2 – 4.3 V, for decreasing currents for an HV-LCO/graphite pouch cell that contains 2% VC. This segment occurred 230 hours after being loaded in the calorimeter and took approximately 50 hours to complete. Figure 6.5a shows the results of fitting the measured heat flow to a time independent model ($L = 0$ in Equation 6.2.2). The resulting

calculated total heat flow for each current is given by the solid lines. This is the same experimental data as presented in Chapter 5 (Figure 5.3), but in Figure 6.5a the calculated heat flow was determined using the software described in Section 6.2.2 with quadratic terms for each flow contribution. While the agreement between the measured and calculated heat flows is good at smaller currents (last chronological segments), there is some deviation for the larger currents (first chronological segments), especially at higher states of charge.

Figure 6.5b shows the results of fitting the measured heat flow to a time dependent model ($L = 0.00367(9) \text{ h}^{-1}$), where again the resulting calculated total heat flow for each segment is given by the solid lines. The agreement between the measured and calculated heat flows is excellent for all currents at all relative states of charge. As was discussed in the previous Chapter, the deviations seen when the current switches between charge and discharge (or vice versa) are due to the response time of the calorimeter and those regions were manually excluded from the fit. The comparison between panels (a) and (b) of Figure 6.5 clearly demonstrates that the inclusion of the time dependent term in the parasitic heat flow makes a significant impact on the overall quality of fit. The RMSE values for the time independent and dependent fits were $3.5 \mu\text{W}$ and $2.6 \mu\text{W}$, respectively. Furthermore, this suggests that the use of a linear function for the time dependence is sufficient, consistent with the open circuit heat flow shown in Figure 6.3.

This analysis was performed for two voltage ranges, 4.2 – 4.3 V and 4.3 – 4.4 V, for two electrolyte additive systems, 2% VC and 2%VC + 1%TTSPi +1%MMDS (V211M). Figure 6.6 shows the fit quality of the experimental heat flow to the time dependent model described by Equation 6.2.2, with RMSE values of (a) $2.6 \mu\text{W}$, (b) $1.7 \mu\text{W}$, (c) $5.5 \mu\text{W}$, and (d) $7.2 \mu\text{W}$.

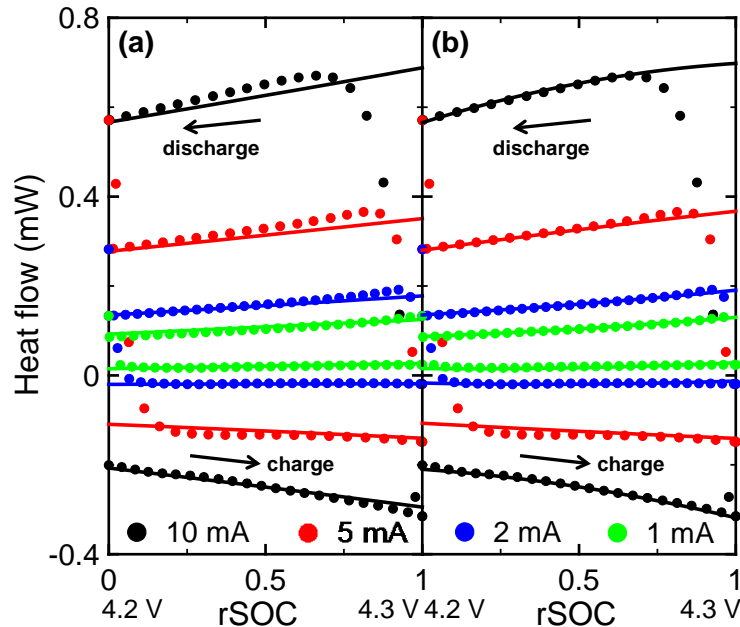


Figure 6.5: Measured heat flow (symbols) as a function of relative state of charge (rSOC) between 4.2 – 4.3 V for an HV-LCO/graphite pouch cell containing 2% VC at various currents: 10 mA (black), 5 mA (red), 2 mA (blue), and 1 mA (green). The extracted total heat flow for each current (solid lines) as a result of fitting the experimental data using (a) a time independent model (Chapter 5) and (b) a model that includes a time dependent parasitic heat term.

Both electrolyte systems studied here are based on the same control electrolyte and therefore same solvent composition, with electrolyte additives added at only 1 – 2% by weight. Therefore, the differences in enthalpies of reaction between the electrodes and electrolyte as a result of the additives are considered to be negligible. An observed difference in parasitic heat flow between cells of the same chemistry with different additive compositions can then be attributed to a decrease in the extent and/or rate of the sum of all parasitic reactions. As an example, the combustion enthalpies for EC and VC are $-1165.9 \text{ kJ/mol}^{227}$ and $-1106.5 \text{ kJ/mol}^{228}$, respectively. The difference of 5% is far smaller than differences in parasitic heat flows observed between cells of varying additive composition.

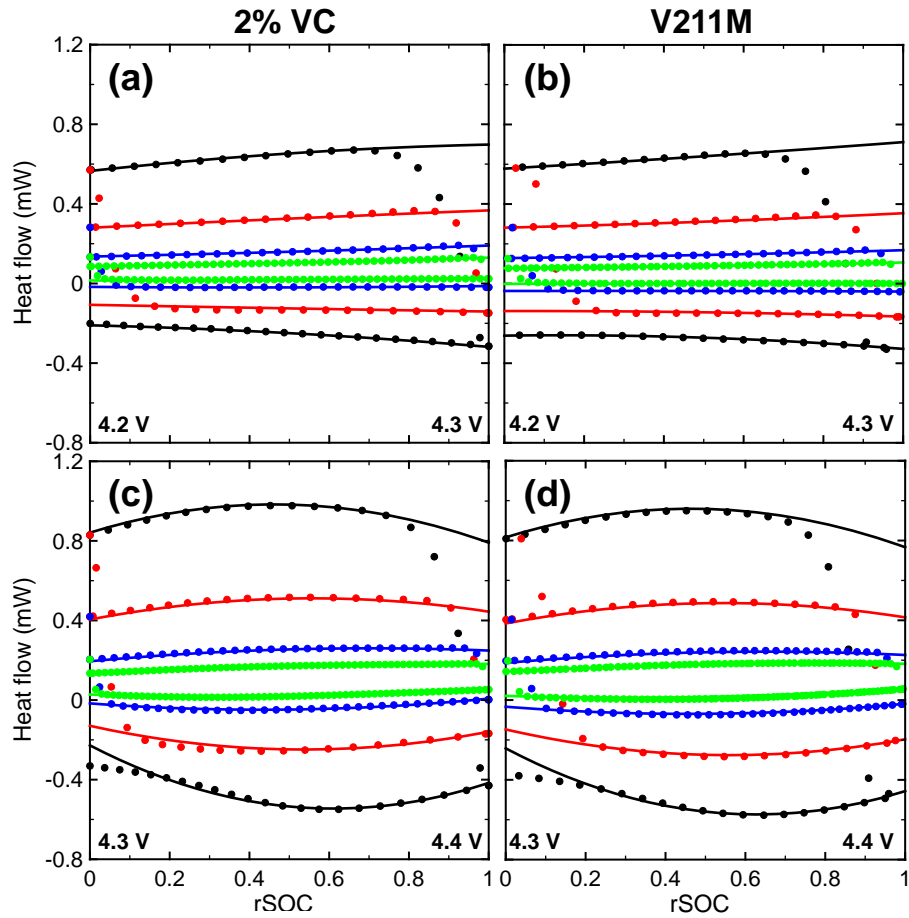


Figure 6.6: Measured (symbols) and calculated (lines) heat flow for HV-LCO/graphite pouch cells at various currents: 10 mA (black), 5 mA (red), 2 mA (blue), and 1 mA (green). Data for cells containing 2% VC in the voltage ranges of (a) 4.2 – 4.3 V and (c) 4.3 – 4.4 V, as well as for cells containing 2% VC + 1% TTSPi + 1% MMDS (V211M) in the ranges of (b) 4.2 – 4.3 V and (d) 4.3 – 4.4 V are shown.

Figure 6.7 shows the extracted parasitic heat flow for HV-LCO/graphite cells over two voltage ranges, 4.2 – 4.3 V and 4.3 – 4.4 V, for two electrolyte additive combinations, 2% VC (red) and V211M (blue). The extracted parasitic heat flows for the time independent ($L = 0$) fits are given by the dashed lines while the time dependent ($L \neq 0$) parasitic heat flows for the 1 mA charge half cycle are given by the solid lines. These extracted parasitic heat flows are compared to the average of the 1 mA charge and discharge total heat flows.

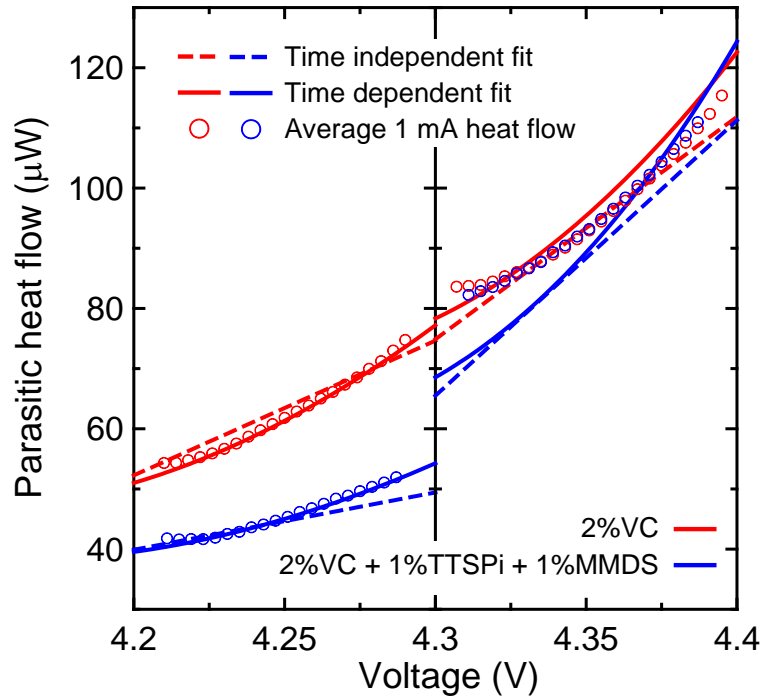


Figure 6.7: Comparison of extracted parasitic heat flow as a function of voltage for an HV-LCO/graphite pouch cell containing 2% VC (red) and 2% VC + 1% TTSPi + 1% MMDS (blue) between a time independent model (dashed lines) and a model that includes a time dependent parasitic heat term (solid lines). The time dependent parasitic heat flow is shown for the 1 mA charge. The averages of the 1 mA charge and discharge total heat flows (open symbols) are also shown.

Figure 6.7 shows that for the lower voltage range, 4.2 – 4.3 V, the time dependent extracted parasitic heat flow is in very good agreement with the average 1 mA heat flow, much more so than the time independent parasitic heat flow. In the higher voltage range, 4.3 – 4.4 V, neither the time dependent nor the time independent extracted parasitic heat flow are in good agreement with the average 1 mA heat flow. Furthermore, there is almost no discontinuity in the parasitic heat flow between voltage segments for the cell containing 2% VC, but a large discontinuous increase in parasitic heat flow between segments for the cell containing V211M despite having identical formation and cycling histories.

Table 6.1 gives the extracted fitting parameters that describe the time and voltage dependence of the heat flow due to parasitic reactions for HV-LCO/graphite pouch cells containing 2% VC and V211M for two voltage ranges, 4.2 – 4.3 V and 4.3 – 4.4 V. The function used to describe the parasitic component of the heat flow is given by:

$$\frac{dq_p}{dt}(z, t, I) = f_{parasitic}(z) \cdot (1 - L\Delta t) = (C_0 + C_1z + C_2z^2) \cdot (1 - L\Delta t) \quad (6.3.1)$$

The uncertainties in the fitting parameters are given by the bracketed numbers. The root mean squared error for the total fit is also given as an indication of the fit quality. The inclusion of the time dependence results in a better fit, as observed in Figure 6.5. The relatively small parameter uncertainties show that values for the parasitic component of the heat flow are well constrained for both voltage and time dependencies. The results presented in Table 6.1 are plotted in Figure 6.8.

Table 6.1: Summary of the parameters describing the heat flow due to parasitic reactions as determined from the fit to the time dependent empirical model for HV-LCO/graphite pouch cells. Comparison is also made with respect to the time independent model. The total root mean squared errors of fits are also given.

	4.2 - 4.3 V			4.3 - 4.4 V		
	2%VC†	2%VC	V211M	2%VC†	2%VC	V211M
C_0 (μW)	47.5 (2)	57.3(3)	44.3(3)	77.8(5)	83.7(6)	58.2(6)
C_1 (μW)	29.9(8)	13.8(6)	11.2(5)	35(1)	19 (1)	15.2(9)
C_2 (μW)	1.1(8)	16.6(6)	8.0(6)	5.9(9)	24 (1)	14.0(9)
L ($\times 10^{-3} \text{ h}^{-1}$)	0†	3.67(9)	4.45(9)	0†	1.18(6)	-8.3(1)
$RMSE$ (μW)	3.5	2.6	1.7	6.0	5.5	7.2

† Time independent model with all quadratic polynomial functions

Figure 6.8 shows the evolution of the time dependent extracted parasitic heat flow as a function of relative state of charge for HV-LCO/graphite cells containing 2% VC (red) and V211M (blue). Within each voltage range the colour gradient follows the chronological order of experiments, the darkest colours (10 mA charge) occurred first and the lightest colours (1 mA discharge) occurred last.

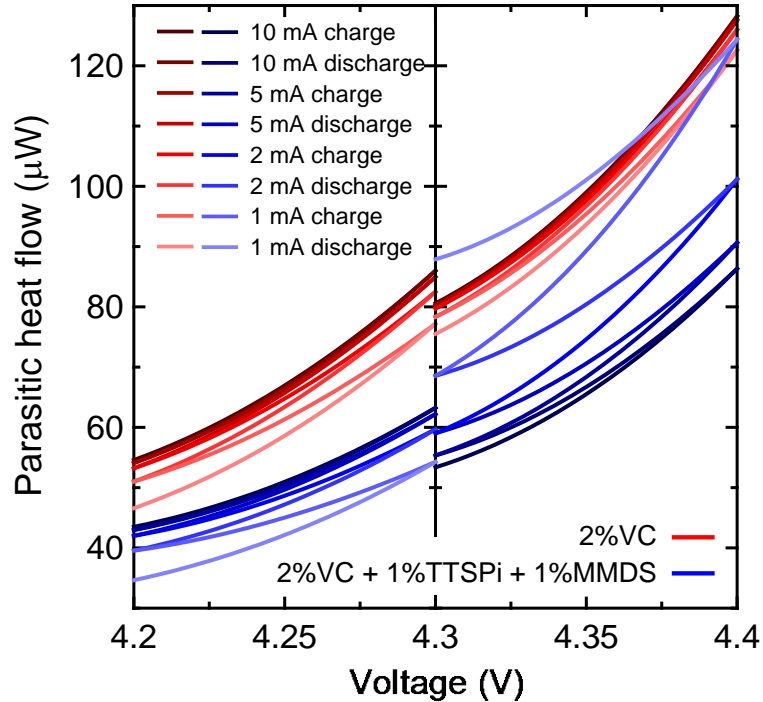


Figure 6.8: Evolution of the extracted parasitic heat flow as a function of voltage and time for HV-LCO/graphite pouch cells containing 2% VC (red) and 2% VC + 1% TTSPi + 1% MMDS (blue) over two voltage segments, 4.2 – 4.3 V and 4.3 – 4.4 V. The colour gradient follows the time sequence over each voltage range, the darkest colours occur first and the lightest occur last.

In the lower voltage range, 4.2 – 4.3 V, the parasitic heat flow for cells with both electrolyte additive choices decreases at approximately the same rate, as also indicated by the similarity between the time dependent fitting parameter, L , in Table 6.1 for both cells. The parasitic heat flow of the cell containing V211M is smaller than for just 2% VC, and the benefit of this additive blend is more pronounced with increased voltage, though the

parasitic heat flow of both cells increases significantly at higher cell voltages. The reduction of parasitic heat flow for the cell containing V211M compared to the 2%VC cell is attributed to a decrease in the rate of parasitic reactions, as discussed in Chapter 5.

The right panel of Figure 6.8 shows that there is a dramatic difference in behaviour at higher voltages, between 4.3 and 4.4 V. The parasitic heat flow for the cell containing 2% VC continues to decrease with time, but at a reduced rate (smaller value of L). The parasitic heat flow for the cell containing V211M begins significantly below that of the 2% VC cell. Surprisingly, the parasitic heat flow increases for V211M with time such that by the 1 mA discharge the parasitic heat flow is greater than for the 2% VC cell. This increase in heat flow due to parasitic chemical reactions is also shown by the negative value of L in Table 6.1 for the V211M cell, showing that this increase is statistically significant and relatively large over the time ranges studied. These results suggest that while beneficial below 4.3 V, above this voltage the electrolyte blend of V211M does not lead to a slowing of parasitic reactions with time, at least over times on the order of 50 hours.

The cause of the observed increase in parasitic heat flow is unknown at this time, although one possible explanation could be the products of electrolyte oxidation at this voltage initiate further degradation reactions. Figure 6.9 shows that the cell containing V211M produced significantly more gas than the cell containing only 2% VC during the cycling procedure, which may lend some credence to the above hypothesis. Further study is required to understand the true cause of this increase in parasitic heat flow. However, it is not believed that the parasitic heat flow will continue to increase in this voltage range for the entire cell lifetime, eventually it should begin to decrease. This rapidly changing and increasing parasitic heat flow explains the discontinuities seen in Figure 6.7 between

the 4.2 – 4.3 V and 4.3 – 4.4 V voltage segments for the V211M cell, as well as the poor agreement between the average 1 mA heat flow and extracted parasitic heat flow in the higher voltage range.

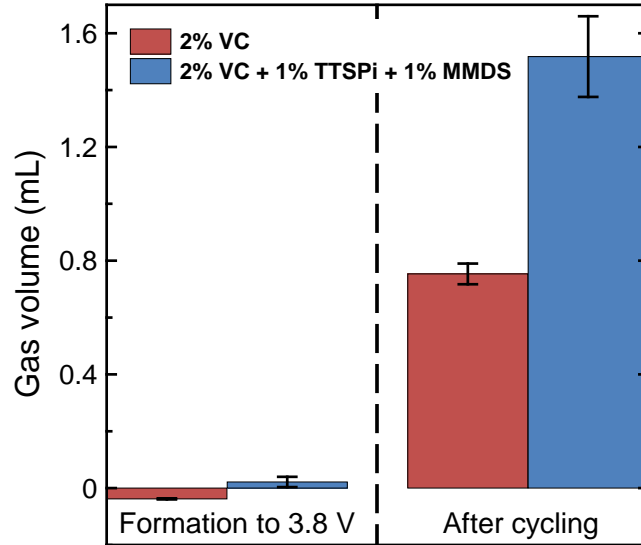


Figure 6.9: Volume of gas produced during the wetting and formation procedure (left) and after the entire cycling procedure (right) for HV-LCO/graphite cells containing 2% VC (red) and V211M (blue).

Figure 6.10 shows the explicit time evolution of the data presented in Figure 6.8. The data are plotted as a function of the experiment time, with $t = 0$ taken as the time the cells were loaded into the calorimeter. The two cells began the variable rate segments at slightly different times, so the time axes for each cell are simply translated such that the scaling is identical for ease of comparison. The bottom ticks (red) correspond to the experiment time of the 2% VC cell, while the top ticks (blue) correspond to the experiment time of the V211M cell.

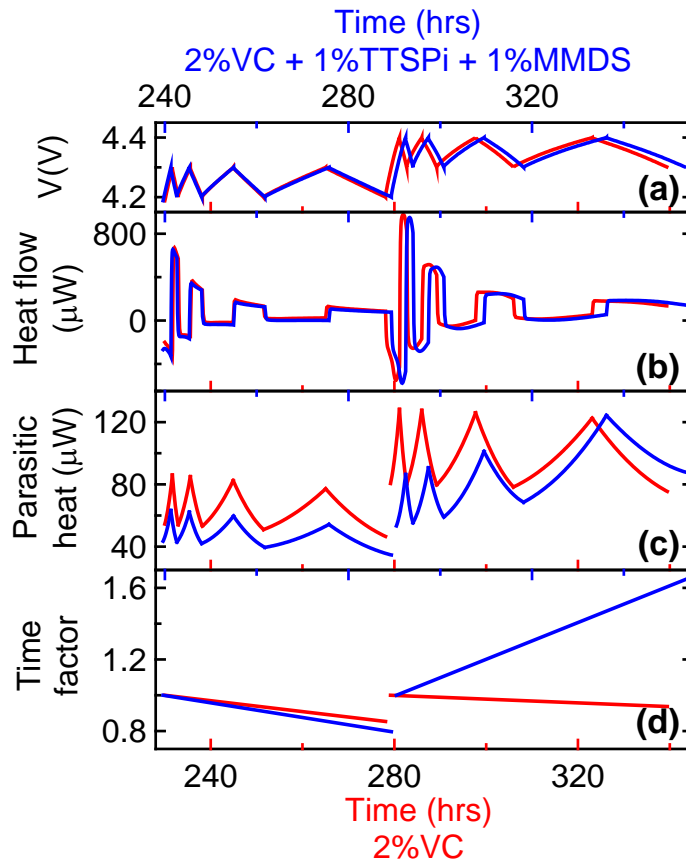


Figure 6.10: Panel (a) shows the voltage versus time during the variable rate experiments for an HV-LCO/graphite pouch cell containing 2% VC (red, bottom axes) and 2% VC + 1% TTSPi + 1% MMDS (blue, top axes). Panel (b) shows the corresponding measured total heat flow. Panel (c) shows the extracted time dependent parasitic heat showing the progression as a function of time. Panel (d) shows the extracted scale factor, $(1 - L\Delta t)$, which multiplies the time independent parasitic heat.

Figure 6.10a shows the cycling procedure of both cells where they are charged and discharged at 10, 5, 2, then 1 mA for each voltage range. Figure 6.10b shows the corresponding measured total heat flow. Figure 6.10c shows the extracted time dependent parasitic heat flow, and clearly shows that the parasitic heat of the V211M cell is below that of the 2% VC cell until the last 1 mA discharge half cycle. Figure 6.10d shows the time factor of the parasitic heat, *i.e.*, the $(1 - L\Delta t)$ term, for each voltage segment where for fitting purposes the $t = 0$ point is set as the start of the voltage range of

interest. Figure 6.10d clearly shows that for the 4.2 – 4.3 V range, the decay rate of the parasitic heat flow between the two additive blends is nearly identical. However, as seen in Figure 6.10, for the 4.3 – 4.4 V range, the parasitic heat flow decreases slowly for the 2% VC cell, but increases in a dramatic fashion for the V211M cell.

6.3.3 Results and Discussion for NMC442/Graphite Pouch Cells

The time dependent empirical model was also used to investigate 4.7 V NMC442/graphite cells, with all heat flow components modeled with polynomials quadratic in rSOC. Figure 6.11 shows good agreement between the measured heat flow and resulting calculated heat flow for cells containing control electrolyte and control + 2% PES + 1% TTSPi + 1% MMDS (P211M) for three voltage ranges examined, 4.2 – 4.3 V, 4.3 – 4.4 V, and 4.4 – 4.5 V.

Table 6.2 presents the extracted fitting parameters that describe the time and voltage dependence of the heat flow due to parasitic chemical reactions for the cells shown in Figure 6.11. As in Table 6.1, the fitting parameters were obtained from fitting the total measured heat flow with the empirical model given by Equation 6.2.2. As shown by the small parameter uncertainties, the extraction of the parasitic component of the heat flow is again well constrained for both voltage and time dependencies. The results presented in Table 6.2 are plotted in Figure 6.12.

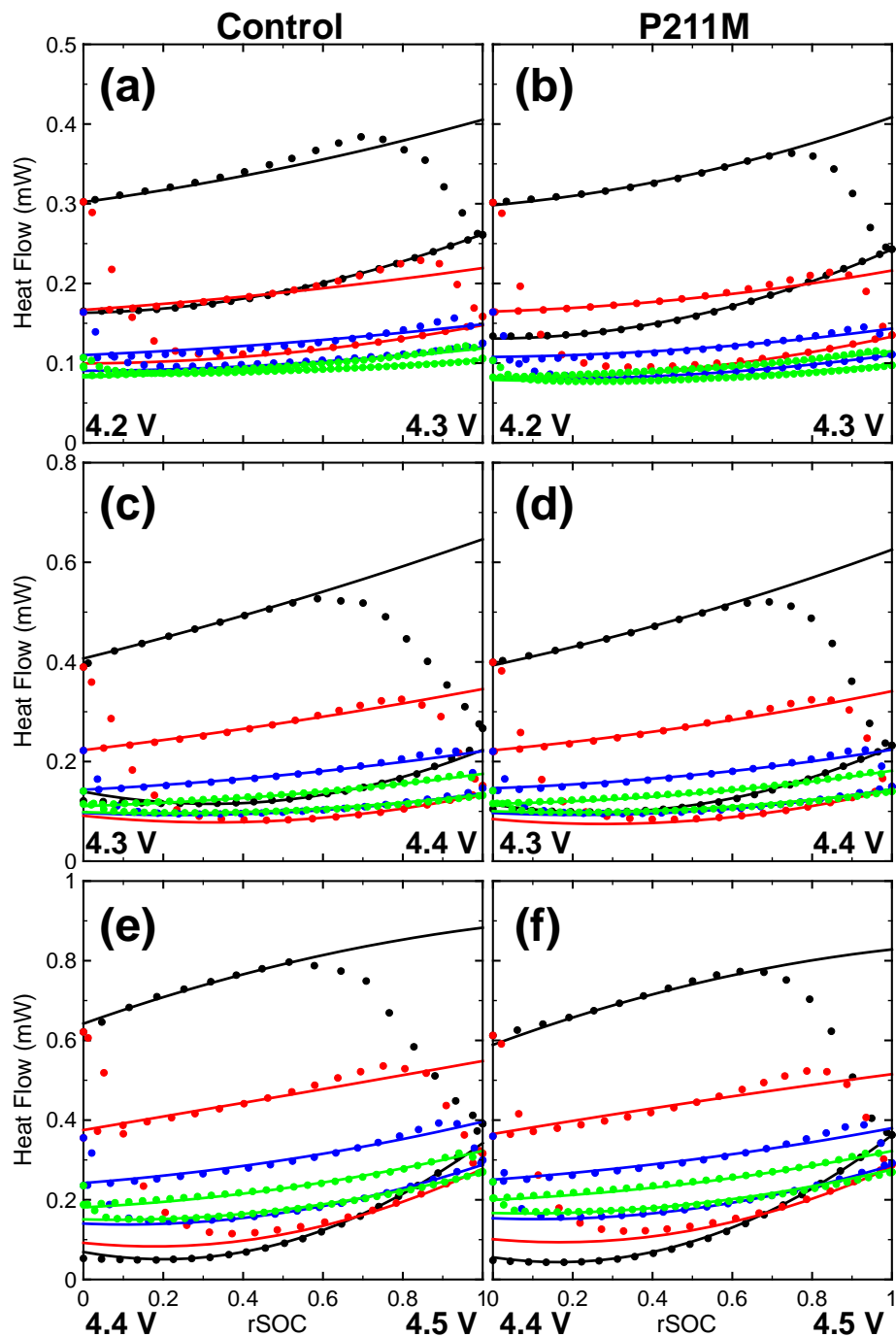


Figure 6.11: Measured (symbols) and calculated (lines) heat flow for NMC442/graphite pouch cells at various currents: 10 mA (black), 5 mA (red), 2 mA (blue), and 1 mA (green). Data for cells containing control electrolyte in the voltage ranges of (a) 4.2 – 4.3 V, (c) 4.3 – 4.4 V, and (e) 4.4 – 4.5 V, as well as for cells containing 2%PES + 1%TTSPi + 1%MMDS (P211M) in the ranges of (b) 4.2 – 4.3 V, (d) 4.3 – 4.4 V, and (f) 4.4 – 4.5 V are shown.

Table 6.2: Summary of the parameters describing the heat flow due to parasitic reactions as determined from the fit to the empirical model for NMC442/graphite pouch cells. The total root mean squared error of the fit is also given.

	4.2 - 4.3 V		4.3 - 4.4 V		4.4 - 4.5 V	
	Control	P211M	Control	P211M	Control	P211M
C_0 (μW)	128.9(1)	97.7(2)	160.2(4)	126.3(3)	250.7(7)	204.4(8)
C_I (μW)	14.1(5)	-3.2(6)	-2.0(8)	-1.6(8)	23(3)	23(2)
C_2 (μW)	28.0(5)	35.8(6)	68(1)	78(1)	127(2)	112(2)
L ($\times 10^{-3} \text{ h}^{-1}$)	5.07(2)	5.77(2)	5.02(6)	5.73(4)	7.03(9)	6.21(8)
$RMSE$ (μW)	2.0	1.7	2.6	2.6	5.9	5.5

Figure 6.12 shows the evolution of the extracted time dependent parasitic heat flow as a function of relative state of charge for NMC442/graphite pouch cells containing no additives (control, black) and P211M (green) for three voltage ranges, 4.2 – 4.3 V, 4.3 – 4.4 V, and 4.4 – 4.5 V. For each voltage range the colour gradient follows the chronological order of experiments, the darkest colours (10 mA charge) occurred first and the lightest colours (1 mA discharge) occurred last.

For both cells, the reduction in parasitic heat flow as a function of time is virtually identical between 4.2 – 4.3 V and 4.3 – 4.4 V, and is larger at the highest voltage range, as also indicated by the values of L in Table 6.2. The reduction over time for the cell containing P211M is larger than for the control cell up to 4.4 V, but is smaller from 4.4 – 4.5 V. The cell containing P211M has a reduced parasitic heat flow compared to the control cell over all voltage ranges and times examined. This is in good agreement with long-term cycling results²²⁹ and EIS experiments^{229,230} which show that

NMC442/graphite pouch cells containing P211M result in higher capacity retention and smaller impedance after high voltage cycling than 2% VC. However, unlike the HV-LCO/graphite cell containing V211M, the parasitic heat flow continues to decrease as would be expected for a passivation type reaction.

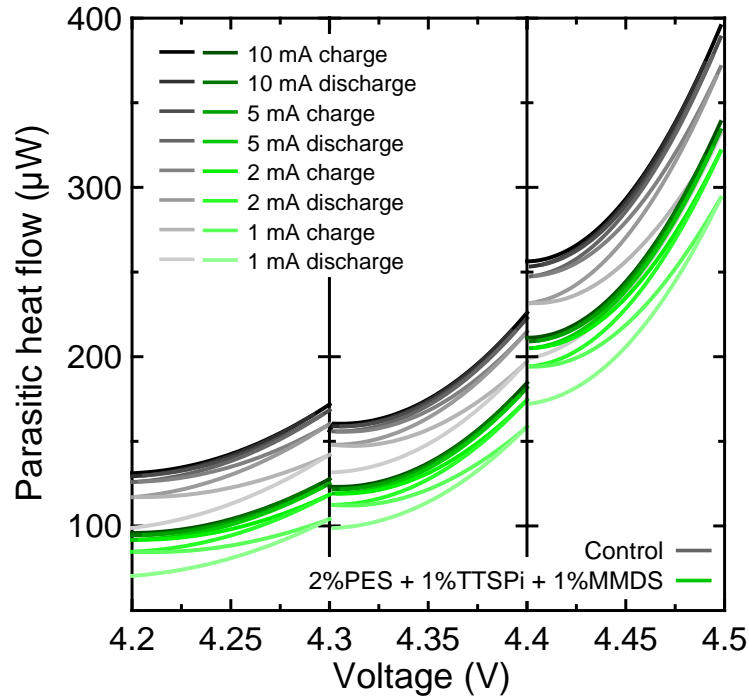


Figure 6.12: Evolution of the extracted parasitic heat flow as a function of voltage and time for an NMC442/graphite pouch cell containing control electrolyte and P211M over three voltage segments, 4.2 – 4.3 V, 4.3 – 4.4 V, and 4.4 – 4.5 V. The colour gradient follows the time sequence over each voltage range, the darkest colours occur first and the lightest occur last.

Although not shown here for brevity, HV-LCO/graphite cells containing P211M also had an increasing parasitic heat flow as a function of time between 4.3 – 4.4 V, and the parasitic heat flow of NMC442/graphite cells containing V211M decreased with time over all voltage ranges.

In the highest voltage range, 4.4 – 4.5 V, both cells show a discontinuous increase in parasitic heat flow compared to the previous voltage range fittings, suggesting either an

increased reaction rate or an initiation of new reactions at a higher voltage. However, as previously mentioned, this increase in parasitic heat flow is accompanied by a greater rate of decrease, L . It should also be noted that while P211M decreases the overall parasitic heat flow compared to control, the magnitude of the parasitic heat flow is still extremely large. Therefore, there is still a significant improvement required in the development of high voltage electrolyte additives and solvents in order to reduce the parasitic heat flow to an acceptable level ($\ll 100 \mu\text{W/Wh}$) and thereby achieve long lifetimes.

Figure 6.13 shows the volume of gas produced during the two formation steps and the cycling protocol. During cycling, the cells containing P211M produced significantly more gas than the control cells. However, the amount of gas produced in the NMC442/graphite cells was substantially less than in the HV-LCO/graphite cells as shown in Figure 6.9, despite the cells being charged to a higher upper cutoff voltage. Combined with the observed differences in high voltage behaviour of the parasitic heat flow between HV-LCO/graphite and NMC442/graphite cells, it is clear that the cell chemistry has a significant effect on the degradation mechanisms and products.

Figure 6.14 shows the explicit time evolution of the data presented in Figure 6.12. The data are plotted as a function of the experiment time, in the same manner as was discussed for Figure 6.10. The rate of change of the parasitic heat flow was nearly identical for both cells for all voltage ranges, and for both cells a slight increase for the highest voltage range, 4.4 – 4.5 V, was observed. This corresponds to an increased overall parasitic heat flow, so while there was an initial increase in heat flow, it was more rapidly reduced with time.

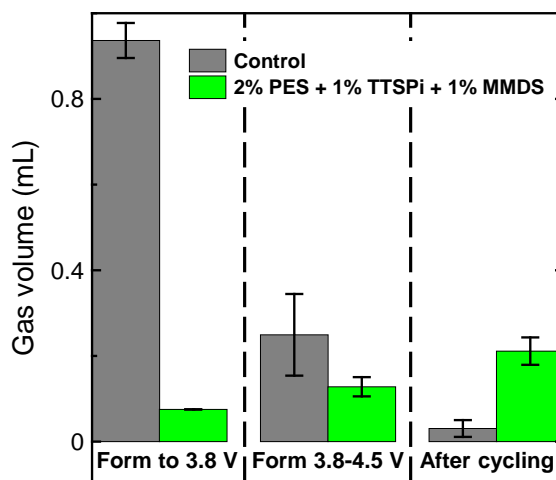


Figure 6.13: Volume of gas produced during the first formation process to 3.8 V (left), during the second formation process between 3.8 – 4.5 V (middle), and after all cycling was completed (right) for NMC442/graphite cells containing control electrolyte (gray) and P211M (green).

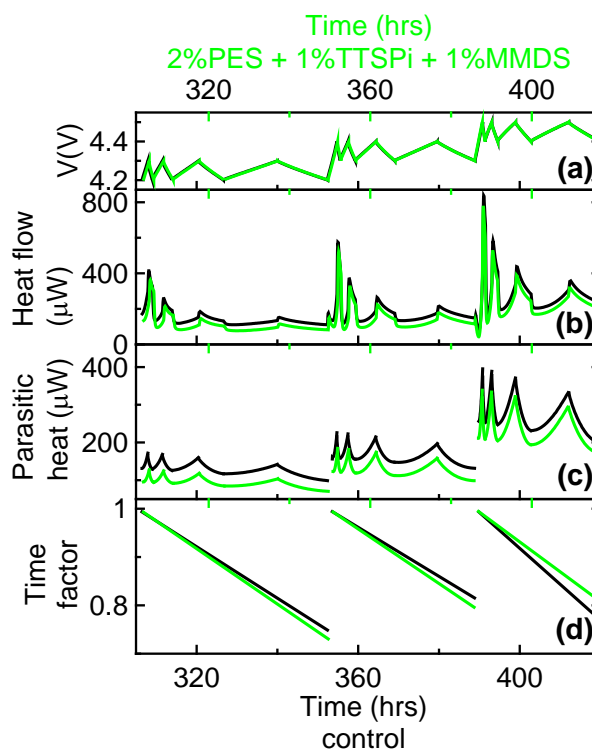


Figure 6.14: Panel (a) shows the voltage over the time frame of the variable rate experiments for an NMC442/graphite pouch cell containing control electrolyte (black, bottom axes) and P211M (green, top axes). Panel (b) shows the corresponding measured total heat flow. Panel (c) shows the extracted time dependent parasitic heat showing the progression as a function of time. Panel (d) shows the extracted scale factor, $(1 - L\Delta t)$, which multiplies the time independent parasitic heat.

Figure 6.15 shows the measured total heat flow as a function of voltage of three identical NMC442/graphite pouch cells containing P211M. The three cells went through initial cycling between 2.8 – 4.3 V at 10 mA, then began narrow range cycling at 1 mA between 4.1 – 4.3 V for 2 cycles. On the third 1 mA cycle, each cell went to a different upper cutoff voltage: 4.3 V (black), 4.5 V (red), and 4.6 V (blue). The remaining three cycles (cycles 4 – 6) were all done between 4.1 and 4.3 V at 1 mA to see the effect of one high voltage segment on the parasitic heat flow at lower voltages. For such 1 mA segments, the parasitic heat flow can be approximated as the average between the charge and discharge total heat flows.

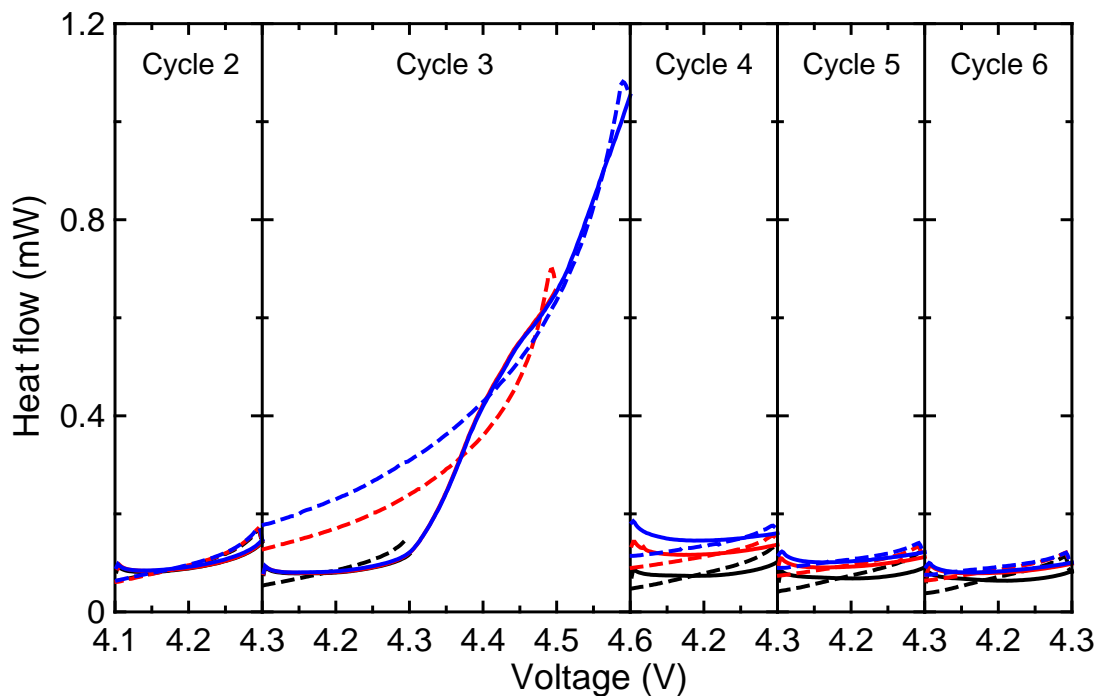


Figure 6.15: Measured heat flow for NMC442/graphite pouch cells containing P211M during 1 mA charge (solid) and discharge (dashed) segments. For cycles 2, 4, 5, and 6 cells were charged and discharged between 4.1 – 4.3 V, while for cycle 3 each cell charged to a different upper cutoff voltage: 4.3 V (black), 4.5 V (red), and 4.6 V (blue).

Figure 6.15 shows that the total heat flow for all three cells at cycle 2 were indistinguishable. In the subsequent cycle, the heat flow for all three cells remained

identical upon charge up to 4.3 V; however the cells charging to 4.5 and 4.6 V produced a significant amount of heat once charged above 4.3 V. The parasitic reactions that occur in these cells have been shown to be highly dependent on voltage. Therefore at higher voltages, where the rate of electrolyte oxidation is markedly increased, a large increase in parasitic heat flow is expected, as was observed. The rapid increase in parasitic heat flow above 4.3 V is also in good agreement with *in situ* gas generation measurements for NMC442/graphite pouch cells that showed a rapid increase in gas generation above 4.3 V.^{135,136} It is important to note that up until cycle 3, none of the three cells had seen a voltage above 4.3 V and so the very large heat flows seen above 4.3 V were not unexpected. However, this large amount of heat flow was retained upon discharge, affecting the lower voltage performance. The higher the upper cutoff voltage, the larger the parasitic heat flow was at lower voltages.

After the one high voltage segment, all three cells returned to cycling between 4.1 – 4.3 V at 1 mA for three cycles. Figure 6.16 shows an expanded view of the measured heat flow for cycles 4 through 6. The heat flow of the one cell that never went above 4.3 V continued to decrease slightly as the contribution from the parasitic heat flow decreased with time as previously discussed. The total heat flow of the 4.5 V and 4.6 V cells were above that of the 4.3 V cell due to increased rate of parasitic reactions. Over the course of cycles 4 to 6, the heat flows of the 4.5 V and 4.6 V cells decreased rapidly such that they nearly returned to the same magnitude as the cell that always remained at lower voltages. This is consistent with the results presented in Table 6.2, Figure 6.12 and Figure 6.14, where at high voltage (> 4.4 V) an increased amount of parasitic heat flow was observed but that parasitic heat flow decreased rapidly with time.

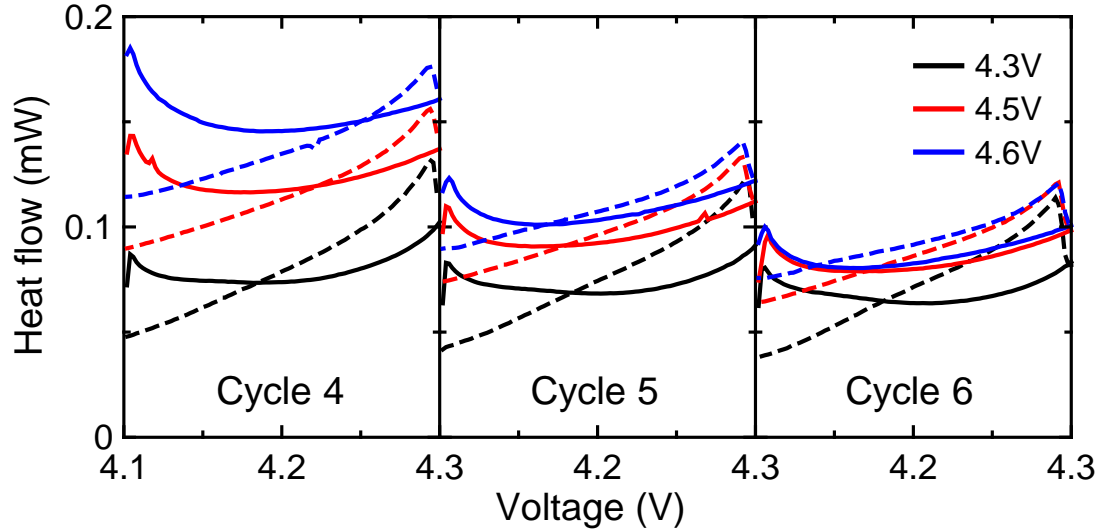


Figure 6.16: Expanded view of heat flow for NMC442/graphite pouch cells containing P211M during 1 mA charge (solid) and discharge (dashed) segments between 4.1 – 4.3 V after one cycle to an upper cutoff voltage of 4.3 V (black), 4.5 V (red), and 4.6 V (blue).

Figure 6.17 shows the voltage and corresponding measured total heat flow as a function of time for the three identical NMC442/graphite pouch cells containing P211M discussed in Figure 6.15 and Figure 6.16. Only the results from 4.1 – 4.3 V at 1 mA (cycles 2, 4, 5, and 6 as shown in Figure 6.15) are shown. The left panels show the voltage and associated heat flow for all three cells during cycle 2, again showing that all three cells were identical prior to the high voltage cycle. The right panels show the measured heat flow for the three 1 mA cycles after the cells were cycled to an upper cutoff voltage of 4.3 V (black), 4.5 V (red), and 4.6 V (blue). The $t = 0$ point was taken as the time at the start of cycle 4 for comparative purposes. As shown in Figure 6.15, the heat flows for the cells that went to higher voltages were initially significantly higher than the 4.3 V cell, but decreased fairly quickly and nearly returned to the level of the low voltage cell. At the start of cycle 4, the heat flow of the 4.6 V cell was 100 μW above that of the 4.3 V, but at the end of cycle 6 that difference was below 40 μW .

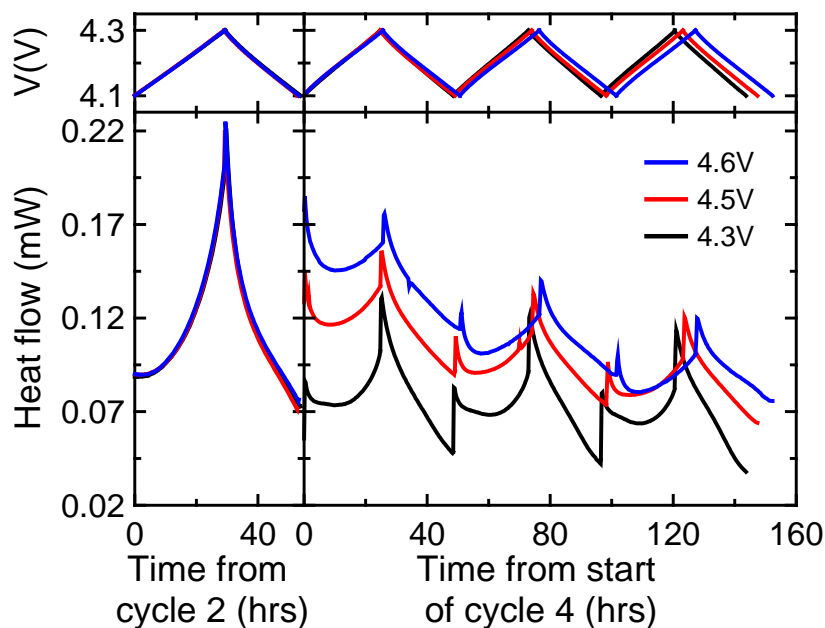


Figure 6.17: Measured heat flow as a function of time (bottom panels) for an NMC442/graphite pouch cell containing P211M for cycles 2, 4, 5, and 6 for cells that went through one cycle (cycle 3) to an upper cutoff voltage of 4.3 V (black), 4.5 V (red), and 4.6 V (blue). Corresponding voltages are shown in the top panels.

From the results presented in this section, it is clear that the behaviour of electrolyte additives is very different at high voltages and for different cell chemistries. While an additive blend such as V211M was very beneficial at lower voltages (< 4.3 V) with HV-LCO/graphite cells, it degraded in a very peculiar fashion above 4.3 V such that the parasitic heat flow increased with time (at least for times on the scale of 50 hours), which was not seen for 2% VC alone. However, a very similar additive blend, P211M, with NMC442/graphite cells did not show any increase in parasitic heat flow over time, even up to 4.5 V. It is clear that the role of electrolyte additives and their degradation pathways are very complex and highly dependent on the cell chemistry, and warrants further investigation.

6.4 DETERMINATION OF THE IMPACT OF ELECTROLYTE ADDITIVES AND SOLVENTS ON NMC811/GRAPHITE POUCH CELLS

6.4.1 Introduction and Motivation

Compared to other NMC materials, Ni-rich oxides such as $\text{Li}[\text{Ni}_{0.8}\text{Mn}_{0.1}\text{Co}_{0.1}]\text{O}_2$ (NMC811) can deliver high specific capacities over narrow voltage ranges (about 200 mAh/g to 4.4 V vs Li/Li^+ , compared to about 160 mAh/g to 4.4 V vs Li/Li^+ for NMC111, for example).^{14,16,231–233} High specific capacities (> 250 mAh/g) have been shown for materials such as Li-rich, Mn-rich NMC, however these are only achieved when the materials are cycled to high voltages (up to 4.6 V vs Li/Li^+).^{234–236} As previously discussed and observed, the stability of the typical carbonate solvents is poor at high voltages. Therefore the motivation of the use of materials such as NMC811 is to deliver the highest energy density possible while maintaining a low cell voltage to minimize parasitic degradation of the electrolyte.

However, it has been shown that such Ni-rich materials have poor charge-discharge capacity retention. This could be a result of electrolyte oxidization at the positive electrode surface^{159,160,218,237,238} and/or structural changes in the material, such as large c-axis shrinkage observed at high voltage.^{16,239–241} This work is therefore aimed at determining the failure mechanism of NMC811 as a function of the voltage range chosen for cycle testing, the results of which will aid in further developments. Isothermal microcalorimetry measurements are well-suited to such an experiment as changes in the active materials can be observed through changes in entropy and electrolyte degradation can be observed through the parasitic heat flow.

6.4.2 Experimental Details

Small 220 mAh machine-made NMC811/graphite pouch cells were obtained dry and sealed from LiFUN Technology. The cells were prepared as described in Chapter 3. The control electrolyte was 1 M LiPF₆ in 3:7 by volume EC:EMC. Electrolyte additives added to control electrolyte used in this work were VC, PES, TTSPi, MMDS, and TAP. The combinations of the above additives studied were 2% VC, 2% VC + 1% TTSPi + 1% MMDS, 2% PES + 1% TTSPi + 1% MMDS, and 2% TAP, where all additive amounts are given as weight percents. Cells containing fluorinated solvents were also examined where the electrolyte was 1 M LiPF₆ in 3:7 by weight of FEC:TFEC. Cells were filled with 0.90 ± 0.01 g for control-based electrolyte and 1.20 ± 0.01 g for FEC:TFEC cells to account for the increased density of the fluorinated solvents. Cells were sealed to 87.5% of full vacuum with a 6 second sealing time at 160°C.

Wetting and formation were done in a $40. \pm 0.1^\circ\text{C}$ temperature-controlled box. All cells were held at 1.5 V for 24 hours to ensure complete wetting, then charged at C/20 to 3.8 V. The cells were then degassed as described in Chapter 3 and went through an additional formation step of charging at C/20 to 4.1 V prior to loading into the calorimeter.

Inside the calorimeter, cells were first left at open circuit conditions for 24 hours to allow for complete thermal equilibration. The cells were charged and discharged between 2.8 – 4.1 V four times at 10 mA (C/20) to allow for partial stabilization of the SEI layers. The cells were then charged to 4.0 V at 10 mA, then proceeded through a charge-discharge segment between 4.0 – 4.1 V at 10 mA, 5 mA, 2 mA, then 1 mA. The cells were charged to 4.1 V at 10 mA, then proceeded through four charge-discharge

segments between 4.1 – 4.2 V at 10 mA for partial SEI stabilization in that voltage range, then were cycled between the same voltage limits for 10 mA, 5 mA, 2mA, then 1 mA. This variable rate procedure was repeated for 4.2 – 4.3 V and 4.3 – 4.4 V.

6.4.3 Results and Discussion

Figure 6.18 shows the voltage vs Li/Li^+ for four NMC811/Li half cells prepared by Jing Li, containing electrolyte composed of 1 M LiPF_6 in 1:2 by volume of EC:DEC, cycled at C/20 between 3.0 – 4.1 V, 3.0 – 4.2 V, 3.0 – 4.3 V, and 3.0 – 4.4 V (all vs. Li/Li^+) at 30°C. Irreversible capacities were about 20 – 25 mAh/g and reversible capacities of 159, 178, 195, and 203 mAh/g from 3.0 – 4.1 V, 4.2 V, 4.3 V, and 4.4 V (vs. Li/Li^+), respectively, were measured. Between 4.3 V and 4.4 V the increase in capacity was less than 10 mAh/g, highlighting the very small gains achieved by extending the upper cutoff voltage.

Figure 6.19 shows the discharge capacity as a function of cycle number for NMC811/graphite pouch cells prepared by Jing Li and Wenda Qiu, containing either 2% VC or P211M added to 1M LiPF_6 in 3:7 by volume EC:EMC. The cells were cycled with a lower cutoff voltage of 3.0 V for 2% VC cells and 2.8 V for P211M cells, and upper cutoff voltages of 4.1 V, 4.2 V, 4.3 V and 4.4 V for both electrolytes. The first two cycles were done at a rate of C/20 then the remaining cycles were done at C/5, all in a 30°C temperature controlled box.

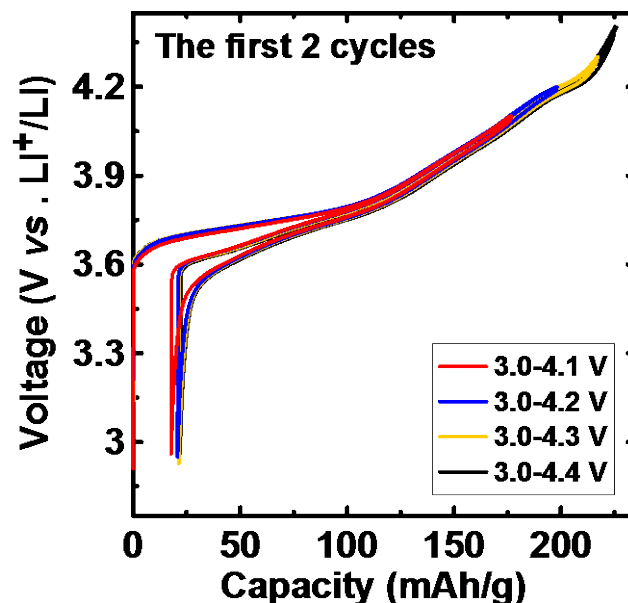


Figure 6.18: The voltage versus capacity curves of NMC811/Li coin cells containing 1 M LiPF₆ in 1:2 by volume EC:DEC electrolyte cycled at C/20 with an upper cutoff voltage of 4.1 V, 4.2 V, 4.3 V and 4.4 V (vs. Li/Li⁺) respectively.

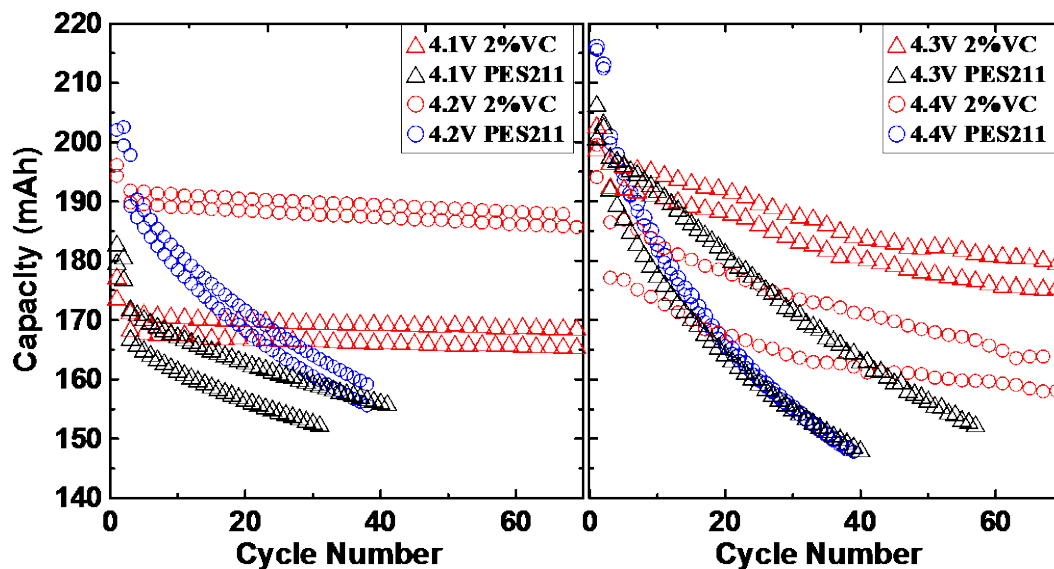


Figure 6.19: Discharge capacity as a function of cycle number for NMC811/graphite pouch cells containing either 2% VC or P211M (called PES211 in legend). The cells were tested with a lower cutoff voltage of 3.0 V for 2% VC cells and 2.8 V for P211M cells, while the upper cutoff voltages were 4.1 V, 4.2 V, 4.3 V and 4.4 V for both electrolytes. The cells were cycled at a rate of C/20 for two cycles and then cycled at a rate of C/5 in a temperature box at 30°C.

Figure 6.19 clearly demonstrates that the cells containing P211M showed dramatically increased capacity fade compared with 2% VC cells cycled to the same voltage. This is surprising as previous results on NMC442/graphite and NMC111/graphite cells with P211M electrolyte show significantly better performance than cells with 2% VC, both in terms of calorimetry measurements shown in the preceding Chapters, UHPC cycling results^{215,229,242}, long term cycling capacity retention^{215,242}, high voltage EIS measurements^{215,230}, and accelerating rate calorimetry results²⁴². This suggests that the interaction between the electrolyte and the Ni-rich surface of NMC811 is very different than for other chemistries examined, as the graphite electrodes have very similar formulations. For both additives, the capacity retention was found to decrease substantially with increased cell voltage, consistent with electrolyte oxidation at high electrode potentials.

To investigate if any serious irreversible structural change of NMC811 occurs during charge and discharge and whether such a change has a significant impact on the long term cycling at the rates tested, a series of *in-situ* x-ray diffraction (XRD) measurements were performed by Jing Li. The details of the data collection and analysis methods are given in Reference [224]. Figure 6.20 shows the results of the analysis of the *in situ* XRD data for the second cycle at C/100 of an NMC811/Li half cell, where the structural information of NMC811 was determined as a function of voltage vs Li/Li⁺.

Figure 6.20a shows that the *c* lattice parameter continually increased from 14.23 Å to 14.47 Å until 4.01 V (first vertical blue dashed line), then decreased smoothly between 4.01 V and 4.2 V vs Li/Li⁺. However, a rapid shrinking of the *c* lattice parameter (13.96 Å at 4.4 V) was observed beginning at 4.2 V (second vertical blue dashed line). Figure 6.20b shows that the *a* lattice parameter gradually decreased throughout the charging

process. The observed changes in both lattice parameters as a function of voltage were mostly reversible, though a small hysteresis was seen between charge and discharge above 4.2 V.

The dramatic change of the c lattice parameter at high voltage vs Li/Li^+ could lead to particle cracking and therefore loss of electrical contact between particles, as well as microstrains²⁴³ in the electrode after extensive cycling. This might be one contributing factor to the poor cycling performance observed for cells cycled to a voltage greater than 4.2 V, as shown in Figure 6.19.

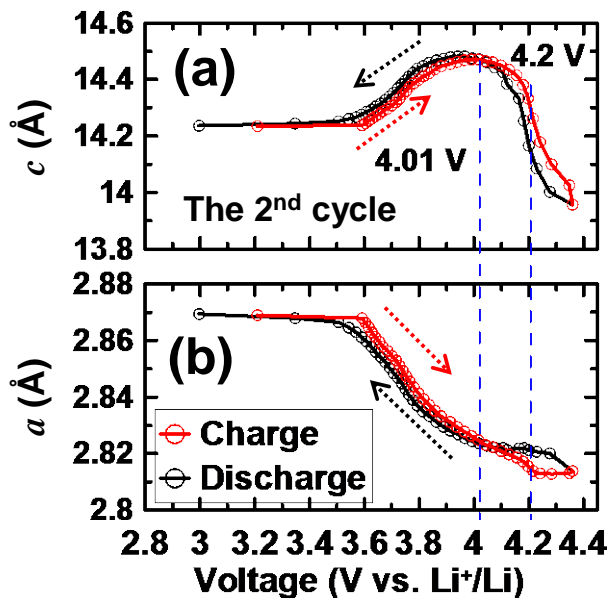


Figure 6.20: The results of Rietveld refinement of *in situ* XRD data for an NMC811/Li half cell showing the extracted (a) c and (b) a lattice parameters as a function of cell voltage during the second charge (red) and discharge (black).

The NMC811/graphite pouch cells containing 2% VC described in Figure 6.19 continued cycling until 200 cycles were reached at C/5 and 30°C to various upper cutoff voltages, then were fully discharged to approximately 0 V and carefully disassembled. The active materials were recovered, and SEM images were taken (not shown here for

brevity, but are shown in Reference [224]). Compared to the pristine electrodes, no significant damage to either aged electrode, such as particle cracking or disconnections between particles, was observed for all upper cutoff voltages examined. Furthermore, *ex situ* XRD measurements showed that the recovered aged electrodes cycled to higher voltages (4.3 and 4.4 V) did not exhibit any significant structural differences compared to the recovered electrodes that were cycled to lower voltages (4.1 and 4.2 V). Therefore, structural changes that occur in the active materials during cycling were not the major contributor to the poor cycling performance of the cells cycled at high voltage. As a result, the role of parasitic reactions must be investigated.

Calorimetry measurements were performed on NMC811/graphite pouch cells as described in Section 6.4.2. The time dependent empirical model was used to fit the data as previously described, with all heat flow components modeled with quadratic functions in rSOC. Figure 6.21 shows a representative data set for cells containing 2% VC. Good agreement was seen between the measured heat flow and resulting calculated heat flow for four voltage ranges examined: 4.0 – 4.1 V, 4.1 – 4.2 V, 4.2 – 4.3 V, and 4.3 – 4.4 V. The calculated RMSE of the fits for each voltage range are given in Figure 6.21.

The fits for the lower voltage ranges, 4.0 – 4.1 V, 4.1 – 4.2 V, and 4.2 – 4.3 V have a total error within the cell-to-cell variation; however in the voltage range of 4.3 – 4.4 V the RMSE is significantly higher (11.1 μ W for 2%VC). This is due to the small capacities in the higher voltage windows, as was highlighted in Figure 6.18. As a result, in the voltage range of 4.3 – 4.4 V, where the measured capacity was approximately 4 – 5 mAh, the response time of the calorimeter almost entirely obscured the measured heat flow at 10 mA (C/22), and impacted a significant portion (~ 40%) of the 5 mA (C/44) heat flow. Significant care was required for the 4.3 – 4.4 V fits to ensure the resulting

component separation made physical sense. Fits for all voltage ranges for all electrolyte systems were of similar quality to those shown in Figure 6.21. Table 6.3 gives a summary of the RMSE values for all fits for all cells.

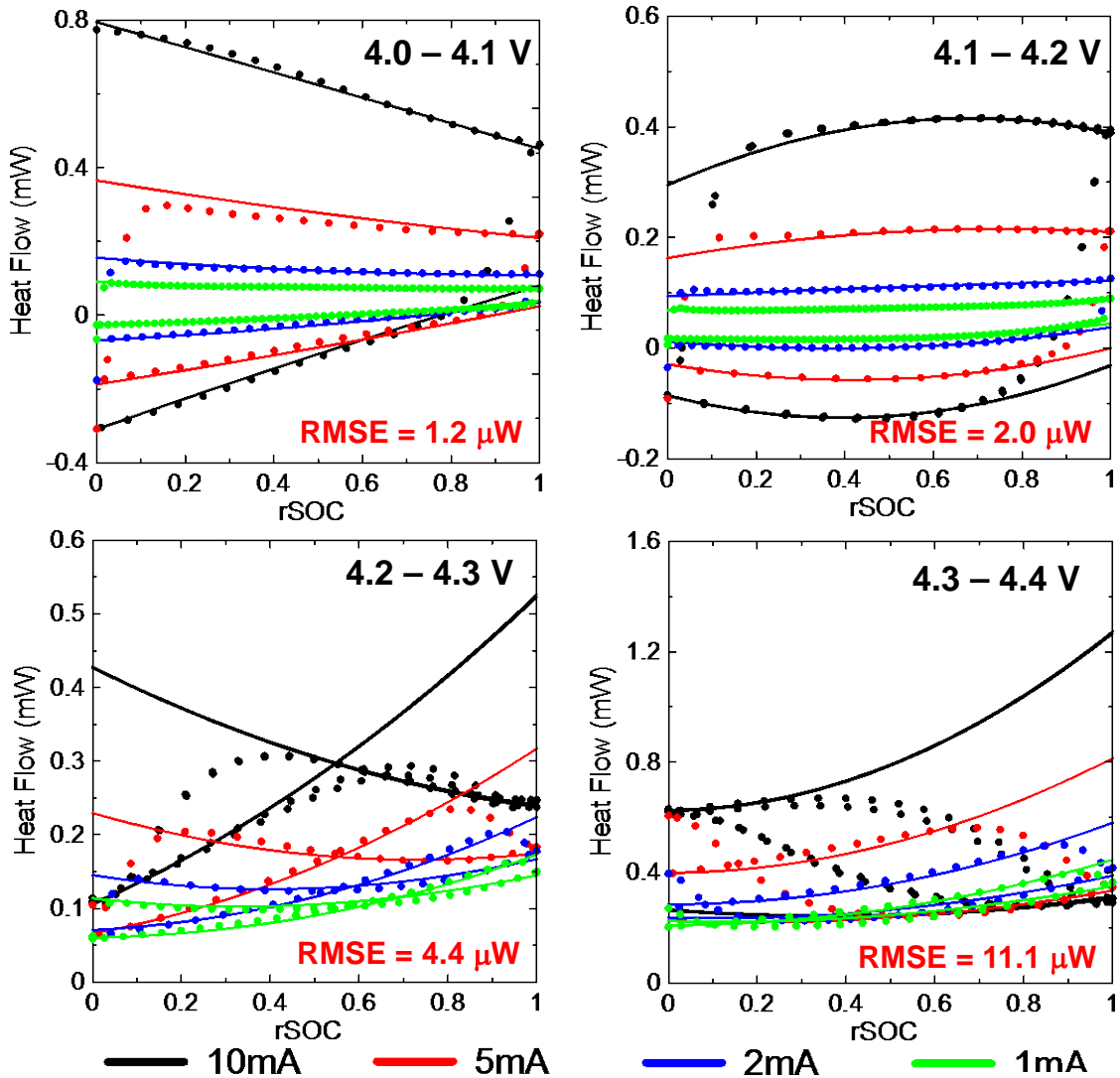


Figure 6.21: Measured (symbols) and calculated (lines) heat flow as a function of rSOC for an NMC811/graphite pouch cell for various currents: 10 mA (black), 5 mA (red), 2 mA (blue), and 1 mA (green). Representative data are shown for a cell containing 2% VC for four voltage ranges, 4.0 – 4.1 V, 4.1 – 4.2 V, 4.2 – 4.3 V, and 4.3 – 4.4 V, as indicated. RMSE of the fits used to generate the calculated heat flows are also given.

Table 6.3: Summary of RMSE of fit for all NMC811/graphite cells for all voltage ranges investigated. Pair cell data are given where available.

Electrolyte	RMSE of fit (μW)			
	4.0 - 4.1 V	4.1 - 4.2 V	4.2 - 4.3 V	4.3 - 4.4 V
Control	3.2	2.9	4.8	10.9
Control + 2% VC	1.2	2.0	4.4	11.1
	1.8	2.2	4.9	11.9
Control + 2% VC + 1% TTSPi + 1% MMDS	1.7	3.0	4.0	8.4
	0.9	1.9	3.9	8.7
Control + 2% PES + 1% TTSP + 1% MMDS	2.5	2.2	5.1	10.5
	1.5	2.9	4.2	9.1
Control + 2% TAP	3.8	3.3	4.2	10.4
FEC:TFEC	2.8	1.4	4.2	9.0
	1.7	1.8	3.5	8.6

Figure 6.22 shows the extracted results for cells containing 2% VC in solid lines and P211M in dashed lines for a 5 mA charge segment in each voltage range. These two electrolytes are discussed here in order to draw comparisons to the experiments discussed above. Both cells have similar heat flows due to polarization throughout the entire voltage range examined during these early cycles. At 5 mA (C/44) the cell polarization was small, as reflected in the magnitude of polarization heat flow. The heat flow associated with changes in entropy was found to be nearly identical for both electrolyte blends, as would be expected since the electrode materials are nominally identical for machine-made pouch cells. Both cells show a large entropic heat flow beginning above 4.2 V. This can be understood with a simple lattice gas model of the positive electrode as discussed in Section 2.2.3, where the configurational entropy decreases dramatically as small amounts of lithium are removed from the already highly delithiated positive

electrode material (the rate of change of lithium content is negative, resulting in an endothermic heat flow).

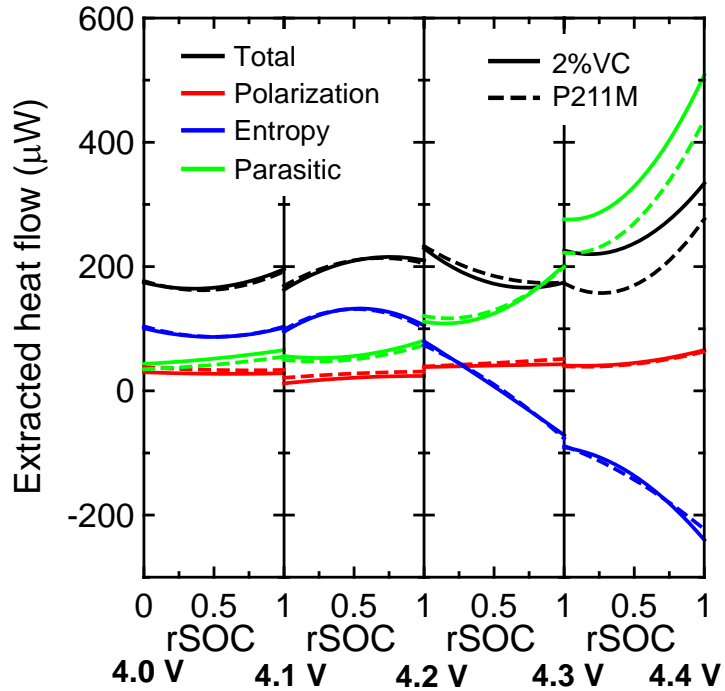


Figure 6.22: The extracted polarization (red), entropic (blue), and parasitic (green) heat flow components of the total heat flow (black) as a function of the rSOC for NMC811/graphite cells containing 2% VC (solid lines) and P211M (dashed lines) for a 5 mA charge segment.

Figure 6.22 also shows that below 4.2 V, cells containing 2% VC and P211M had very similar parasitic heat flows that increased minimally as a function of voltage. Between 4.2 and 4.3 V, the heat flow due to parasitic reactions began to increase dramatically for both electrolytes. Above 4.3 V, the parasitic heat flow continued to increase very rapidly, but the addition of the P211M additive blend reduced the parasitic heat flow as compared to the cell containing 2% VC. The rapid increase in parasitic heat flow above 4.2 V suggests that the highly delithiated positive electrode surface becomes very reactive towards the electrolyte at high potentials. Therefore, it is suggested that the onset of severe parasitic reactions between electrode material and electrolyte above 4.2 V

(as shown by Figure 6.22) is responsible for the poor capacity retention for cells cycled to 4.3 or 4.4 V.

However, the cycling experiments (Figure 6.19) showed that cells containing P211M had an increased capacity fade compared to cells containing 2% VC. This is contradictory to the extracted parasitic heat flow for these two cells (Figure 6.22). There are a few possible explanations for such a discrepancy. The cycling experiments were done at a rate of C/5, while the calorimetry experiments were done at rates varying from C/22 to C/220. Therefore, differences in impedance would have a far greater impact on the higher rate cycling. The difference between the average charge and discharge voltages, ΔV , was tracked during the cycling experiments, as described in Reference [224]. Table 6.4 gives a summary of the measured ΔV values for cycles 4 and 50.

Table 6.4: Summary of measured ΔV for cycles 4 and 50 for cells containing 2% VC or P211M cycled to various upper cutoff voltages.

Upper cutoff voltage	ΔV (V)			
	Cycle 4		Cycle 50	
	2%VC	P211M	2%VC	P211M
4.1 V	0.046	0.055	0.045	0.072
4.2 V	0.046	0.062	0.051	0.114
4.3 V	0.056	0.067	0.086	0.145
4.4 V	0.079	0.073	0.116	0.169

Cells containing P211M had an increased ΔV compared to 2% VC up to 4.3 V, indicating an increase in impedance, in good agreement with the heat flow component due to polarization shown in Figure 6.22. Between cycles 4 and 50, the ΔV of cells

containing 2% VC remained roughly constant to 4.2 V, then increased for cells cycled to 4.3 and 4.4 V. However, by comparison, the ΔV for all P211M cells increased dramatically between cycles 4 and 50. Such a difference in impedance could be one contributing factor to the seemingly contradictory results.

It is also possible that processes that occur at lower cell voltages have a significant impact on the observed capacity degradation. The determination of the parasitic heat flow was done only at the top of charge; except for the first four initial full-range cycles, the cells did not discharge below 3.9 V. In contrast, during the cycling experiments cells were discharged to either 3.0 V (2% VC) or 2.8 V (P211M) and spent nearly half of the total experiment time at a cell voltage below 3.9 V. Furthermore, this may also suggest that the parasitic heat flow is dominated by reactions that occur at the positive electrode and do not result in the loss of active lithium.

While it is difficult to definitively pinpoint the causes of the discrepancy between the cycling and calorimetry measurements, it is clear that the “simple” capacity fade measurements that are routinely performed for lithium ion cells do not tell the full story.

Figure 6.23 shows the extracted heat flow components as a function of rSOC resulting from the fit to the time dependent empirical model for all electrolytes investigated in NMC811/graphite pouch cells for a 5 mA charge segment. The polarization and change in entropy heat flow components are very similar between all cells, as expected for machine-made pouch cells. This similarity between all cells, as well as the continuity between voltage segments, implies that the time dependent empirical model gives a good description of the experimental data. The larger cell-to-cell variations observed at the higher voltage ranges are a result of the difficulty in fitting the

data in that range, as previously discussed. The extracted parasitic heat flow varies significantly depending on the electrolyte composition.

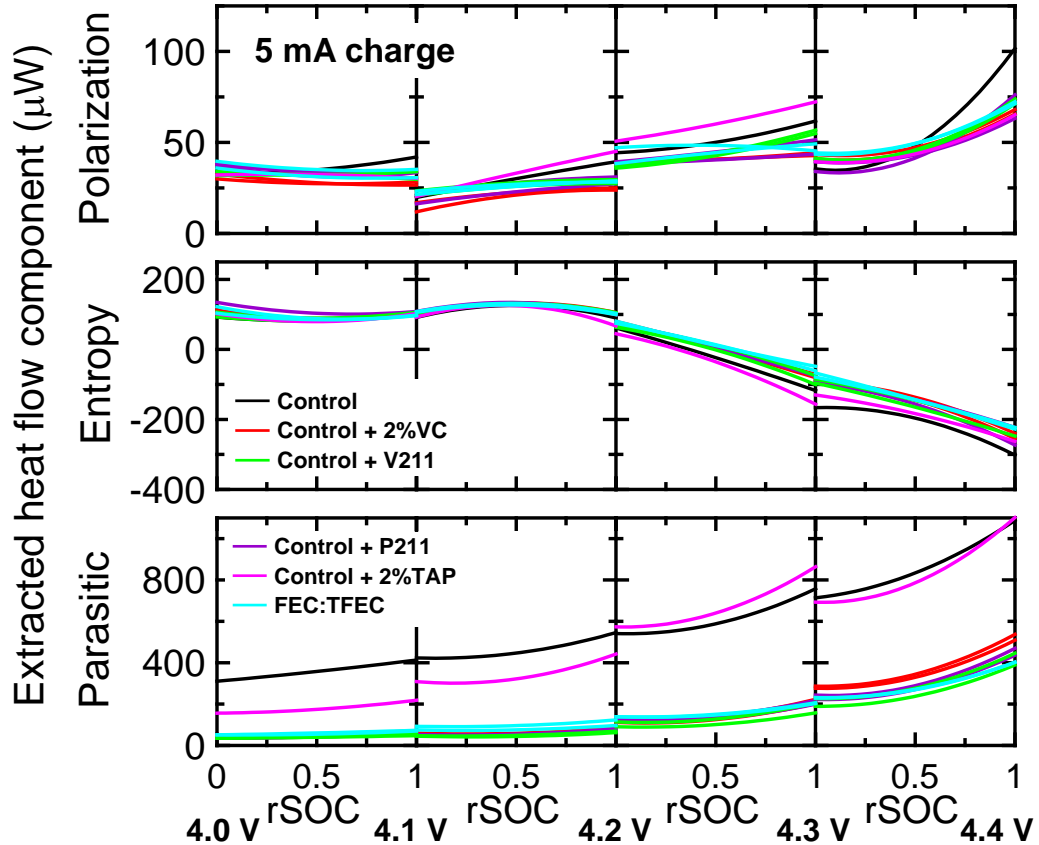


Figure 6.23: The extracted polarization (top), entropic (middle), and parasitic (bottom) heat flow components of the total heat flow as a function of the rSOC for NMC811/graphite cells for the 5 mA charge segment for four voltage ranges, 4.0 – 4.1 V, 4.1 – 4.2 V, 4.2 – 4.3 V, and 4.3 – 4.4V. Data shown for cells containing control electrolyte (black), 2% VC (red), V211M (green), P211M (purple), 2% TAP (magenta), and FEC:TFEC electrolyte (cyan). Pair cell data shown where available.

Figure 6.24 shows the extracted parasitic heat flow on an expanded scale as a function of rSOC for the 5 mA charge segment in each of four voltage segments for all electrolytes tested. For all cells tested, the parasitic heat flow increases dramatically above 4.2 V, as previously discussed in the context of 2%VC and P211M cells. Figure 6.24 also shows that the parasitic heat flow of the cells containing control and control +

2% TAP electrolyte are significantly larger than the other electrolytes tested. Such a comparatively large parasitic heat flow for control electrolyte was also observed in NMC111/graphite cells, as shown in Chapters 4 and 5.

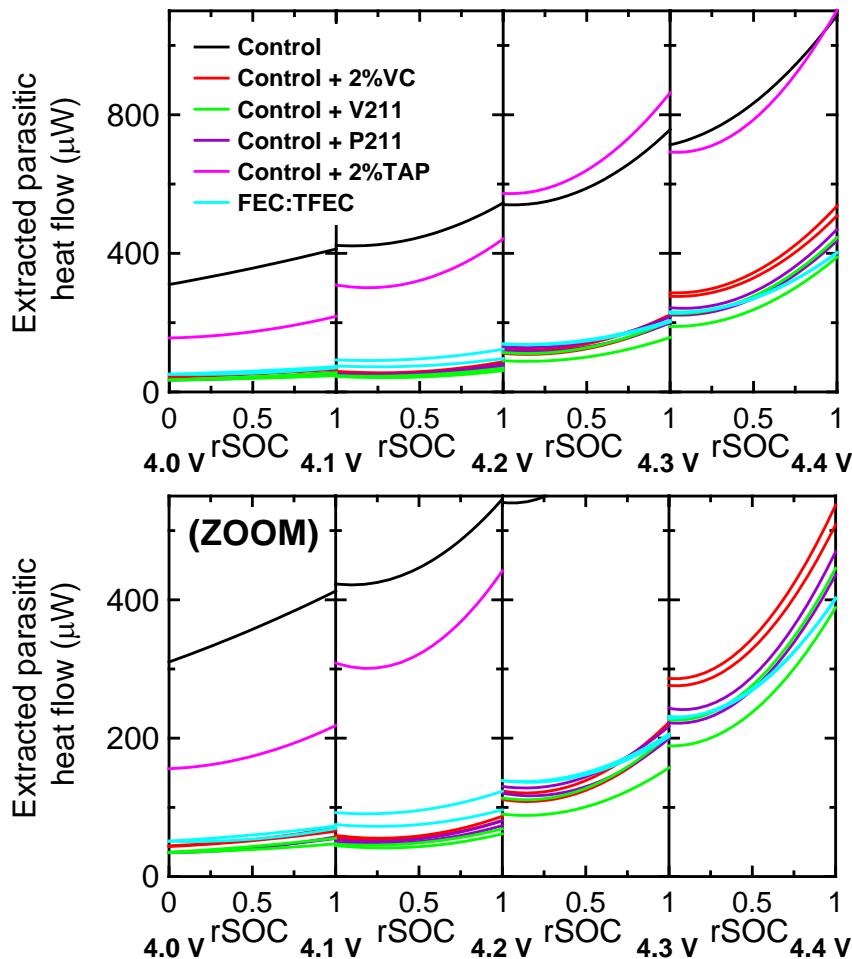


Figure 6.24: Extracted parasitic heat flow as a function of rSOC for NMC811/graphite pouch cells containing a variety of electrolytes as indicated in the legend during the 5 mA charge segment for each of four voltage ranges. The bottom panel shows a zoomed in view of the cells with the lowest parasitic heat flows.

The cell containing 2% TAP also had a very large parasitic heat flow. X-ray photoelectron spectroscopy (XPS) measurements have shown that the inclusion of TAP results in very thick SEI films on both electrodes of NMC442/graphite pouch cells²⁴⁴ as a result of continual polymerization of the TAP molecule that begins at 3.8 V.²⁴⁴⁻²⁴⁶ As a

result of such thick protective films, NMC442/graphite cells containing 1 – 2 % TAP had higher CE values, lower charge slippages and voltage drops during storage compared to control electrolyte. It is therefore suggested that a portion of the large parasitic heat flow is a result of heat generation from the TAP polymerization reaction in addition to any other electrolyte degradation occurring.

The bottom panel of Figure 6.24 shows a magnification of the data for cells with the lowest parasitic heat flows. In every voltage range, the cell containing control + V211M had the lowest parasitic heat flow. As a function of voltage, the cells containing control-based electrolyte all had a very similar parasitic heat flow profile. However, the cell containing FEC:TFEC solvent had a larger parasitic heat flow at low voltages (< 4.25 V), but the rate of increase at high voltages was much lower than control-based cells, such that at 4.4 V the FEC:TFEC cells have the second lowest observed parasitic heat flow. This is consistent with the higher oxidation potential of FEC as compared to EC.⁵⁷

For clarity and to aid in the discussion of impact of electrolyte at high voltages, the extracted 5 mA charge parasitic heat flow from 4.3 – 4.4 V is replotted in Figure 6.25a, showing only the cells with the lowest parasitic heat flows. While the parasitic heat flow was significantly reduced compared to control, the values are still very large and would have a substantial impact on the cell lifetime. As was previously mentioned, the capacity gained by extending the upper cutoff voltage from 4.3 V to 4.4 V in these cells is only about 5 mAh, which is 2% of the total capacity. Therefore, the small increase in energy density is not worth the cost of the rapid increase in the rate of parasitic reactions. Figure 6.25 also shows a large pair cell variation. This is likely due to difficulty in fitting due to the small capacity, and could also be partially due to the increased rate of parasitic reactions as was discussed in Chapter 5.

Figure 6.25a shows the parasitic heat flow for the 5 mA charge segment, while Figure 6.25b is for the 1 mA charge segment. The change in parasitic heat flow between the two segments is a result of the time dependent term in the empirical model. A summary of the time dependence of the parasitic heat flow for all voltage ranges and electrolytes studied is shown in Figure 6.26.

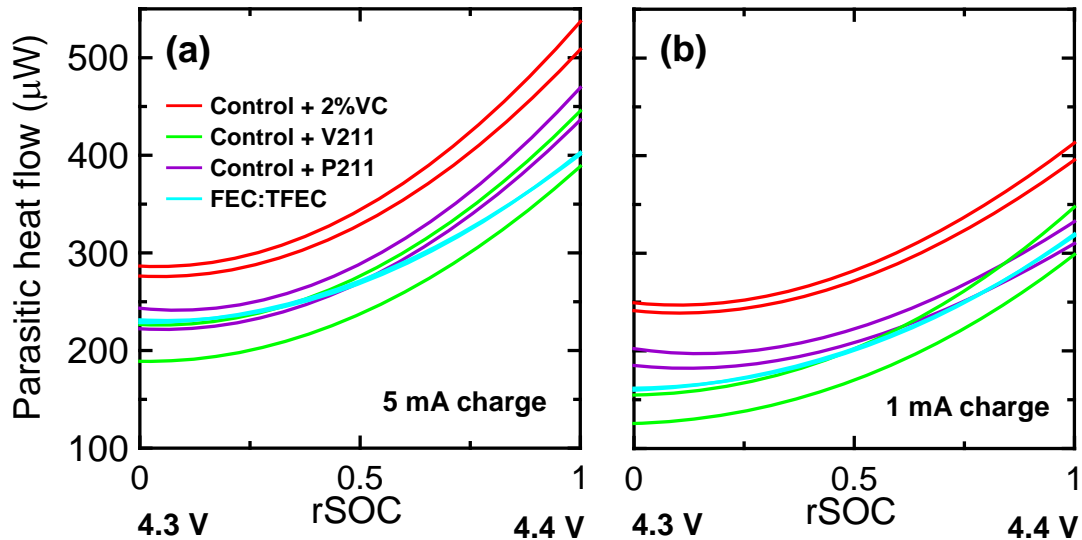


Figure 6.25: Extracted parasitic heat flow as a function of rSOC between 4.3 – 4.4 V for NMC811/graphite pouch cells containing electrolytes as indicated in legend for the (a) 5 mA and (b) 1 mA charge segments. Pair cell data shown for all cells.

Figure 6.26 summarizes the time dependence of the parasitic heat flow by comparing the extracted value at the top of charge for the 10 mA (first chronological) segment and the 1 mA (last chronological) segment of each voltage range examined. The rate of decrease of the parasitic heat flow is shown by the difference between the two heat flows, as well as the time factor, $-L$, in Equation 6.2.2. A larger negative time factor implies an increase in the passivation rate. Therefore an electrolyte additive which gives a small parasitic heat flow and a large negative time factor is desired. In this regard,

despite the initially higher parasitic heat flow, cells containing P211M should ultimately have lower parasitic heat flows than those containing V211M, for example.

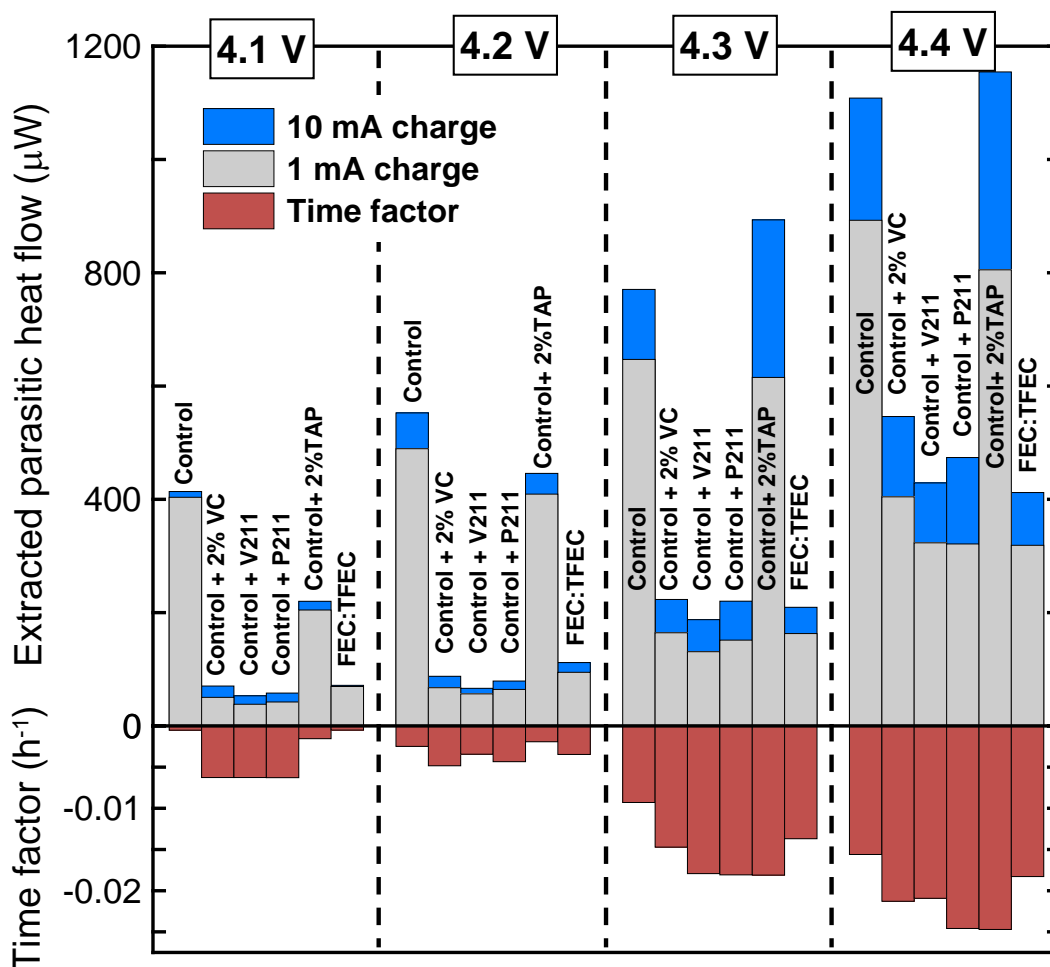


Figure 6.26: Summary of the time dependent parasitic heat flow measured at the top of charge for NMC811/graphite cells containing electrolytes over four voltage ranges for the 10 mA cycle (blue) and 1 mA cycle (gray). The extracted time factor (red) over each voltage range is also indicated. Pair cell data were averaged where available (all cells except control and control + 2% TAP).

Figure 6.26 also shows that a large increase in parasitic heat flow, like that observed between 4.2 V and 4.3 V, and again between 4.3 V and 4.4 V, is accompanied by a more negative time factor (an increase in L). This suggests an initiation of new reactions, or a change in the dominant reaction pathway, that causes a new passivation process to occur. This may also be explained by high voltage degradation of SEI

components which would also result in exposed electrode surfaces and a rapidly decreasing heat flow due to passivation. This correlation between a rapid increase in parasitic heat flow and L is also in agreement with the results for NMC442/graphite cells charged to different upper cutoff voltages (Figure 6.15 and Figure 6.17) that showed that large parasitic heat flows were rapidly reduced after a single high voltage cycle.

This is also in good agreement with *in situ* gas generation measurements performed by Julian Self on the same pouch NMC811/graphite pouch cells. Figure 6.27 shows the gas generation for cells charged at C/20 to 4.7 V for the first time (formation). The cells containing control electrolyte produce significantly more gas than those containing additives, which suggests that the large parasitic heat flow observed for the control cell is likely related to a gas-producing reaction.

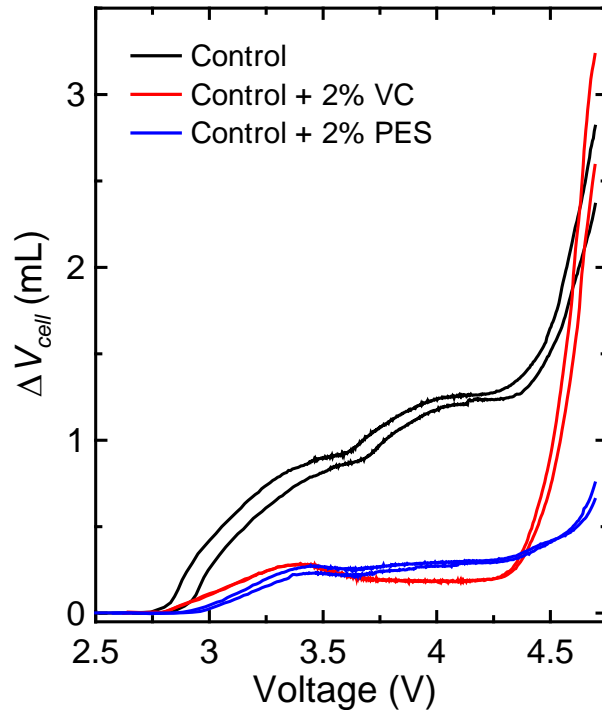


Figure 6.27: *In situ* gas generation as a function of cell voltage for NMC811/graphite pouch cells containing control (red), 2%VC (black), and 2%PES (blue) during the first C/20 charge up to 4.7 V at 40°C. Data collected and provided by Julian Self.

Furthermore, cells containing control electrolyte and 2% VC showed rapid onset of gas generated at the positive electrode beginning at approximately 4.3 V. The gas generation data also suggest that there is an initiation of new reactions, or a change in the dominant reaction pathway at high cell voltages, which, in conjunction with the parasitic heat flow results, suggests that the high voltage parasitic reactions occurring in the NMC811/graphite cells containing control electrolyte or 2% VC produce gas as a by-product. In NMC442/graphite pouch cells, where a rapid gas onset is also observed around 4.3 V, the high voltage gas composition was largely CO₂,¹³⁶ thought to be resulting from the oxidation of EC^{247–250}.

However, Figure 6.27 also shows that such a rapid gas onset is not observed until much higher cell voltages (> 4.5 V) for electrolyte containing 2% PES, while the calorimetry results on cells containing P211M show a rapid increase in parasitic heat flow beginning at 4.3 V. While this may be attributable to the presence of MMDS and TTSPi, it can also suggest that the reactions occurring in PES-containing cells prevent the formation of gas, and instead result in solid insoluble products. The deposition of such solid products on the electrode surfaces is also in good agreement with the increase in impedance observed for P211M-containing NMC811/graphite cells compared to cells with 2% VC (Table 6.4). As was observed with the long-term cycling experiments shown in Figure 6.19, such high impedance films can have a significant impact on the capacity retention during even moderate-rate cycling, despite lowering the rate of parasitic reactions. Further work is required to understand the underlying reaction mechanisms of these complex electrolyte-electrode systems.

6.5 CONCLUSIONS

The inclusion of a time dependent term in the parasitic heat flow proved to be very valuable, not only in terms of quality of fit, but in providing additional information on the reactivity of electrolyte additives with various cell chemistries as a function of voltage and time. This will aid in efforts to understand how electrolyte additives are functioning and degrading, as well as giving some insight into choosing an appropriate cell chemistry and electrolyte additive blend for the desired operating conditions.

The parasitic heat flow as a function of voltage and time was determined for three cell chemistries, and the effect of certain additive and solvent combinations was examined. Ternary additive blends reduced the parasitic heat flow below 4.3 V for HV-LCO/graphite cells and for all voltages examined (up to 4.5 V) for NMC442/graphite cells. However, above 4.3 V for HV-LCO/graphite cells it was found that the ternary VC-based additive blends reacted in such a way that the parasitic heat flow increased with time, an effect not seen for NMC442/graphite cells. Additionally, the extraction of the parasitic heat flow for NMC811/graphite cells showed that the primary failure mechanism of NMC811 is related to the parasitic reaction between the electrolyte and charged electrode surface.

CHAPTER 7

EXAMINATION OF THE ROBUSTNESS OF THE TIME

DEPENDENT EMPIRICAL MODEL

7.1 INTRODUCTION AND MOTIVATION

The empirical model used to describe the heat flow during narrow voltage range segments that was developed throughout Chapters 5 and 6 assumed that the heat flow component due to polarization was proportional to the square of the current. This was based on the assumption that the contribution of the inherent voltage hysteresis to the total overpotential was negligible, as discussed in Chapter 3. However, since such small currents are used, it must be determined whether or not the hysteresis is small compared to the polarization due to internal resistance. Therefore, in the first section of this Chapter, the impact of the inclusion of a heat flow component due to hysteresis is explored for NMC442/graphite pouch cells.

The robustness of the empirical model is further explored in Section 7.3 through the investigation of the impact of differences in the data collection and analysis methods. This includes examining if there is any observable difference between cycling in the narrow voltage ranges using a current that increases or decreases in magnitude with time, if an increased number of current steps can improve the quality of fit, or if cycling over the entire top of charge but only fitting small voltage ranges is equivalent to the previously used narrow voltage segment method.

7.2 INCLUSION OF A HEAT FLOW COMPONENT DUE TO HYSTERESIS

7.2.1 Identification of the Need of a Hysteresis Term for NMC442/Graphite Cells

The examination of all extracted heat flow components using the time dependent empirical model for NMC811/graphite cells (Chapter 6, Figure 6.22) showed good continuity between voltage segments and good agreement between cells where expected. Figure 7.1 shows a corresponding examination of the time dependent extracted heat flow components for NMC442/graphite cells (experimental details of these cells are the same as those given in Chapter 6).

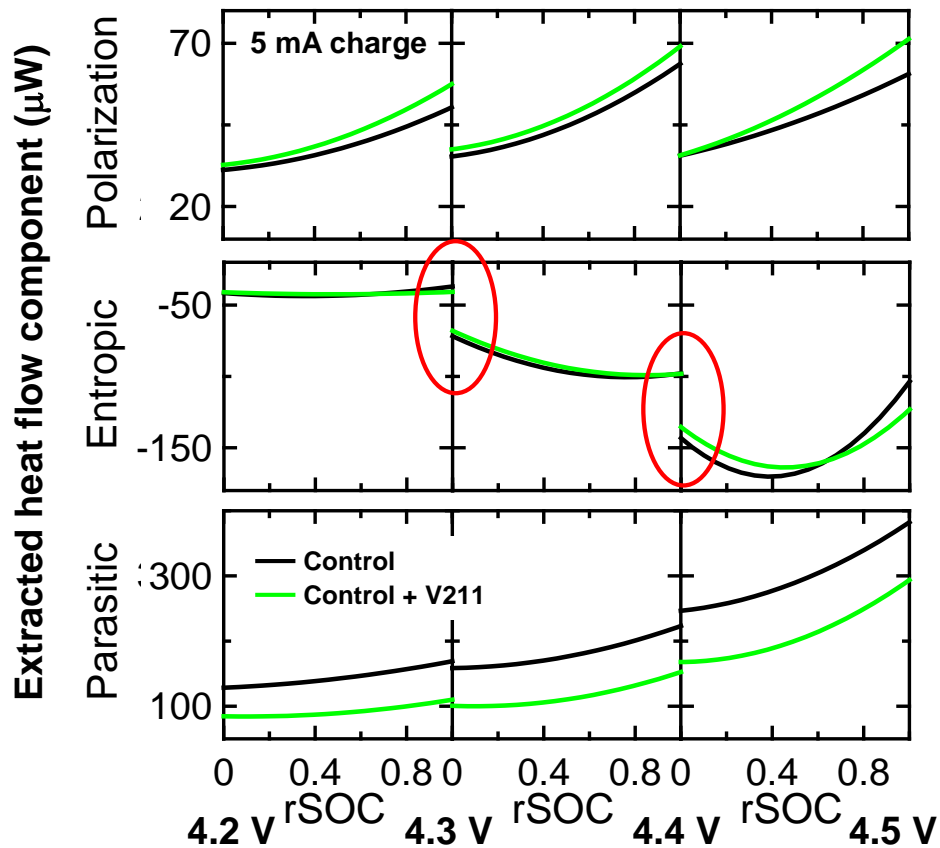


Figure 7.1: The extracted polarization (top), entropic (middle), and parasitic (bottom) heat flow components as a function of rSOC for NMC442/graphite pouch cells for the 5 mA charge segment for three voltage ranges: 4.2 – 4.3 V, 4.3 – 4.4 V, 4.4 – 4.5 V. Data are shown for cells containing control (black) and control + V211M (green) electrolyte. Red ovals highlight discontinuities in the entropic heat flow components between ranges.

In contrast to the results for NMC811/graphite pouch cells, the polarization and change in entropy components show large discontinuities between voltage segments, as indicated in Figure 7.1 by red ovals. The extracted components and discontinuities for both electrolytes examined were very similar, indicating that the discontinuities were not the result of a simple error in fitting for one file, but rather a systematic error in the determination of the current-dependent heat flow terms.

Figure 7.2 shows the electrochemical data for an NMC442/graphite pouch cell containing V211M during the narrow voltage range calorimeter experiments between 4.2 – 4.3 V, 4.3 – 4.4 V, and 4.4 – 4.5 V. For all voltage segments, it is anticipated that the capacity increases with a smaller current, as was discussed in Chapter 2. Figure 7.2 shows that this was the case for all segments except the 10 mA charge, which had an anomalously large capacity. This is an unfortunate result of the experimental protocol. For example, for the 4.2 – 4.3 V range, the 10 mA charge segment is a continuation of a charge segment started from 4.1 V, while for all other currents the charge segment immediately follows a discharge to 4.2 V. As a consequence, the irreversible capacity for the 10 mA cycle is systematically larger than those obtained for the lower rate cycles, leading to errors in the rSOC for the 10 mA data for the charge segment. Therefore, the first correction to be made for the NMC442/graphite cells is the exclusion of the 10 mA charge data. This does not impact the 10 mA discharge data.

Figure 7.3 shows the voltage as a function of the relative state of charge for the NMC442/graphite pouch cell for the 5, 2, and 1 mA cycles. If the cells had no inherent hysteresis, the separation between the charge and discharge voltage curves would tend to zero as the limit of zero current is approached. Figure 7.3 shows the separation between

the voltage curves, equal to twice the overpotential, does in fact decrease with decreasing current, but is clearly not tending to zero.

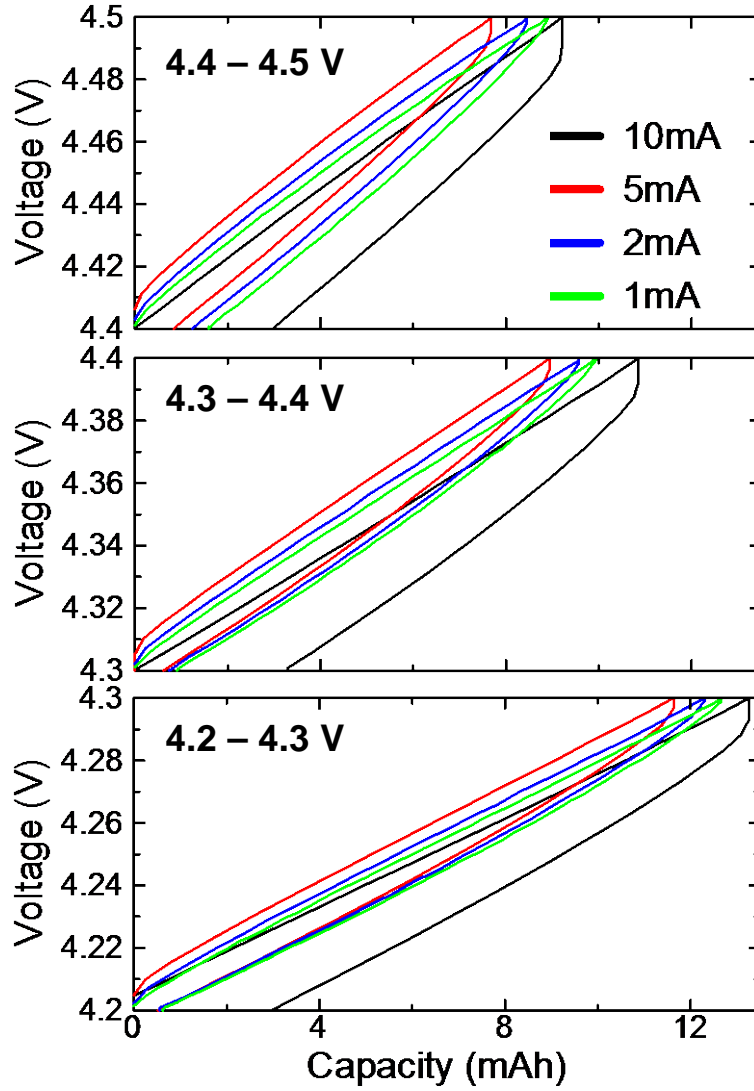


Figure 7.2: Voltage versus capacity for charge and discharge cycles at 10 mA (black), 5 mA (red), 2 mA (blue), and 1 mA (green) for an NMC442/graphite pouch cell containing V211M. Data are shown for three voltage ranges: 4.2 – 4.3 V (bottom), 4.3 – 4.4 V (middle), and 4.4 – 4.5 V (top), where capacity was set to zero at the start of every charge cycle.

As discussed in Chapter 2, the overpotential is given by:

$$\eta = IR_{internal} + V_{hysteresis} \quad (7.2.1)$$

Therefore, in order to determine the relative impact of hysteresis, the measured overpotential can be plotted as a function of current such that $V_{hysteresis}$ is the y-intercept of such a graph.

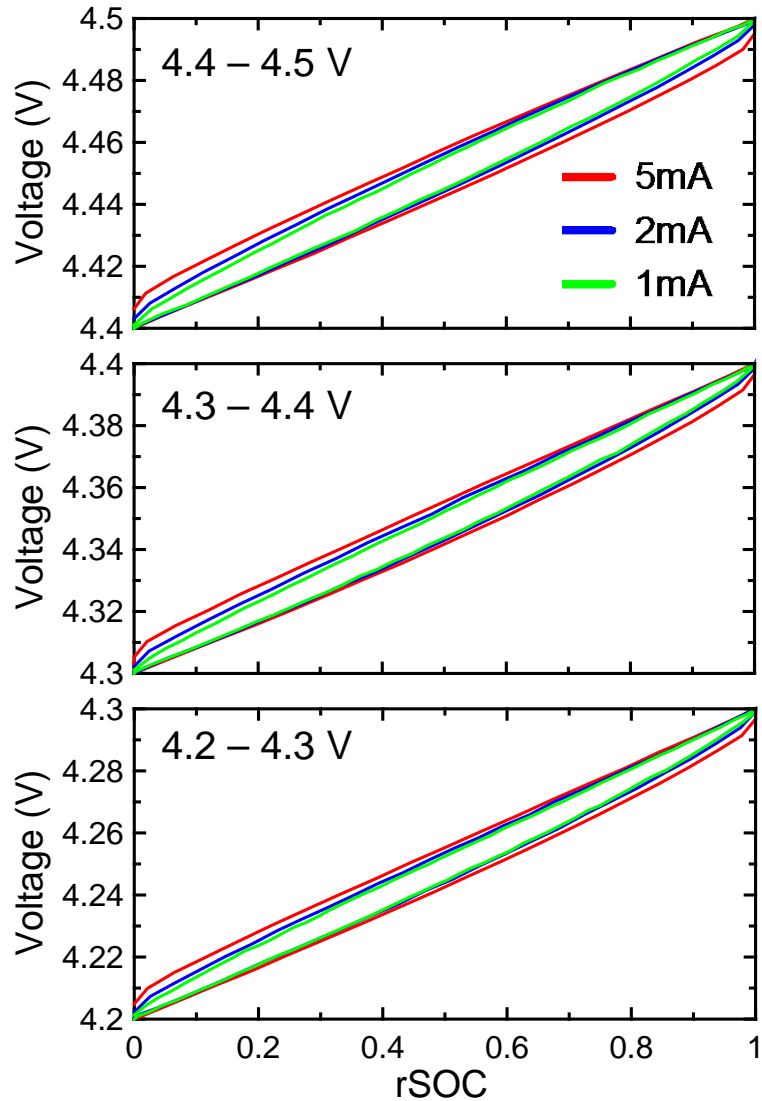


Figure 7.3: Voltage as a function of rSOC for charge and discharge cycles at 5 mA (red), 2 mA (blue), and 1 mA (green) for an NMC442/graphite cell containing V211M.

Figure 7.4 shows the overpotential as a function of current for each of the three narrow voltage ranges examined for the NMC442/graphite pouch cell. The overpotential was calculated as half of the voltage difference between charge and discharge averaged

over the rSOC range of 0.45 to 0.55 in 0.025 increments, giving an approximate overpotential at 0.5 rSOC. A linear function of the form given by Equation 7.2.1 was fit to the data and the extracted parameters are given in Table 7.1.

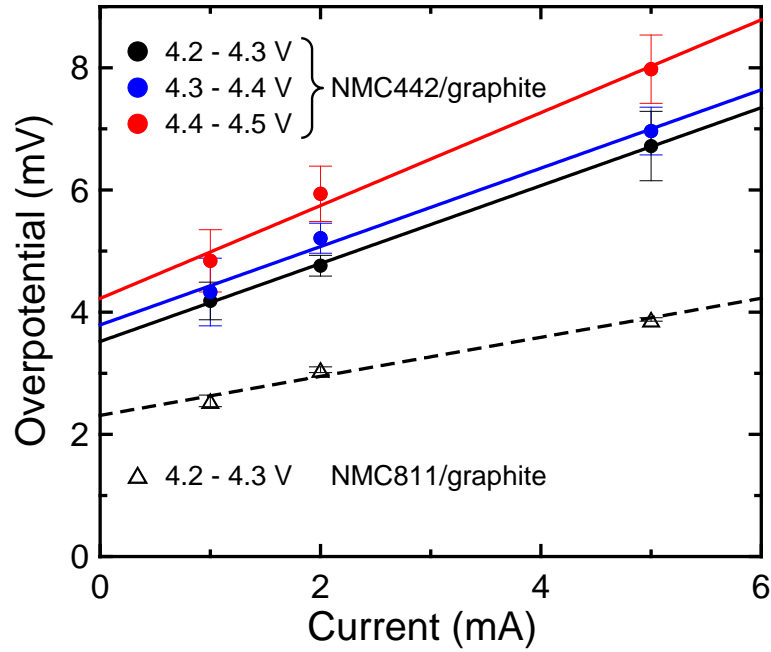


Figure 7.4: Overpotential as a function of current for NMC442/graphite (solid circles) and NMC811/graphite (open triangles) pouch cells containing V211M calculated at approximately 0.5 rSOC in each voltage range. Results of linear fits are given by lines.

Table 7.1: Summary of extracted $R_{internal}$ and $V_{hysteresis}$ values and R^2 of linear fit.

	NMC442/graphite			NMC811/graphite
	4.2 - 4.3 V	4.3 - 4.4 V	4.4 - 4.5 V	4.2 - 4.3 V
Slope ($R_{internal}$) (Ω)	0.638	0.641	0.760	0.320
Intercept ($V_{hysteresis}$) (mV)	3.52	3.79	4.22	2.31
R^2	0.999	0.992	0.988	0.979

Figure 7.4 and Table 7.1 show that NMC442/graphite cells have inherent hysteresis, such that the assumption that $V_{hysteresis}$ is negligible would be an oversimplification for these cells. These data also show that both the hysteresis and the internal cell resistance increase with cell voltage. The heat flow associated with the hysteresis is proportional to $|I|$, and therefore the exclusion of this term in the heat flow model results in errors in both polarization ($\propto I^2$) and entropic ($\propto I$) components, as shown in Figure 7.1.

Figure 7.4 shows a comparison to the measured overpotential and extracted hysteresis voltage of an NMC811/graphite pouch cell containing V211M electrolyte. For the same voltage range, both the hysteresis and internal cell resistance for the NMC811/graphite cell were significantly smaller than for the NMC442/graphite cell. However, the assumption that $V_{hysteresis}$ is negligible does not hold here either, and this would also produce errors in the polarization and entropic heat flow terms. This was less noticeable than for the NMC442/graphite cells. Figure 7.4 shows that if the fit was forced through (0,0) for NMC811/graphite, as would be the case for $V_{hysteresis} = 0$, this would produce a smaller error than if the same was done for the NMC442/graphite cell. Furthermore, the magnitude of the entropic heat flow component for the NMC811/graphite cell was much larger, such that a small discontinuity between voltage segments is difficult to observe in Figure 6.22. Therefore it is likely that the extraction of the current dependent heat flow terms for the NMC811/graphite cells could be improved, but the analysis presented in Chapter 6 provides a good approximation, and the extracted parasitic heat flow would be essentially unchanged, as will be demonstrated here.

The impact of hysteresis on the measured heat flow for NMC442/graphite cells can be examined using the average of the heat flows observed during charge and

discharge. At a given state of charge, the average heat flow is due to the overpotential and parasitic reactions. Figure 7.5 shows an example of the determination of the average heat flow and its evolution with current.

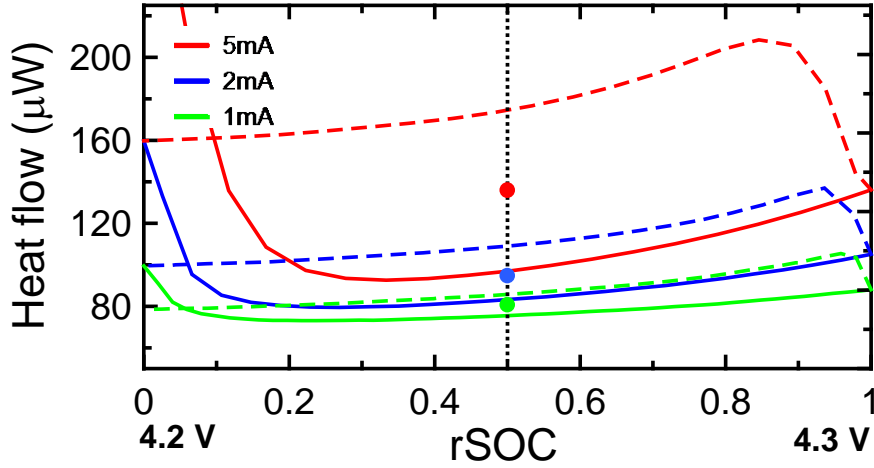


Figure 7.5: Measured heat flow during charge (solid lines) and discharge (dashed lines) at 5 mA (red), 2 mA (blue), and 1 mA (green) between 4.2 – 4.3 V for an NMC442/graphite pouch cell containing V211M. Average heat flows (symbols) at 0.5 rSOC (black dashed line) are also indicated.

Figure 7.6 shows the average heat flow plotted as a function of current at rSOC = 0.5 for the three voltage segments examined. A predominately linear dependence is observed, which again shows that voltage hysteresis plays a significant role in the measured overpotential and corresponding heat flow. Therefore, especially for NMC442/graphite cells which have a measureable inherent hysteresis, the heat flow due to the overpotential is a result of internal cell resistance (called polarization to remain consistent with previous Chapters) and hysteresis, that is:

$$\left(\frac{dq}{dt}\right)_{\text{overpotential}} = \left(\frac{dq}{dt}\right)_{\text{polarization}} + \left(\frac{dq}{dt}\right)_{\text{hysteresis}} \quad (7.2.2)$$

$$|I\eta| = I^2 R_{\text{internal}} + |I|V_{\text{hysteresis}} \quad (7.2.3)$$

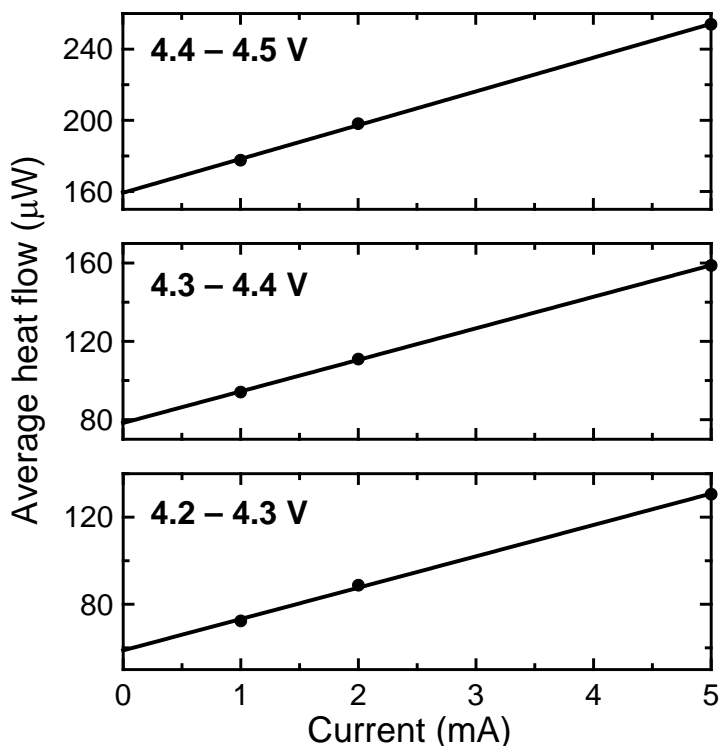


Figure 7.6: Average heat flow as a function of current (symbols) for an NMC442/graphite pouch cell containing V211M for three voltage ranges: 4.2 – 4.3 V (bottom), 4.3 – 4.4 V (middle), and 4.4 – 4.5 V (top). Linear fits through the data are given by solid lines.

7.2.2 Hysteresis in Electrode Materials

Both active electrode materials can exhibit inherent hysteresis. The hysteresis observed in several carbon-based electrodes has been shown to be linked to the ratio of hydrogen to carbon in the active material.^{175,251,252} Instead of intercalating into the graphite structure, lithium can bind at the hydrogen-terminated edges, resulting in a structural change of the host due to the transition from sp^2 -bonded carbon to sp^3 .

Hysteresis in positive electrode materials has not been widely studied, with exception of the Li- and Mn-rich NMC materials which show highly path-dependent intercalation and deintercalation processes.²⁵³ Recently, Dreyer *et al.*¹⁷⁴ showed that in

addition to mechanical stress effects, hysteresis observed in two-phase materials such as LiFePO_4 is thermodynamic in origin and a result of one-by-one, or “domino-cascade”²⁵⁴ charging and discharging processes of interconnected individual particles. This has also been suggested to account for the hysteresis observed in the plateau region in graphite.²⁵⁵

An estimate of the impact of each electrode on the total measured hysteresis in the cells used throughout this thesis can be determined through half cell measurements. Figure 7.7 shows the measured voltage as a function of the relative state of discharge (rSOD) for a graphite/Li half cell coin cell collected by Chris Burns, where an rSOD = 1 represents the fully lithiated (discharged) state of graphite. The data shown correspond to the 2+1 plateau region of the graphite voltage curve¹⁹⁴, where the top of charge occurs in full cells. The graphite electrode was provided by Medtronic (Medtronic plc, Fridley, MN) and contained roughly 95% active material. The cell was cycled between 1.2 V – 1 mV at 2 μA (C/2000), then between 1.2 V – 5 mV at 4 μA (C/1000) and 40 μA (C/100).

In the same manner as described previously, the overpotential can be plotted as a function of current to extract the hysteresis voltage. Figure 7.8 shows such data for rSOD values of 0.70, 0.74, 0.78, and 0.82. Throughout the plateau region, the overpotential decreases as a function of rSOD. In a full cell, if graphite was the sole source of hysteresis, this would translate to a decrease in overpotential as a function of rSOC. However, Figure 7.4 shows an increase in overpotential as a function of rSOC, and therefore hysteresis in the positive electrode material should be explored.

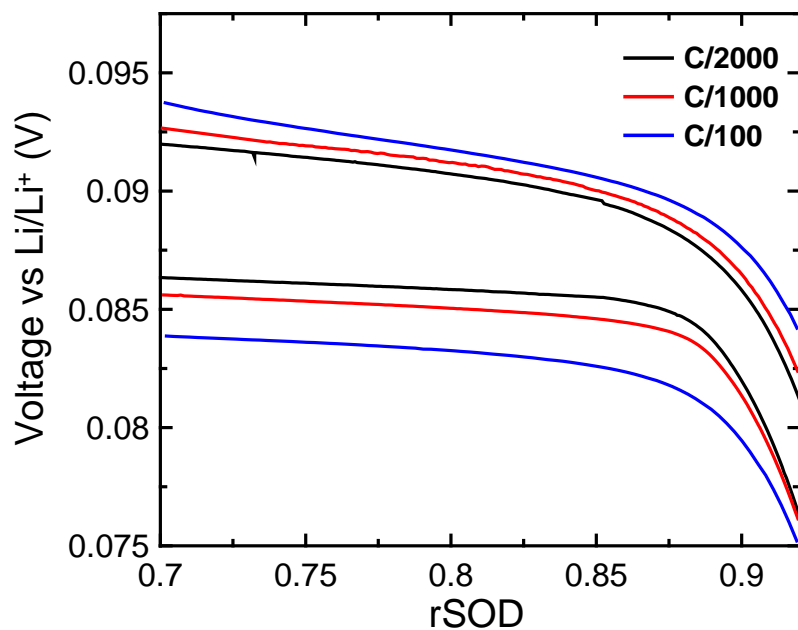


Figure 7.7: Voltage as a function of rSOD for a graphite/Li half cell at three currents: C/2000 (black), C/1000 (red), and C/100 (blue). Data collected and provided by Chris Burns.

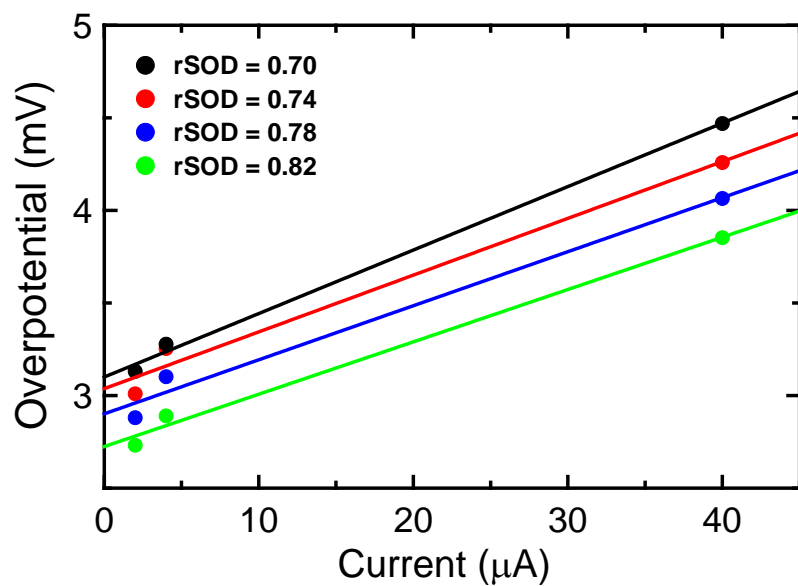


Figure 7.8: Overpotential as a function of current for a graphite/Li half cell (symbols) at approximate rSOD values of 0.70 (black), 0.74 (red), 0.78 (blue), and 0.82 (green). Results of linear fits are given by lines.

Figure 7.9 shows the measured voltage as a function of rSOC for NMC442/Li, NMC111/Li, NMC811/Li, and HV-LCO/Li half cell coin cells that were cycled from 3.9 – 4.3 V vs Li/Li⁺ at C/20, C/30, C/40, C/50, and C/100. The positive electrodes for the coin cells were punched from the single-sided areas of the corresponding electrodes extracted from pouch cells. To determine the effect of the positive electrode on the hysteresis voltage, the overpotential at rSOC = 0.5 (~ 4.1 V for NMC cells and ~ 4.0 V for LCO cell) for each current was calculated by taking half of the voltage difference between charge and discharge. Figure 7.10 shows the overpotential as a function of rSOC for the positive half cells examined, and Table 7.2 gives the extracted parameters from a linear fit to the data.

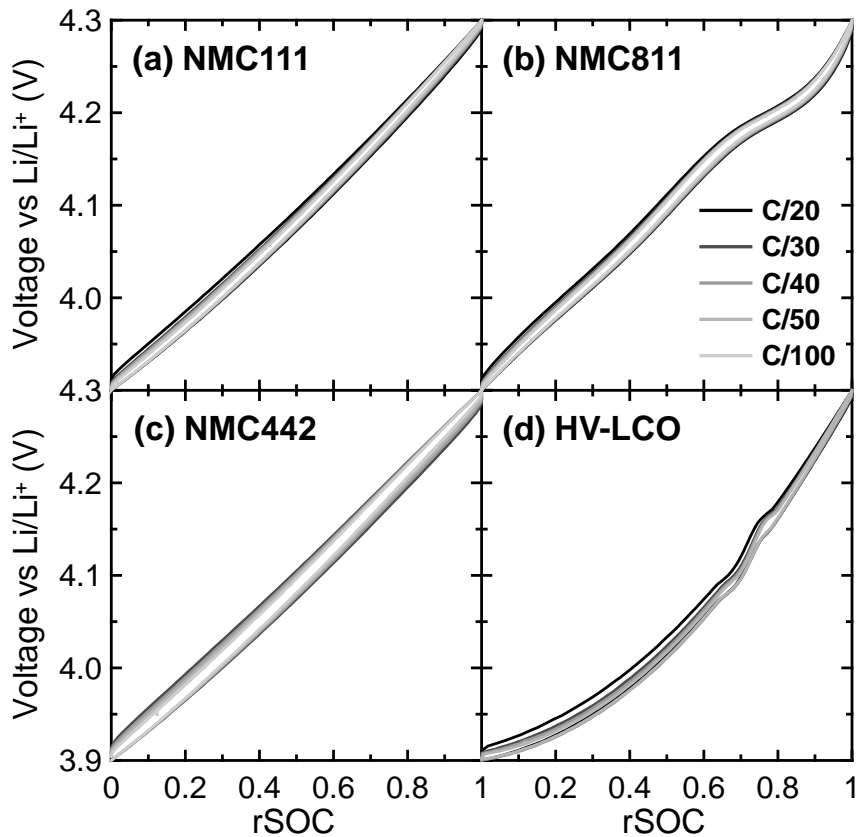


Figure 7.9: Voltage as a function of rSOC for (a) NMC111/Li, (b) NMC811/Li, (c) NMC442/Li, and (d) HV-LCO/Li half cells at five rates: C/20, C/30, C/40, C/50, and C/100, as indicated in the legend.

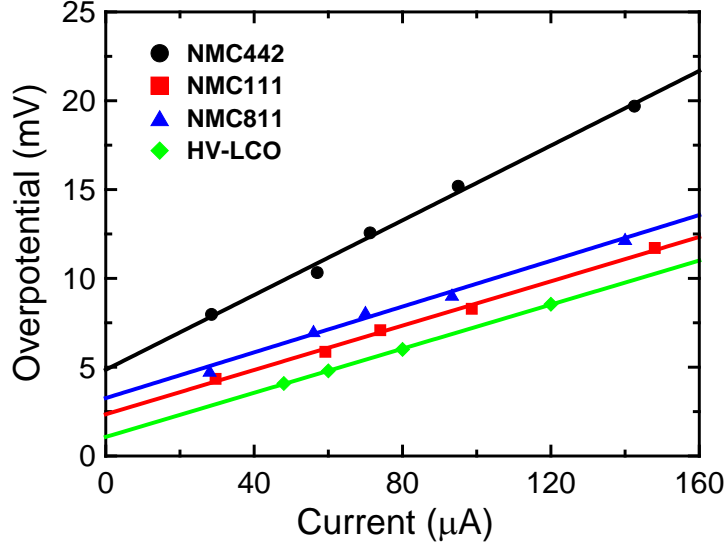


Figure 7.10: Overpotential as a function of current for NMC442/Li (black), NMC111/Li (red), NMC811 (blue), and HV-LCO/Li (green) half cells at 0.5 rSOC (4.1 V for NMC cells and 4.0 V for HV-LCO cell). Results of linear fits are given by solid lines.

Table 7.2: Summary of extracted $R_{internal}$ and $V_{hysteresis}$ values and R^2 of linear fit for positive electrode half cells.

	NMC442	NMC111	NMC811	HV-LCO
Slope ($R_{internal}$) (Ω)	105(4)	62(2)	64(3)	62(1)
Intercept ($V_{hysteresis}$) (mV)	4.9(4)	2.3(1)	3.3(3)	1.08(6)
$V_{average}$ at rSOC = 0.5 (V)	4.089	4.082	4.098	4.014
R^2	0.994	0.996	0.992	0.999

Figure 7.10 and Table 7.2 show that NMC442 has a larger inherent hysteresis than the other NMC materials and HV-LCO. This is in good agreement with the results of the full cells shown in Figure 7.4, suggesting that hysteresis in the positive electrode material

has a larger influence on the full cell hysteresis than does the hysteresis of the negative electrode.

7.2.3 The Time Dependent Empirical Model Including Hysteresis

Building upon the time dependent empirical heat flow model developed in Chapter 6 (Equation 6.2.2), the heat flow due to hysteresis, given by Equation 7.2.3, is incorporated to give:

$$\frac{dq}{dt} = f_{polarization}(z) \cdot I^2 + f_{hysteresis} \cdot |I| + f_{entropy}(z) \cdot I + f_{parasitic}(z) \cdot (1 - L\Delta t) \quad (7.2.4)$$

where, for the example of quadratic functions, the functions are given by:

$$f_{polarization}(z) = A_0 + A_1z + A_2z^2 \quad (7.2.5)$$

$$f_{entropy}(z) = B_0 + B_1z + B_2z^2 \quad (7.2.6)$$

$$f_{parasitic}(z) = C_0 + C_1z + C_2z^2 \quad (7.2.7)$$

$$f_{hysteresis}(z) = D_0 + D_1z + D_2z^2 \quad (7.2.8)$$

where the parameter variables describing each function were selected to maintain consistency with results presented in previous Chapters. As a result, the in-house fitting software was updated to include a heat flow component from hysteresis. Figure 7.11 shows a screenshot of the updated software being used to fit the heat flow for an NMC442/graphite pouch cell containing control electrolyte between 4.2 – 4.3 V, where the rSOC-dependent terms of the hysteresis heat flow component were fixed to 0. The fitting methods used in this version of the software remained unchanged, and was described in Section 6.2.3.

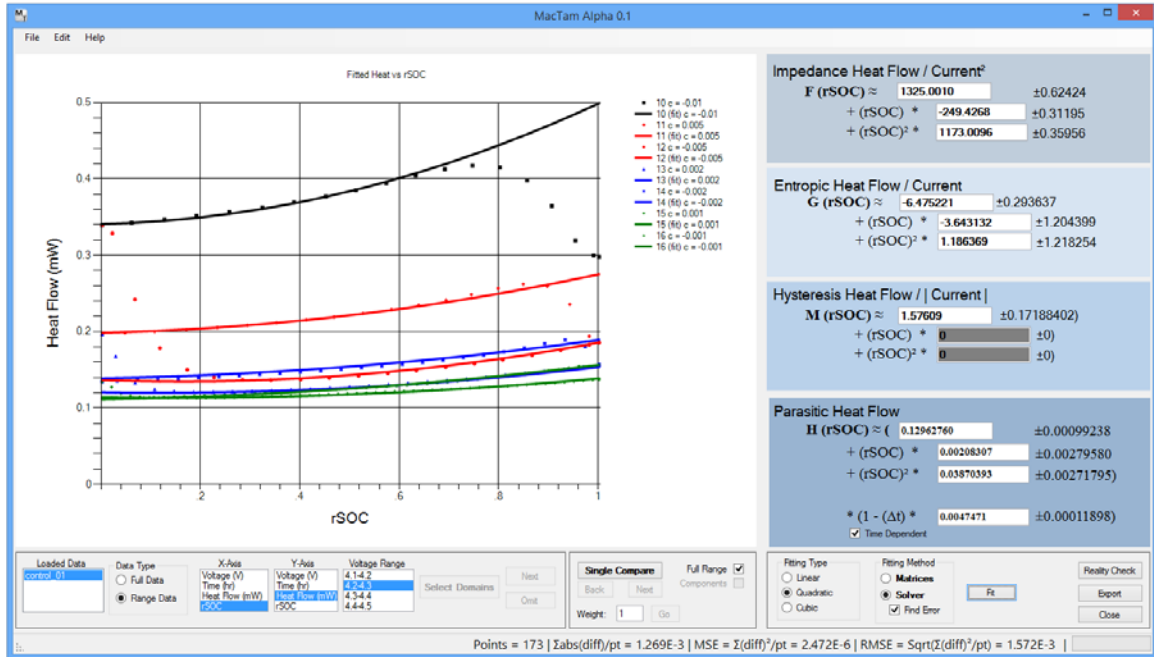


Figure 7.11: Screenshot of modified in-house developed software used to fit heat flow data with the time dependent empirical model including hysteresis.

In order to investigate the impact of the inclusion of the heat flow due to hysteresis, four trial fitting methods were examined:

- (i). Use data from all currents, all heat flow components fit with quadratics
- (ii). Exclude 10 mA charge data, all heat flow components fit with quadratics
- (iii). Exclude 10 mA charge and discharge data, $A_0 = A_1 = A_2 = 0$ (no polarization)
- (iv). Exclude 10 mA charge data, $D_1 = D_2 = 0$ (hysteresis constant with rSOC)

The trial data was for an NMC442/graphite pouch cell containing V211M electrolyte, as described previously and in Chapter 6. Figure 7.12 through Figure 7.15 show the resulting extracted heat flow components as a function of rSOC over three voltage ranges: 4.2 – 4.3 V, 4.3 – 4.4 V, and 4.4 – 4.5 V, for the fitting methods (i) through (iv), respectively. All components are plotted for the 5 mA charge segment for each range.

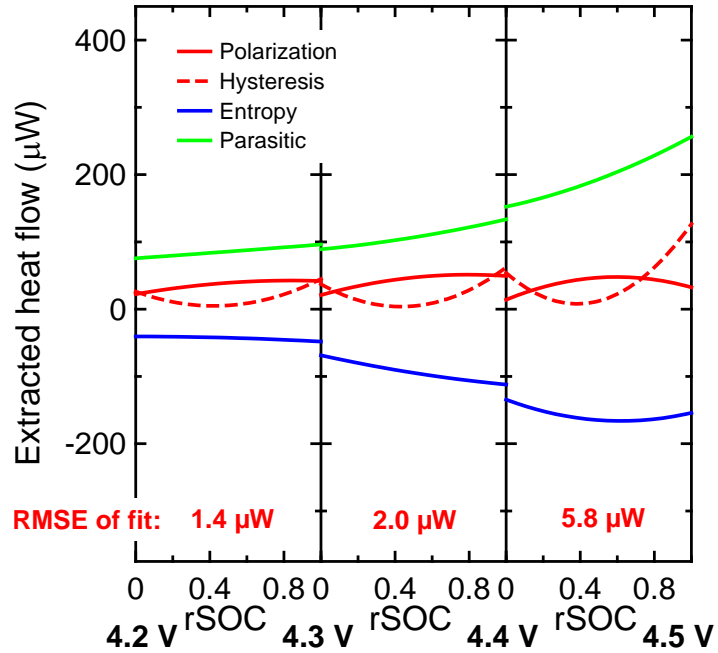


Figure 7.12: Extracted heat flows resulting from fitting method (i) during a 5 mA charge due to polarization (red solid line), hysteresis (red dashed line), changes in entropy (blue), and parasitic reactions (green).

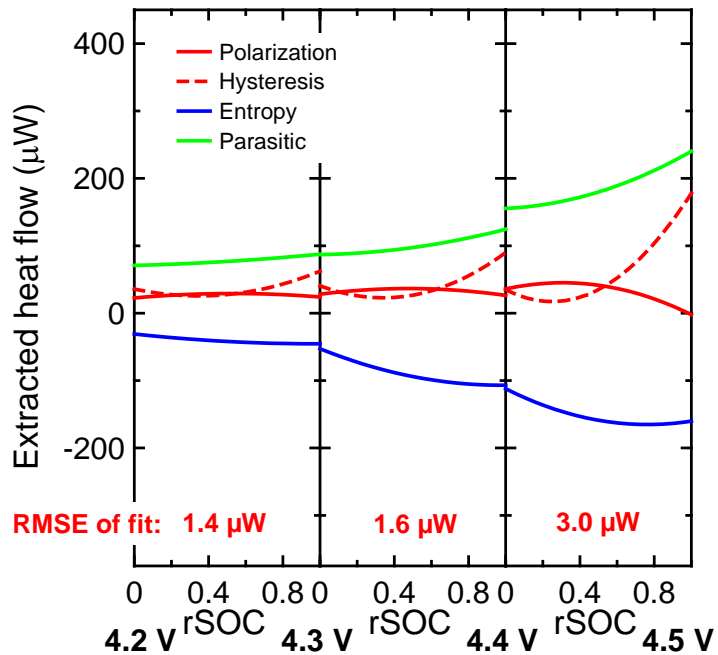


Figure 7.13: Extracted heat flows resulting from fitting method (ii) during a 5 mA charge due to hysteresis (red dashed line), changes in entropy (blue), and parasitic reactions (green).

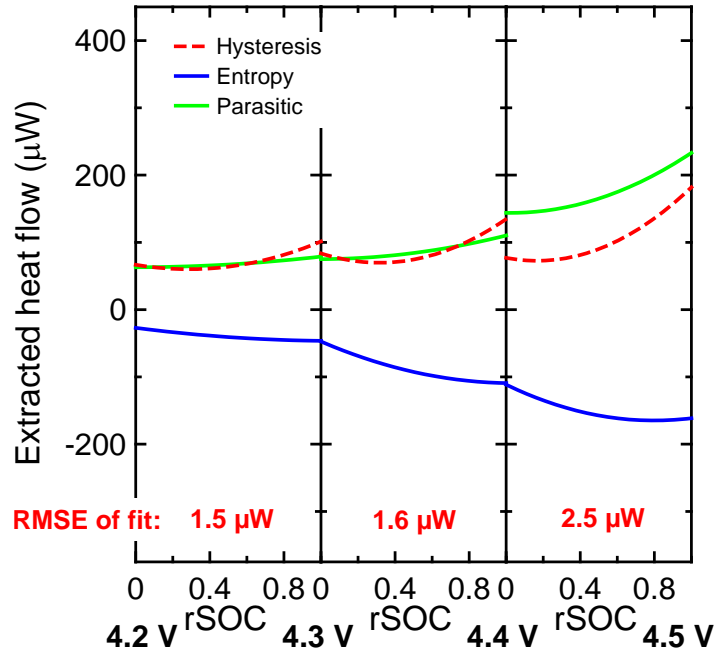


Figure 7.14: Extracted heat flows resulting from fitting method (iii) during a 5 mA charge due to polarization (red solid line), hysteresis (red dashed line), changes in entropy (blue), and parasitic reactions (green).

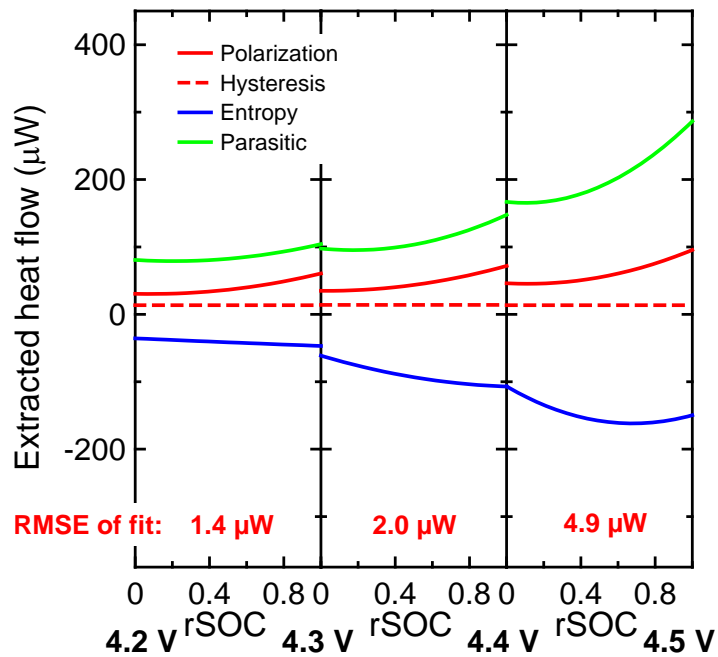


Figure 7.15: Extracted heat flows resulting from fitting method (iv) during a 5 mA charge due to polarization (red solid line), hysteresis (red dashed line), changes in entropy (blue), and parasitic reactions (green).

Trials (i) and (ii) (Figure 7.12 and Figure 7.13), where polarization and hysteresis were modeled using polynomial functions, give unphysical behaviour as a function of state of charge for both of those terms. The mirroring of the hysteresis and polarization heat flows indicate that these terms are poorly constrained and highly correlated when both allowed to vary with rSOC.

Trial (iii) (Figure 7.14) excluded all 10 mA data, and fixed the polarization heat flow component to zero. Good fits to the experimental data were achieved, and the continuity of the entropic component of heat flow was dramatically improved compared to Figure 7.1. From Figure 7.4 and Table 7.1, the hysteresis voltage is on the order of 4 mV, which at 5 mA would result in a heat flow of 20 μ W. However, the extracted hysteresis heat flow from fitting method (iii) ranges from 50 to 200 μ W. Therefore, both the polarization and hysteresis terms need to be included, which requires the use of the 10 mA discharge data and constraints to be placed at least one of the two terms.

Trial (iv) (Figure 7.15) included both polarization and hysteresis components, while constraining the hysteresis heat flow to a constant value for each voltage range (all rSOC-dependent parameters fixed to zero). Figure 7.4 and Table 7.1 show that the hysteresis voltage does not change appreciably as a function of voltage, while frequency response analysis experiments²³⁰ have shown that the charge transfer resistance can change dramatically as a function of voltage. Therefore the hysteresis component was chosen to be the constrained term. Figure 7.15 shows that fitting method (iv) improved the continuity of the entropic heat flow term across voltage range segments, and extracted a physically consistent value of heat flow due to hysteresis. In the voltage range of 4.2 – 4.3 V, the extracted hysteresis voltage was 2.7(2) mV ($f_{hysteresis} = V_{hysteresis}$ for $D_1 = D_2 = 0$ in Equation 7.2.8), in good agreement with the extracted results given in Table 7.1. There

are still discontinuities between voltage ranges for the polarization component, and small slope mismatches for the entropic component. This is mainly attributed to increased uncertainty at the rSOC extremes for each voltage range, since half the data were excluded due to the impact of the calorimeter response time.

As an additional verification of fitting method (iv), as previously discussed, the extracted parasitic heat flow is well approximated by the average of the charge and discharge heat flows at 1 mA. Figure 7.16 shows that for all voltage ranges examined, the extracted parasitic heat flow indeed lies virtually at the midpoint between the 1 mA charge and discharge heat flows. Therefore, fitting method (iv) is considered a good description of the heat flow of NMC442/graphite pouch cells, and as a result, is used herein when the heat flow due to hysteresis is included.

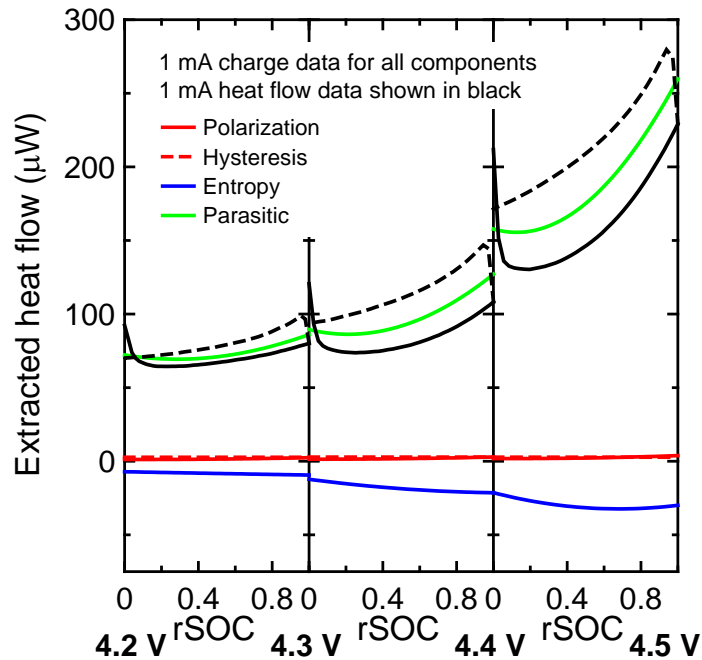


Figure 7.16: Extracted heat flows resulting from fitting method (iv) during a 1 mA charge due to polarization (red solid line), hysteresis (red dashed line), changes in entropy (blue), and parasitic reactions (green). The total measured heat flow (black) during charge (solid) and discharge (dashed) are also shown.

Figure 7.17 shows a separation of all extracted heat flow components for NMC442/graphite pouch cells using the time dependent empirical model including hysteresis. In contrast to the results presented in Figure 7.1, the discontinuities in entropic heat flow between voltage segments have been reduced, while maintaining good agreement between cells. The impact and difference between control and V211M, along with a variety of other additives and solvents are discussed in detail in Chapter 8.

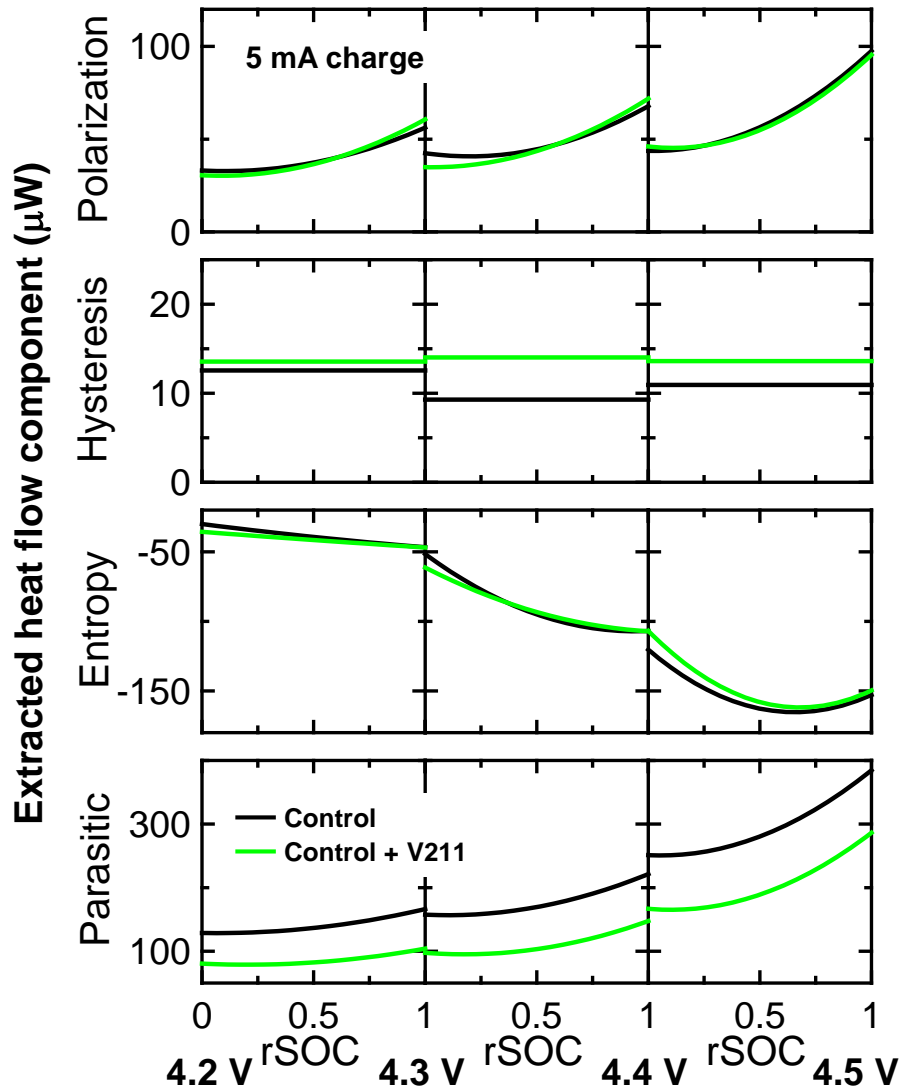


Figure 7.17: The extracted polarization, hysteresis, entropic, and parasitic heat flow components as a function of rSOC for NMC442/graphite pouch cells for the 5 mA charge segment for three sequential voltage ranges: 4.2 – 4.3 V, 4.3 – 4.4 V, 4.4 – 4.5 V. Data are shown for cells containing control (black) and control + V211M (green) electrolyte.

In order to verify that the extracted parasitic heat flow results previously discussed are still valid, Figure 7.18 shows a comparison of the extracted parasitic heat flow from fitting the data to the time dependent and the hysteresis-containing time dependent empirical models. There is a slight variance in curvature as a function of rSOC in each voltage range. However, the difference in extracted parasitic heat flows between the 3- and 4-component models is similar for both control and V211M cells and for all voltage ranges. Therefore, the exclusion of the hysteresis component for the cell chemistries analyzed in previous Chapters does not have a significant impact of the extracted parasitic heat flow, and the conclusions remain valid.

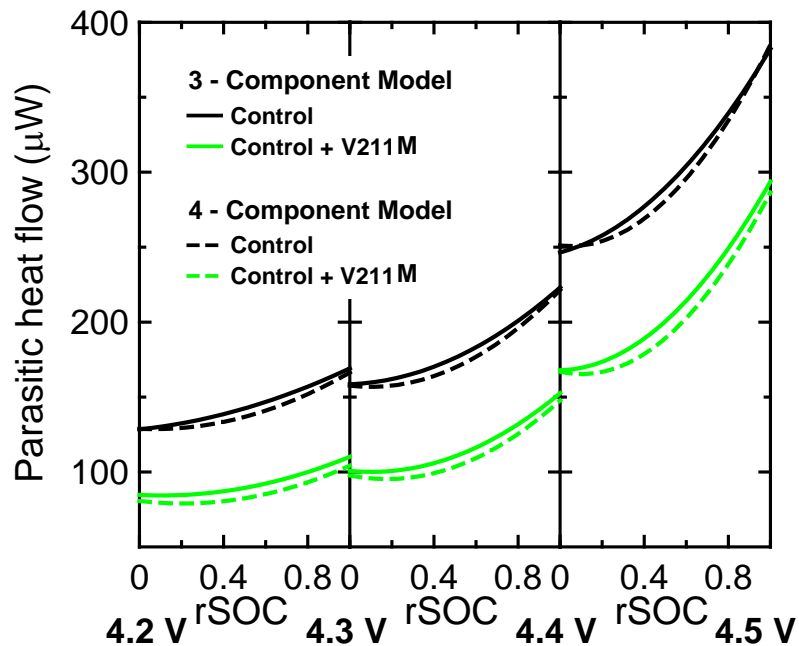


Figure 7.18: Comparison of the extracted parasitic heat flow determined using the three-component time dependent empirical model (solid lines) and the four-component model that includes hysteresis (dashed lines). Data are shown for NMC442/graphite cells containing control (black) and V211M (green) electrolyte for the 5 mA charge segments.

7.3 IMPACT OF DIFFERENCES IN DATA COLLECTION METHODOLOGIES

7.3.1 Increasing versus Decreasing Current

In all of the previous narrow voltage range experiments, the current was decreased for each successive cycle, starting from 10 mA and ending at 1 mA. There was no fundamental reason for this decision, and as such, there should be no difference in the extracted heat flow components if the order of current steps was reversed.

In order to test this hypothesis, two NMC811/graphite pouch cells containing P211M electrolyte were constructed, formed, and proceeded through the full experimental protocol described in Section 6.4.2. Following that experiment, both cells were discharged at 10 mA to 4.1 V. One cell was cycled between 4.1 – 4.2 V at 5 mA, 3 mA, 2 mA, then 1 mA (decreasing current), while the other was cycled in the same voltage range at 1 mA, 2 mA, 3 mA, then 5 mA (increasing current). Two cells were used instead of a single cell cycled with both increasing and decreasing currents. This was done so that comparisons could be made over the same time window since formation. The small error due to cell-to-cell variation was deemed an acceptable compromise.

Figure 7.19 shows the measured heat flow for the two NMC811/graphite cells, as well as the total calculated heat flow resulting from a fit to the time dependent empirical model. All parameters were quadratic in rSOC and hysteresis was not included. Fitting was performed using the in-house software discussed in Chapter 6. The data were collected between 690 – 760 h after being loaded in the calorimeter. There was a remarkable similarity in the measured heat flow for all currents, and the agreement between the measured and calculated heat flows was good for both cells. The extracted parameters describing the parasitic heat flow for both cells are given in Table 7.3.

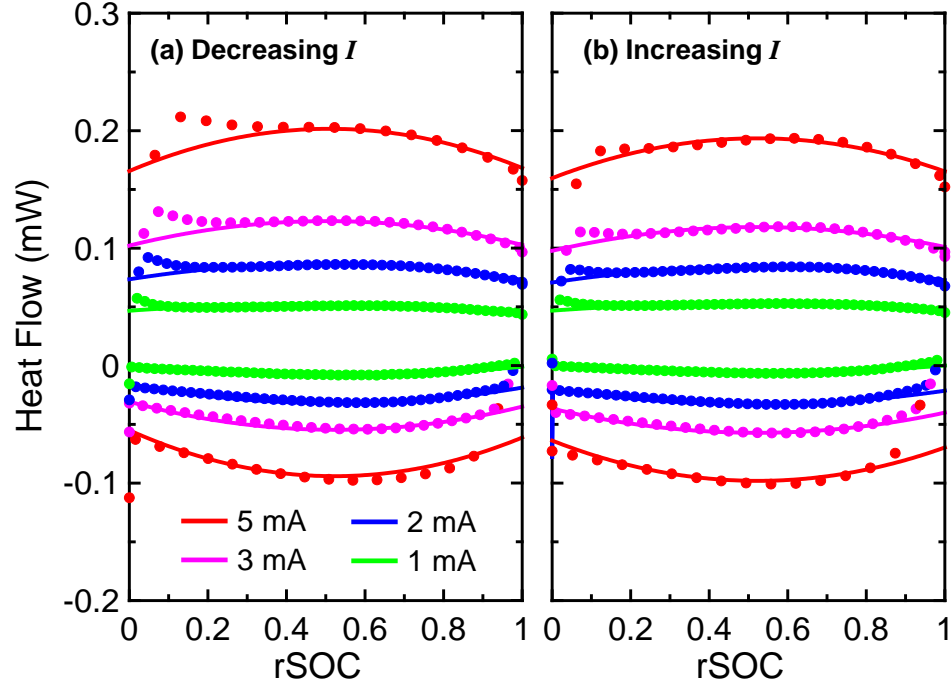


Figure 7.19: Measured (symbols) and calculated (lines) heat flow for NMC811/graphite pouch cells containing P211M cycled between 4.1 – 4.2 V with (a) decreasing currents and (b) increasing currents.

Table 7.3: Comparison of extracted parasitic heat flow parameters for NMC811/graphite cells containing P211M between 4.1 – 4.2 V for decreasing and increasing currents. RMSE of fits are also given.

NMC811/graphite with P211M		
4.1 - 4.2 V		
	Decreasing I	Increasing I
C_0 (μW)	24.9(1)	25.0(1)
C_1 (μW)	-5.0(6)	-5.4(7)
C_2 (μW)	3.76(9)	3.51(9)
L (h^{-1})	0.00230(5)	0.00228(5)
RMSE (μW)	1.8	2.5

With exception of C_2 , the extracted parasitic heat flow parameters for both data collection methods were within error of each other, and the values of C_2 were still very similar and fell well within the cell-to-cell variation. This confirms that the order in which data are collected for the narrow voltage range variable current experiments has no discernable impact on the extracted heat flow.

7.3.2 Impact of Current Choice

In order to verify that the developed method of using four currents is sufficient, the impact of the selection of the magnitude and number of currents used in the narrow voltage range experiments on the resulting quality of fit was investigated. Two NMC442/graphite pouch cells containing P211M were used, where one was the same cell described in Chapter 6, while the other cell was made at a later date according to the same procedure. The only difference between the cells was the currents used in the narrow range experiments. As previously described, the first cell proceeded through the narrow voltage ranges with currents of 10 mA, 5 mA, 2 mA, then 1 mA, and is referred to as the 4- I (four current) cell. The second cell was cycled using currents of 7 mA, 5 mA, 4 mA, 3 mA, 2 mA, then 1 mA and is referred to as the 6- I (six current) cell.

According to the discussion in Section 7.2, the experimental heat flow data were fit to the time dependent empirical heat flow model including a constant hysteresis term. The charge segment of the first current used was omitted from all fits. Figure 7.20 shows a representative fit for the 4.2 – 4.3 V voltage segment for both the 4- I and 6- I cells. Due to the increased number of current steps and the lower currents used, the data for the two voltage segments were collected at different times after formation and the 6- I data took a

longer time to collect. As a result, the measured heat flow for the 6-*I* cell was expected to be lower than for the 4-*I* cell. Examining the difference between Figure 7.20a and Figure 7.20b shows that the 6-*I* cell indeed had a lower heat flow for common currents. Figure 7.20 also shows that the fits of the 4-*I* and 6-*I* data to the empirical model were both very good for the 4.2 – 4.3 V segment, with RMSE values of 1.5 μ W and 1.3 μ W, respectively.

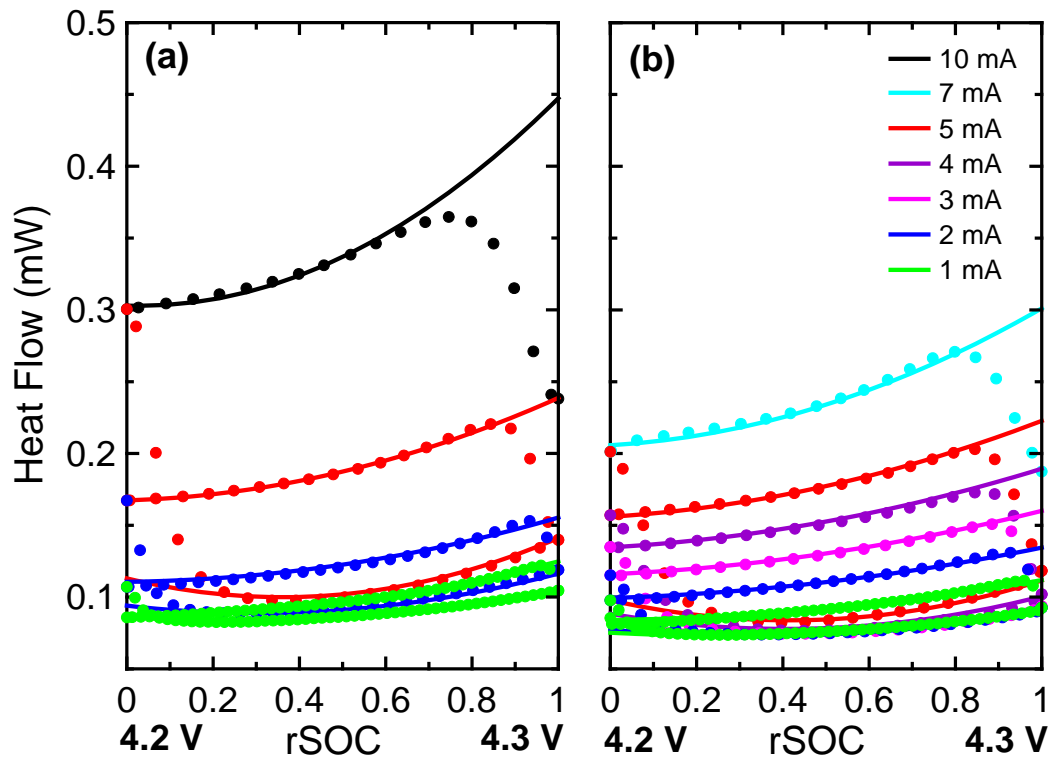


Figure 7.20: Measured (symbols) and calculated (lines) heat flow for NMC442/graphite pouch cells containing P211M cycled between 4.2 – 4.3 V using (a) four currents and (b) six currents, as indicated in the legend.

Table 7.4 provides a summary of all extracted parameters resulting from fitting all voltage ranges examined, allowing a comparison between the 4-*I* and 6-*I* cells, where the parameters are defined in Equations 7.2.5 through 7.2.8. The RMSE of the fit as well as the start and end times of the data collection for each voltage range are also given. The

extracted parameters related to polarization, changes in entropy, and hysteresis are all very similar between the 4-*I* and 6-*I* cells, as would be expected for nominally identical cells.

Table 7.4: Summary and comparison of extracted parameters of all heat flow components of NMC442/graphite pouch cells for three voltage ranges: 4.2 – 4.3 V, 4.3 – 4.4 V, 4.4 – 4.5 V for four- and six-current measurements. RMSE and time at the start and end of the data collection are also given.

	4.2 - 4.3 V		4.3 - 4.4 V		4.4 - 4.5 V	
	4- <i>I</i>	6- <i>I</i>	4- <i>I</i>	6- <i>I</i>	4- <i>I</i>	6- <i>I</i>
A_0 ($\mu\text{W}/\text{mA}^2$)	1.22(4)	1.36(3)	1.35(4)	1.37(4)	1.70(6)	1.85(6)
A_I ($\mu\text{W}/\text{mA}^2$)	-0.76(4)	-0.76(4)	-0.59(3)	-0.56(5)	-1.18(9)	-1.12(8)
A_2 ($\mu\text{W}/\text{mA}^2$)	1.46(8)	1.51(9)	1.84(8)	1.88(8)	2.8(1)	2.8(1)
B_0 ($\mu\text{W}/\text{mA}$)	-5.66(6)	-5.87(6)	-10.88(9)	-11.4(1)	-21.3(1)	-20.8(3)
B_I ($\mu\text{W}/\text{mA}$)	-7.95(5)	-8.6(3)	-19.7(2)	-20.5(5)	-34.7(4)	-39(1)
B_2 ($\mu\text{W}/\text{mA}$)	3.85(5)	3.3(3)	8.0(2)	7.2(5)	25.7(4)	27(1)
C_0 (μW)	98.7(2)	81.4(3)	128.0(4)	111.6(4)	216.7(6)	216.1(5)
C_I (μW)	-13.3(8)	-5.6(5)	-24(1)	-13.1(8)	-15(2)	-8(1)
C_2 (μW)	46.4(7)	27.4(4)	87(1)	56.0(7)	153(3)	117(1)
D_0 ($\mu\text{W}/\text{mA}$)	2.66(6)	2.41(5)	2.90(9)	2.85(8)	2.45(8)	2.9(2)
L ($\times 10^{-3} \text{ h}^{-1}$)	4.83(3)	1.42(4)	4.73(6)	0.39(8)	5.36(8)	2.77(4)
RMSE (μW)	1.5	1.3	2.2	1.8	4.2	3.4
t_{start} (h)†	306	324	353	386	389	433
t_{end} (h)†	350	382	387	430	418	479

† Times measured with respect to the time of insertion into the calorimeter

The parameters describing the parasitic heat flow of the 6-*I* cell are smaller than for the 4-*I* cell, but as previously mentioned, this is thought to be a result of the differences in time since formation and the time taken to collect the data for that voltage range. There is also a large difference in the time factor, L , between the two cells. This

may be a result of the longer experiment times for the 6-*I* cell, where it is possible that the assumption of a linearly decreasing parasitic heat flow no longer holds. This may also be a result of slightly different histories relating to cell preparation. The 4-*I* cells were degassed within 2 h of reaching 3.8 V, while the 6-*I* cells were at 3.8 V for nearly 12 h before being degassed. The second degas for both the 4-*I* and 6-*I* cells was done approximately 8 h after being charged to 4.5 V, however the 4-*I* cells were left overnight before being loaded into the calorimeter while the 6-*I* cells were loaded immediately after the second degas. The above differences in cell preparation could result in differences in SEI layer stabilities, which would result in different time factors.

Table 7.4 also shows that the RMSE of the 6-*I* cell are consistently lower than for the 4-*I* cell for all voltage ranges examined. This suggests that the inclusion of more currents into the narrow voltage range experiments improves the quality of fit. However, the fit improvement comes at a cost of an increased experiment time, which can also result in a deviation from the linear time dependence approximation that was introduced in Chapter 6. Therefore, an alternative interpretation of the results presented in Table 7.4 is that the four current approach used throughout this thesis (10, 5, 2, and 1 mA cycles) represents a good balance between sufficient current steps and a minimization of experiment time, without a significant impact on the overall fit quality.

7.3.3 Impact of Variable Current Experiments over Wider Voltage Ranges

The time dependent empirical model which includes hysteresis was shown to be a good description of NMC442/graphite cells; however, there were still some small discontinuities observed between voltage segments, as shown in Figure 7.17. These are

thought to arise mainly due to the exclusion of data at both rSOC extremes in the narrow voltage ranges due to the response time of the calorimeter. Therefore, it is useful to examine the impact of collecting data over a wider voltage range where only the pertinent voltage range is fit.

Figure 7.21 shows the experimental protocol of two NMC442/graphite cells with P211M-containing electrolyte as previously discussed. Both cells were initially cycled at 10 mA four times between 2.8 – 4.5 V. One cell then proceeded through the narrow voltage range segments of 4.1 – 4.2 V, 4.2 – 4.3 V, 4.3 – 4.4 V, and 4.4 – 4.5 V (referred to as the narrow range cell), while the other cell was cycled between 4.1 – 4.5 V (wide range cell). For both cells, cycling in each voltage range was done at currents of 7 mA, 5 mA, 4 mA, 3 mA, 2 mA, and 1 mA.

As was shown and discussed in Chapter 6, the parasitic heat flow decreases approximately linearly over the time ranges of ~50 h used in the narrow voltage range experiments. However, cycling between 4.1 – 4.5 V for the 6 currents listed above took approximately 280 h. Therefore, the entire cycling protocol (four 10 mA cycles followed by variable current cycling, herein called one iteration) was repeated twice. This was done so that during the second iteration the SEI layers are more stabilized and the assumption of a linearly decreasing parasitic heat flow, even over large time windows, remains valid. The data collected during the first iteration were used in Section 7.3.2, and the data collected during the second iteration were used here, as noted by the large times after insertion in the calorimeter in Figure 7.21.

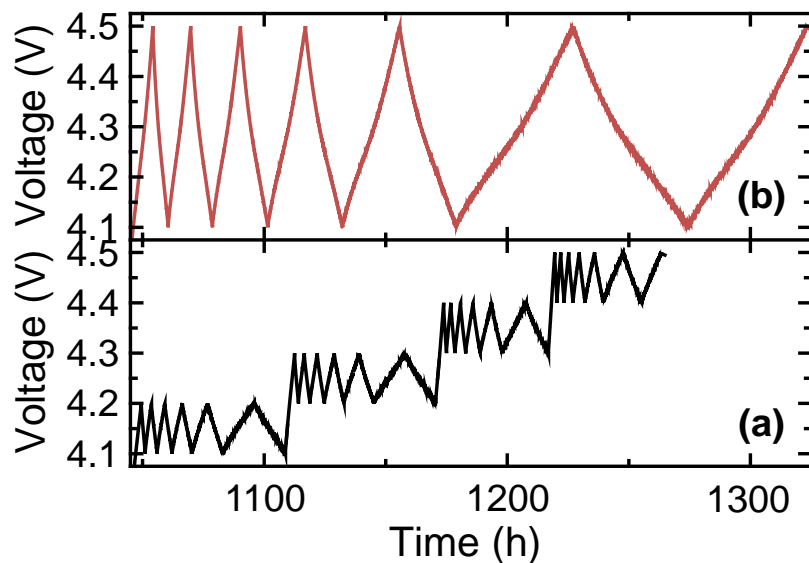


Figure 7.21: Voltage as a function of time since insertion into the calorimeter showing the experimental protocol of cycling cells with variable currents over (a) multiple narrow voltage ranges, and (b) one wide voltage range.

In order to compare the heat flow in the same voltage segments for the two data collection methods, the appropriate rSOC ranges need to be selected for the wide range cell. For the wide range cell, rSOC values of approximately 0, 0.25, 0.6, 0.8, and 1 corresponded to 4.1 V, 4.2 V, 4.3 V, 4.4 V, and 4.5 V, respectively. Therefore, for example to model the heat flow between 4.2 – 4.3 V for the wide range cell, only data from rSOC = 0.25 to 0.6 were included. The measured heat flow was fit using the time dependent empirical model including a constant hysteresis term for both cells (all other parameters were quadratic in rSOC), as previously discussed. Figure 7.22 shows the agreement between the measured and calculated heat flow for the narrow voltage range cell (Figure 7.22a) and the wide range cell (Figure 7.22b) in the voltage range of 4.2 – 4.3 V. The agreement was good for both cells over all current segments, with exception of the 5 mA charge of the wide range cell. As a result, the RMSE of the wide range cell (2.3 μW) was slightly larger than the narrow range cell (1.5 μW).

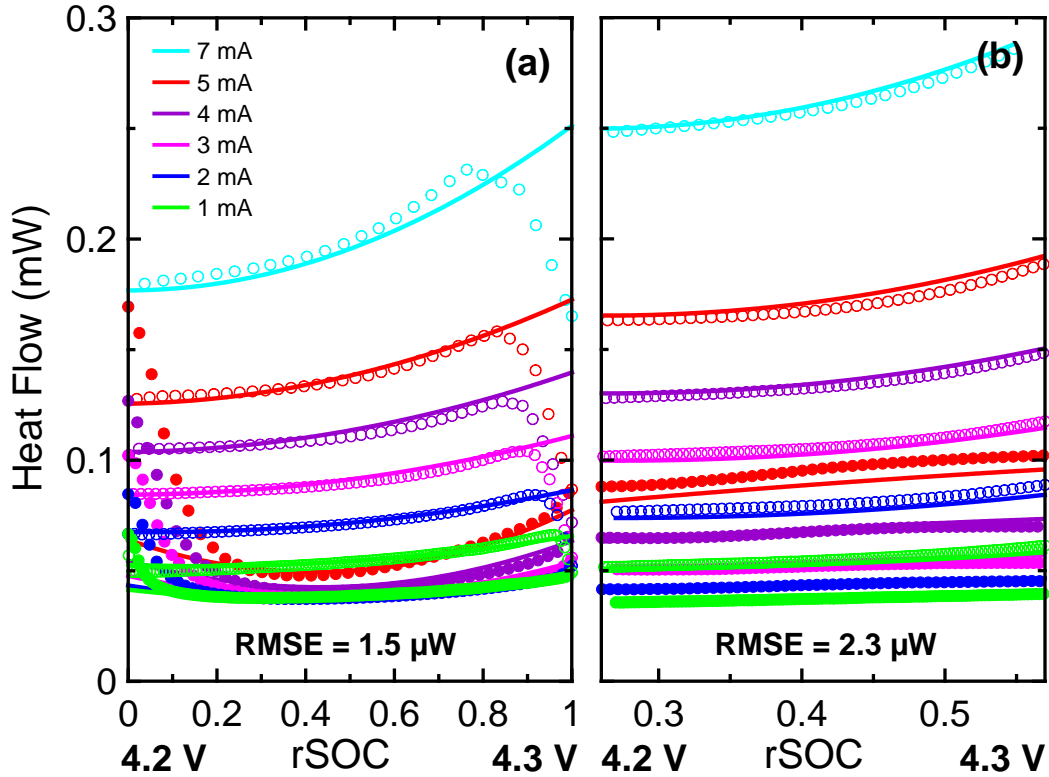


Figure 7.22: Calculated (lines) and measured heat flow during charge (solid symbols) and discharge (open symbols) for NMC442/graphite pouch cells containing P211M between 4.2 – 4.3 V for cells cycled between (a) 4.2 – 4.3 V and (b) 4.1 – 4.5 V at currents indicated in the legend.

In addition to the 4.2 – 4.3 V voltage range, the same fitting procedure was used to analyze the 4.3 – 4.4 V range. Figure 7.23 shows the separation of the total heat flow into its extracted components for 4.2 – 4.3 V and 4.3 – 4.4 V during the 5 mA charge segments for both data collection methods. Pair cell data for the wide voltage range experiment are shown. The extracted heat flow components for the wide range cells are much more smooth and continuous through the two voltage ranges than for the narrow range cell, suggesting that the discontinuities seen in the narrow voltage range experiments are indeed artefacts arising from the calorimeter response.

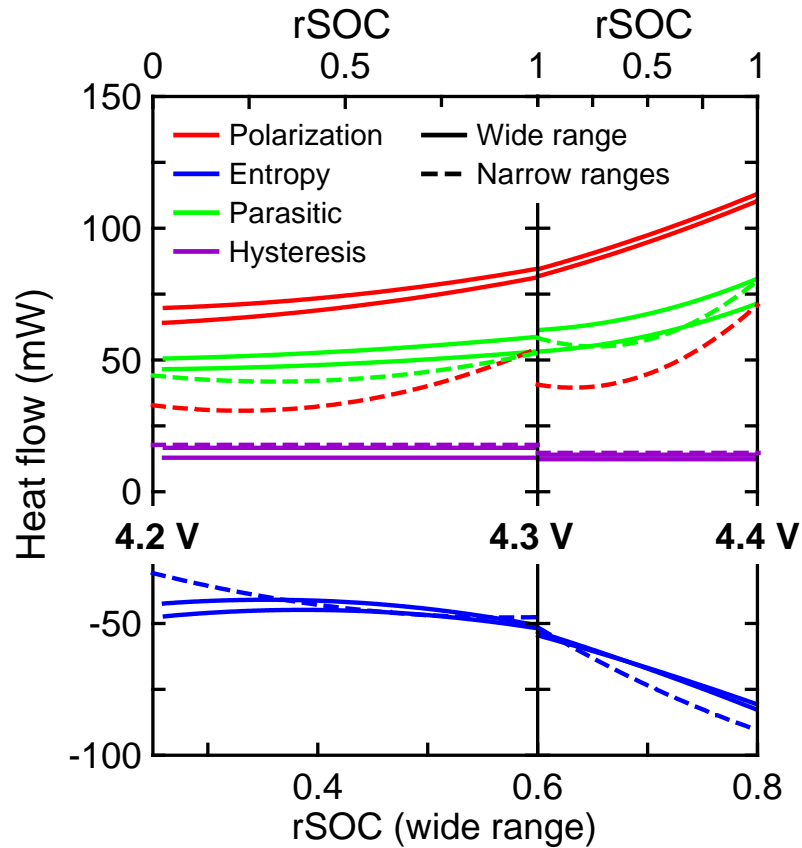


Figure 7.23: Extracted components of total heat flow due to polarization (red), hysteresis (purple), changes in entropy (blue), and parasitic reactions during 5 mA charge segments between 4.2 V and 4.4 V for NMC442/graphite pouch cells cycled over narrow voltage ranges (dashed lines, top axes) and a wide voltage range (solid lines, bottom axis).

Figure 7.23 also shows a very significant difference in the extracted heat flow due to polarization between the narrow and wide range cells. The wide range cells show a dramatically increased heat flow due to polarization and thereby cell resistance. As was observed in Chapter 6 (Figure 6.15), cycling to a high upper cutoff voltage can significantly impact the lower voltage behaviour. It has also been shown using careful EIS experiments of the same NMC442/graphite pouch cells that the charge transfer impedance increases as a function of voltage.^{229,230} Therefore, it is suggested that the repeated exposure to high cell voltages for the wide range cell resulted in an increase in cell resistance at the lower voltages.

The extracted parasitic heat flows for the narrow and wide range cells are similar between 4.3 – 4.4 V, but between 4.2 – 4.3 V the parasitic heat flow is slightly lower for the narrow range cell. This is consistent with the results presented in Chapter 6 where it was observed that high voltage cycling can influence and increase the lower voltage parasitic heat flows.

So while the extracted heat flow components from the wide range experiment were smooth and continuous between fitted voltage segments, the values appear to have been affected by the exposure of the cell to high voltage on every cycle. Such wide range experiments are more representative of typical battery use; however, to carefully explore the dependence of each heat flow component on cell voltage, it is important to minimize any influence from higher voltage behaviour. Therefore, a blend of the two data collection methods described above would provide a good compromise. It is proposed that the narrow range cycling should be extended by approximately 20 mV on both charge and discharge, while the data are only fit for the voltage range of interest. For example, to fit the heat flow between 4.2 – 4.3 V, cycling should be done between 4.18 – 4.32 V.

7.4 CONCLUSIONS

In the previous Chapters, the impact of hysteresis was treated as negligible, and for the cell chemistries examined this appeared to be a reasonable assumption. However, in the first section of this Chapter, it was shown that inherent hysteresis in NMC442/graphite pouch cells was larger than for other chemistries and should not be

neglected. The time dependent empirical heat flow model was modified to include the heat flow due to hysteresis and resulted in a significantly improved quality of fit.

The robustness of the empirical model was further explored by examining different data collection and fitting methodologies. It was found that changing the order of current steps had virtually no impact on the extracted heat flow components, a four-current narrow range cycling protocol was likely sufficient, but some extra data collected on either side of the intended voltage range should improve the smoothness and continuity of the extracted heat flow components. Overall, it was demonstrated that the data collection process and the empirical model developed up to now are sound.

The time dependent empirical model which includes a constant hysteresis term will be used throughout the next two chapters to explore the impact of electrolyte choice in high voltage NMC442/graphite cells.

CHAPTER 8

DETERMINATION OF THE IMPACT OF HIGH VOLTAGE ELECTROLYTE ADDITIVES AND SOLVENTS

8.1 INTRODUCTION AND MOTIVATION

In the previous Chapters, methods of extracting the individual heat flow contributions were developed for several cell chemistries. In this Chapter, the time dependent empirical model that includes hysteresis is used to determine the impact of electrolyte composition on NMC442/graphite cells up to 4.7 V. The operation of cells at such high voltages is challenging mainly due to the oxidative instability of the electrolyte components. Two approaches to reduce the rate of such parasitic reactions are the use of electrolyte additives or non-carbonate solvents as discussed in Chapter 1. The impact of additive and solvent choices on the time dependent parasitic heat flow and therefore the parasitic reaction rate up to 4.7 V are investigated here.

8.2 EXPERIMENTAL DETAILS

Small machine-made NMC442/graphite pouch cells balanced for 4.7 V operation were obtained dry and sealed from LiFUN Technology and were prepared as described in Chapter 3. The electrolyte compositions used in this study and the amounts added to the cells are given in Table 8.1. Once filled with electrolyte, the cells were sealed at 85% of full vacuum with a 6 second sealing time at 165°C. Wetting and formation were done as previously described in Chapter 6.

Table 8.1: Summary of electrolyte compositions examined and amounts added to NMC442/graphite pouch cells.

Shorthand name	Salt	Solvent†	Additives‡	Amount added
control	1 M LiPF ₆	3:7 v:v EC:EMC	none	0.900 g
2%VC	1 M LiPF ₆	3:7 v:v EC:EMC	2% VC	0.900 g
2%PES	1 M LiPF ₆	3:7 v:v EC:EMC	2% PES	0.900 g
2%TAP*	1 M LiPF ₆	3:7 v:v EC:EMC	2% TAP	0.900 g
V211M	1 M LiPF ₆	3:7 v:v EC:EMC	2%VC + 1% TTSPi + 1% MMDS	0.900 g
P211M	1 M LiPF ₆	3:7 v:v EC:EMC	2%PES + 1% TTSPi + 1% MMDS	0.900 g
FEC:TFEC	1 M LiPF ₆	3:7 w:w FEC:TFEC	none	1.20 g
EA+LiFSI**	0.55 M LiPF ₆ + 6 m LiFSI	EA	none	0.800 mL
MP:VC**	1 M LiPF ₆	95:5 w:w MP:VC	none	0.800 mL

† v:v = ratio by volume, w:w = ratio by weight

‡ Added as weight percent

* Cells prepared by Sarah Hyatt

** Cells prepared by Sarah Hyatt according to procedure developed by Rémi Petibon

Once transferred to the calorimeter, all cells proceeded through a 24 h open circuit equilibration followed by four cycles at 10 mA (C/26) between 2.8 – 4.5 V. The cells then proceeded into variable rate tests for the voltage ranges of 4.1 – 4.2 V, 4.2 – 4.3 V, 4.3 – 4.4 V, and 4.4 – 4.5 V at currents of 10, 5, 2, and 1 mA. All cells except for EA+LiFSI and MP:VC were then discharged to 4.1 V at 10 mA, cycled between 4.1 – 4.5 V at 1 mA, then cycled from 4.1 – 4.7 V at 1 mA. The cells containing 2% TAP were removed from the calorimeter before the completion of the final discharge, at approximately 4.5 V.

8.3 DETERMINATION OF THE IMPACT OF ELECTROLYTE COMPOSITION ON 4.7 V NMC442/GRAPHITE CELLS

8.3.1 Determination of the Impact of Electrolyte Composition up to 4.5 V

The time dependent empirical model including hysteresis introduced in Chapter 7, and given by Equation 7.2.4, was used to fit narrow voltage range heat flow data from NMC442/graphite pouch cells. The heat flow components describing polarization, changes in entropy, and parasitic reactions were modeled with polynomials quadratic in rSOC, while the hysteresis component was modeled with no rSOC-dependence. The experimental heat flows were fit to the model using the in-house developed software described previously.

Figure 8.1 shows a representative example of the comparison between measured and calculated heat flow in the voltage ranges of 4.2 – 4.3 V, 4.3 – 4.4 V, and 4.4 – 4.5 V, for decreasing currents applied to an NMC442/graphite pouch cell containing V211M. The heat flow obtained for the 10 mA charge segment was excluded from all fits, as discussed in Chapter 7. Good agreements are shown for all voltage segments, and similar qualities of fits were achieved for all electrolyte compositions, with exception of the EA+LiFSI and MP:VC cells. Table 8.2 gives the RMSE values of all fits for all cells examined, and pair cell data are given where available. Pair cells were not made for 2% VC and 2% PES containing cells, and one of two FEC:TFEC cells developed small microshorts which led to several spikes in the heat flow and was therefore excluded from the fits. The EA+LiFSI and MP:VC cells showed severe electrolyte oxidation, as will be shown, which made fitting the experimental data very difficult, leading to large RMSE values.

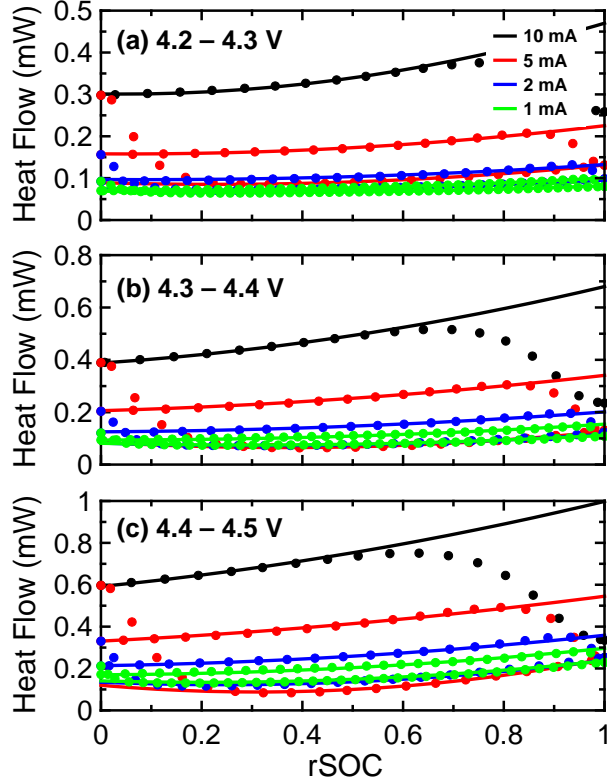


Figure 8.1: Measured (symbols) and calculated (lines) heat flow for an NMC442/graphite pouch cell containing V211M at 10 mA (black), 5 mA (red), 2 mA (blue), and 1 mA (green) in the voltage ranges of (a) 4.2 – 4.3 V, (b) 4.3 – 4.4 V, and (c) 4.4 – 4.5 V.

Table 8.2: Summary of RMSE of fit for all NMC442/graphite cells for all voltage ranges examined. Pair cell data are given where available.

Cell	RMSE of fit (μW)					
	4.2 - 4.3 V		4.3 - 4.4 V		4.4 - 4.5 V	
control	1.9	1.7	2.3	2.2	4.8	4.7
2%VC	2.0		2.0		4.4	
2%PES	1.7		1.9		4.4	
2%TAP	1.6	1.5	2.8	3.6	6.3	5.5
V211M	1.4	1.6	2.0	2.0	4.9	4.8
P211M	1.5	1.4	2.2	2.0	4.2	3.8
FEC:TFEC	2.2		1.9		3.9	
EA+LiFSI	3.0	4.3	2.4	3.4	25	22
MP:VC	2.9	4.5	5.5	6.4	19	22

Figure 8.2 shows the extracted heat flow components as a function of rSOC for NMC442/graphite cells resulting from the fit to the time dependent empirical model including a constant hysteresis component. Data for the 5 mA charge segment in each voltage range are shown for all cells except for EA+LiFSI and MP:VC.

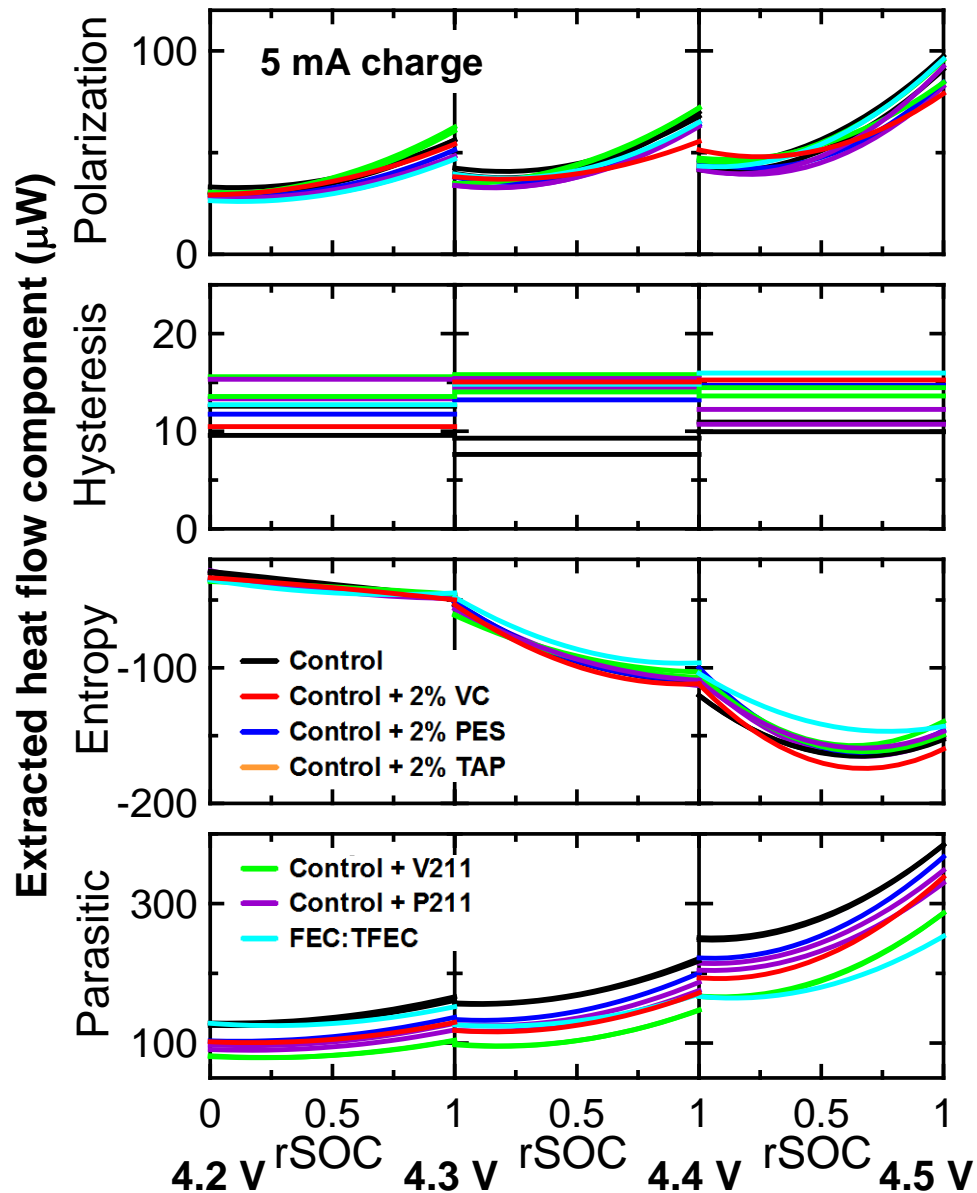


Figure 8.2: The extracted heat flow components resulting from polarization, hysteresis, changes in entropy, and parasitic reactions as a function of rSOC for NMC442/graphite cells during the 5 mA charge segment for three voltage ranges: 4.2 – 4.3 V, 4.3 – 4.4 V, and 4.4 – 4.5 V. Data shown for electrolyte compositions as indicated in the legend and pair cell data are shown where available.

The polarization, hysteresis, and entropic components of the heat flow are very similar between cells, as expected for machine-made pouch cells and as was previously seen with other cell chemistries. The discontinuities in the polarization and entropic heat flows between voltage ranges were discussed in Chapter 7, and thought to primarily be a result of the calorimeter response time. There are significant differences in the extracted parasitic heat flows depending on the electrolyte composition. Figure 8.3 shows a magnification of the extracted parasitic heat flow for the 5 mA charge segment, including the results for the EA+LiFSI and MP:VC cells.

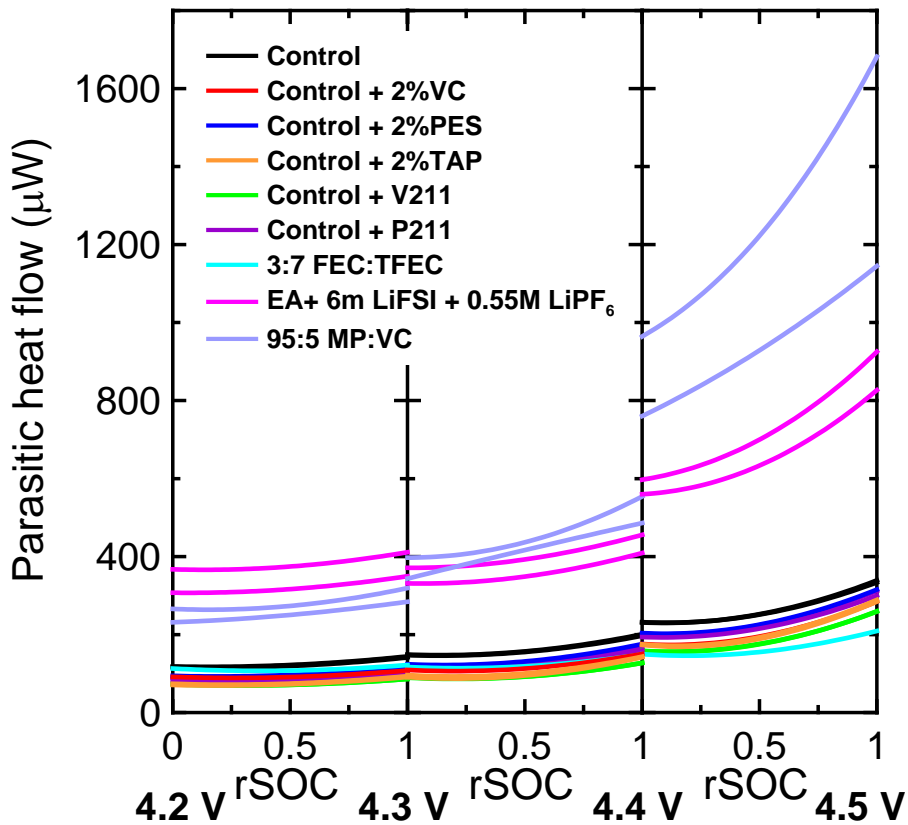


Figure 8.3: Extracted parasitic heat flow as a function of rSOC for NMC442/graphite pouch cells containing electrolyte compositions as indicated in the legend during the 5 mA charge segment for each of three voltage ranges.

The parasitic heat flow observed for the cells containing the linear carboxylic esters (EA and MP) was dramatically larger than for cells containing control-based or fluorinated solvents. Petibon *et al.*⁶⁴ showed that NMC111/graphite pouch cells cycled to an upper cutoff voltage of 4.2 V with 95:5 MP:VC exhibit similar coulombic efficiencies and capacity retentions than control + 2% VC cells (with 3:7 EC:EMC solvent). However, the 95:5 MP:VC cells also showed larger charge endpoint capacity slippage rates and therefore parasitic reaction rates at the positive electrode. In a different study, Petibon *et al.*⁶³ also showed that NMC111/graphite and NMC442/graphite pouch cells containing EA+LiFSI were able to be cycled to 4.2 V and 4.4 V, respectively for 700 – 800 h. No direct comparisons to EC:EMC-based cells were made by Petibon *et al.*⁶³, but a comparison between data in the two papers show that the capacity fade rate was more than tripled for cells containing EA+LiFSI compared to control electrolyte (respective capacity losses of 7 mAh and 2 mAh over 35 cycles at C/5 to 4.2 V under the same experimental conditions). Therefore, large parasitic heat flows shown in Figure 8.3 of the cells containing linear carboxylic esters at high voltages performance are not surprising. However, the large discontinuous increase in parasitic heat flow between 4.3 – 4.4 V and 4.4 – 4.5 V suggest that these solvent systems are very sensitive to the upper cutoff voltage, and it is likely that the initial formation and four cycles with an upper cutoff voltage of 4.5 V had a significant detrimental impact on the lower voltage operation, resulting in the very large parasitic heat flows observed for these cells over the entire voltage range examined.

In order to better assess the performance of the cells containing control-based and fluorinated solvents, Figure 8.3 is replotted with the results of the EA+LiFSI and MP:VC cells excluded. Figure 8.4 shows such a magnified view of the cells with the lowest

parasitic heat flows. Out of these cells, the cells containing control electrolyte have the largest parasitic heat flows, but they are only moderately larger than those of the additive-containing cells. This is in contrast to results from NMC111/graphite and NMC811/graphite pouch cells (Figures 5.9 and 6.23, respectively) where control cells showed significantly larger parasitic heat flows than those containing additives.

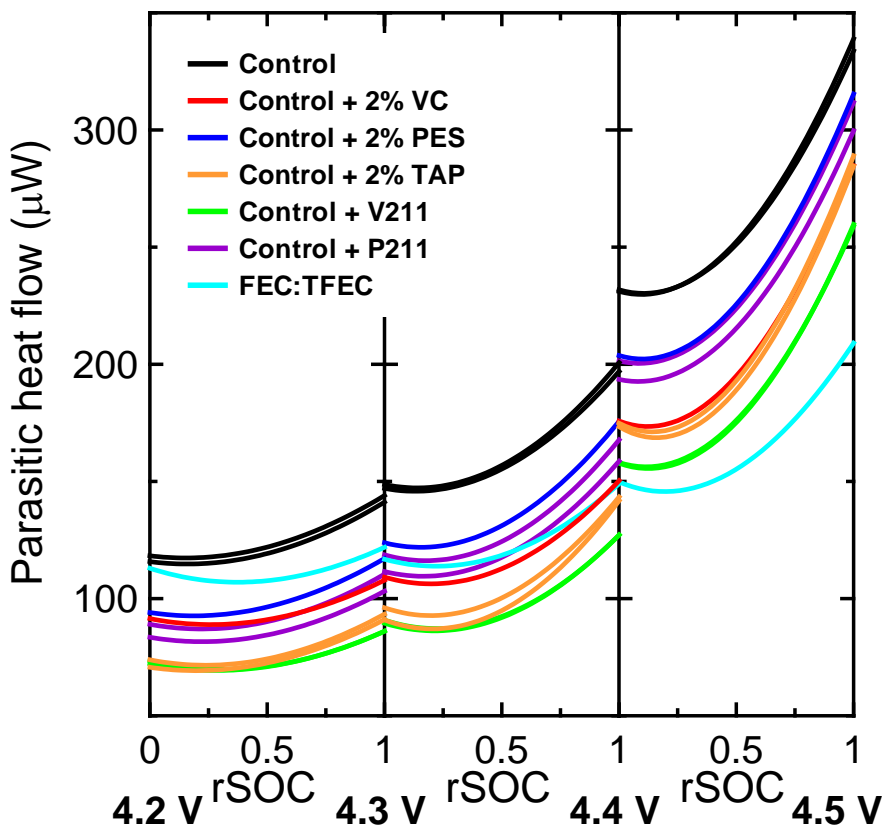


Figure 8.4: Extracted parasitic heat flow as a function of rSOC for NMC442/graphite pouch cells containing control-based or fluorinated solvents as indicated in the legend. Data are shown for the 5 mA charge segment for each of the three voltage ranges.

This was also observed in UHPC experiments by Nie *et al.*²⁵⁶ The coulombic efficiency and charge endpoint capacity slippage were dramatically worse for control compared to 2% VC in NMC111/graphite pouch cells cycled to 4.2 V, but control was only slightly worse than 2% PES in NMC442/graphite pouch cells cycled to 4.4 V. It is

possible that the initial formation and cycling to high voltage (> 4.4 V) results in oxidation reaction products creating a protective SEI on the positive electrode which decreases the electrode-electrolyte reactivity for subsequent cycles, or at the very least dramatically changes the SEI composition and/or structure. It is clear that further work is required to understand the differences in parasitic heat flow for control electrolyte across multiple cell chemistries.

Figure 8.4 also shows that all additive combinations with control solvent result in a reduced parasitic heat flow, in good agreement with previous results. At the lower voltages examined, the cells containing 2% TAP had the lowest parasitic heat flow, which is surprising in context of the results of NMC811/graphite pouch cells (Figure 6.23), where 2% TAP had a significantly larger parasitic heat flow than cells containing 2% VC, V211M, and P211M. This may be a similar effect to that proposed for the control cells, or could be related to an increased reactivity of the NMC811 positive electrode surface. Again, further work is required to understand the substantial differences in additive behaviours as a function of cell chemistry.

In the intermediate voltage range, 4.3 – 4.4 V, the cells containing V211M had the smallest parasitic heat flow, in good agreement with all previous results for all cell chemistries. It is also noteworthy that the addition of 1% TTSPi and 1% MMDS to 2% VC has a more pronounced impact on the parasitic heat flow than when added to 2% PES, and the VC-containing additive blends show reduced parasitic heat flows than the PES-containing counterparts. However, it has been shown that the PES-containing electrolyte blends provide a significant improvement in gas generation, charge transfer impedance, and cycle life compared to VC-based blends.^{133–136,160,230} Therefore, the end-use of the cell needs to be a critical factor in the electrolyte design.

Figure 8.4 also shows that the parasitic heat flow of the cell containing FEC:TFEC solvent has a noticeably different voltage dependence than cells containing control solvent. At 4.2 V, the parasitic heat flow was comparable to the control cell, but by the start of the 4.4 V segment and up to 4.5 V, the FEC:TFEC cell had the lowest parasitic heat flow. The reduced rate of increase as a function of voltage is in good agreement with the increased oxidation potential of FEC and other fluorinated solvents compared to EC and carbonate solvents.^{46,53,54,57} While it is assumed here that the observed reduction in parasitic heat flow for FEC:TFEC is primarily a result of a decreased reaction rate, a difference in the enthalpy of reaction would also result in a difference in parasitic heat flow. No data were available for EC and FEC, but the condensed phase enthalpy of combustion for benzene and fluorobenzene are -3267.5 ± 0.4 kJ/mol²⁵⁷ and -3101.6 ± 0.6 kJ/mol²⁵⁸, respectively. Therefore the reaction enthalpy may be slightly lower for the oxidation of FEC compared to EC, but it is not expected to be significantly different, such that the reduction in parasitic heat flow is a result of a reduced reaction rate. The difference in reaction enthalpies will be investigated in more detail in Chapter 9.

Figure 8.5 summarizes the time dependence of the parasitic heat flow by comparing the extracted value at the top of charge for the 10 mA (first chronological) and 1 mA (last chronological) segments of each voltage range examined. The time factors, $-L$ in Equation 7.2.4, are also shown. The cells containing control-based electrolyte and FEC:TFEC have a decreasing parasitic heat flow as a function of time, consistent with passivation processes. For control, 2% VC, 2% PES, and 2% TAP cells, the large parasitic heat flows observed at 4.5 V are accompanied by more negative time factors (increased L), as was observed in NMC811/graphite cells. However, very little difference in the time factor was observed as a function of voltage for cells containing V211M or

P211M, despite the large high voltage increase in parasitic heat flow. At high voltage, the cell containing FEC:TFEC showed both a low parasitic heat flow and a large rate of decrease, highlighting the benefit of such fluorinated solvent systems.

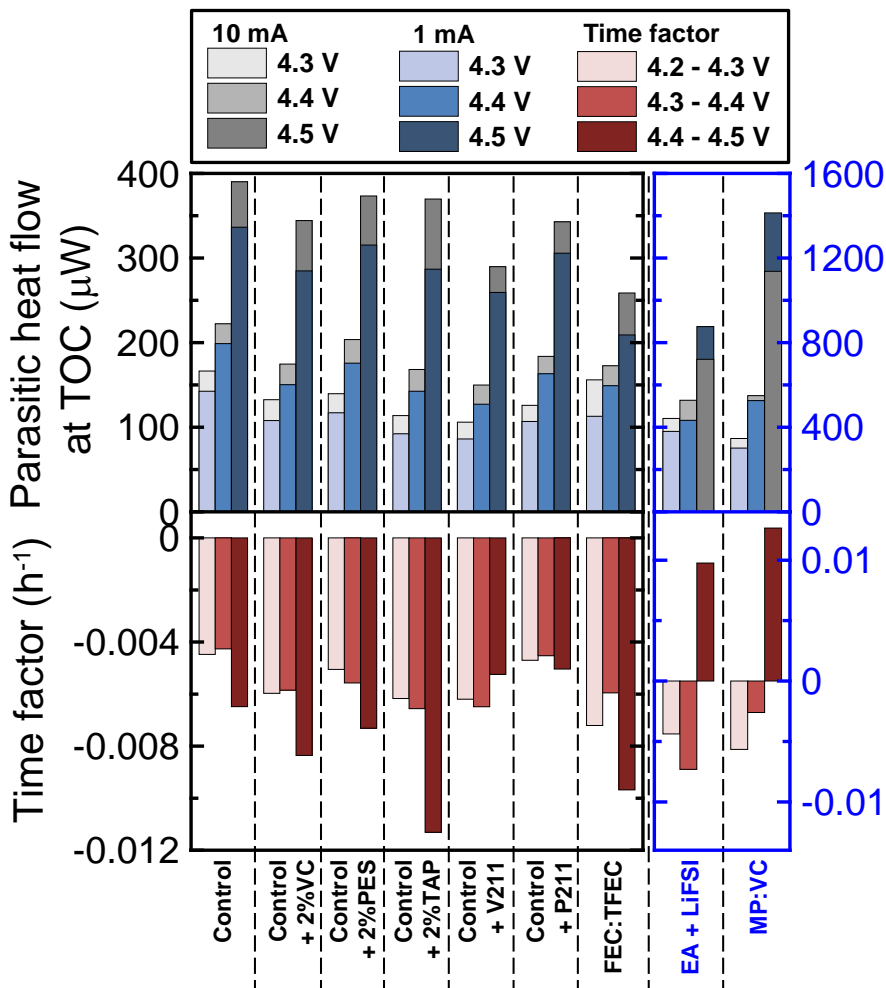


Figure 8.5: Summary of the time dependent parasitic heat flow measured at the top of charge for NMC442/graphite cells over three voltage ranges as indicated in the legend for the 10 mA cycle (grey) and 1 mA cycle (blue). The extracted time factor (red) over each voltage range is also indicated. Pair cell data were averaged where available. Cells containing EA+LiFSI and MP:VC are plotted on different scales given by the blue axes.

Figure 8.5 also shows that cells containing EA+LiFSI or MP:VC have dramatically higher parasitic heat flows, as was shown in Figure 8.3. Furthermore, between 4.4 – 4.5 V the parasitic heat flow increased rapidly as a function of time. This

further supports the conclusion of the linear carboxylic esters being very sensitive to upper cutoff voltage and therefore the initial formation and cycling to 4.5 V being highly damaging to the cells.

8.3.2 Using 1 mA Cycles to Determine the Impact of Electrolyte Composition up to 4.7 V

Following the narrow range cycling discussed in the previous section, all NMC442/graphite cells except EA+LiFSI and MP:VC were cycled between 4.1 – 4.5 V then between 4.1 – 4.7 V, both at 1 mA. As described several times in previous Chapters, the average of the 1 mA charge and discharge heat flows is a good approximation to the parasitic heat flow. Figure 8.6a shows the average 1 mA heat flow for the 4.1 – 4.5 V cycle (data only shown between 4.2 – 4.5 V for ease of comparison with previous sections). The trends and impacts of electrolyte composition observed in Figure 8.4 are repeated here.

Figure 8.6b shows the average 1 mA heat flow for the 4.1 – 4.7 V cycle, again only plotted starting from 4.2 V. The magnitude of the parasitic heat flow up to 4.7 V is very large and is > 1 mW at 4.7 V for all cells containing control solvent. As was discussed in Chapter 4, a parasitic heat flow on the order of 100 μ W or 0.1 mW would consume all of the electrolyte in these pouch cells within one year. Therefore, all of the cells tested here would have significantly shortened lifetimes if cycled to 4.7 V. Comparisons between Figure 8.6a and Figure 8.6b show that the average 1 mA heat flow at lower voltages was highly impacted by the exposure to high voltage for all cells containing control electrolyte.

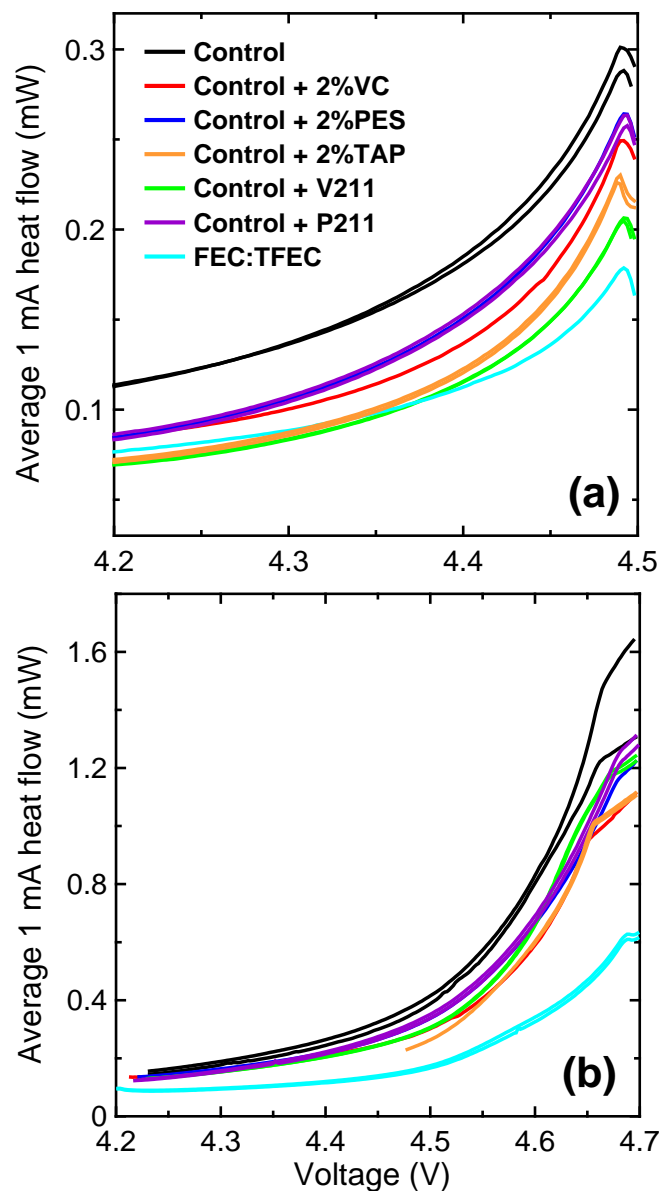


Figure 8.6: Average of 1 mA charge and discharge heat flows as a function of voltage for NMC442/graphite cells containing electrolytes as indicated in the legend between (a) 4.2 – 4.5 V and (b) 4.2 – 4.7 V.

Figure 8.7 shows a direct comparison of the average 1 mA heat flows between 4.2 – 4.5 V during the narrow voltage range cycling (Section 8.3.1), the 1 mA 4.1 – 4.5 V cycle (Figure 8.6a) and the 1 mA 4.1 – 4.7 V cycle (Figure 8.6b) for cells containing control + P211M and FEC:TFEC as an example.

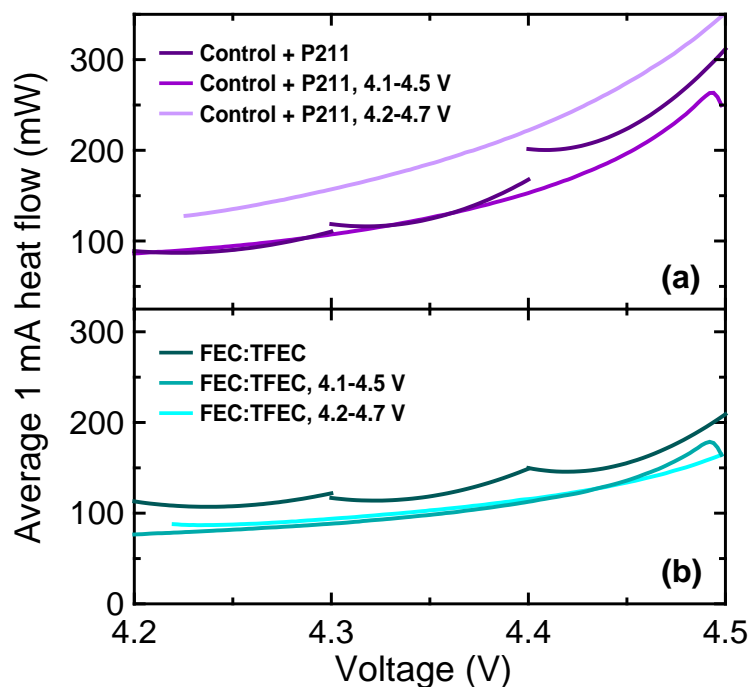


Figure 8.7: Average of 1 mA charge and discharge heat flows as a function of voltage between 4.2 – 4.5 V during narrow voltage range cycling (darkest), 1 mA 4.1 – 4.5 V cycle (medium), and 1 mA 4.1 – 4.7 V cycle (lightest) for NMC442/graphite pouch cells containing (a) control + P211M (purple) and (b) FEC:TFEC (teal).

Figure 8.7a shows that for a P211-containing cell, the average heat flow for the 1 mA 4.1 – 4.5 V cycle is reduced between 4.4 – 4.5 V compared to the narrow voltage range results, as would be expected from the decrease in parasitic heat flow as a function of time. However, the average heat flows are virtually the same between 4.2 – 4.4 V. This is coincidental, as the narrow range data were collected from 306 – 351 h and 353 – 387 h for 4.2 – 4.3 V and 4.3 – 4.4 V, respectively, while the 4.1 – 4.5 V cycle occurred between 457 – 555 h, and thus the heat flow during the 4.1 – 4.5 V cycle should be smaller than during the narrow range cycles. This can therefore be thought of as an effective increase in parasitic heat flow as a result of the high voltage cycling. This is in good agreement with results presented in Chapter 6, where the heat flow produced from a high voltage cycle increased the subsequent heat flow observed at lower voltages. This is

further exemplified by the average heat flow from the 4.1 – 4.7 V cycle, where a large increase compared to the previous cycle was observed. This irreversible increase in parasitic heat flow resulting from a high voltage cycle suggests a change in the dominant reaction pathway. This is further supported by results from EIS^{219,230}, XPS²⁵⁹, UHPC cycling²⁵⁶, and *in situ* gas production¹³⁶, which have all observed differences between moderate voltage and high voltage operation of cells containing control-based electrolytes. The nature of these reaction pathways is unknown at this time and requires further study.

Figure 8.7b shows the same evolution in average heat flow for a cell containing FEC:TFEC solvent. The average 1 mA heat flow for the 4.1 – 4.5 V cycle is reduced over the entire voltage range compared to the narrow range cycles. As expected from the time dependence of the parasitic heat flow, the reduction of the average heat flow is larger between 4.2 – 4.3 V (first chronologically in narrow range cycles) than from 4.3 – 4.4 V and 4.4 – 4.5 V. Therefore, it is suggested that up to 4.5 V, the parasitic reactions occurring in cells containing FEC:TFEC continue to passivate the electrode surfaces and no new reactions are initiated. The average 1 mA heat flow for the 4.1 – 4.7 V cycle is very similar to that of the 4.1 – 4.5 V cycle, therefore there is an effective increase in the parasitic heat flow at lower voltages once the effect of time is considered, but to a significantly reduced degree than observed for the P211M cell.

The effects of the high voltage cycling on the P211M and FEC:TFEC cells are more easily discerned by looking directly at the measured 1 mA heat flow. Figure 8.8 shows a comparison of the 1 mA measured heat flow for the narrow range cycles, 4.1 – 4.5V cycle, and 4.1 – 4.7 V cycle. Figure 8.8a and Figure 8.8b (magnified view) show results for the cell containing P211M, and show that the heat flow during charge

continually decreased as would be expected. However, charging to 4.7 V resulted in a very significant heat flow which was retained during discharge, which resulted in an increased average heat flow (Figure 8.7a). Figure 8.8c and Figure 8.8d (magnified view) show the results for the cell containing FEC:TFEC, and show similar behaviour to the P211M cell. However, the heat flows for the FEC:TFEC cell are significantly smaller (by about a factor of 2) and the impact of charging to 4.7 V is less severe. Therefore, when a cell is charged to a high voltage and a new reaction is initiated, the average 1 mA heat flow is not an accurate measure of the parasitic heat flow as the charge and discharge heat flows are dramatically different, as demonstrated in Figure 8.8.

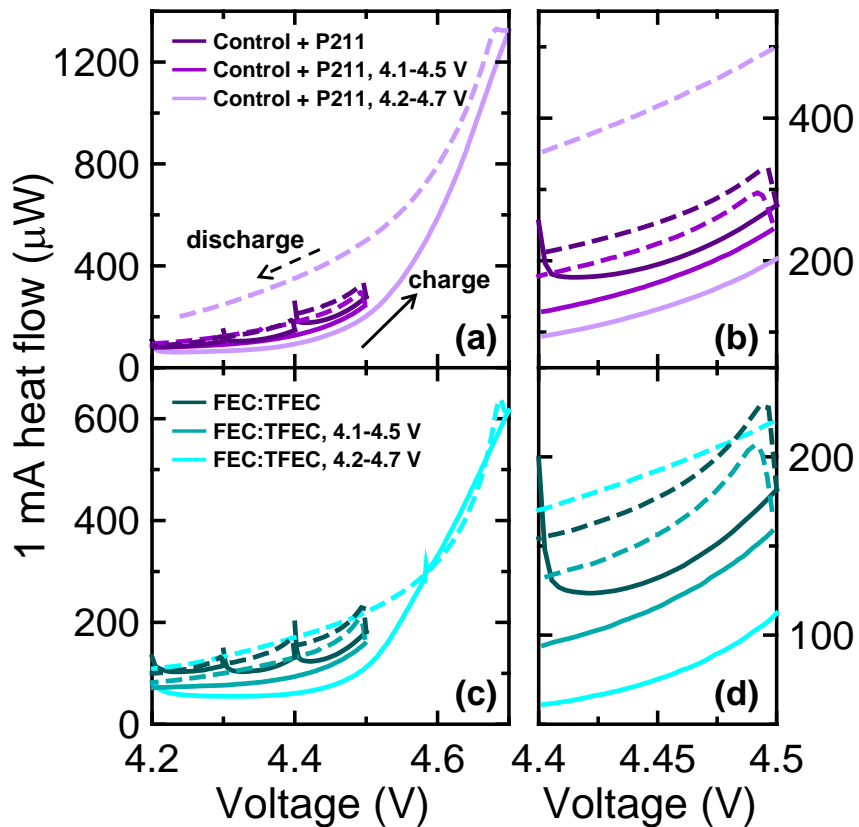


Figure 8.8: Measured heat flow during 1 mA charge (solid) and discharge (dashed) as a function of voltage during narrow voltage range cycling (darkest), 1 mA 4.1 – 4.5 V cycle (medium), and 1 mA 4.1 – 4.7 V cycle (lightest) for NMC442/graphite pouch cells containing (a) control + P211M (purple) and (c) FEC:TFEC (teal). Panels (b) and (d) are magnifications of (a) and (c), respectively.

Even though the calorimetry results presented in this Chapter can only extract the total parasitic heat flow and cannot explicitly separate the effect of reaction rate and the enthalpy of reaction, the above results clearly demonstrate that the fluorinated solvents are beneficial for high voltage operation of NMC442/graphite cells. This is consistent with the increased oxidation potential of such fluorinated compounds.

8.4 COMPARISON OF PARASITIC HEAT FLOW RESULTS TO CELL PERFORMANCE

Figure 8.9 shows the normalized discharge capacity as a function of cycle number for NMC442/graphite pouch cells containing 2% VC or FEC:TFEC that were cycled between 2.8 – 4.5 V at 40 mA (~C/5) using a Maccor charger. These NMC442/graphite pouch cells were from a different manufacturing batch than those used in the calorimetry experiments described in the previous sections, and were found to be balanced for approximately 4.5 V operation. However, cell preparation, electrolyte filling, wetting, and formation procedures were all identical, and were all done by Sarah Hyatt. Figure 8.9 shows that the observed capacity fade for the cell containing FEC:TFEC is significantly less than the cell containing control solvent to which 2% VC was added. This is in good agreement with the calorimetry results in Section 8.3.

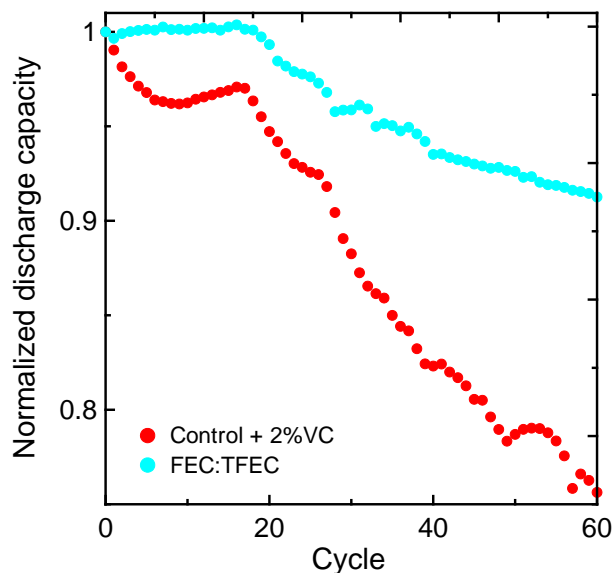


Figure 8.9: Normalized discharge capacity as a function of cycle number for NMC442/graphite pouch cells containing 2%VC (red) and FEC:TFEC (cyan) cycled between 2.8 – 4.5 V at 40 mA ($\sim C/5$).

To further confirm the results of the isothermal microcalorimetry experiments, the extracted parasitic heat flow shown in Figure 8.4 would predict that a cell containing control electrolyte with any of the additive combinations examined (2% VC, 2% PES, 2% TAP, V211M, or P211M) would have a better cell performance than a cell containing FEC:TFEC between 4.2 – 4.3 V, but the reverse would be true between 4.4 – 4.5 V. Therefore, NMC442/graphite pouch cells of the same batch and preparation methods as used for the calorimetry experiments, containing either V211M or FEC:TFEC were initially cycled using a Maccor charger four times between 2.8 – 4.5 V at 10 mA in a 40 ± 0.1 °C temperature-controlled box. One set of cells (one of each electrolyte composition) were then cycled between 4.2 – 4.3 V at 2 mA, while the other set were cycled between 4.4 – 4.5 V at 2 mA.

Figure 8.10a shows the measured charge capacity for the narrow voltage range cycling as a function of cycle number for the four cells described above. During 4.2 – 4.3

V cycling, the cell containing V211M showed very little capacity fade while the fade was much more pronounced for the cell containing FEC:TFEC. This is in good agreement with the extracted parasitic heat flow results shown in Figure 8.4.

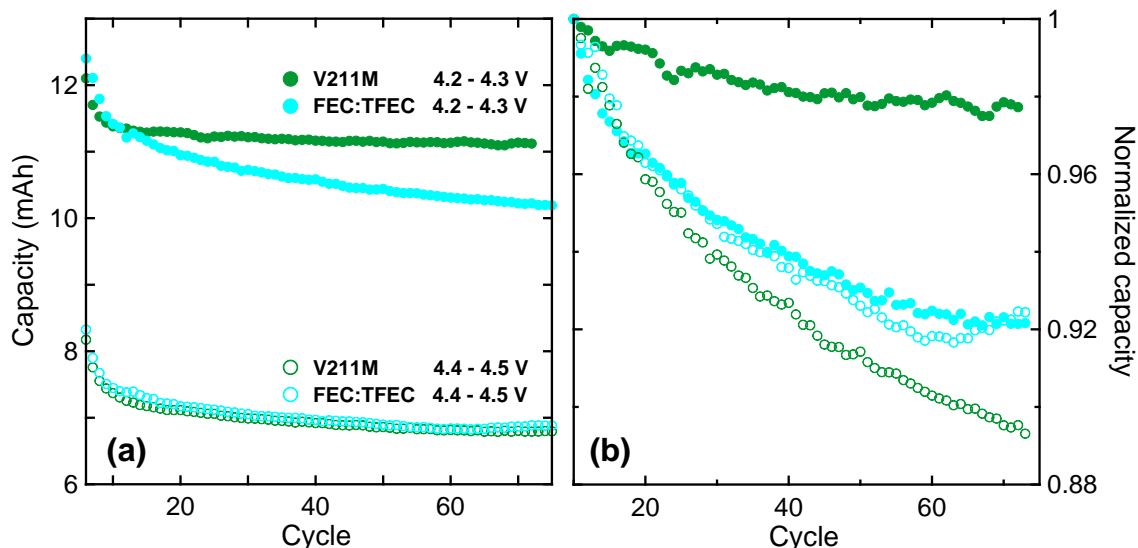


Figure 8.10: (a) Charge capacity as a function of cycle number for NMC442/graphite cells containing V211M (green) and FEC:TFEC (cyan) cycled at 2 mA between 4.2 – 4.3 V (solid symbols) and 4.4 – 4.5 V (open symbols). (b) Corresponding normalized charge capacity as a function of cycle number.

Figure 8.10b shows the corresponding normalized charge capacity, where the normalization was done to the cycle 10 capacity (fourth narrow range cycle). This clearly demonstrates that in terms of capacity retention, the cell containing V211M out-performs the cell containing FEC:TFEC when cycled between 4.2 – 4.3 V. However, when cycled between 4.4 – 4.5 V, the cell containing FEC:TFEC maintained approximately the same fade rate as was observed between 4.2 – 4.3 V, while the V211M fade rate increased substantially for the higher voltage cycling. This is in excellent agreement with the extracted parasitic heat flow results, as well the 1 mA cycling results shown in Figure 8.8. Both experiments suggested a high voltage onset of new parasitic reactions or change in dominant reaction pathway for cell containing control solvent, while FEC:TFEC cells

maintained the same, or similar, dominant reaction pathway to at least 4.5 V. The cycling and parasitic heat flow results also suggest that the FEC:TFEC cells have an increased rate of reaction of lower voltage processes occurring at the negative electrode compared to V211M cells. The relative benefit of FEC:TFEC is therefore only apparent at high voltage once the rate of electrolyte oxidation of control-based electrolyte increases significantly. This therefore suggests that the FEC:TFEC electrolyte system could be further improved through the use of electrolyte additives that promote SEI formation on the negative electrode.

Following the calorimetry experiments described in Section 8.3, the cells containing control, 2% VC, 2%PES, V211M, P211M, and FEC:TFEC were discharged to near 0 V and transferred to an argon-filled glovebox. They were then punctured with a gas extraction device for gas chromatography-mass spectrometry (GC-MS) experiments (results of which are not shown here due to problems with contamination), and fully disassembled. Disassembly was done by Sarah Hyatt with help from Rémi Petibon. Figure 8.11 shows photographs of both sides of the separators (one side in contact with the negative electrode and the other with the positive electrode) that were removed from the cells containing control, P211M, and FEC:TFEC. The separators extracted from cells containing 2% VC, 2% PES, and V211M were virtually indistinguishable from that of the P211M cell. As discussed in Chapter 3, the side in contact with the positive electrode was coated with Al_2O_3 to minimize oxidation of the polyethylene.

The separators extracted from the cells containing control and P211M showed pronounced brown discolouration on both sides of the separator, while the separator from the cell containing FEC:TFEC had almost no discolouration on the side in contact with the negative electrode and minimal discolouration on the positive side. It is thought that

the brown discoloration is an indication of the oxidation of the polypropylene. This is then also in qualitative agreement with the parasitic heat flow results.

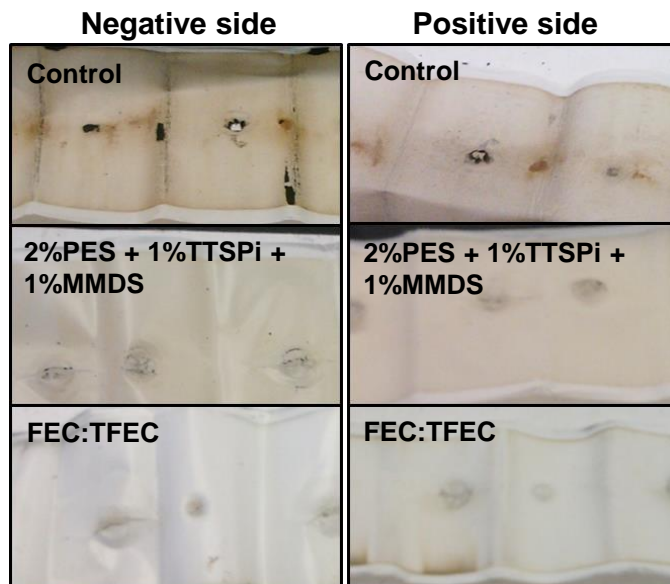


Figure 8.11: Images of separator from fully disassembled cells after being removed from calorimeter. Side in contact with the negative electrode shown in left column and side in contact with positive electrode in right column. Images shown for cells containing control (top), P211M (middle), and FEC:TFEC (bottom). Holes were made by a gas extraction device for GC-MS experiments done by Rémi Petibon.

Figure 8.12 shows the volume of gas produced during the two formation procedures and during the entire experimental protocol performed inside the calorimeter. The volumes were determined using the *ex situ* technique described in Section 3.3. Cells containing control and 2% TAP showed a large volume of gas produced during the first formation to 3.8 V, which has been shown to be a result of gas produced at the negative electrode.^{135,136} The gas produced during the second formation step to 4.5 V is thought to originate from the positive electrode.^{135,136} The middle panel of Figure 8.12 shows that cells containing PES produce less gas at the positive electrode than cells containing VC when cycled to high voltages, in agreement with previously published results.^{133–136}

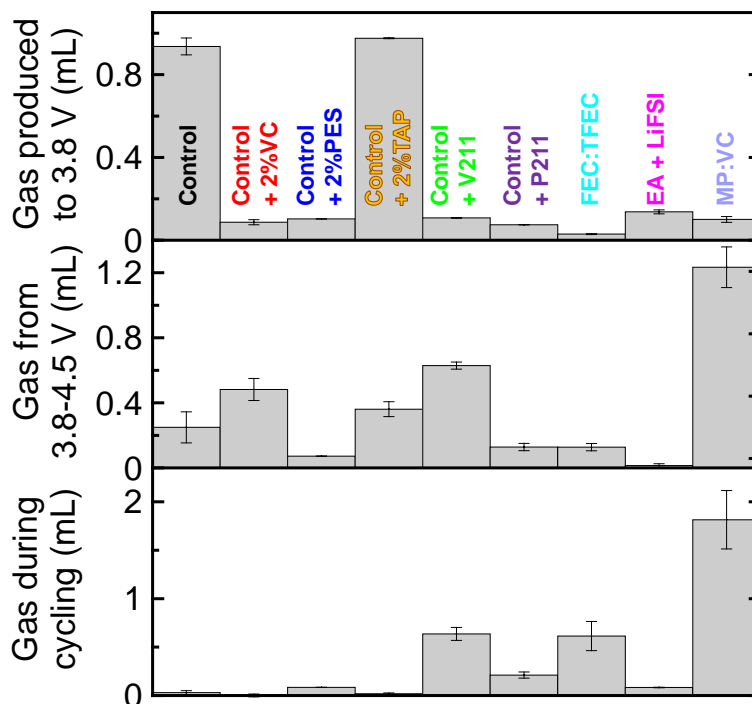


Figure 8.12: Volume of gas produced during the first formation process to 3.8 V (top), during the second formation process between 3.8 – 4.5 V (middle), and after all cycling was completed in the calorimeter (bottom) for NMC442/graphite cells containing electrolyte compositions as indicated.

The bottom panel of Figure 8.12 shows that after the calorimetry cycling protocol, the cells containing control electrolyte or single additives (2% VC, PES, or TAP) showed almost no net gas production. With such *ex situ* measurements it is not possible to know whether no gas was produced throughout the entire cycling protocol, or whether the gas was produced and then consumed, as was observed by Self *et al.*¹³⁶ The cells containing TTSPi and MMDS in addition to either VC or PES produced a significant amount of gas, especially V211M. Preliminary GC-MS measurements suggest this gas is fluorotrimethylsilane (FSi(CH₃)₃) which results from the decomposition of TTSPi above 4.35 V, though possible contamination could not be ruled out. The cell containing FEC:TFEC also produced a large volume of gas during the calorimeter cycling. This is in

agreement with *in situ* gas measurements that showed that FEC-containing electrolytes continually produced gas and no gas consumption was observed.¹³⁶ Furthermore, despite both having exceptionally large parasitic heat flows, cells containing EA+LiFSI produced almost no gas during cycling while MP:VC produced nearly 2 mL (sufficient to cause significant bulging and loss of stack pressure).

The combination of parasitic heat flow measurements with gas production measurements may help guide efforts in determining the dominant reaction pathways of electrolyte degradation. For example, the primary degradation mechanism of EA+LiFSI to 4.5 V must either result in liquid or solid products, or if any gas is produced it must be subsequently consumed, while the reaction of MP:VC should form a large amount of gaseous products which are not consumed. Correlation of the voltage dependence of the parasitic heat flow and *in situ* gas production and/or consumption would therefore be of significant impact and should be examined. In addition, both liquid and gas-phase GS-MS and surface characterization techniques such as XPS should be closely examined and correlated to parasitic heat flow results. In particular, an emphasis on the changes of the decomposition products occurring between 4.3 – 4.5 V would be of distinct interest.

8.5 CONCLUSIONS

The inclusion of a constant hysteresis term into the time dependent empirical model allowed for fitting of the heat flow from high voltage NMC442/graphite cells. The effect of electrolyte composition, including both additives and solvents, was examined. All cells, regardless of electrolyte composition, exhibited very large parasitic heat flows at high voltages (> 4.35 V). The inclusion of additives to control-based electrolyte

reduced the parasitic heat flow, as previously demonstrated for several cell chemistries. Furthermore, it was shown that changing the solvent composition had a profound effect on the parasitic heat flow. Esters such as EA and MP were very sensitive to upper cutoff voltage and are possibly only appropriate for low voltage applications. Cells containing fluorinated carbonate solvents showed a significantly decreased parasitic heat flow at voltages > 4.4 V compared to EC-based cells, but little advantage < 4.4 V. However, gas generation measurements show that cells containing FEC continually produce gas, which is a significant problem for soft-sided pouch cells. However, the increased low voltage parasitic heat flow and gas production may be addressed using electrolyte additives, which would make the FEC-based solvents even more attractive.

The results presented here also showed that the effect of high voltage cycling on the parasitic heat flow observed on the subsequent lower voltage cycles are indicative of a change in the dominant reaction pathway. This was observed for EC-based cells above 4.4 V and was significant when charged to 4.7 V, but was not observed for FEC-based cells up to 4.5 V. This suggests that the benefit of the fluorinated solvent systems arises from an increase in stability of the passivation films and reaction products.

CHAPTER 9

THE USE OF OPEN CIRCUIT EXPERIMENTS TO EXAMINE THE ORIGIN AND IMPLICATIONS OF THE PARASITIC HEAT FLOW

9.1 INTRODUCTION AND MOTIVATION

Throughout the previous Chapters, the parasitic heat flow was extracted as a function of voltage and time for closed circuit conditions. This was determined as the heat flow resulting from all processes with no current dependence. However, this offered no indication of the nature of the reaction processes occurring in the cell. Due to the possibility of various different parasitic processes, it is important to investigate the origin of the parasitic heat flow. In this Chapter, this is done using open circuit measurements such that the only source of heat flow is a result of parasitic reactions. First, a series of thought experiments examine the expected open circuit heat flow for simple model systems of two reaction types; a reversible shuttle and an irreversible non-shuttle process. These are then used to interpret long term measurements of the open circuit heat flow for NMC442/graphite pouch cells containing P211M at various voltages.

9.2 THOUGHT EXPERIMENTS

Due to the wide variety of possible parasitic reactions occurring in a cell, it is worth examining the consequences of certain reaction types and comparing those conclusions to experimental results. In particular, to further understand the meaning and implications of the parasitic heat flow, the measured heat flow during open circuit

conditions were examined. First, let us consider the simple case of an ideal cell with no internal impedance, where no parasitic reactions occur, that is connected to a resistor. Figure 9.1a shows a schematic of such a system where the resistor is located inside the calorimeter and Figure 9.1b shows the case where the resistor is outside the calorimeter. When the resistor is located inside the calorimeter (Figure 9.1a), the heat flow measured by the calorimeter is the sum of the power dissipated through the resistor (i.e., the dissipation current times the cell voltage), and the heat flow associated with changes in entropy of the positive and negative electrode materials during discharge. However, when the resistor is located outside the calorimeter (Figure 9.1b), the measured heat flow is only a result of the changes in entropy of the electrode materials during discharge.²⁶⁰

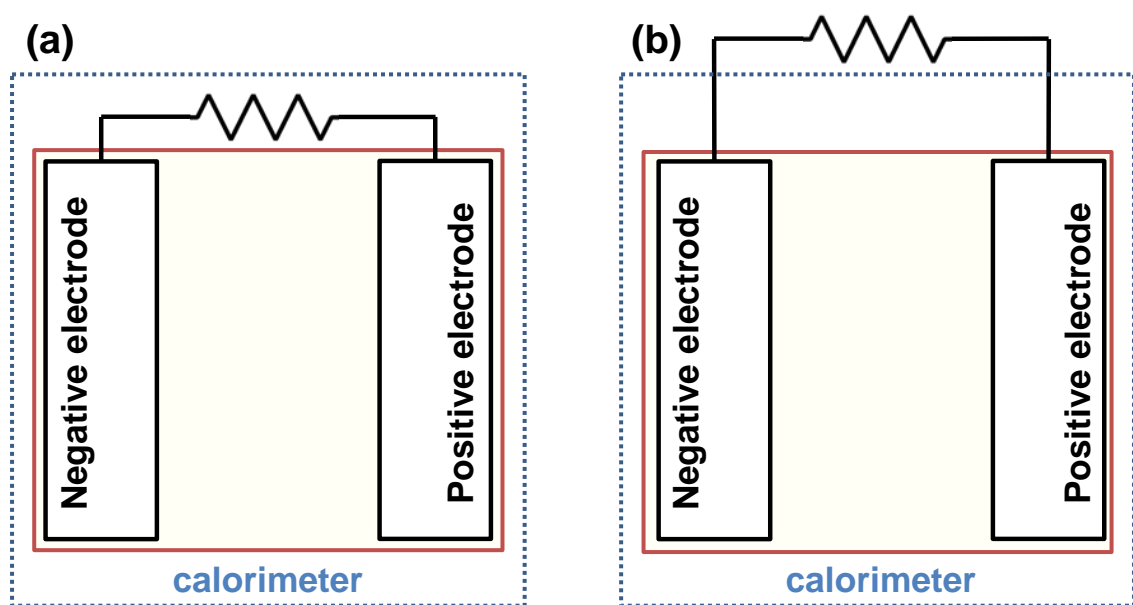


Figure 9.1: Schematic of an idealized cell connected to a resistor for the case of (a) the resistor inside the calorimeter and (b) the resistor outside the calorimeter.

Building upon the simple resistor model, the expected open circuit heat flow for two degradation processes were investigated. Figure 9.2a shows a schematic of a chemical shuttle process where a molecule S is oxidized at the positive electrode and is

re-formed through reduction at the negative electrode.^{98,261,262} Figure 9.2b shows a schematic of a non-shuttle mechanism where an electrolyte component X is first oxidized at the positive electrode, then reduced at the negative electrode to form reaction products rather than re-forming X. Figure 9.2b shows a solid reaction product that precipitates on the negative electrode for illustrative purposes. Even though no external current is applied, Figure 9.2 shows that for both cases, Li^+ is deintercalated from the negative electrode and intercalated into the positive electrode, while the oxidized molecule (S^+ or X^+) travels from the positive to the negative electrode. This process generates a parasitic current, denoted by I_p .

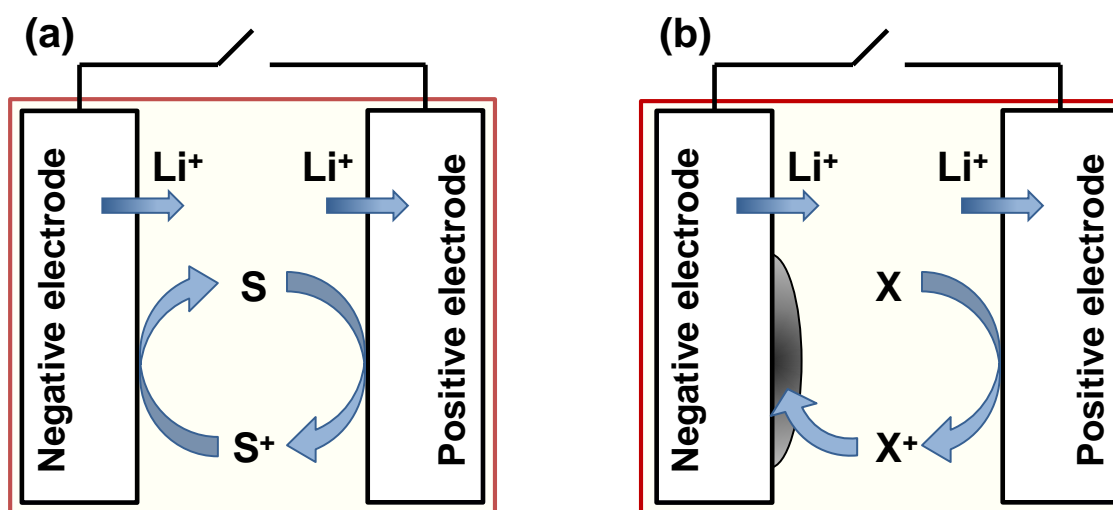
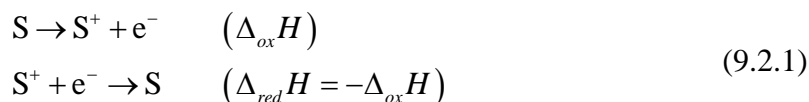


Figure 9.2: Schematics of (a) shuttle mechanism and (b) electrolyte oxidation and subsequent formation of reduction products occurring during open circuit conditions.

For the case of a shuttle mechanism (Figure 9.2a), the enthalpy of oxidation, $\Delta_{ox}H$, at the positive electrode is equal and opposite to the enthalpy of reduction, $\Delta_{red}H$, at the negative electrode. That is:



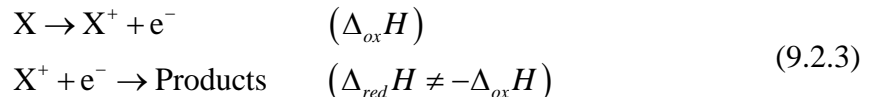
Therefore, the heat flow due to the net enthalpy of reaction is zero ($\Delta_{ox}H + \Delta_{red}H = 0$) for a shuttle process. However, the flow of charge still results in a heat flow. Starting from the derived expression of heat flow in Chapter (Equation 2.2.12), the open circuit heat flow where a shuttle mechanism is the only source of parasitic reactions is given by:

$$\frac{dq}{dt}_{OCV,shuttle} = |I_p V_{eq}| + \frac{T}{e} \left[\left(\frac{ds_+}{dx} \right) - \left(\frac{ds_-}{dx} \right) \right] I_p \quad (9.2.2)$$

where the work associated with moving the electron through the external circuit is zero for open circuit conditions. Therefore the heat flow resulting from shuttle mechanism is equivalent to an ideal cell with resistor inside a calorimeter (Figure 9.1a).

The heat flow associated with the change in entropy for a parasitic current is very small. For example, the extracted entropic heat flow for NMC442/graphite pouch cells was approximately -100 μ W during a 5 mA charge at 4.35 V (Chapter 8, Figure 8.2). Therefore, for a small parasitic heat flow, using 10 μ A as an example, the associated entropic heat flow component for a parasitic current is on the order of 0.2 μ W, while the heat flow due to $|I_p V_{eq}|$ is on the order of 40 μ W. As a result, the open circuit heat flow for a shuttle mechanism is approximately given by $|I_p V_{eq}|$. This is in agreement with results for LiFePO₄/Li_{4/3}Ti_{5/3}O₄ coin cells containing a known chemical redox shuttle, 2,5-ditertbutyl-1,4-dimethoxybenzene, where a known current was applied and the heat flow during the operation of the shuttle was measured.²⁶¹

For the case of a non-shuttle mechanism (Figure 9.2b), the enthalpies of oxidation at the positive and reduction at the negative are no longer equal and opposite, and therefore there is a net heat flow due to parasitic reactions. That is:



Therefore, the open circuit heat flow where i number of non-shuttle mechanisms are the source of parasitic reactions is given by:

$$\frac{dq}{dt}_{OCV, non-shuttle} = |I_p V_{eq}| + \frac{T}{e} \left[\left(\frac{ds_+}{dx} \right) - \left(\frac{ds_-}{dx} \right) \right] I_p + \sum_i (k_i \cdot (-\Delta_r H_i)) \quad (9.2.4)$$

where k_i is the reaction rate and $\Delta_r H_i$ is the reaction enthalpy for the i^{th} reaction. The negative sign arises by convention; an exothermic reaction (negative $\Delta_r H$) is measured as positive heat flow in the calorimeter. For the example given by Equation 9.2.3, the heat flow associated with the reaction enthalpies would be given by:

$$\sum_i (k_i \cdot (-\Delta_r H_i)) = -k_{ox} \Delta_{ox} H - k_{red} \Delta_{red} H \quad (9.2.5)$$

In order to maintain charge neutrality in the electrolyte and electrodes²⁶³, for the simple mechanism given by Equation 9.2.3, the reaction rates of oxidation and reduction must be equal, and must be given by I_p/F where F is the Faraday constant. As for the case of the shuttle mechanism, the heat flow associated with entropy changes for a parasitic current is very small and therefore the open circuit heat flow for a non-shuttle mechanism will be approximately given by $|I_p V_{eq}|$ plus the contribution from the reaction enthalpies. For the case presented above, this is given by:

$$\frac{dq}{dt}_{OCV, non-shuttle} \simeq |I_p V_{eq}| - \frac{I_p}{F} (\Delta_{ox} H + \Delta_{red} H) \quad (9.2.6)$$

Therefore, if the observed open circuit heat flow differs from $|I_p V_{eq}|$, this is an indication that the parasitic reactions occurring are not a result of shuttle-type processes and that the reactants are irreversibly consumed. However, a single reaction pair as described by Equation 9.2.3 is a large oversimplification of processes occurring in a real cell, as many reactions might occur and many different products could be formed, some of which

would not contribute to a parasitic current. Therefore, the more general form given by Equation 9.2.4 would be the more appropriate description of the system. Regardless, any deviation from $|I_p V_{eq}|$ would indicate the presence of non-shuttle type reactions. It should also be noted that the above analysis of the open circuit heat flow is equivalent to the parasitic heat flow determined during closed circuit conditions.

9.3 OPEN CIRCUIT HEAT FLOW MEASUREMENTS

9.3.1 Experimental Details

Four machine-made NMC442/graphite pouch cells from a later manufacturing batch than the cells described in previous Chapters were prepared as described in Chapter 3. All cells contained 0.90 g of control electrolyte to which the P211M blend was added. Once filled with electrolyte, the cells were sealed at 87.5% of full vacuum with a 5 s sealing time at 160°C.

The cells were charged at C/20 to 1.5 V, held for 24 h, charged at C/20 to 3.8 V, and then degassed as previously described. Two of the cells were then charged to 4.0 V and the other two to 4.4 V, both at C/20. All cells were then degassed and loaded into the calorimeter. For identification purposes, the two groups of cells are designated as low-V and high-V, respectively. While inside the calorimeter all cells were first allowed 24 hours to thermally equilibrate, then were cycled with a Maccor Series 4000 charger system. The low-V cells then went through the following protocol:

1. {2.8 – 4.0 V at 10 mA} x4
2. {3.9 – 4.0 V} at 5, 4, 2, then 1 mA

3. {Charge to 4.0 V at 1 mA, then OCV for 100 h} x 3
4. {3.9 – 4.0 V} and {4.0 – 4.1 V} each at 5, 4, 2, then 1 mA
5. {Charge to 4.1 V at 1 mA, then OCV for 100 h} x 3
6. {3.9 – 4.0 V}, {4.0 – 4.1 V}, and {4.1 – 4.2 V} each at 5, 4, 2, then 1 mA
7. {Charge to 4.2 V at 1 mA, then OCV for 100 h} x 3
8. Repeat step 6
9. Repeat step 7
10. {3.9 – 4.0 V}, {4.0 – 4.1 V}, {4.1 – 4.2 V}, and {4.2 – 4.3 V} at 5, 4, 2, 1 mA
11. {Charge to 4.3 V at 1 mA, then OCV for 100 h} x 3

The high-V cells went through the following protocol:

1. {2.8 – 4.4 V at 10 mA} x4
2. {4.0 – 4.1 V}, {4.1 – 4.2 V}, {4.2 – 4.3 V}, {4.3 – 4.4 V} each at 5, 4, 2, 1 mA
3. Discharge to 4.1 V at 1 mA, then {OCV for 100 h, charge to 4.1 V at 1 mA} x3
4. Repeat step 2
5. Discharge to 4.2 V at 1 mA, then {OCV for 100 h, charge to 4.2 V at 1 mA} x3
6. Repeat step 2
7. Discharge to 4.3 V at 1 mA, then {OCV for 100 h, charge to 4.3 V at 1 mA} x3
8. Repeat step 2
9. Discharge to 4.4 V at 1 mA, then {OCV for 100 h, charge to 4.4 V at 1 mA} x3
10. Repeat step 2

For both types of cells, only the evolution of the OCV heat flow will be examined here.

9.3.2 Long Term Open Circuit Heat Flow Measurements

Figure 9.3a shows the measured heat flow during protocol step 5 of a low-V cell, where the cell was charged at 1 mA to 4.1 V, then went open circuit for a total of 300 h with 1 mA top-up charges to 4.1 V every 100 h. As expected from previous results, the open circuit heat flow decreases as a function of time. Figure 9.3b shows the corresponding measured voltage as a function of open circuit time. The voltage decay, which is known to be caused by parasitic reactions occurring at the positive electrode^{97,264}, decreases over time, in good agreement with the evolution of the heat flow.

The parasitic current, I_p , is given by the rate of capacity loss, which can be determined from the rate of change of voltage with time, as:

$$I_p = \frac{dQ}{dt} = \left(\frac{dQ}{dV} \right) \left(\frac{dV}{dt} \right) \quad (9.2.7)$$

where Q is the capacity and dQ/dV is known as the differential capacity. In order to calculate I_p , the differential capacity was determined using a positive half cell coin cell, made using the same positive electrode as used in the pouch cells. The discharge capacity data were collected by David Wang on the ultra high precision charger at 40°C at a rate of C/50. In order to convert to the full cell differential capacity, the graphite electrode potential vs Li/Li⁺ was subtracted from the positive half cell voltage (0.07 V over the voltage range of interest here). In order to determine the rate of voltage decay, the observed voltage as a function of time was determined using an average of exponential and second order polynomial functions. This average was done to minimize errors in taking the derivative of one simple function, as errors in curvature are greatly amplified

when taking a derivative. Only the last 50 h of every 100 h voltage segment was used to determine dV/dt to avoid interference of any voltage drops due to concentration gradient relaxation within the electrodes and electrolyte.

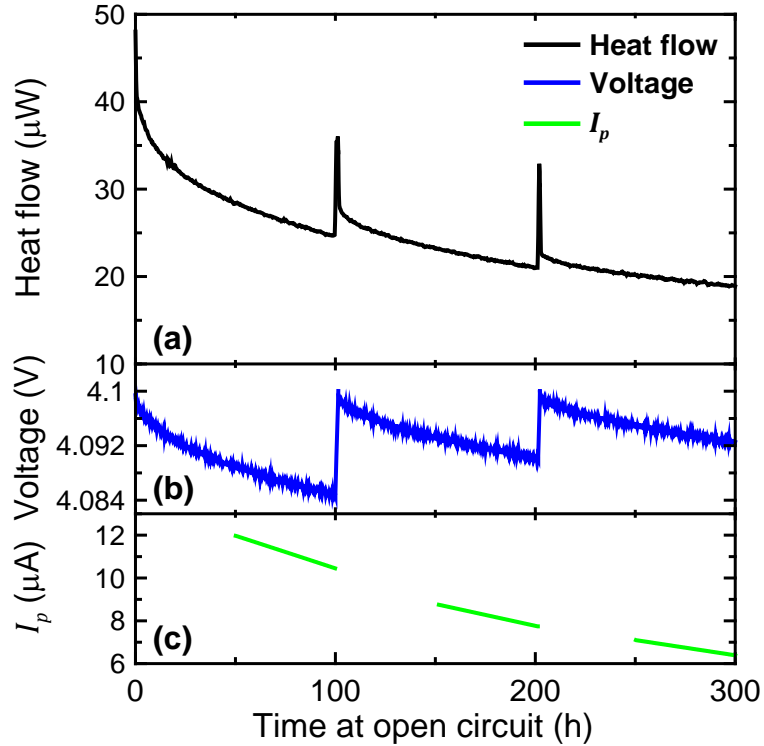


Figure 9.3: (a) Measured open circuit heat flow (black) and (b) corresponding voltage as a function of time at open circuit starting at 4.1 V for a low-V cell. (c) Calculated magnitude of the parasitic current (green) also shown.

Figure 9.3c shows the absolute value of the parasitic current, calculated using Equation 9.2.7. The magnitude of the parasitic current decreases as a function of time under OCV conditions, from approximately 12 μA after 50 h to 6.5 μA after 300 h. It should be noted that over the voltage ranges examined here dV/dt , and therefore the parasitic current, is only sensitive to lithiation state of the positive electrode. The graphite electrode is in the 2+1 plateau¹⁹⁴ and therefore its potential vs Li/Li^+ is constant (shown in Chapter 1, Figure 1.2). The extracted parasitic current was then used to calculate a heat flow equivalent to $|I_p V|$ in order to compare to the measured open circuit heat flow.

Figure 9.4 shows the results of this analysis, as well as that for the open circuit voltage segments starting at 4.2 V (step 7) and 4.3 V (step 11) for the low-V cells, as well as the open circuit segments starting at 4.1 V, 4.2 V, and 4.3 V (steps 3, 5, and 7, respectively) for the high-V cells. The 4.1 V, 4.2 V, and 4.3 V open circuit segments began at 738, 1297, and 2708 h after being loaded into the calorimeter, respectively for the low-V cell, and at 407, 964, and 1511 h, respectively for the high-V cell.

Figure 9.4a shows the comparison of the measured open circuit heat flow starting at 4.1 V to the calculated values of $|I_p V|$ for the low-V cell shown in Figure 9.3. The measured heat flow is smaller than $|I_p V|$ for all three open circuit segments. By comparison to Equation 9.2.4, the observed difference between the two values indicates that there is a net non-zero reaction enthalpy and therefore non-shuttle processes are occurring. However, this does not exclude the possibility of shuttle-type reactions also occurring, but the non-shuttle type reactions must proceed with a large enough rate to result in a noticeable difference between the heat flow and $|I_p V|$. Furthermore, as stated previously, the heat flow associated with the change in entropy of the two electrodes is negligible for small parasitic currents. The decreased value of the heat flow compared to $|I_p V|$ indicates that the net average reaction enthalpy is endothermic.

Figure 9.4b and Figure 9.4c show the same analysis for the OCV segments beginning at 4.2 V (step 7) and 4.3 V (step 11) for the low-V cells. At 4.2 V (Figure 9.4b), the difference between the measured heat flow and $|I_p V|$ is similar to the differences observed at 4.1 V (Figure 9.4a). At 4.3 V (Figure 9.4c), the difference becomes larger, which would represent either a transition to an increasingly endothermic net average reaction enthalpy, an increase in average reaction rate, or some combination thereof. At

175 h into each open circuit segment, the differences between the measured heat flow and $|I_p V|$ for the 4.1, 4.2, and 4.3 V segments were 12, 11, and 18 μW , respectively.

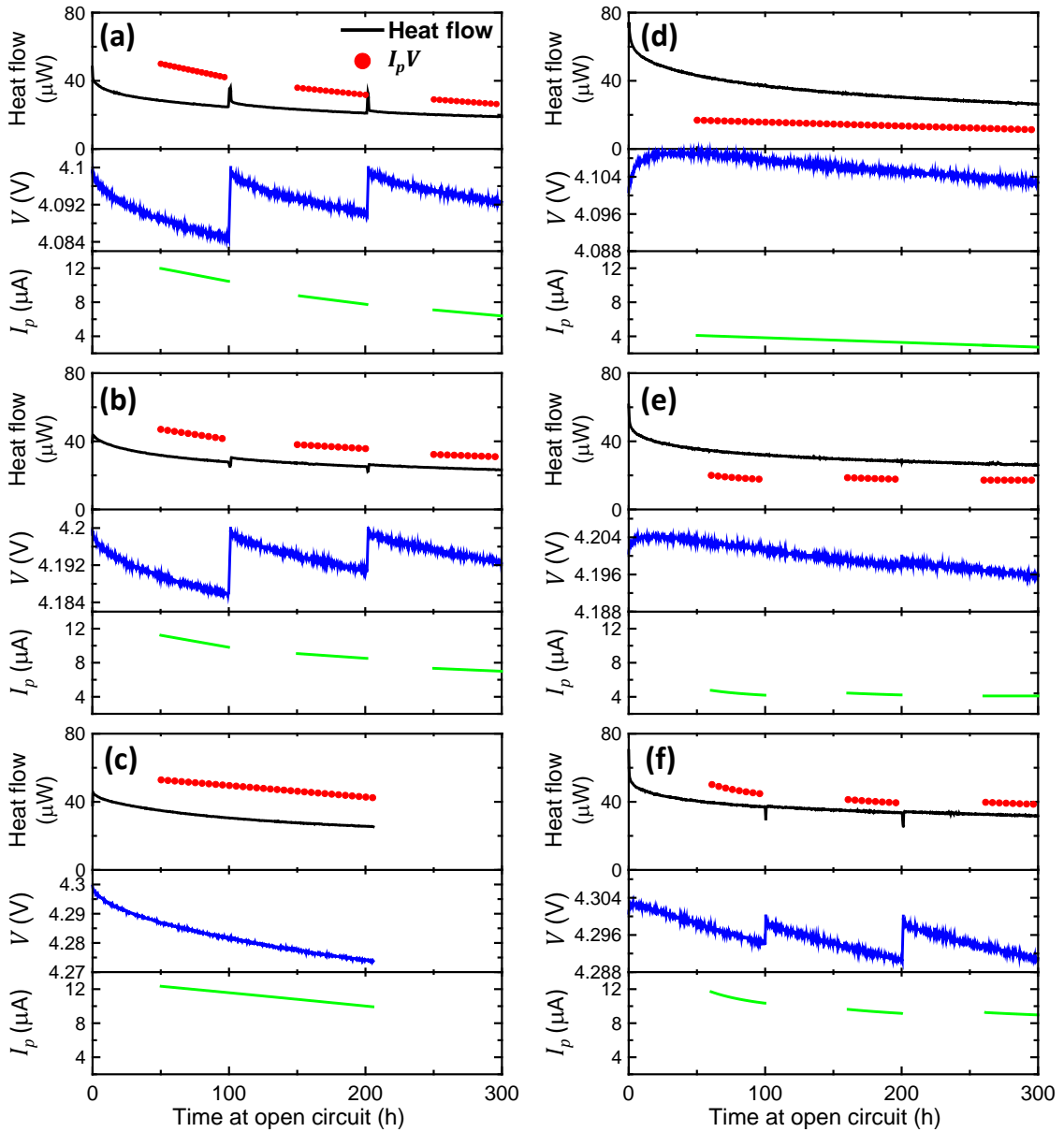


Figure 9.4: Measured open circuit heat flow (black), corresponding measured voltage (blue), calculated I_p (green) and heat flow from $|I_p V|$ (red) as a function of time at open circuit for low-V cells starting from (a) 4.1 V, (b) 4.2 V, and (c) 4.3 V, and for high-V cells starting from (d) 4.1 V, (e) 4.2 V, and (f) 4.3 V.

Figure 9.4d, Figure 9.4e, and Figure 9.4f show the corresponding analysis for OCV segments beginning at 4.1, 4.2, and 4.3 V, respectively for a high-V cell.

Immediately apparent in both Figure 9.4d and Figure 9.4e is the difference in the voltage decay behaviour (and therefore I_p) compared to the low-V cell. This is a result of differences in experimental protocol leading up to the OCV segments. The low-V cells approached the open circuit voltage from a 1 mA charge from a lower voltage, while the high-V cells approached the open circuit from a 1 mA discharge from a higher voltage. As a result, voltage relaxation due to polarization will result in a voltage drop for the low-V cells and a voltage increase for the high-V cells. Therefore, the low-V cells will result in an overestimated I_p , while the high-V cells will underestimate I_p . It is also seen that the voltage decay due to parasitic reactions was not sufficient to drop the voltage below the open circuit set point for the 4.1 V segment or the first two 4.2 V segments, so no top-up charge occurred for those segments.

Figure 9.4d, Figure 9.4e, and Figure 9.4f also show that the observed difference between the measured open circuit heat flow and the calculated $|I_p V|$ changes as a function of the open circuit voltage. During the 4.1 V (Figure 9.4d) and 4.2 V (Figure 9.4e) OCV segments, the measured heat flow is larger than $|I_p V|$ for the high-V cells, which indicates an exothermic net average reaction enthalpy. This is in contrast to the net endothermic enthalpy for the low-V cell. However, the high-V cell was cycled to 4.4 V immediately preceding the open circuit measurements and therefore the chemical species present within the cell, and the corresponding parasitic reactions, would be expected to be very different than for cells that were never charged above the starting open circuit voltage. This is consistent with previous calorimetry results, where one cycle to a high voltage resulted in an increase in the parasitic heat flow observed for subsequent low voltage cycles.

As a function of voltage, the difference between the heat flow and $|I_p V|$ becomes more negative for the low-V cell and transitions from large and positive at 4.1 V to small and negative at 4.3 V for the high-V cell. For both cells this is consistent with a gradual change in the dominant reaction mechanism as a function of voltage. As an example, a large voltage-dependent increase in the reaction rate of an endothermic reaction would explain the voltage-dependent trends in both the low-V and high-V cells. This would then also suggest that the processes that occur at high voltages (> 4.3 V) are not favourable at lower voltages (< 4.3 V) in these cells, such that the products produced at high voltage react through different mechanisms (i.e., exothermic process or processes that do not result in a parasitic current) depending on the electrode potentials. Such a proposal is also consistent with the observed increase in time factor (rate of decrease of parasitic heat flow) as a function of voltage. It was previously suggested that the increase in the time factor was possibly a result of SEI damage and re-formation. Krause *et al.*¹⁷³ extracted a parasitic reaction enthalpy of -212 kJ/mol (exothermic) for the SEI formation processes on graphite electrodes. Therefore, if the electrodes are being re-passivated following high voltage cycles, a net exothermic reaction enthalpy is not unexpected. Such a process would also not result in a change in the lithium content at the positive electrode, which is consistent with the very small parasitic current observed in Figure 9.4d and Figure 9.4e.

The observed trend of an increasingly endothermic dominant reaction is also consistent with the increase of gas production as a function of voltage, as has been observed for such NMC442/graphite pouch cells.^{135,136} Reactions converting liquid or solid reactants to a gaseous products have large positive changes in reaction entropy, $\Delta_r S$.

This results in a decrease in free energy, which can result in endothermic reactions becoming favourable.

Figure 9.4 only shows results from one low-V and one high-V cell for clarity. Pair cell data were collected as discussed in Section 9.3.1; therefore, Figure 9.5 shows an example of the agreement of the measured heat flows and voltages for the 4.1 V OCV segments for all four cells (two low-V and two high-V). Both the measured heat flow and voltage decay are virtually indistinguishable between pair cells. Therefore the results and analysis shown Figure 9.4 are not limited by cell-to-cell variability, and the largest source of error is attributed to the determination of dV/dt due to taking the derivative of a fitted curve and relaxation effects as previously discussed.

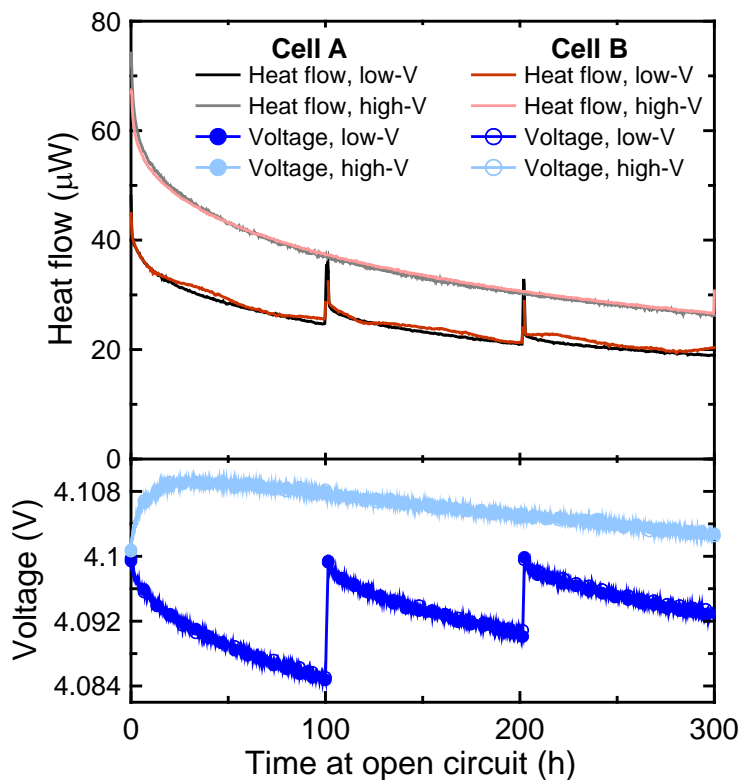


Figure 9.5: Measured open circuit open heat as a function of time at open circuit starting at 4.1 V for two low-V pair cells (black and dark red), and two high-V pair cells (grey and light red). Corresponding measured voltage also shown for the two low-V pair cells (solid and open dark blue circles) and two high-V pair cells (solid and open light blue circles).

The low-V cells went through two open circuit segments beginning at 4.2 V as outlined in Section 9.3.1 (steps 7 and 9). For the cell shown in Figure 9.4, the two OCV segments began at 1297 h and 1915 h after loading into the calorimeter, respectively, and between the two segments the cell was not charged above 4.2 V. Figure 9.6 shows a comparison of the measured heat flow and voltage, as well as the calculated $|I_p|$ and $|I_p V|$ values between steps 7 and 9. Both the open circuit heat flow and the parasitic current were decreased for step 9 compared to step 7, as would be expected for passivation-type processes.

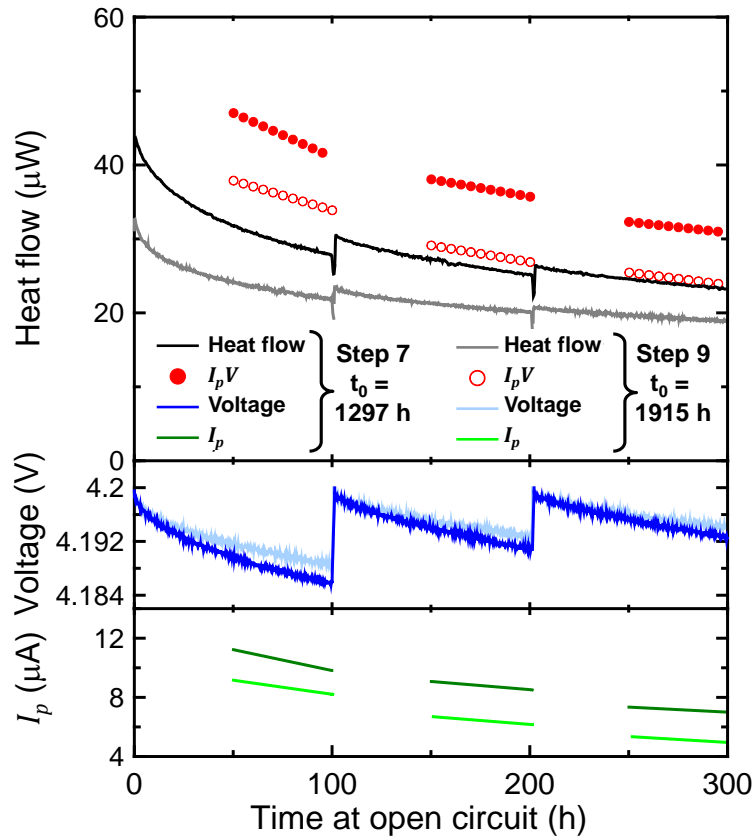


Figure 9.6: Measured open circuit heat flow as a function of time for a low-V cell during two open circuit segments starting at 4.2 V; one starting at 1297 h (black) and a second starting at 1915 h (grey) after being loaded in the calorimeter. Corresponding voltages (dark and light blue, respectively), calculated $|I_p|$ values (dark and light green, respectively), and calculated $|I_p V|$ values (solid and open red circles, respectively) are also shown.

For the same voltage range it would be expected that the net enthalpy of reaction would remain constant but the reaction rate would decrease. This is qualitatively seen in Figure 9.6, where the difference between the measured heat flow and the calculated $|I_p V|$ values decreases by approximately the same fraction as the parasitic current. This is cautiously quantified in Table 9.1 under the large assumption that the parasitic reactions occurring in the cell all result in a parasitic current and that the open circuit heat flow can be approximated by:

$$\frac{dq}{dt}_{ocv} = |I_p V| - \frac{I_p}{F} (\Delta_r H^{ave}) \quad (9.2.8)$$

where $\Delta_r H^{ave}$ is the weighted average of all reaction enthalpies. As stated above, this ignores any contribution from reactions not resulting in a parasitic current measurable by dV/dt , such as the formation of SEI components on the negative electrode.

Table 9.1: Comparison of measured heat flow, calculated $|I_p V|$ values, the difference between them, and an extracted average reaction enthalpy at three time points in steps 7 and 9 (4.2 V OCV segments) of a low-V cell.

Time		Heat flow (μW)	$I_p V$ (μW)	Heat Flow - $I_p V$ (μW)	I_p (μA)	$\Delta_r H^{ave, \dagger}$ (kJ/mol)
$t_0 + 75$ h	Step 7	29.4(1)	44.1(8)	-14.7(9)	10.5(2)	135(11)
	Step 9	23.2(1)	35.9(8)	-12.7(9)	8.7(2)	141(14)
$t_0 + 175$ h	Step 7	26.1(1)	36.9(8)	-10.8(9)	8.8(2)	118(13)
	Step 9	20.7(1)	28(6)	-7.3(7)	6.4(1)	110(12)
$t_0 + 275$ h	Step 7	23.9(1)	31.6(5)	-7.7(6)	7.2(1)	103(10)
	Step 9	19.4(1)	26.1(5)	-6.7(6)	5.2(1)	124(14)

\dagger Assuming all reactions result in a parasitic current

As a result of such a simplification, the extracted values of $\Delta_r H^{ave}$ are not intended to be true measures of the average reaction enthalpy. However, the extracted values are useful in showing that, between the two open circuit segments, the reaction pathways have not changed appreciably, and that the decrease in open circuit heat flow is almost entirely a result of a decrease in the parasitic reaction rate.

9.4 CONCLUSIONS

In this Chapter, simple model systems were used to interpret the meaning of the parasitic heat flow, by determining the impact of the reaction type on the expected open circuit heat flow. It was observed that a large fraction of the parasitic heat flow is a result of the passage of parasitic current through the cell. Therefore, the differences observed in the extracted parasitic heat flows throughout the previous Chapters are predominantly a result of differences in the reaction rate. Deviations between the measured heat flow and $|I_p V|$ were shown to indicate the presence of irreversible non-shuttle reactions. The dominant reaction mechanism is suggested to change as a function of voltage, and it was suggested that this was a result of an increase in the rate of largely endothermic reactions which may be associated with gas production.

Results presented in this Chapter are preliminary and primarily qualitative, mostly due to data collection methods and difficulties in the accurate determination of the parasitic current. Future work is required to minimize errors and extract meaningful reaction enthalpies. A voltage hold should be done prior to the open circuit segments to minimize the contribution of concentration gradient relaxation. The voltage should also be measured on high precision equipment tailored for open circuit measurements, where

the voltage is only measured periodically and is properly disconnected (true open circuit) between measurements to minimize current draw through the charger channel.

This can then also be extended to various additive and solvent systems such as those explored previously to determine the impact of the electrolyte composition.

CHAPTER 10

CONCLUSIONS AND FUTURE WORK

10.1 CONCLUSIONS

This thesis introduced the use of isothermal microcalorimetry as a tool for the accurate measurement and quantification of the heat flow associated with parasitic reactions that cause lithium ion cell degradation. This was applied to the study of the impact of electrolyte composition across many cell chemistries. This method is rapid, *in operando*, and the results are a direct function of cell voltage. This provides a significant advantage over more standard electrochemical techniques that can only extract the cycle-averaged impact of electrolyte composition, in which case any voltage dependencies are determined in indirect and discrete manners.

The majority of the work presented here focused on the development of the method to extract and interpret the parasitic heat flow as a function of both voltage and time. The initial experiments presented in Chapter 4 used a comparative method where the heat flows of NMC111/graphite pouch cells which varied only in electrolyte additive composition were examined. The observed differences in the total heat flows were then attributed to differences in the parasitic heat flow. It was shown that ternary electrolyte additive blends containing 2% VC, 1% TTSPi, and 1% of a sulfur-containing additive had the largest reductions in heat flow, and that these results were very well correlated to UHPC and long-term cycling experiments. It was also found that the additives had the most profound impact at higher voltages, indicating that the additives were reducing the rate of parasitic reactions that occur at the positive electrode.

In order to extract the parasitic heat flow, and not just indirectly monitor its effect, Chapter 5 presented the use of an empirical three-component model of the heat flow. The heat flow was measured for cells undergoing narrow voltage range cycling at various currents, and it was shown that fitting that data to the empirical model allowed for the separation of the total heat flow into individual components. Particular emphasis was placed on the heat flow resulting from parasitic reactions, and presented the first direct measurements of the voltage-dependent impact of the electrolyte composition on the parasitic reactions occurring within the cells. This allowed for comparisons between cell chemistries, which showed that for the same electrolyte composition, HV-LCO/graphite pouch cells had lower parasitic heat flows than NMC111/graphite cells. This was attributed to differences in both the positive and negative electrodes.

The empirical model was further developed and improved throughout this work by adding a time dependence to the parasitic heat flow in Chapter 6 and including the heat flow associated with inherent hysteresis in Chapters 7 and 8. As the model was developed, it was applied to the determination of the impact of a variety of electrolyte additives, additive blends, and solvents on several different cell chemistries.

The inclusion of the time dependence into the parasitic heat flow provided additional information on the functionality of the electrolyte additives. Of particular importance, the time-dependent parasitic heat flow highlighted profound changes in the parasitic reaction mechanism at high voltage for HV-LCO/graphite cells containing V211M. An increasing parasitic heat flow as a function of time was observed when cycled between 4.3 – 4.4 V. However, when cycled between 4.2 – 4.3 V, the same additive blend had a small and decreasing parasitic heat flow as a function of time. Furthermore, such behaviour was not observed for the same and similar electrolyte

compositions for NMC442/graphite cells, indicating that the parasitic reactions are a result of electrolyte-electrode interactions and are very sensitive to changes in either component. This example highlights the utility of the time-dependent empirical model to rapidly extract the voltage dependence of the parasitic reactions, in terms of changes to both the reaction rate and the dominant reaction mechanism. However, complementary experiments such as XPS, GS-MS, theoretical calculations, and *in situ* gas generation measurements are required to identify the products of such reactions and to propose possible parasitic reaction pathways.

Further time-dependent experiments on NMC442/graphite and NMC811/graphite cells also showed a change in the dominant parasitic reaction mechanisms as a function of voltage. When a large increase in the parasitic heat flow was observed, it was accompanied by an increase in the time factor (rate of parasitic heat flow decrease). One possible explanation is the protective SEI layers on the electrodes are disrupted, either through the high voltage oxidation of previously existing components or the interaction of newly formed reaction products with existing components. Such processes result in exposed electrode surfaces which would then be quickly passivated, leading to increases in both the parasitic heat flow and the time factor. This was found to be well-correlated to the onset of gas production. The voltage-dependent change in the dominant reaction pathways is also supported by other experimental results such as XPS, *in situ* gas generation, UHPC cycling, etc.^{133,136,219,256,259}

Throughout this work there was a particular focus on high voltage studies since operating cells under such conditions presents a significant challenge due to the oxidative instability of the electrolyte components. This challenge must be addressed for next-generation batteries where high energy densities are achieved by increasing the upper

cutoff voltage. The calorimetry experiments presented here showed that the parasitic heat flows observed above 4.3 V are very large, regardless of the electrolyte composition used. Experiments on NMC442/graphite pouch cells up to 4.7 V containing various solvents and additives showed several differences in parasitic heat flow behaviour. The linear carboxylic esters are particularly sensitive to the upper cutoff voltage and had a rapidly increasing parasitic heat flow as a function of time above 4.4 V. The comparison of the control solvents (3:7 EC:EMC) to the fluorinated solvents (3:7 FEC:TFEC) showed a distinct difference in the voltage dependence of the parasitic heat flow. Below 4.4 V, the cell containing control + V211M showed the lowest parasitic heat flow and narrow range cycling experiments between 4.2 – 4.3 V showed good capacity retention. However, at high voltage (> 4.4 V), there was a large increase in parasitic heat flow and narrow range cycling experiments between 4.4 – 4.5 V showed poor capacity retention. In contrast, the cell containing FEC:TFEC had a larger parasitic heat flow at low voltage, but the voltage-dependent increase of the parasitic heat flow was reduced such that above 4.4 V, the FEC:TFEC cell had the lowest parasitic heat flow. Narrow voltage range cycling experiments showed the same capacity retention as a function of cycle number regardless of the voltage range. These results suggested that the control + V211M cells had more effective passivation layers at the negative electrode but experienced a large amount of electrolyte oxidation at the positive electrode at high voltages, while FEC:TFEC results in a worse passivation layer at the negative electrode (larger parasitic reaction rate at low voltage), but reduced electrolyte oxidation at the positive electrode.

Once the method of extracting the parasitic heat flow was developed, the meaning and origin of that heat flow was explored using thought experiments and open circuit measurements. It was demonstrated that a large portion of the observed parasitic heat

flow is a result of the flow of parasitic current, and therefore the previously observed differences in parasitic heat flow can be primarily attributed to differences in the parasitic reaction rate.

The comparison of the observed open circuit heat flow and the heat flow from the parasitic current indicated that reactions include irreversible non-shuttle processes. The dominant reaction mechanism was found to change as a function of voltage, and it was suggested that this was a result of an increase in the rate of largely endothermic reactions which may be associated with gas production. This analysis was largely qualitative and was only performed for one cell chemistry and one electrolyte composition. However, it served to lay the groundwork for future high-impact experiments to further the understanding of on the nature of the parasitic reactions that lead to cell failure.

Overall, the technique of isothermal microcalorimetry has been shown to be particularly well suited to the study of the impact of electrolyte composition on the parasitic reactions occurring within lithium ion cells. The results of such experiments have provided valuable insight on the complex roles of the electrode and electrolyte compositions on those reactions, as well as revealing how those roles depend on both voltage and time.

10.2 FUTURE WORK

With the method of extracting the parasitic heat flow now established, future work can focus on how such data can be used to further the understanding of the nature of the parasitic reactions. As was discussed in Chapter 9, the open circuit heat flow can be used to determine the relative impacts of the reaction rate and net reaction enthalpy. However,

there are small experimental adjustments that should be made in order to collect reliable data such that quantitative conclusions can be made. As discussed in Chapter 9, since the largest error was associated with the calculation of the parasitic current, prior to the start of the open circuit segments, there should be a voltage hold to eliminate the concentration gradients within the electrodes that occur during cycling. Furthermore, these experiments should be performed using charging equipment that is tailored for open circuit measurements such as “smart storage” systems where the voltage is measured intermittently and the cells are properly disconnected (true open circuit) between measurements. Such systems minimize current draw through the charger and the noise in voltage data. These experiments should also be used to investigate the impact of electrolyte and electrode compositions. With such improvements in the data collection methodology, the separation of the parasitic reaction rate from the average reaction enthalpy of reactions associated with the parasitic current will be possible. This will also allow for the determination of the average reaction enthalpy of current-independent reactions.

The separation of these components of the parasitic heat flow would also be aided by performing the experiments at various temperatures. The TAMIII isothermal bath temperature can be set between 15 and 150°C, and can also be programmed to vary as a function of time over the course of an experiment, either as a temperature ramp or in discrete temperature steps. Or, if one had especially deep pockets, a second or third calorimeter could be used to study cells with identical histories across two or three temperatures simultaneously.

Over a moderate temperature range (e.g., 20 to 50 °C) the change in the parasitic heat flow as a function of temperature can be used to separate the reaction rate and

average enthalpy of reaction, assuming that no new reactions are activated at increased temperatures. The reaction rate, and therefore the parasitic current, will increase as a function of temperature, while the enthalpy would remain approximately constant for the same reaction mechanism. As developed in Chapter 9, the difference between the measured open circuit heat flow and $|I_p V|$ is equal to the sum of over all i reactions of the reaction rate times the reaction enthalpy of the i^{th} reaction. Reaction rates normally vary exponentially as a function of temperature, and therefore fitting the temperature dependence of this difference will allow for the extraction of the average reaction enthalpy and provide information of the kinetics of the parasitic reactions.

Higher temperature experiments can also be used to investigate whether any new reactions are initiated. This would be observed as deviations from extrapolated lower temperature performance. Such experiments will be useful in examining potential additives for high temperature applications. Also of particular importance will be determining whether accelerating aging tests, where the temperature is raised to increase the rate of parasitic degradation, can be used to accurately predict low temperature long-term cell lifetimes, or whether the high temperature parasitic reactions have little resemblance to those occurring at low or moderate temperatures.

Once the method of accurately extracting the average reaction enthalpy is developed, it will be particularly important to examine the impact of electrolyte composition, especially when different solvent systems are used. Throughout this thesis, it was assumed that the differences in reaction enthalpies were negligible and that the differences in the observed parasitic heat flow were a result of differences in reaction rate. The results presented in Chapter 9 showed that a significant portion of the parasitic heat flow was indeed a result of the parasitic current (reaction rate). However, the impact of

the electrolyte composition on the reaction enthalpy should be verified through open circuit measurements for cells containing various electrolyte compositions.

Furthermore, the concurrent use of ultra high precision coulometry can also aid in the separation of the reaction rate from the average enthalpy of reaction. The UHPC cycling of cells allows for the accurate determination of the coulombic efficiency (CE) and charge endpoint capacity slippage. These parameters can then be correlated to the extracted parasitic heat flow. The CE can be used to calculate the amount of charge lost during a cycle, and is given by:

$$\text{moles of charge lost} = \frac{\text{capacity lost}}{(F/3600)} = \frac{Q_c - Q_d}{(F/3600)} = \frac{Q_c(1-CE)}{(F/3600)} \quad (10.2.1)$$

where Q_c and Q_d are the charge and discharge capacities for one cycle, respectively, and F is the Faraday constant. To account for the CE being a cycle-averaged parameter, the parasitic heat flow must be integrated over the same cycle to give a parasitic energy. As was discussed in Chapter 9, this parasitic heat flow has contributions from both the passage of parasitic current in the cell and the weighted average of all reaction enthalpies. Therefore, significant care must be taken when correlating the amount of charge lost to the parasitic energy in order to separate the two contributions. This is especially true when using the CE measurements as the charge lost also includes contributions from active Li lost to the SEI which would not result in a parasitic current. Therefore the correlation of the parasitic heat flow to the charge endpoint capacity slippage would also be of high importance, as Smith *et al.*⁷⁰ showed that it is related to parasitic reactions occurring at the positive electrode, and therefore the parasitic current. The comparison between CE and charge endpoint capacity slippage correlations to the parasitic heat flow would then allow for a comparison of the effect of electrolyte oxidation at the positive

electrode compared to the parasitic current-independent mechanisms. This will allow for a better understanding of how electrolyte additives and solvents impact the parasitic reactions on both electrodes. Such an analysis would allow for a study of the voltage dependence, and therefore is considered complementary to the OCV experiments.

It is important to note that the variable rate narrow voltage range experiments used to extract the parasitic heat flow throughout this thesis are not well-suited for the extraction of the CE and charge endpoint capacity slippage. In the narrow range cycling protocol each successive cycle is done at a smaller current. The starting rSOC during charge is determined from the previous higher current cycle. Therefore, due to polarization effects, this reduces the charge capacity compared to the achieved discharge capacity. This leads to anomalously large CE values and underestimated amounts of charge lost. This effect is more pronounced with larger currents and would be a nonlinear error as a function of cycle number. Furthermore, between successive endpoints the cells would be discharged and charged at two different currents, leading to an overestimation of the charge endpoint capacity slippage. Therefore, it is proposed that UHPC measurements should be done using multiple 1 mA cycles at the top of charge. This increases the experiment time, but allows for the accurate determination of CE and charge endpoint slippage while simultaneously providing a good measure of the parasitic heat flow.

Isothermal microcalorimetry is also particularly well suited to the study of how various aging mechanisms influence cell performance. For example, it will be of importance to determine the relative impact of storage after formation (shelf-life) for various times, states of charge, and temperatures. These results could also be compared to cells that were cycled at similar conditions to determine any differences between shelf-

life and cycle-life. Using the empirical model to fit the heat flow of such cells will be of significant importance, as changes in the parasitic reactions would be observed through differences in the parasitic heat flow. Furthermore, changes in the active materials could be observed through differences in the heat flow associated with changes in entropy. Such experiments would require long-term planning to begin tests well ahead of the intended calorimeter experiment time. Working in units of 12 calorimeter channels, such an experiment could be set up using two groups of 12 cells, one group of cells that were stored and the another group of cells that were cycled. A proposed experiment is presented here. In the storage group, 2 cells would be used “fresh” (minimal time after formation), and 4 cells would have undergone storage at: (1) 50% SOC at 20°C, (2) 50% SOC at 40°C, (3) 90% SOC at 20°C, and (4) 90% SOC at 40°C for a period of 1 year, while another 4 cells would undergo the same storage protocols, but for 6 months. The two remaining calorimeter spots could be used for duplicate cells for verification of reproducibility. A similar experiment batch would be used for cells which are cycled, where instead of different storage at states of charge, cycling would be performed to either a low upper cutoff voltage (e.g., 4.0 V) or a high upper cutoff voltage (e.g., 4.4 V), again at two different temperatures.

Finally, and more broadly, in order to further the understanding of the impact of electrolyte composition on the parasitic reactions and cell lifetime, correlations need to be quantitatively made between the parasitic heat flow and the results of other experiments such as EIS, XPS, GC-MS, FTIR spectroscopy, *in situ* gas measurements, electron microscopy, theoretical calculations, etc. Cells where calorimetric data show a change in the dominant reaction pathway as a function of voltage can be used to target other experiments. For example, determining whether the change in reaction mechanism

corresponds to differences in the electrode surface species (XPS, FTIR), changes in the concentrations of electrolyte components (GS-MS), production or consumption of gas (*in situ* gas), nature of gaseous species (GC-MS), changes in the SEI thicknesses on both electrodes (microscopy, XPS, EIS), some or all of the above, etc. The possible identification of the dominant reaction mechanisms that ultimately cause cell failure can lead to smarter electrolyte development in using components to mitigate such reactions. It may turn out that dramatic changes in both the electrode and electrolyte design are necessary to overcome the significant challenges of operating at high voltages. It is clear that a large collaborative effort is required to understand the degradation reactions in lithium ion cells, of which isothermal microcalorimetry has been shown to provide an important piece to the puzzle.

REFERENCES

1. Tesla Motors Inc., *Model S Quick Guide* (2014).
2. Chevrolet Warranty and Extended Protection Info, 2014 Warranty Details, <http://www.chevrolet.com/owners/warranty.html> (accessed March 8, 2015).
3. Nissan USA, 2015 Leaf® Charging and Range, <http://www.nissanusa.com/electric-cars/leaf/charging-range/battery> (accessed March 8, 2015).
4. Bosch BPT- 5 Hybrid, The Battery Service Life, <http://bosch-solar-storage.com/the-battery/service-life/> (accessed March 7, 2015).
5. Saft Batteries, Press Releases, <http://www.saftbatteries.com/press/press-releases/saft-launches-world%E2%80%99s-first-long-term-warranty-extension-option-domestic-li-ion> (accessed March 8, 2015).
6. K. Xu, *Chem. Rev.*, **114**, 11503–11618 (2014).
7. J. C. Burns, A. Kassam, N. N. Sinha, L. E. Downie, L. Solnickova, B. M. Way, and J. R. Dahn, *J. Electrochem. Soc.*, **160**, A1451–A1456 (2013).
8. D. Aurbach, B. Markovsky, G. Salitra, E. Markevich, Y. Talyossef, M. Koltypin, L. Nazar, B. Ellis, and D. Kovacheva, *J. Power Sources*, **165**, 491–499 (2007).
9. T. Reddy, *Linden's Handbook of Batteries, 4th Edition*, 4th ed., p. 1200, McGraw-Hill Professional, (2010).
10. H. M. Dahn, A. J. Smith, J. C. Burns, D. A. Stevens, and J. R. Dahn, *J. Electrochem. Soc.*, **159**, A1405–A1409 (2012).
11. K. Mizushima, P. C. Jones, P. J. Wiseman, and J. B. Goodenough, *Mater. Res. Bull.*, **15**, 783–789 (1980).
12. Z. Liu, A. Yu, and J. Y. Lee, *J. Power Sources*, **81–82**, 416–419 (1999).
13. T. Ohzuku and Y. Makimura, *Chem. Lett.*, **30**, 642–643 (2001).
14. Z. Lu, D. D. MacNeil, and J. R. Dahn, *Electrochem. Solid-State Lett.*, **4**, A200–A203 (2001).
15. J. K. Ngala, N. A. Chernova, M. Ma, M. Mamak, P. Y. Zavalij, and M. S. Whittingham, *J. Mater. Chem.*, **14**, 214–220 (2004).
16. M.-H. Kim, H.-S. Shin, D. Shin, and Y.-K. Sun, *J. Power Sources*, **159**, 1328–1333 (2006).

17. J. S. Weaving, F. Coowar, D. A. Teagle, J. Cullen, V. Dass, P. Bindin, R. Green, and W. J. Macklin, *J. Power Sources*, **97–98**, 733–735 (2001).
18. D. Guerard and A. Herold, *Carbon*, **13**, 337–345 (1975).
19. R. Fong, U. von Sacken, and J. R. Dahn, *J. Electrochem. Soc.*, **137**, 2009–2013 (1990).
20. H. Selig and L. B. Ebert, *Adv. in Inorg. Chem. and Radiochem.*, **23**, 281–327 (1980).
21. S. S. Zhang and T. R. Jow, *J. Power Sources*, **109**, 458–464 (2002).
22. J. M. Tarascon and D. Guyomard, *Solid State Ion.*, **69**, 293–305 (1994).
23. D. Aurbach, Y. Ein-Ely, and A. Zaban, *J. Electrochem. Soc.*, **141**, L1–L3 (1994).
24. D. Aurbach, A. Zaban, A. Schechter, Y. Ein-Eli, E. Zinigrad, and B. Markovsky, *J. Electrochem. Soc.*, **142**, 2873–2882 (1995).
25. D. Aurbach, Y. Ein-Eli, B. Markovsky, A. Zaban, S. Luski, Y. Carmeli, and H. Yamin, *J. Electrochem. Soc.*, **142**, 2882–2890 (1995).
26. K. Takata, M. Morita, Y. Matsuda, and K. Matsui, *J. Electrochem. Soc.*, **132**, 126–128 (1985).
27. S. S. Zhang, K. Xu, and T. R. Jow, *J. Electrochem. Soc.*, **149**, A586–A590 (2002).
28. M. Armand, M. Gauthier, and D. Muller, US Patent 5021308 A (1991).
29. J. R. Dahn, U. von Sacken, M. W. Juzkow, and H. Al-Janaby, *J. Electrochem. Soc.*, **138**, 2207–2211 (1991).
30. A. Webber, *J. Electrochem. Soc.*, **138**, 2586–2590 (1991).
31. M. Ue, *J. Electrochem. Soc.*, **141**, 3336–3342 (1994).
32. J. L. Nowinski, P. Lightfoot, and P. G. Bruce, *J. Mater. Chem.*, **4**, 1579–1580 (1994).
33. M. Ue, M. Takeda, M. Takehara, and S. Mori, *J. Electrochem. Soc.*, **144**, 2684–2688 (1997).
34. M. Ue, A. Murakami, and S. Nakamura, *J. Electrochem. Soc.*, **149**, A1572–A1577 (2002).
35. G. G. Eshetu, S. Grugeon, G. Gachot, D. Mathiron, M. Armand, and S. Laruelle, *Electrochimica Acta*, **102**, 133–141 (2013).

36. H.-B. Han, S.-S. Zhou, D.-J. Zhang, S.-W. Feng, L.-F. Li, K. Liu, W.-F. Feng, J. Nie, H. Li, X.-J. Huang, M. Armand, and Z.-B. Zhou, *J. Power Sources*, **196**, 3623–3632 (2011).
37. L. Zhang, L. Chai, L. Zhang, M. Shen, X. Zhang, V. S. Battaglia, T. Stephenson, and H. Zheng, *Electrochimica Acta*, **127**, 39–44 (2014).
38. K. Xu, S. Zhang, T. R. Jow, W. Xu, and C. A. Angell, *Electrochem. Solid-State Lett.*, **5**, A26–A29 (2002).
39. K. Xu, S. Zhang, B. A. Poese, and T. R. Jow, *Electrochem. Solid-State Lett.*, **5**, A259–A262 (2002).
40. K. Xu, U. Lee, S. Zhang, M. Wood, and T. R. Jow, *Electrochem. Solid-State Lett.*, **6**, A144–A148 (2003).
41. K. Xu, S. Zhang, and T. R. Jow, *Electrochem. Solid-State Lett.*, **8**, A365–A368 (2005).
42. S. Shui Zhang, *Electrochem. Commun.*, **8**, 1423–1428 (2006).
43. S. S. Zhang, K. Xu, and T. R. Jow, *J. Power Sources*, **156**, 629–633 (2006).
44. T. R. Jow, K. Xu, and S. Zhang, US Patent 7172834 B1 (2007).
45. S. S. Zhang, *J. Power Sources*, **162**, 1379–1394 (2006).
46. K. Xu, *Chem. Rev.*, **104**, 4303–4418 (2004).
47. Q. Zhong, A. Bonakdarpour, M. Zhang, Y. Gao, and J. R. Dahn, *J. Electrochem. Soc.*, **144**, 205–213 (1997).
48. T. Ohzuku, S. Takeda, and M. Iwanaga, *J. Power Sources*, **81–82**, 90–94 (1999).
49. M. Egashira, H. Takahashi, S. Okada, and J. Yamaki, *J. Power Sources*, **92**, 267–271 (2001).
50. K. Xu and C. A. Angell, *J. Electrochem. Soc.*, **145**, L70–L72 (1998).
51. J. Wolfenstine and J. Allen, *J. Power Sources*, **142**, 389–390 (2005).
52. L. Yang, B. Ravdel, and B. L. Lucht, *Electrochem. Solid-State Lett.*, **13**, A95–A97 (2010).
53. T. Achiha, T. Nakajima, Y. Ohzawa, M. Koh, A. Yamauchi, M. Kagawa, and H. Aoyama, *J. Electrochem. Soc.*, **157**, A707–A712 (2010).
54. Z. Zhang, L. Hu, H. Wu, W. Weng, M. Koh, P. C. Redfern, L. A. Curtiss, and K. Amine, *Energy Environ. Sci.*, **6**, 1806–1810 (2013).

55. R. Mogi, M. Inaba, S.-K. Jeong, Y. Iriyama, T. Abe, and Z. Ogumi, *J. Electrochem. Soc.*, **149**, A1578–A1583 (2002).
56. H. Mao, J. N. Reimers, and U. V. Sacken, US Patent 5891592 A (1999).
57. M. C. Smart, B. V. Ratnakumar, V. S. Ryan-Mowrey, S. Surampudi, G. K. S. Prakash, J. Hu, and I. Cheung, *J. Power Sources*, **119–121**, 359–367 (2003).
58. L. Hu, Z. Zhang, and K. Amine, *Electrochem. Commun.*, **35**, 76–79 (2013).
59. L. Hu, Z. Xue, K. Amine, and Z. Zhang, *J. Electrochem. Soc.*, **161**, A1777–A1781 (2014).
60. T. Okumura and R. Inoue, US Patent 20110195319 (2011).
61. T. Okumura, R. Inoue, and T. Abe, US Patent 20110171501 (2011).
62. M. C. Smart, B. V. Ratnakumar, and S. Surampudi, *J. Electrochem. Soc.*, **149**, A361–A370 (2002).
63. R. Petibon, C. P. Aiken, L. Ma, D. Xiong, and J. R. Dahn, *Electrochimica Acta*, **154**, 287–293 (2015).
64. R. Petibon, J. Harlow, D. B. Le, and J. R. Dahn, *Electrochimica Acta*, **154**, 227–234 (2015).
65. P. Arora and Z. Zhang, *Chem. Rev.*, **104**, 4419–4462 (2004).
66. S. S. Zhang, *J. Power Sources*, **164**, 351–364 (2007).
67. X. Huang, *J. Solid State Electrochem.*, **15**, 649–662 (2010).
68. X. Chen, W. Xu, J. Xiao, M. H. Engelhard, F. Ding, D. Mei, D. Hu, J. Zhang, and J.-G. Zhang, *J. Power Sources*, **213**, 160–168 (2012).
69. A. J. Smith, J. C. Burns, and J. R. Dahn, *Electrochem. Solid-State Lett.*, **13**, A177–A179 (2010).
70. A. J. Smith, J. C. Burns, D. Xiong, and J. R. Dahn, *J. Electrochem. Soc.*, **158**, A1136–A1142 (2011).
71. A. J. Smith, J. C. Burns, S. Trussler, and J. R. Dahn, *J. Electrochem. Soc.*, **157**, A196–A202 (2010).
72. P. Ganesh, P. R. C. Kent, and D. Jiang, *J. Phys. Chem. C*, **116**, 24476–24481 (2012).
73. V. A. Agubra and J. W. Fergus, *J. Power Sources*, **268**, 153–162 (2014).

74. X. Zhang, R. Kostecki, T. J. Richardson, J. K. Pugh, and P. N. Ross, *J. Electrochem. Soc.*, **148**, A1341–A1345 (2001).
75. J. Xia, N. N. Sinha, L. P. Chen, G. Y. Kim, D. J. Xiong, and J. R. Dahn, *J. Electrochem. Soc.*, **161**, A84–A88 (2014).
76. J. Xia, N. N. Sinha, L. P. Chen, and J. R. Dahn, *J. Electrochem. Soc.*, **161**, A264–A274 (2014).
77. E. Peled, *J. Electrochem. Soc.*, **126**, 2047–2051 (1979).
78. D. Aurbach, Y. Ein-Eli, O. C. (Youngman), Y. Carmeli, M. Babai, and H. Yamin, *J. Electrochem. Soc.*, **141**, 603–611 (1994).
79. E. Endo, K. Tanaka, and K. Sekai, *J. Electrochem. Soc.*, **147**, 4029–4033 (2000).
80. M. Nie and B. L. Lucht, *J. Electrochem. Soc.*, **161**, A1001–A1006 (2014).
81. I. A. Shkrob, Y. Zhu, T. W. Marin, and D. Abraham, *J. Phys. Chem. C*, **117**, 19255–19269 (2013).
82. X. J. Wang, H. S. Lee, H. Li, X. Q. Yang, and X. J. Huang, *Electrochem. Commun.*, **12**, 386–389 (2010).
83. E. Peled, D. Golodnitsky, and G. Ardel, *J. Electrochem. Soc.*, **144**, L208–L210 (1997).
84. P. Verma, P. Maire, and P. Novák, *Electrochimica Acta*, **55**, 6332–6341 (2010).
85. M. Nie, D. Chalasani, D. P. Abraham, Y. Chen, A. Bose, and B. L. Lucht, *J. Phys. Chem. C*, **117**, 1257–1267 (2013).
86. R. Dedryvère, H. Martinez, S. Leroy, D. Lemordant, F. Bonhomme, P. Biensan, and D. Gonbeau, *J. Power Sources*, **174**, 462–468 (2007).
87. R. Dedryvère, S. Laruelle, S. Grugeon, L. Gireaud, J.-M. Tarascon, and D. Gonbeau, *J. Electrochem. Soc.*, **152**, A689–A696 (2005).
88. D. Aurbach, K. Gamolsky, B. Markovsky, G. Salitra, Y. Gofer, U. Heider, R. Oesten, and M. Schmidt, *J. Electrochem. Soc.*, **147**, 1322–1331 (2000).
89. D. Aurbach, B. Markovsky, A. Rodkin, M. Cojocar, E. Levi, and H.-J. Kim, *Electrochimica Acta*, **47**, 1899–1911 (2002).
90. D. Aurbach, B. Markovsky, A. Rodkin, E. Levi, Y. S. Cohen, H.-J. Kim, and M. Schmidt, *Electrochimica Acta*, **47**, 4291–4306 (2002).
91. C. Yogi, D. Takamatsu, K. Yamanaka, H. Arai, Y. Uchimoto, K. Kojima, I. Watanabe, T. Ohta, and Z. Ogumi, *J. Power Sources*, **248**, 994–999 (2014).

92. M. Xu, N. Tsiouvaras, A. Garsuch, H. A. Gasteiger, and B. L. Lucht, *J. Phys. Chem. C*, **118**, 7363–7368 (2014).
93. T. Liu, A. Garsuch, F. Chesneau, and B. L. Lucht, *J. Power Sources*, **269**, 920–926 (2014).
94. H. J. Ploehn, P. Ramadass, and R. E. White, *J. Electrochem. Soc.*, **151**, A456–A462 (2004).
95. D. Lu, M. Xu, L. Zhou, A. Garsuch, and B. L. Lucht, *J. Electrochem. Soc.*, **160**, A3138–A3143 (2013).
96. R. Fathi, J. C. Burns, D. A. Stevens, H. Ye, C. Hu, G. Jain, E. Scott, C. Schmidt, and J. R. Dahn, *J. Electrochem. Soc.*, **161**, A1572–A1579 (2014).
97. N. N. Sinha, A. J. Smith, J. C. Burns, G. Jain, K. W. Eberman, E. Scott, J. P. Gardner, and J. R. Dahn, *J. Electrochem. Soc.*, **158**, A1194–A1201 (2011).
98. J. Chen, C. Buhrmester, and J. R. Dahn, *Electrochem. Solid-State Lett.*, **8**, A59–A62 (2005).
99. J. Vetter, P. Novák, M. R. Wagner, C. Veit, K.-C. Möller, J. O. Besenhard, M. Winter, M. Wohlfahrt-Mehrens, C. Vogler, and A. Hammouche, *J. Power Sources*, **147**, 269–281 (2005).
100. W. Choi and A. Manthiram, *J. Electrochem. Soc.*, **153**, A1760 (2006).
101. K. Amine, J. Liu, and I. Belharouak, *Electrochem. Commun.*, **7**, 669–673 (2005).
102. G. G. Amatucci, J. M. Tarascon, and L. C. Klein, *Solid State Ion.*, **83**, 167–173 (1996).
103. N. P. W. Pieczonka, Z. Liu, P. Lu, K. L. Olson, J. Moote, B. R. Powell, and J.-H. Kim, *J. Phys. Chem. C*, **117**, 15947–15957 (2013).
104. J.-P. Boeue and B. Simon, US Patent 5626981 (1997).
105. D. Aurbach, K. Gamolsky, B. Markovsky, Y. Gofer, M. Schmidt, and U. Heider, *Electrochimica Acta*, **47**, 1423–1439 (2002).
106. H. Ota, Y. Sakata, A. Inoue, and S. Yamaguchi, *J. Electrochem. Soc.*, **151**, A1659–A1669 (2004).
107. D. P. Abraham, M. M. Furczon, S.-H. Kang, D. W. Dees, and A. N. Jansen, *J. Power Sources*, **180**, 612–620 (2008).
108. L. E. Ouatani, R. Dedryvère, C. Siret, P. Biensan, S. Reynaud, P. Iratçabal, and D. Gonbeau, *J. Electrochem. Soc.*, **156**, A103–A113 (2009).

109. L. E. Ouatani, R. Dedryvère, C. Siret, P. Biensan, and D. Gonbeau, *J. Electrochem. Soc.*, **156**, A468–A477 (2009).
110. C. Chen, Y. E. Hyung, D. R. Vissers, and K. Amine, US Patent 7026074 (2006).
111. G. Chen, G. V. Zhuang, T. J. Richardson, G. Liu, and P. N. Ross, *Electrochem. Solid-State Lett.*, **8**, A344–A347 (2005).
112. Y. Hu, W. Kong, Z. Wang, H. Li, X. Huang, and L. Chen, *Electrochem. Solid-State Lett.*, **7**, A442–A446 (2004).
113. J. M. Vollmer, L. A. Curtiss, D. R. Vissers, and K. Amine, *J. Electrochem. Soc.*, **151**, A178–A183 (2004).
114. J. Li, W. Yao, Y. S. Meng, and Y. Yang, *J. Phys. Chem. C*, **112**, 12550–12556 (2008).
115. K. Abe, H. Yoshitake, T. Kitakura, T. Hattori, H. Wang, and M. Yoshio, *Electrochimica Acta*, **49**, 4613–4622 (2004).
116. R. McMillan, H. Slegel, Z. Shu, and W. Wang, *J. Power Sources*, **81–82**, 20–26 (1999).
117. S. S. Zhang, K. Xu, and T. R. Jow, *Electrochem. Solid-State Lett.*, **5**, A206–A208 (2002).
118. S. S. Zhang, K. Xu, and T. R. Jow, *J. Power Sources*, **113**, 166–172 (2003).
119. J. Barker, F. Gao, M. Y. Saidi, and C. Scordilis-Kelley, US Patent 5846673 (1998).
120. E. Wang, D. Ofer, W. Bowden, N. Iltchev, R. Moses, and K. Brandt, *J. Electrochem. Soc.*, **147**, 4023–4028 (2000).
121. K. Takechi and T. Shiga, US Patent 6235431 (2001).
122. Z. Chen, W. Q. Lu, J. Liu, and K. Amine, *Electrochimica Acta*, **51**, 3322–3326 (2006).
123. M. Koide, H. Sugimoto, M. Takahashi, H. Takase, and S. Tsujioka, European Union Patent 1195834 (2002).
124. S. Tsujioka, H. Takase, M. Takahashi, H. Sugimoto, and M. Koide, US Patent 6787267 (2004).
125. J. W. Braithwaite, A. Gonzales, G. Nagasubramanian, S. J. Lucero, D. E. Peebles, J. A. Ohlhausen, and W. R. Cieslak, *J. Electrochem. Soc.*, **146**, 448–456 (1999).
126. B. H. Loo, Y. G. Lee, and D. O. Frazier, *J. Phys. Chem.*, **89**, 4672–4676 (1985).

127. J. C. Burns, G. Jain, A. J. Smith, K. W. Eberman, E. Scott, J. P. Gardner, and J. R. Dahn, *J. Electrochem. Soc.*, **158**, A255–A261 (2011).
128. D. Xiong, J. C. Burns, A. J. Smith, N. Sinha, and J. R. Dahn, *J. Electrochem. Soc.*, **158**, A1431–A1435 (2011).
129. J. C. Burns, N. N. Sinha, D. J. Coyle, G. Jain, C. M. VanElzen, W. M. Lamanna, A. Xiao, E. Scott, J. P. Gardner, and J. R. Dahn, *J. Electrochem. Soc.*, **159**, A85–A90 (2011).
130. N. N. Sinha, J. C. Burns, and J. R. Dahn, *J. Electrochem. Soc.*, **160**, A709–A714 (2013).
131. R. Petibon, C. P. Aiken, N. N. Sinha, J. C. Burns, H. Ye, C. M. VanElzen, G. Jain, S. Trussler, and J. R. Dahn, *J. Electrochem. Soc.*, **160**, A117–A124 (2013).
132. L. E. Downie, K. J. Nelson, R. Petibon, V. L. Chevrier, and J. R. Dahn, *ECS Electrochem. Lett.*, **2**, A106–A109 (2013).
133. K. J. Nelson, J. Xia, and J. R. Dahn, *J. Electrochem. Soc.*, **161**, A1884–A1889 (2014).
134. J. Xia, L. Ma, C. P. Aiken, K. J. Nelson, L. P. Chen, and J. R. Dahn, *J. Electrochem. Soc.*, **161**, A1634–A1641 (2014).
135. C. P. Aiken, J. Self, R. Petibon, X. Xia, J. M. Paulsen, and J. R. Dahn, *J. Electrochem. Soc.*, **162**, A760–A767 (2015).
136. J. Self, C. P. Aiken, R. Petibon, and J. R. Dahn, *J. Electrochem. Soc.*, **162**, A796–A802 (2015).
137. B. Li, M. Xu, T. Li, W. Li, and S. Hu, *Electrochem. Commun.*, **17**, 92–95 (2012).
138. B. Li, M. Xu, B. Li, Y. Liu, L. Yang, W. Li, and S. Hu, *Electrochimica Acta*, **105**, 1–6 (2013).
139. B. Li, Y. Wang, H. Rong, Y. Wang, J. Liu, L. Xing, M. Xu, and W. Li, *J. Mater. Chem. A*, **1**, 12954–12961 (2013).
140. L. Madec, J. Xia, R. Petibon, K. J. Nelson, J.-P. Sun, I. G. Hill, and J. R. Dahn, *J. Phys. Chem. C*, **118**, 29608–29622 (2014).
141. L. Xing, W. Li, M. Xu, T. Li, and L. Zhou, *J. Power Sources*, **196**, 7044–7047 (2011).
142. X. Zuo, C. Fan, X. Xiao, J. Liu, and J. Nan, *J. Power Sources*, **219**, 94–99 (2012).
143. X. Zuo, C. Fan, X. Xiao, J. Liu, and J. Nan, *ECS Electrochem. Lett.*, **1**, A50–A53 (2012).

144. T. Kumeuchi, K. Zama, and D. Kono, US Patent 20120227253 (2012).
145. T. Huang, M. Wu, W. Wang, Y. Pan, and G. Fang, *J. Power Sources*, **262**, 303–309 (2014).
146. A. Terahara, T. Yamamoto, and K. Nakane, US Patent 6379846 (2002).
147. V. Bhat, G. Cheng, S. Kaye, B. Li, R. Olugbile, and J. H. Yang, US Patent 20120315536 (2012).
148. S. Mai, M. Xu, X. Liao, J. Hu, H. Lin, L. Xing, Y. Liao, X. Li, and W. Li, *Electrochimica Acta*, **147**, 565–571 (2014).
149. H. Rong, M. Xu, L. Xing, and W. Li, *J. Power Sources*, **261**, 148–155 (2014).
150. G. Yan, X. Li, Z. Wang, H. Guo, and C. Wang, *J. Power Sources*, **248**, 1306–1311 (2014).
151. Y.-M. Song, J.-G. Han, S. Park, K. T. Lee, and N.-S. Choi, *J. Mater. Chem. A*, **2**, 9506–9513 (2014).
152. N. N. Sinha, J. C. Burns, and J. R. Dahn, *J. Electrochem. Soc.*, **161**, A1084–A1089 (2014).
153. H. Gan, E. S. Takeuchi, and R. Rubino, US Patent 6919141 (2005).
154. Y. Yamada, K. Furukawa, K. Sodeyama, K. Kikuchi, M. Yaegashi, Y. Tateyama, and A. Yamada, *J. Am. Chem. Soc.*, **136**, 5039–5046 (2014).
155. R. Wang, X. Li, Z. Wang, H. Guo, M. Su, and T. Hou, *J. Alloys Compd.*, **624**, 74–84 (2015).
156. K. Abe, K. Miyoshi, T. Hattori, Y. Ushigoe, and H. Yoshitake, *J. Power Sources*, **184**, 449–455 (2008).
157. Y. Zhu, Y. Li, M. Bettge, and D. P. Abraham, *Electrochimica Acta*, **110**, 191–199 (2013).
158. D. Y. Wang, N. N. Sinha, R. Petibon, J. C. Burns, and J. R. Dahn, *J. Power Sources*, **251**, 311–318 (2014).
159. D. Y. Wang, N. N. Sinha, J. C. Burns, R. Petibon, and J. R. Dahn, *J. Power Sources*, **270**, 68–78 (2014).
160. D. Y. Wang, J. Xia, L. Ma, K. J. Nelson, J. E. Harlow, D. Xiong, L. E. Downie, R. Petibon, J. C. Burns, A. Xiao, W. M. Lamanna, and J. R. Dahn, *J. Electrochem. Soc.*, **161**, A1818–A1827 (2014).

161. J. Xia, C. P. Aiken, L. Ma, G. Y. Kim, J. C. Burns, L. P. Chen, and J. R. Dahn, *J. Electrochem. Soc.*, **161**, A1149–A1157 (2014).
162. A. L. Lavoisier and P. S. Laplace, *Mém. Acad. R. Sci.*, 355 – 408 (1780).
163. I. Wadsö, *Acta Chem. Scand.*, **22**, 927–937 (1968).
164. J. Suurkuusk and I. Wadsö, *J. Chem. Thermodyn.*, **6**, 667–679 (1974).
165. I. Wadsö and R. N. Goldberg, *Pure Appl. Chem.*, **73**, 1625 – 1639 (2001).
166. TA Instruments, TAM Basic Theory And Applications Training Course (2007).
167. J. R. Dahn, W. R. McKinnon, J. J. Murray, R. R. Haering, R. S. McMillan, and A. H. Rivers-Bowerman, *Phys. Rev. B*, **32**, 3316–3318 (1985).
168. D. Bernardi, E. Pawlikowski, and J. Newman, *J. Electrochem. Soc.*, **132**, 5–12 (1985).
169. L. Rao and J. Newman, *J. Electrochem. Soc.*, **144**, 2697–2704 (1997).
170. L. D. Hansen and H. Frank, *J. Electrochem. Soc.*, **134**, 1–7 (1987).
171. L. D. Hansen and R. M. Hart, *J. Electrochem. Soc.*, **125**, 842–845 (1978).
172. K. E. Thomas and J. Newman, *J. Power Sources*, **119–121**, 844–849 (2003).
173. L. J. Krause, L. D. Jensen, and J. R. Dahn, *J. Electrochem. Soc.*, **159**, A937–A943 (2012).
174. W. Dreyer, J. Jamnik, C. Guhlke, R. Huth, J. Moškon, and M. Gaberšček, *Nat. Mater.*, **9**, 448–453 (2010).
175. T. Zheng, W. R. McKinnon, and J. R. Dahn, *J. Electrochem. Soc.*, **143**, 2137–2145 (1996).
176. R. Chandrasekaran, *J. Power Sources*, **262**, 501–513 (2014).
177. R. Zhao, J. Gu, and J. Liu, *J. Power Sources*, **266**, 422–432 (2014).
178. E. Markevich, M. D. Levi, and D. Aurbach, *J. Electroanal. Chem.*, **580**, 231–237 (2005).
179. D. W. Dees, S. Kawauchi, D. P. Abraham, and J. Prakash, *J. Power Sources*, **189**, 263–268 (2009).
180. W. R. McKinnon, J. R. Dahn, J. J. Murray, R. R. Haering, R. S. McMillan, and A. H. Rivers-Bowerman, *J. Phys. C Solid State Phys.*, **19**, 5135 (1986).

181. F. Reif, *Fundamentals of Statistical and Thermal Physics*, p. 672, Waveland Press, (2009).
182. S. A. Hallaj, R. Venkatachalapathy, J. Prakash, and J. R. Selman, *J. Electrochem. Soc.*, **147**, 2432–2436 (2000).
183. W. Lu and J. Prakash, *J. Electrochem. Soc.*, **150**, A262–A266 (2003).
184. H. Yang and J. Prakash, *J. Electrochem. Soc.*, **151**, A1222–A1229 (2004).
185. Y. Kobayashi, H. Miyashiro, K. Kumai, K. Takei, T. Iwahori, and I. Uchida, *J. Electrochem. Soc.*, **149**, A978–A982 (2002).
186. H. Bang, H. Yang, Y. K. Sun, and J. Prakash, *J. Electrochem. Soc.*, **152**, A421–A428 (2005).
187. W. Lu, I. Belharouak, D. Vissers, and K. Amine, *J. Electrochem. Soc.*, **153**, A2147–A2151 (2006).
188. S. Al Hallaj, J. Prakash, and J. R. Selman, *J. Power Sources*, **87**, 186–194 (2000).
189. J.-S. Hong, H. Maleki, S. Al Hallaj, L. Redey, and J. R. Selman, *J. Electrochem. Soc.*, **145**, 1489–1501 (1998).
190. K. Onda, H. Kameyama, T. Hanamoto, and K. Ito, *J. Electrochem. Soc.*, **150**, A285–A291 (2003).
191. K. Onda, T. Ohshima, M. Nakayama, K. Fukuda, and T. Araki, *J. Power Sources*, **158**, 535–542 (2006).
192. J. P. Schmidt, A. Weber, and E. Ivers-Tiffée, *Electrochimica Acta*, **137**, 311–319 (2014).
193. C. Forgez, D. Vinh Do, G. Friedrich, M. Morcrette, and C. Delacourt, *J. Power Sources*, **195**, 2961–2968 (2010).
194. J. R. Dahn, *Phys. Rev. B*, **44**, 9170–9177 (1991).
195. J. N. Reimers and J. R. Dahn, *J. Electrochem. Soc.*, **139**, 2091–2097 (1992).
196. Y. Saito, K. Takano, K. Kanari, A. Negishi, K. Nozaki, and K. Kato, *J. Power Sources*, **97–98**, 688–692 (2001).
197. J.-S. Kim, J. Prakash, and J. R. Selman, *Electrochem. Solid-State Lett.*, **4**, A141–A144 (2001).
198. W. Lu, I. Belharouak, S. H. Park, Y. K. Sun, and K. Amine, *Electrochimica Acta*, **52**, 5837–5842 (2007).

199. K. E. Thomas and J. Newman, *J. Electrochem. Soc.*, **150**, A176–A192 (2003).
200. H. Joachin, T. D. Kaun, K. Zaghieb, and J. Prakash, *J. Electrochem. Soc.*, **156**, A401–A406 (2009).
201. W. Lu, I. Belharouak, J. Liu, and K. Amine, *J. Electrochem. Soc.*, **154**, A114–A118 (2007).
202. Y. Saito, K. Kanari, and K. Takano, *J. Power Sources*, **68**, 451–454 (1997).
203. Y. Saito, M. Shikano, and H. Kobayashi, *J. Power Sources*, **244**, 294–299 (2013).
204. W. Lu, I. Belharouak, J. Liu, and K. Amine, *J. Power Sources*, **174**, 673–677 (2007).
205. V. L. Chevrier, L. Liu, D. B. Le, J. Lund, B. Molla, K. Reimer, L. J. Krause, L. D. Jensen, E. Figgemeier, and K. W. Eberman, *J. Electrochem. Soc.*, **161**, A783–A791 (2014).
206. J. C. Burns, L. J. Krause, D.-B. Le, L. D. Jensen, A. J. Smith, D. Xiong, and J. R. Dahn, *J. Electrochem. Soc.*, **158**, A1417–A1422 (2011).
207. D. L. Wood III, J. Li, and C. Daniel, *J. Power Sources*, **275**, 234–242 (2015).
208. P.-C. J. Chiang, M.-S. Wu, and J.-C. Lin, *Electrochem. Solid-State Lett.*, **8**, A423–A427 (2005).
209. J. Li, E. Murphy, J. Winnick, and P. A. Kohl, *J. Power Sources*, **102**, 302–309 (2001).
210. T. M. Bond, J. C. Burns, D. A. Stevens, H. M. Dahn, and J. R. Dahn, *J. Electrochem. Soc.*, **160**, A521–A527 (2013).
211. C. P. Aiken, J. Xia, D. Y. Wang, D. A. Stevens, S. Trussler, and J. R. Dahn, *J. Electrochem. Soc.*, **161**, A1548–A1554 (2014).
212. M. E. Brown, *Handbook of Thermal Analysis and Calorimetry: Principles and Practice*, p. 725, Elsevier, (1998).
213. LakeShore Cyrotronics, Cryogenic Wire Technical Specifications, <http://www.lakeshore.com/products/Cryogenic-Accessories/Wire/Pages/Specifications.aspx> (accessed June 12, 2015).
214. A. J. Smith, J. C. Burns, X. Zhao, D. Xiong, and J. R. Dahn, *J. Electrochem. Soc.*, **158**, A447–A452 (2011).
215. L. Ma, D. Y. Wang, L. E. Downie, J. Xia, K. J. Nelson, N. N. Sinha, and J. R. Dahn, *J. Electrochem. Soc.*, **161**, A1261–A1265 (2014).

216. J.-M. Atebamba, J. Moskon, S. Pejovnik, and M. Gaberscek, *J. Electrochem. Soc.*, **157**, A1218–A1228 (2010).
217. J. C. Burns, R. Petibon, K. J. Nelson, N. N. Sinha, A. Kassam, B. M. Way, and J. R. Dahn, *J. Electrochem. Soc.*, **160**, A1668–A1674 (2013).
218. L. E. Downie and J. R. Dahn, *J. Electrochem. Soc.*, **161**, A1782–A1787 (2014).
219. M. Broussely, P. Biensan, F. Bonhomme, P. Blanchard, S. Herreyre, K. Nechev, and R. J. Staniewicz, *J. Power Sources*, **146**, 90–96 (2005).
220. S. Krueger, R. Kloepsch, J. Li, S. Nowak, S. Passerini, and M. Winter, *J. Electrochem. Soc.*, **160**, A542–A548 (2013).
221. G. Yan, X. Li, Z. Wang, H. Guo, and C. Wang, *J. Power Sources*, **248**, 1306–1311 (2014).
222. M. Winter, P. Novák, and A. Monnier, *J. Electrochem. Soc.*, **145**, 428–436 (1998).
223. L. Downie, S. R. Hyatt, A. T. B. Wright, and J. R. Dahn, *J. Phys. Chem. C*, **118**, 29533–29541 (2014).
224. J. Li, L. E. Downie, L. Ma, W. Qiu, and J. R. Dahn, *J. Electrochem. Soc.*, **162**, A1401–A1408 (2015).
225. G. Strang, *Introduction to Linear Algebra*, p. 584, Wellesley-Cambridge Press, (2003).
226. D. C. Harris, *J. Chem. Educ.*, **75**, 119 (1998).
227. W. L. Calhoun, *J. Chem. Eng. Data*, **28**, 146–148 (1983).
228. J. K. Choi and M. J. Joncich, *J. Chem. Eng. Data*, **16**, 87–90 (1971).
229. L. Ma, J. Xia, and J. R. Dahn, *J. Electrochem. Soc.*, **161**, A2250–A2254 (2014).
230. K. J. Nelson, G. L. d'Eon, A. T. B. Wright, L. Ma, J. Xia, and J. R. Dahn, *J. Electrochem. Soc.*, **162**, A1046–A1054 (2015).
231. H.-J. Noh, S. Youn, C. S. Yoon, and Y.-K. Sun, *J. Power Sources*, **233**, 121–130 (2013).
232. Y.-K. Sun, D.-J. Lee, Y. J. Lee, Z. Chen, and S.-T. Myung, *ACS Appl. Mater. Interfaces*, **5**, 11434–11440 (2013).
233. J.-H. Shim, C.-Y. Kim, S.-W. Cho, A. Missiul, J.-K. Kim, Y. J. Ahn, and S. Lee, *Electrochimica Acta*, **138**, 15–21 (2014).



234. X. Xiang, J. C. Knight, W. Li, and A. Manthiram, *J. Phys. Chem. C*, **118**, 21826–21833 (2014).
235. C. R. Fell, M. Chi, Y. S. Meng, and J. L. Jones, *Solid State Ion.*, **207**, 44–49 (2012).
236. C. R. Fell, D. Qian, K. J. Carroll, M. Chi, J. L. Jones, and Y. S. Meng, *Chem. Mater.*, **25**, 1621–1629 (2013).
237. D. Y. Wang, A. Xiao, L. Wells, and J. R. Dahn, *J. Electrochem. Soc.*, **162**, A169–A175 (2014).
238. L. Ma, J. Xia, X. Xia, and J. R. Dahn, *J. Electrochem. Soc.*, **161**, A1495–A1498 (2014).
239. D.-H. Cho, C.-H. Jo, W. Cho, Y.-J. Kim, H. Yashiro, Y.-K. Sun, and S.-T. Myung, *J. Electrochem. Soc.*, **161**, A920–A926 (2014).
240. H. Shi, X. Wang, P. Hou, E. Zhou, J. Guo, J. Zhang, D. Wang, F. Guo, D. Song, X. Shi, and L. Zhang, *J. Alloys Compd.*, **587**, 710–716 (2014).
241. W. Li, J. N. Reimers, and J. R. Dahn, *Solid State Ion.*, **67**, 123–130 (1993).
242. L. Ma, J. Xia, and J. R. Dahn, *J. Electrochem. Soc.*, **162**, A1170–A1174 (2015).
243. K. Amine and Y. Sun, *Nano Lett.*, **14**, 4873–4880 (2014).
244. J. Xia, L. Ma, W. Qiu, L. Madec, L. D. Ellis, K. J. Nelson, Z. Lu, and J. R. Dahn, *In Preparation*.
245. J. G. Frick, J. W. Weaver, R. L. Arceneaux, and M. F. Stansbury, *J. Polym. Sci.*, **20**, 307–315 (1956).
246. B. I. Chaudhary, J. M. Cogen, and J. S. Parent, *J. Therm. Anal. Calorim.*, **105**, 279–285 (2011).
247. M. Onuki, S. Kinoshita, Y. Sakata, M. Yanagidate, Y. Otake, M. Ue, and M. Deguchi, *J. Electrochem. Soc.*, **155**, A794–A797 (2008).
248. L. Xing, W. Li, C. Wang, F. Gu, M. Xu, C. Tan, and J. Yi, *J. Phys. Chem. B*, **113**, 16596–16602 (2009).
249. L. Xing and O. Borodin, *Phys. Chem. Chem. Phys.*, **14**, 12838–12843 (2012).
250. M. Holzapfel, A. Würsig, W. Scheifele, J. Vetter, and P. Novák, *J. Power Sources*, **174**, 1156–1160 (2007).
251. T. Zheng and J. R. Dahn, *J. Power Sources*, **68**, 201–203 (1997).
252. E. Buiel and J. R. Dahn, *Electrochimica Acta*, **45**, 121–130 (1999).

253. J. R. Croy, K. G. Gallagher, M. Balasubramanian, Z. Chen, Y. Ren, D. Kim, S.-H. Kang, D. W. Dees, and M. M. Thackeray, *J. Phys. Chem. C*, **117**, 6525–6536 (2013).
254. C. Delmas, M. Maccario, L. Croguennec, F. Le Cras, and F. Weill, *Nat. Mater.*, **7**, 665–671 (2008).
255. K. G. Gallagher, D. W. Dees, A. N. Jansen, D. P. Abraham, and S.-H. Kang, *J. Electrochem. Soc.*, **159**, A2029–A2037 (2012).
256. M. Nie, J. Xia, L. Ma, and J. R. Dahn, *In Preparation*.
257. W. D. Good and N. K. Smith, *J. Chem. Eng. Data*, **14**, 102–106 (1969).
258. W. D. Good, D. W. Scott, and G. Waddington, *J. Phys. Chem.*, **60**, 1080–1089 (1956).
259. L. Madec, J. Xia, and J. R. Dahn, *In Preparation*.
260. E. J. Prosen and J. C. Colbert, *J. Res. Natl. Bur. Stand.*, **85**, 193–203 (1980).
261. J. R. Dahn, J. Jiang, L. M. Moshurchak, M. D. Fleischauer, C. Buhrmester, and L. J. Krause, *J. Electrochem. Soc.*, **152**, A1283–A1289 (2005).
262. Z. Chen, Y. Qin, and K. Amine, *Electrochimica Acta*, **54**, 5605–5613 (2009).
263. T. J. Rademaker, G. R. A. Akkermans, D. L. Danilov, and P. H. L. Notten, *J. Electrochem. Soc.*, **161**, E3365–E3372 (2014).
264. A. J. Smith, N. N. Sinha, and J. R. Dahn, *J. Electrochem. Soc.*, **160**, A235–A242 (2013).


APPENDIX A

LICENSE AGREEMENTS

Copyright license agreements for reprinted articles used in this thesis are given here.

Home
Account Info
Help
Live Chat



Title: A novel and precise measuring method for the entropy of lithium-ion cells: ΔS via electrothermal impedance spectroscopy

Publication: Electrochimica Acta

Publisher: Elsevier

Date: 10 August 2014

Copyright © 2014 Elsevier Ltd. All rights reserved.

Logged in as:
Laura Downie
Account #: 3000898815

LOGOUT

Order Completed

Thank you very much for your order.

This is a License Agreement between Laura Downie ("You") and Elsevier ("Elsevier"). The license consists of your order details, the terms and conditions provided by Elsevier, and the [payment terms and conditions](#).

[Get the printable license.](#)

License Number	3632070430778
License date	May 18, 2015
Licensed content publisher	Elsevier
Licensed content publication	Electrochimica Acta
Licensed content title	A novel and precise measuring method for the entropy of lithium-ion cells: ΔS via electrothermal impedance spectroscopy
Licensed content author	None
Licensed content date	10 August 2014
Licensed content volume number	137
Licensed content issue number	n/a
Number of pages	9
Type of Use	reuse in a thesis/dissertation
Portion	figures/tables/illustrations
Number of figures/tables/illustrations	1
Format	both print and electronic
Are you the author of this Elsevier article?	No
Will you be translating?	No
Original figure numbers	8
Title of your thesis/dissertation	The application of isothermal microcalorimetry to the study of parasitic reactions in lithium ion batteries
Expected completion date	Jul 2015
Estimated size (number of pages)	250
Elsevier VAT number	GB 494 6272 12
Permissions price	0.00 USD
VAT/Local Sales Tax	0.00 USD / 0.00 GBP
Total	0.00 USD

ORDER MORE...

CLOSE WINDOW

Copyright © 2015 Copyright Clearance Center, Inc. All Rights Reserved. [Privacy statement](#), [Terms and Conditions](#). Comments? We would like to hear from you. E-mail us at customer@copyright.com

**Title:**

Determination of the Time
Dependent Parasitic Heat Flow in
Lithium Ion Cells Using
Isothermal Microcalorimetry

Logged in as:

Laura Downie

Account #:

3000898815

Author:

L. E. Downie, S. R. Hyatt, A. T. B.
Wright, et al

[LOGOUT](#)**Publication:**

The Journal of Physical Chemistry
C

Publisher:

American Chemical Society

Date:

Dec 1, 2014

Copyright © 2014, American Chemical Society

PERMISSION/LICENSE IS GRANTED FOR YOUR ORDER AT NO CHARGE

This type of permission/license, instead of the standard Terms & Conditions, is sent to you because no fee is being charged for your order. Please note the following:

- Permission is granted for your request in both print and electronic formats, and translations.
- If figures and/or tables were requested, they may be adapted or used in part.
- Please print this page for your records and send a copy of it to your publisher/graduate school.
- Appropriate credit for the requested material should be given as follows: "Reprinted (adapted) with permission from (COMPLETE REFERENCE CITATION). Copyright (YEAR) American Chemical Society." Insert appropriate information in place of the capitalized words.
- One-time permission is granted only for the use specified in your request. No additional uses are granted (such as derivative works or other editions). For any other uses, please submit a new request.

[BACK](#)[CLOSE WINDOW](#)

Copyright © 2015 Copyright Clearance Center, Inc. All Rights Reserved. [Privacy statement](#), [Terms and Conditions](#).
Comments? We would like to hear from you. E-mail us at customercare@copyright.com